Diss. ETH No. 21004

Contributions Towards Optimized Antennas for On-Body Operation

A dissertation submitted to the

ETH ZURICH

for the degree of
Doctor of Sciences

presented by

CHUNG-HUAN LI

MSc National Taiwan University of Science and Technology
born 20 05 1979
citizen of Taiwan

accepted on the recommendation of

Prof. Dr. G. Szekely, examiner
Prof. Dr. N. Kuster, co-examiner
Prof. T. Samaras, co-examiner

2013

Contents

v

Summary

The number of mobile phone subscribers, as reported by the International Telecommunication Union, surpassed the six billion milestone in October 2012; each of these phones includes various transmitters operating at different frequencies. Mobile transmitters became pervasive throughout the world within three decades of the first deployments in Tokyo in 1979, which was followed by the introduction of the Nordic Mobile Telephone (NMT) system in northern European countries in 1981. Within the next few months, 4th generation (4G) handsets will be fully deployed. During the last decade, wireless data networks in offices, homes, and public spaces (airports, trains, hotels, etc.) have also become widespread. This explosion in the usage of handheld transmitters has generated the need for research on small efficient antennas and associated exposure risk assessments.

The coupling mechanisms of transmitters in close proximity to the body (head and trunk), including dependence on head and body shape (external anatomy), complex tissue distribution (internal anatomy), age, ears, implants, antenna factors, etc., have been studied in detail during the last ten years. A large portion of the research related to these issues was conducted by PhD students at the ETH and IT'IS Foundation during the 1990s and early 2000s. This research resulted in new guidelines for antenna development, product standards, and was fundamental to progress in risk assessment related to the radiofrequency (RF) exposure associated with mobile phone use.

In this thesis, some of the main remaining unresolved issues, namely, the effect of the hand on antenna performance and RF exposure of the hand and head, is addressed. In the first study of Part I (Chapter 4), the effect of the hand on over-the-air (OTA) performance of the transmitter is investigated. The objectives were to provide input for standardization and tools

for optimization of handheld transmitters. The results of the study reveal that testing the OTA performance without the hand (standard practice at the time of the study) correlates only poorly to real-life performance. The significance of hand parameters with respect to OTA performance impairments were, in order of importance: 1) the position of the index finger; 2) the distance between the phone case and palm; 3) the position of the remaining fingers; 4) the size of the hand; 5) dielectric parameters; and 6) wrist length and tilt. An unexpected finding of the study is that the presence of the hand may increase the exposure of the head in some cases. This, together with further evidence from experimental studies conducted by industry, laid the groundwork for the second study.

In the second study of Part I (Chapter 5), the influence of the user's hand holding a mobile phone to the ear on the peak spatial specific absorption rate (psSAR) averaged for 1g and 10g samples of head tissue was investigated both experimentally and computationally, and the results compared to current measurement standards, i.e., the measurement of SAR in a head phantom without a hand present. The mechanisms of interaction between the hand and mobile phone models were studied. In addition, simulations and measurements at 900 and 1800 MHz were conducted to elucidate the hand grip parameters that lead to higher SAR in the head. Numerical simulations were conducted on four mobile phone models, and parameters such as the palm-phone distance and hand position were varied. Measurements were made on 46 commercial mobile phones, and the maximum psSAR at different hand positions and palm-phone distances was recorded. Both simulations and measurements demonstrate that the increase in the psSAR inside the head caused by the presence of the hand may exceed 2.5 dB. Furthermore, the psSAR is sensitive to hand grip, i.e., the variations can exceed 3 dB.

The last study of Part I (Chapter 6) describes remaining questions regarding the exposure of the hand, i.e., the fingers and palm. First, the mechanisms of absorption in the hand of electromagnetic (EM) fields in the 900 to 3700 MHz frequency range was analyzed, and the envelope of the psSAR of the hand with respect to the psSAR limits calculated. Further investigations included whether a standardized test method based on a flat phantom is conservative. The results demonstrate that the absorption of RF energy in the hand is larger than that predicted by testing with a flat phantom; enhancements of several dB are observed, depending on the model parameters. The results are used to generate correction factors for conservative estimation of

SAR in the hand measured with flat phantoms.

These studies have been published in peer-reviewed journals and presented to standards groups and government agencies. Over-the-air (OTA) evaluations are currently conducted with hand phantoms included. The groups that develop product standards for demonstration of compliance with safety limits are currently working to integrate this knowledge into the next revision of the standards.

While Part I addresses the issue of how to optimize antennas that minimally couple with the human body with maximized omni-directional radiation, Part II focuses on the counter task of developing antenna configurations that couple effectively to specific tissue regions (tumors) while minimizing exposure of healthy tissues and radiation into the environment. Hyperthermia (HT) was considered a promising treatment modality already during the 1970s and 1980s, until two large clinical trials showed that HT correlates only poorly with recovery rates of cancer patients. Today, it is believed that the lack of proper applicators and reliable treatment tools were largely responsible for the failure of HT in the clinical trials. The complexity and difficulty involved in designing HT applicators, especially for non-invasive application (external delivery of EM power), was underestimated.

Part II begins with a brief background and the biological rationale of HT treatment, and a literature review of the EM technology used and proposed for noninvasive HT applications, including low-frequency methods, phased arrays at RF frequencies, and some alternative approaches. The final study (Chapter 10) describes the design of a novel HT applicator, based on a phased array of cavity-backed slot antennas, developed for treatment of tumors in the head-and-neck region. The design of the antenna array as well as optimization of patient positioning based on the location of the tumor is covered, as we have found that the position of the body, which had been overlooked in previous studies, is critical for optimized exposure. A real patient model was tested with this applicator and the optimized position, and the results show that more than 90% of the tumor volume can be irradiated with sufficient EM exposure, without the development of non-target hotspots. The applicator design has significant advantages over the current prototypes currently being tested in clinical trials.

These findings form the basis of a treatment approach currently in use at the ERASMUS MC Oncology Center in Rotterdam and also serve as input towards development of next generation applicators to be employed at the University of Zurich in 2014.

Zusammenfassung

Die Zahl der Nutzer von Mobiltelefonen, die von der Internationalen Fernmeldeunion (ITU) angegeben wird, überschritt im Oktober 2012 die Marke von sechs Milliarden. Jedes dieser Mobiltelefone enthält unterschiedliche Sender, die auf verschiedenen Frequenzen arbeiten. Nach ihrem ersten Einsatz in Tokio im Jahre 1979, dem 1981 die Einführung des Nordic Mobile Telephone (NMT) Systems in den Ländern Nordeuropas folgte, durchdrangen tragbare Sender innerhalb dreier Jahrzehnte die ganze Welt. In den kommenden Monaten werden Mobilgeräte der vierten Generation (4G) vollständig eingeführt. Während des vergangenen Jahrzehnts wurden drahtlose Datennetze am Arbeitsplatz, zu Hause und an öffentlichen Plätzen (an Flughäfen, in Zügen, in Hotels usw.) ebenfalls allgegenwärtig. Durch diese Explosion bei der Nutzung tragbarer Sender entstand neuer Forschungsbedarf auf den Gebieten der Entwicklung kleiner und effizienter Antennen und der Bewertung der Risiken durch die mit ihrer Verwendung einhergehende Belastung.

Die Kopplungsmechanismen von Sendern in unmittelbarer Nähe des Körpers (Kopf und Rumpf) einschliesslich der Abhängigkeit von der Form des Kopfes und des Körpers (externe Anatomie), von der komplexen Verteilung der Körpergewebe (interne Anatomie), vom Alter, von den Ohren, von Implantaten, von den Eigenschaften der Antenne usw. wurden in den vergangenen zehn Jahren im Detail untersucht. Ein Grossteil der Forschung auf diesen Gebieten wurde von Doktoranden der ETH und der IT'IS Foundation in den 1990er und 2000er Jahren durchgeführt. Die Forschungsarbeiten führten zu neuen Richtlinien für die Antennenentwicklung und für Produktnormen, und sie waren entscheidend für Fortschritte bei der Abschätzung der Risiken durch Belastung durch Hochfrequenz (HF) beim Gebrauch von Mobiltelefonen.

Diese Arbeit befasst sich mit einigen der wesentlichen unbeantwortet gebliebenen Fragen, nämlich mit dem Einfluss der Hand auf die Betriebseigenschaften der Antenne und auf die Belastung des Kopfes und der Hand selbst. In der ersten Studie des ersten Teils (Kapitel 4) wird der Einfluss der Hand auf die Freiraumübertragungseigenschaften (over-the-air performance) des Senders untersucht. Zielsetzung war es, zur Standardisierung und zu Werkzeugen für die Optimierung tragbarer Sender beizutragen. Die Ergebnisse der Studie zeigten, dass die Messung der Freiraumübertragungseigenschaften ohne die Hand (gängige Praxis zur Zeit der Studie) nur mangelhaften Aufschluss über die Leistungsfähigkeit in realen Situationen gibt. Die Bedeutung der Parameter der Hand im Bezug auf die festgestellte Beeinträchtigung der Freiraumübertragungseigenschaften sind (nach Stellenwert geordnet): 1) die Position des Zeigefingers, 2) der Abstand zwischen dem Gehäuse des Telefons und der Handfläche, 3) die Position der übrigen Finger, 4) die Grösse der Hand, 5) die dielektrischen Eigenschaften und 6) die Länge und Neigung des Handgelenks. Ein unerwartetes Ergebnis der Studie war, dass die Gegenwart der Hand in manchen Fällen zu einem Anstieg der Belastung des Kopfes führt. Dies - zusammen mit weiteren Anhaltspunkten aus Messungen, die von der Industrie durchgeführt worden waren - legte die Grundlagen für die zweite Studie.

In der zweiten Studie des Teiles I (Kapitel 5) untersuchte ich sowohl messtechnisch als auch mittels numerischer Simulationen den Einfluss der Hand des Benutzers eines am Ohr gehaltenen Mobiltelefons auf die über 1 g und 10 g Kopfgewebe gemittelte Peak-Spatial-Average-SAR und verglich die Ergebnisse mit den geläufigen Messnormen, die die Bestimmung der SAR in einem Kopfphantom ohne Verwendung einer Hand definieren. Die Mechanismen der Beeinflussung zwischen Hand und Mobiltelefonmodellen werden untersucht, und zusätzlich werden Simulationen und Messungen bei 900 MHz und 1800 MHz durchgeführt, um diejenigen Parameter des Griffs zu erklären, die zu höherer SAR im Kopf führen. Vier Modelle von Mobiltelefonen wurden simuliert, und Parameter wie z. B. der Abstand zwischen Handfläche und Telefon und die Position der Hand wurden variiert. 46 handelsübliche Mobiltelefone wurden gemessen und ihre maximale Peak-Spatial-Average-SAR bei unterschiedlichen Handpositionen und Abständen zwischen Handfläche und Telefon aufgezeichnet. Sowohl die Simulationen als auch die Messungen zeigen, dass der Anstieg der Peak-Spatial-Average-SAR im Kopf, der durch die Hand verursacht wird, 2,5 dB überschreiten kann. Zudem reagiert die Peak-Spatial-Average-SAR empfindlich auf die

Eigenschaften des Griffs, d. h., die Unterschiede können 3 dB überschreiten.

Die letzte Studie des Teiles I (Kapitel 6) beschreibt verbleibende Fragen im Hinblick auf die Belastung der Hand, d. h. der Finger und der Handfläche. Zuerst wurde der Absorptionsmechanismus elektromagnetischer (EM) Felder in der Hand im Frequenzbereich von 900 MHz bis 3700 MHz analysiert, und eine Hüllkurve für die Peak-Spatial-Average-SAR im Bezug auf die Grenzwerte wird berechnet. Weiterhin untersuchten wir, ob ein standardisiertes Testverfahren mit einem Flachphantom ein konservatives Ergebnis liefert. Die Ergebnisse zeigen, dass die Absorption der HF-Energie in der Hand grösser ist als die durch das Flachphantom bestimmten Werte. In Abhängigkeit von den Modellparametern wurden Erhöhungen von einigen dB beobachtet. Mit diesen Ergebnissen wurden Korrekturfaktoren bestimmt, mit denen sich die SAR in der Hand durch Messung an einem Flachphantom konservativ bestimmen lässt.

Diese Studien wurden in referierten Fachzeitschriften veröffentlicht und Normierungsausschüssen und Regierungsbehörden vorgestellt. Bei der Ermittlung der Freiraumübertragungseigenschaften (over-the-air performance) werden derzeit Handphantome verwendet. Die Ausschüsse, die Produktnormen zur Überprüfung der Grenzwerte entwickeln, bereiten die Einbindung der Erkenntnisse dieser Arbeit in die nächsten Revisionen der Normen vor.

Während sich Teil I mit der Frage nach der Optimierung von Antennen befasst, die möglichst wenig Energie in den menschlichen Körper einkoppeln und gleichzeitig über bestmögliche Rundstrahleigenschaften verfügen, konzentriert sich Teil II auf die entgegengesetzten Fragestellung, nämlich auf die Entwicklung von Antennenkonfigurationen, die effektiv in bestimmte Geweberegionen (Tumore) einkoppeln, wobei die Belastung des gesunden Gewebes und die Abstrahlung in die Umgebung minimiert werden sollen. Die Hyperthermie (HT) wurde bereits in den siebziger und achtziger Jahren des vergangenen Jahrhunderts als vielversprechendes Behandlungsverfahren betrachtet, bis zwei klinische Grossstudien zeigten, dass HT-Behandlung nur in mangelhaftem Zusammenhang mit den Genesungsraten von Krebspatienten steht. Heute glaubt man, dass der Mangel an geeigneten HT-Applikatoren und zuverlässigen Behandlungswerkzeugen allgemein für das Scheitern der HT in den klinischen Studien verantwortlich zu machen ist. Die Komplexität und die Schwierigkeiten bei der Entwicklung von HT-Applikatoren wurden insbesondere bei nichtinvasiver Anwendung (Applikation der HF-Leistung von aussen) unterschätzt.

Teil II beginnt mit einer kurzen Zusammenfassung der Grundlagen und des biologischen Prinzips der HT-Behandlung sowie mit einer Literaturübersicht zu bereits verwendeten und neu vorgeschlagenen EM-Technologien für nicht-invasive HT-Anwendungen. Diese schliesst auch Niederfrequenzmethoden, Phased-Array-Antennen (HF) und einige alternative Ansätze mit ein. Die abschliessende Studie (Kapitel 10) beschreibt den Entwurf eines neuartigen HT-Applikators, der auf einem Phased-Array aus Schlitzantennen basiert und für die Behandlung von Tumoren im Kopf- und Halsbereich entwickelt wurde. Der Entwurf des Antennenarrays und die Optimierung der Lage des Patienten an Hand der Position des Tumors wird beschrieben, da ein Ergebnis der Studie war, dass die Lage des Körpers für die optimierte Anwendung entscheidend ist - ein Ergebnis, das in vorangegangenen Studien übersehen wurde. Das Modell eines realen Patienten wird mit diesem Applikator in optimierter Lage getestet, und die Ergebnisse zeigen, dass mehr als 90 % des Tumors mit ausreichender Belastung durch elektromagnetische Felder bestrahlt werden kann, ohne dass es zu Hotspots ausserhalb der Zielregion kommt. Dieser Applikator hat massgebliche Vorteile gegenüber anderen aktuellen Prototypen, die derzeit in klinischen Tests untersucht werden.

Diese Ergebnisse bilden die Basis eines Behandlungsansatzes, der zur Zeit beim ERASMUS MC Zentrum für Onkologie in Rotterdam verwendet wird. Darüberhinaus dienen sie als Beitrag zur Entwicklung der Folgegeneration von Applikatoren, die im Jahre 2014 an der Universität Zürich verwendet werden wird.

Acknowledgments

I was fortunate to join a more than excellent software team when I started my PhD at the IT'IS Foundation in April 2007. The support and friendship I experienced from all members of this organization is more than any PhD Student could hope for. First and foremost, my deepest gratitude goes to my group leader, Dr. Nik Chavannes, and the Foundation director, Prof. Niels Kuster, for giving me the chance to carry out this thesis. I would especially like to thank Nik for his excellent leadership of our group, for his always outstanding scientific advice, and also for his support throughout this thesis as a friend. Furthermore, I would like to thank the Foundation's associate director, Dr. Myles Capstick, for his support and for being my project leader in hyperthermia treatment and the UWB link-budget evaluation. Also, I wish to thank Prof. Theodoros Samaras for agreeing without hesitation to be a co-examiner of my thesis.

It would not have been possible to complete this work without a professional academic environment, and I would like to express my gratitude to Prof. Szekely and his staff for welcoming me into their excellent research group and for supervising my work.

This thesis was generously supported by the Swiss Commission for Technology and Innovation (CTI) and Schmid & Partner Engineering AG (SPEAG), as well as Zurich Med Tech (ZMT). Special thanks go to the Nokia Research Center NRC, Finland, and Motorola Electronics Private Ltd., Singapore, for providing detailed CAD data and for their friendly cooperation.

My very special thanks go to all the people involved in the SEMCAD X project. In particular, Dr. Erdem Ofli for his great and generous support in aspects both academic and non-academic. Erdem has been a mentor to me during my entire PhD study. I also really appreciate my colleague and friend

Chapter 1

Objectives and Overviews

1.1 Objectives and Methods

Prior to joining the IT'IS Foundation, I worked for an antenna company, developing antennas for handheld devices. My main experience and research interests were body-mounted antennas, and I became frustrated with the general performance of antennas integrated in handsets and also with the lack of knowledge available for the optimization of such antennas. Consequently, in April 2007 I joined the IT'IS Foundation, already recognized as a leading research group in this field, as a Ph.D. student. At that time, the main open research questions related to body-mounted antennas were 1) the effect of the hand on handset antenna performance and 2) the optimization of antenna arrays for hyperthermia (HT). As the IT'IS Foundation had recently begun to be active in the field of hyperthermia applicators and treatment planning tools, I decided to tackle both problems for my PhD studies, which resulted in the following main objectives:

- To close the knowledge gaps regarding the effects of the user's hand on mobile phone antenna performance and the specific absorption rate (SAR) in the user's head and hand. As this issue had not been studied comprehensively before, the results of the investigation would provide important insight for antenna engineers and also for the product standards (compliance testing with electromagnetic (EM) safety limits and over-the-air (OTA) performance evaluations). The research

included the following three studies:

- – systematic evaluation and weighting of the hand parameters that affect OTA performance;

- – assessment and quantification of the presence of the hand on the exposure of the head;

- – investigation of the absorption mechanism in the hand and proposals for conservative methodology for demonstrating compliance of the induced SAR values in the hand with safety limits.

- To investigate optimized antenna configurations for non-invasive HT treatment. The research was divided into the following subparts:

- – a comprehensive review of HT applicators;

- – development of a novel HT applicator design for the head and neck region;

- – evaluation of the effects of optimized patient positioning on treatment efficacy.

Fundamental to the success of my PhD studies were the methods and tools available at the ETH and the IT'IS Foundation. The primary tool used in my studies and to which I was able to contribute some novel features (not part of this thesis) was SEMCAD X. This was jointly developed by the IT'IS Foundation and Schmid & Partner Engineering AG (Zurich, Switzerland) and commercialized by the latter. The SEMCAD X radiofrequency (RF) solver is a highly optimized implementation of the Yee algorithm [19] heavily accelerated on graphics processing units (GPUs) (also pioneered by SEMCAD X). SEMCAD X has proven to be a very effective simulation package for the design and evaluation of body-mounted transmitters. Furthermore, the tool is fully compatible for simulations with the Virtual Population of the IT'IS Foundation, today's quasi-standard for anatomical models. For experimental validation, I was able to rely on the advanced near-field laboratory at the IT'IS Foundation, which comprises RF chambers and state-of-the-art analysis instrumentation, including several DASY52 NEO and iSAR systems.

1.2 Overview Chapter

My PhD studies are described in the following, subdivided into two parts:

- Part I

  - *Chapter 2* reviews the basic mechanisms of interactions between a user's hand and an antenna.

  - *Chapter 3* is a review of the literature regarding hand effects on mobile phone antenna performance.

  - *Chapter 4* studies the effect of the user's hand on mobile phone antenna performance, with different types of mobile phones considered.

  - *Chapter 5* investigates the effect of the user's hand on SAR in the head. The objectives were to investigate scenarios and assess levels of SAR increase due to the presence of the user's hand.

  - *Chapter 6* fills the knowledge gap regarding the exposure of the hand holding a mobile phone: mechanisms of SAR coupling to the hand are analyzed, the maximum SAR envelope is determined, and potential methodologies for demonstration of compliance are investigated.

  - *Chapter 7* summarizes the studies on interactions between the user's hand and mobile phone antennas.

- Part II

  - *Chapter 8* introduces HT treatment and discusses the rationale for conducting HT treatment, including the results of biological studies and clinical trials.

  - *Chapter 9* is a literature review of HT technology based on non-invasive EM power, including the introduction of proposed applicator designs, the algorithms used to optimize the magnitude and phase of each antenna for a given target, and discussion of various general topics.

  - *Chapter 10* proposes a novel design for a HT applicator for tumors of the head and neck region, based on an antenna array; the investigation includes the single-element and array design,

as well as the optimization of patient positioning in the applicator for tumors at different locations.

– *Chapter 11* summarizes the studies on HT treatment with non-invasive EM power.

1.3 Overview Publications

Journal Papers

1. C.-H. Li, E. Ofli, N. Chavannes and N. Kuster. Effects of Hand Phantom on Mobile Phone Antenna Performance. *IEEE Transactions on Antennas and Propagation*. 57(9):2763-2770, 2009.

2. E. Ofli, C.-H. Li, N. Chavannes and N. Kuster. Analysis and Optimization of Mobile Phone Antenna Radiation Performance in the Presence of Head and Hand Phantoms. *Turk. J. Elec. Engin*. 16(1):67-77, 2008.

3. C.-H. Li, M. Douglas, E. Ofli, B. Derat, S. Gabriel, N. Chavannes and N. Kuster, N. Influence of the Hand on the Specific Absorption Rate in the Head. *IEEE Transactions on Antennas and Propagation*. 60(2):1066-1074, 2012.

4. C.-H. Li, M. Douglas, E. Ofli, N. Chavannes, Q. Balzano, and N. Kuster. Mechanisms of RF Electromagnetic Field Absorption in Human Hands and Fingers. *IEEE Transactions on Microwave Theory and Techniques*. 60(7):2267-2276, 2012.

Conference Papers

1. C.-H. Li, E. Ofli, N. Chavannes, E. Cherubini, H. Gerber, N. Kuster. Effects of hand phantom and different use patterns on mobile phone antenna radiation performance. *IEEE Antennas and Propagation Society International Symposium, AP-S 2008*. 1-4, 2008

2. C.-H. Li, E. Ofli, N. Chavannes and N. Kuster. The Effects of Hand Phantom on Mobile Phone Antenna OTA Performance. *European Conference on Antennas and Propagation, 2007. EuCAP 2007*. 1-5, 2007.

3. C.-H. Li, E. Ofli, N. Chavannes and N. Kuster. SAR and Efficiency Performance of Mobile Phone Antenna with Different User Hand Positions. *IEEE Antennas and Propagation Society International Symposium, AP-S 2009*. 1-4, 2009.

4. C.-H. Li, M. Douglas, E. Ofli, B. Derat, N. Chavannes and N. Kuster. Analysis of the Hand Effect on Head SAR with Generic and CAD Phone Models Using FDTD. *IEEE Antennas and Propagation Society International Symposium, AP-S 2010*. 1-4, 2010.

5. C.-H. Li, E. Ofli, N. Chavannes and N. Kuster. The Influence of the User Hand on Mobile Phone Antenna Performance in Data Mode. *European Conference on Antennas and Propagation, 2007. EuCAP 2009*. 449-452, 2009.

6. M. G. Douglas, B. Derat, C.-H. Li, X.-W. Liao, E. Ofli, N. Chavannes and N. Kuster. Reliability of Specific Absorption Rate Measurements in the Head Using Standardized Hand Phantoms. *European Conference on Antennas and Propagation, 2010. EuCAP 2010*, 1-4, 2010.

7. C.-H. Li, M. Capstick, E. Neufeld, N. Chavannes and N. Kuster. Optimization of Patient Position in Hyperthermia Treatment for Head and Neck Region. *IEEE Antennas and Propagation Society International Symposium, AP-S 2009*, 1-4, 2009.

8. C.-H. Li, M. Douglas, E. Ofli, B. Derat, and N. Kuster. User's Hand Effect on the Specific Absorption Rate in the Head. *IEEE Antennas and Propagation Society International Symposium, AP-S 2011*. 141-144, 2011.

9. A. A. H. Azremi, J. Ilvonen, C.-H. Li, J. Holopainen, P. Vainikainen. Influence of the User's Hand on Mutual Coupling of Dual-Antenna Structures on Mobile Terminal. *European Conference on Antennas and Propagation, 2007. EuCAP 2012*. 1222-1226, 2012.

10. X.-L. Chen, S. Benkler, C.-H. Li, N. Chavannes and N. Kuster. Low Frequency Electromagnetic Field Exposure Study with Posable Human Body Model. *IEEE International Symposium on Electromagnetic Compatibility (EMC)*. 702-705, 2010.

11. C.-H. Li, P. Futter, N. Chavannes and N. Kuster. Investigation of the Shielding on the Mobile Phone PCB Using FDTD. *Asia-Pacific Symposium on Electromagnetic Compatibility (APEMC)*. 657-659, 2010.

12. C.-H. Li, P. Futter, N. Chavannes and N. Kuster. Effects of PCB Shielding on Trace Coupling Using FDTD. *European Conference on Antennas and Propagation, 2010. EuCAP 2010*. 1-2, 2010.

13. C.-H. Li, J. Jekkonen, G. Tudosie, N. Chavannes and N. Kuster. Study of Mutual Coupling on Mobile Phone PCB with Shielding Using FDTD. *IEEE International Symposium on Electromagnetic Compatibility (EMC)*. 419-424, 2010.

Part I

EM Interaction Between the User Hand and the Mobile Phone Antenna

Chapter 2

Introduction to the Hand Effects Studies

Effects of high dielectric permittivity and lossy or dissipative (high dielectric constant and Joule losses or loss tangent) medium (DLM) on antennas have been studied for decades for scientific, technical and medical applications. It is well known that DLM, such as human tissue or sea water, can significantly affect antenna performance and behavior by its proximity [1]. The background and basic physics of the hand effects studies conducted for this thesis are introduced in this chapter. Simple scenarios are used to illustrate the change of antenna performance due to the presence of DLM. The findings in the simple scenarios are applied to explain the mechanisms of hand-antenna interaction. The current RF safety standards regarding the hands of cell phone users are also discussed as the studies presented herein aim at filling the knowledge gaps in these standards. Finally, an outline of the studies on human hand exposure to RF energy from cell phones is presented at the end of this chapter.

2.1 Antennas in the Proximity of DLM

If an antenna is immersed into DLM without insulation, RF conduction and displacement currents excited by the antenna flow into the material. The power loss due to the current flow is much higher compared to that of an

insulated antenna [1, 21]. This feature has been commonly used for therapy by RF ablation. In addition, the input impedance of the antenna is sensitive to the medium characteristics due to direct contact. This sensitivity is suitable for probing material properties [1]. However, the power loss due to the direct contact is not desirable in most applications related to communication, such as antennas on a submarine, biometry or mobile phones. The radiation efficiency can be significantly improved if the antenna is insulated from DLM. Thus, the performance of insulated antennas in DLM is analyzed in following sections.

When a linear or loop antenna is placed parallel to and at a short distance from a planar slab of DLM, most power is radiated into the DLM [22, 23]. As reported by Smith *et al.*, this has been widely applied in ground penetrating radar to increase the antenna directivity. In addition, the input impedance also varies with the presence of DLM. If the distance is shorter than a quarter-wavelength, both resistance and reactance of a half-wavelength dipole antenna increase with DLM's proximity [24].

The interaction mechanism between a linear antenna and DLM can be illustrated by the case of a linear antenna in an eccentric insulation, whose theory was developed by King *et al.* [26, 27, 28]. The geometry is shown in Figure 2.1. Material properties in regions 1 and 2 are set as air and DLM, respectively.
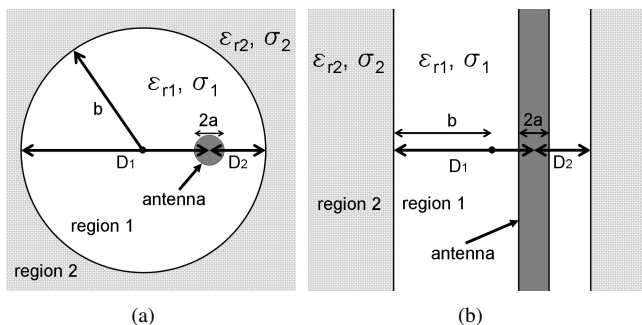
Figure 2.1: The (a) transverse and (b) axial view of a linear antenna with radius a coated with DLM (region 2) [27].

The current distribution on the insulated antenna behaves like that of a

lossy transmission line [26, 29]. The values a and b in Figure 2.1 are the inner and outer radius of the equivalent eccentric coaxial cable, respectively. Unlike a regular coaxial cable, the current on the DLM is displacement current instead of conduction current as illustrated in Figure 2.2(a) [28]. The wave travels along the antenna with great attenuation due to the power radiated into region 2. The phenomenon can be observed in the distribution of the Poynting vector, as seen in Figure 2.2(b). This is a section of a half-wavelength dipole antenna buried in a borehole of DLM, so it behaves like two quarter-wavelength open-end transmission lines. In region 1, the power flows in the axial direction as a standing wave of an open-end transmission line. In region 2, the Poynting vectors point in the radial direction as the power radiates out in this region, so the insulation of the antenna from the DLM enhances the radiation.

(a)   (b)
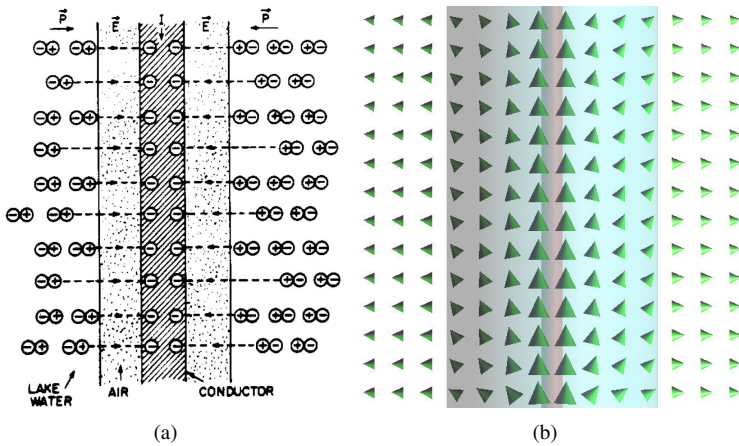
Figure 2.2: (a) An antenna with an insulation layer immersed in a dissipative high dielectric constant behaves like a transmission line because the DLM acts as the outer conductor with displacement current induced on its surface [28]. (b) The distribution of the Poynting vector shows that the wave travels mainly in the axial direction in region 1 as a transmission line, but radiates in the radial direction in region 2.

The propagation constant of this equivalent coaxial transmission line can

be derived as follows [27]

$$k_L^2 = k_1^2 \left(1 + \frac{2\Delta_0}{\Omega_a k_2 (D_1 + D_2)}\right) = (\beta + j\alpha)^2, \qquad (2.1)$$

where α and β are attenuation and phase constant respectively, and

$$
\begin{aligned}
k_i &= \omega\{\mu_0[\varepsilon_{ri} + j(\frac{\sigma_i}{\omega})]\}^{0.5} \qquad i = 1, 2, \\
\Omega_a &= \frac{1}{2} ln \frac{x_0[(D_1 + D_2)^2 - 2x_0(D_1 - D_2)]}{[x_0 - \frac{1}{2}(D_1 - D_2)](D_1 + D_2)^2}, \\
x_0 &= \frac{1}{D_1 - D_2}\left\{\left[\frac{1}{2}(D_1^2 + D_2^2) - a^2\right] - \right. \\
&\quad \left. \left[(\frac{1}{2}(D_1^2 + D_2^2) - a^2)^2 - \frac{1}{4}(D_1^2 + D_2^2)^2\right]^{0.5}\right\}, \qquad (2.2)
\end{aligned}
$$

where ε_{ri}, σ_i, D_1 and D_2 are defined in Figure 2.1, and

$$
\begin{aligned}
\Delta_0 &= \frac{H_0^{(1)}(\frac{1}{2}k_2(D_1 + D_2))}{H_1^{(1)}(\frac{1}{2}k_2(D_1 + D_2))} + \\
&\quad 2 \sum_{m=1}^{\infty} (\frac{2x_0(D_1 - D_2)}{(D_1 + D_2)^2})^m \frac{H_m^{(1)}(\frac{1}{2}k_2(D_1 + D_2))}{H_{m+1}^{(1)}(\frac{1}{2}k_2(D_1 + D_2))}, \qquad (2.3)
\end{aligned}
$$

where $H_m^{(1)}$ is the Hankel function of the first kind of order m.

Figure 2.3 shows the propagation constant (α and β, as defined in Equation 2.1) of the transmission line with different D_1 values while D_2 is 0.5 cm[1]. The phase constant is normalized to that in region 1. If D_1 is smaller than 3 cm, the transmission line has high attenuation and phase velocity. The near-field in this case becomes significantly different from that in free space or with planar medium, which leads to different impedance levels. Moreover, the characteristic impedance of the equivalent transmission line is lower than that in free space. Thus, the H-field around the antenna insulated in region 1 is higher than that without DLM.

---

[1]The D_2 value and D_1 range chosen here are typical values for the palm-phone and phone-head distance, respectively.

(a)   (b)
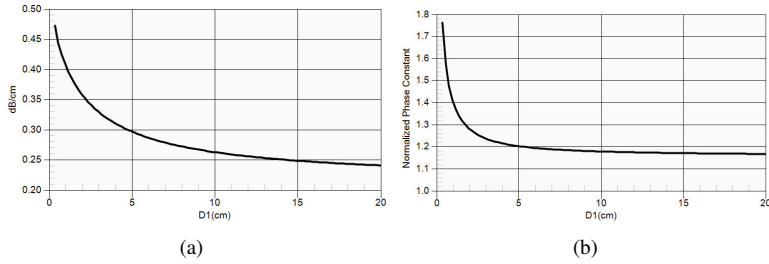
Figure 2.3: The (a) attenuation constant (α) and (b) phase constant (β) in Equation 2.1 with different D_1. The phase constant is normalized to that in region 1 (see Figure 2.1). ($D_2 = 0.5$ cm, $a = 0.1$ cm, $\varepsilon_{r2} = 40$, $\sigma_2 = 1$ S/m, 900 MHz)

The eccentricity can also distort the radiation pattern of the antenna [28, 30]. As shown in Figure 2.4, the directivity on the D_2 side is higher with larger b. A linear antenna above planar DLM is a special case of eccentric insulation with an infinite ratio between D_1 and D_2. As discussed above, the antenna has higher directivity if it is closer to the DLM slab. Thus, the radiation pattern can be controlled by D_1 and D_2, which can be applied in geophysical probing [30].

This part of the thesis summarizes the studies on the effects of the human hand on the performance of mobile phone antennas. The phenomena about the proximity of DLM reviewed in this section will therefore be applied to analyze the mechanisms of the hand-antenna interaction.

2.2 Presence of a User's Hand

During a voice call, a mobile phone is held by the user's hand next to the side of the head as in the talk mode seen in Figure 2.5. The hand and head are therefore typically in the reactive near field of the antenna and can significantly influence the radiation pattern, radiated efficiency, RF current coupling within the device and antenna impedance. Human tissues (skin, muscle, bone, etc.) are lossy dielectric materials at mobile phone frequencies [31, 32] and therefore absorb power from the antenna.

The effects of user's head have been widely studied in terms of both an-
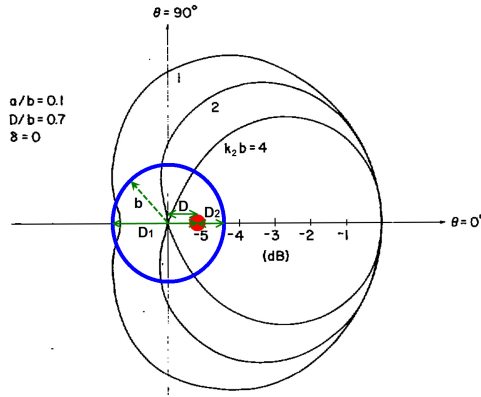
Figure 2.4: The radiation patterns of the antenna in Figure 2.1 for different values of radius b [27] [28]. (δ is the loss tangent angle of the material in region 2.)

Figure 2.5: The influence of a user's hand on the mobile phone antenna performance is mainly evaluated in the talk mode

tenna performance and Specific Absorption Rate (SAR) [33, 34, 35, 36, 37]. Compared to the head, a user's hand may have a more pronounced influence and it is a non-trivial topic for the following reasons. Firstly, a human hand has a much more complex geometry than the head. Secondly, a hand can be

in different positions with different grips, so the influence variation is much greater than that of the head. Finally, establishing a standard procedure and hand phantom for evaluating hand effects needs to consider various issues, such as meaningful positioning, definitions of hand grip and dimensions, and feasibility and repeatability of measurements.

The scenario in Figure 2.1 can be treated as a simplification of a mobile phone (dipole antenna) being held by a hand next to the head (DLM) with head-phone distance D_2 and palm-phone distance D_1. According to the study above, the presence of a hand can alter antenna performance in terms of input impedance, near-field distribution and far-field pattern. A decrease in palm-phone distance (D_2) can increase the loss in the hand and head [27] and attract more power radiating towards the hand. Figure 2.3 shows that k_L is not sensitive to the distance when it is longer than 3 cm. This indicates that part of the hand, such as the palm, has little influence on the near-field when it is more than 3 cm far from the antenna at 900 MHz. When a mobile phone is held by a hand, the hand only partially covers the mobile phone. As mentioned above, significant mismatch occurs between the fields with and without cover by the hand. Thus, if the coverage includes the feeding point of the mobile phone, the power generated from the feeding point would be confined under the hand.

When part of a hand, such as a finger tip, is very close to the antenna, the disturbance of the EM field due to the hand can be interpreted with the concept of a quasi-static field. This concept was proposed by Kuster *et al.* for explaining the mechanisms of SAR distribution in a head next to a mobile phone [38, 39]. If the E-field is higher than the H-field, the hand would cause more field distortion than power absorption due to high permittivity in the hand. On the contrary, quasi-static H-field distribution is not disturbed by the hand considerably, so a high H-field can lead to high power absorption because of the conduction current induced in the hand. It is well known that the proximity of DLM can lower the quality factor of the antenna because the stored magnetic energy in the hand is converted into power loss. Besides, the antenna is virtually larger by the combination of the conducting current on the antenna and the displacement current induced on the hand. An increase in antenna size usually leads to a decrease in the quality factor.

Although the simple scenario explains the basic mechanisms, an over-simplified scenario does not provide accurate estimation. In addition, the semi-3D scenario may not reveal all the phenomena occurring in the real

world. For that reason, many studies, including the studies in this thesis, investigate human body and hand effects on mobile phone antennas by numerical and experimental methods.

2.3   Status of the Effects of a User's Hand in the Product Standards

2.3.1   Mobile Phone Antenna Performance

Over-the-air (OTA) performance of mobile phones is determined by measuring the radiated 3D RF power and receiver performance in an anechoic chamber while the phone is placed with or without a Specific Anthropomorphic Mannequin (SAM) head filled with head simulation liquids in touch position. The results of the tests are summarized in two single values of merit referenced as Total Radiation Power (TRP) and Total Isotropic Sensitivity (TIS) that aim to provide a quantification for the performance of the phone in real-world usage conditions [12].

In April 2009, hand phantoms were released for an OTA test plan for certification of mobile telephones, developed by the CTIA [12], as shown in Figure 2.6. User studies were conducted in this standard in order to define four different hand grips representing the majority of devices, depending on the device width, form factor and usage mode [40][2]. One grip and one position are defined for the measurement of each mobile phone. The hand phantoms have homogeneous dielectric properties representing the parameters of a dry palm [41]. The hand models include a spacer for accurate mobile phone positioning. The spacer is made of low loss and low permittivity material so as to be non-perturbing to the fields around the antenna.

2.3.2   Safety Concerns

Regarding exposure and health issues, one quantity of importance related to the absorbed power is the Specific Absorption Rate (SAR), and SAR limits are established in international exposure standards for the whole-body averaged SAR and peak spatial-averaged SAR (psSAR) averaged over 1 g or

---

[2]This hand model is for testing mobile phones whose width is between 56 and 72 mm. Mobile devices wider than 72 mm are not considered in the current version of the standard.
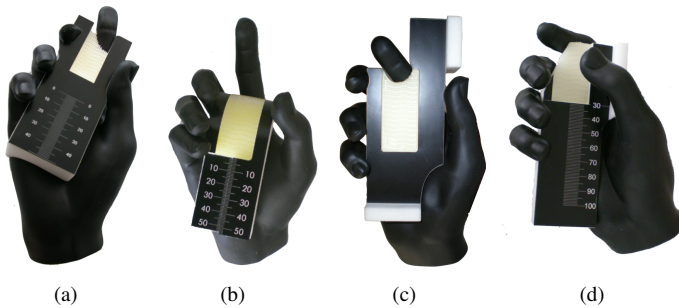
Figure 2.6: The CTIA-defined anthropomorphic hand phantoms for (a) candybar style, (b) clam-shell style and (c) wide mobile phones (like PDAs) in talk mode. (d) is a model also developed for data mode. The spacer attached on the palm is for phone positioning.

10 g of tissue [42, 43, 44]. Measurement standards and national regulations have been established to evaluate the psSAR in the user when using a mobile phone so that compliance with the exposure standards can be demonstrated [15, 14, 45].

These measurement standards do not specify the use of a hand model when measuring the SAR in the head because previous studies cited by the standards concluded that the SAR in the head is generally reduced when the hand is introduced [46, 47, 48, 49, 50]. A 1995 paper by Balzano *et al.* reported that the change in psSAR in the head due to the hand was negligible for large phones having sleeve dipole antennas and 10-30% lower for flip phones if the palm is in direct contact with the case [46]. A 1996 study by Meier with real hands and four mobile phones at 900 MHz and 1800 MHz showed that the psSAR in the head typically dropped significantly [47]. psSAR increases in the head above the measurement uncertainty were not observed. Measurements were limited to three fixed hand positions. A study by Kuster *et al.* in 1997 of twenty mobile phones came to the same conclusions [48]. A numerical study by Meyer *et al.* in 2001 with two simplified mobile phone models found an increase in psSAR in the head in one of the two cases of only 7% [49]. In the same year, Francavilla *et al.* simulated a mobile phone with a monopole antenna and a magnetic resonance (MR) image based anatomical hand model, and the study concluded

that head SAR is not changed considerably by a user's hand [51].

However, recent studies have found cases where the hand can significantly increase the psSAR in the user [52, 42]. Using anthropometric hand models, a study of body-worn devices by Francavilla and Schiavoni found that the psSAR in the body can increase by between 30% and 40% when the user's hand is holding the mobile phone [52]. Measurements were made on four mobile phones, and simulations were conducted on simplified mobile phone models with helical or whip antennas. In addition, it was found that head-SAR variation due to hand position is considerable [53, 54]. The variation could be up to 40% and 85% when the antenna is at the top and bottom, respectively [55].

Since the publication of these studies, several technological changes have taken place. Mobile phones have become smaller and antenna designs and locations have changed. Improvements in simulation tools and measurement systems have also been developed. The integration of CAD modeling of human anatomy into simulation tools and advanced algorithms for posing the anatomy have made it possible to study the influence of different hand grips [17]. The significant progress of computational tools and dramatic increase in processor speed have made it possible to simulate large parameter sets in a reasonable time. The development of fast SAR measurement systems has made it possible to measure large sample sizes of mobile phones [56]. Additionally, standardized hand phantoms have recently become available. The phantoms represent average hands for radio-frequency analysis of mobile phone performance. The same rationale applies to SAR measurement as to OTA performance testing.

Regarding the exposure in the hand, the peak spatial specific absorption rate (psSAR) averaged over any 10 g of tissues (psSAR10g) is limited to 4 W/kg for general public exposure of a person's hands [43, 44]. A standardized test method has recently been defined in IEC 62209-2 [15] for evaluating compliance with this limit in a user's hand holding a wireless device. The test method calls for measurements in a well-defined flat phantom. The flat phantom is filled with a homogeneous liquid to allow for scanning of the electric field probe. The dielectric parameters of the liquid are standardized to ensure that the psSAR in the phantom is conservative compared to that in a person [15]. Several aspects of the measurement standard are chosen to ensure low measurement uncertainty. Measurements in a hand model are not recommended because the electric field probe is large compared to the finger dimensions, resulting in higher measurement uncertainty due to bound-

ary effects and insufficient volume of material in the measurement region [15]. The standard document acknowledges that the use of a flat phantom to represent a conservative exposure of psSAR in the hand lacks supporting data, and our initial simulations of psSAR10g in anatomical hand models found that, in some cases, the flat phantom can underestimate the SAR in the hand.

2.4 Hand Studies in this Thesis

The studies conducted in this thesis regarding hand effects include:

- Review of studies of hand effects: This review starts by introducing the hand models used in these papers. The hand effects on mobile phone antenna performance are thoroughly reviewed. In addition, other scenarios and solutions for suppressing the hand effect are also introduced.

- Hand effects in OTA performance: A comprehensive study is carried out in this thesis to evaluate the effects of different parameters of a hand phantom such as homogeneity, material, hand dimensions, hand positions and hand grip, etc. Hand models have now been included in the current version of the standard for antenna performance measurement (Figure 2.6, [12]), and this study serves as a knowledge database for the standard during the development of the hand phantoms.

- Hand effects in head SAR: This study is an investigation of the influence of the user's hand on the radiated performance of a mobile phone, psSAR averaged over 1 g and 10 g in the head of the user. Recent papers have found that the psSAR in the head can be increased by the presence of the hand in some cases. The study in this thesis quantifies and analyzes the mechanism of the SAR increase in the head due to the hand, and it shows that the current measurement method may not be conservative.

- Estimation of hand SAR: The absorption of electromagnetic fields in the hand is investigated over the 900 to 3700 MHz frequency range. This enables the determination of the envelope of the psSAR in the hand. It also provides a basis for deriving measurement procedures

for evaluating compliance of wireless devices with SAR limits in the hands. Both plane waves and dipole antennas are used to investigate the patterns of RF absorption in hand and finger tissue models for far-field and near-field exposures[3].

---

[3]Although this thesis focuses on on-the-body operation, the analysis of SAR distribution illuminated by plane waves is very helpful in gaining physical insight of the absorption mechanisms.

Chapter 3

Literature Review of Hand Effects

The objective of this chapter is to provide a comprehensive literature review of studies of hand effects on mobile phone antenna. The performance of a mobile phone antenna is evaluated in terms of radiation and power absorption by human tissues. This review mainly focuses on studies about hand effects on radiation performance, as only limited papers exist reporting hand effects on safety compliance. Since analytical (or semi-analytical) approaches are limited by modeling complexity, most studies in this topic are conducted with numerical or experimental methods.

The geometrical complexity of the human hand requires various hand models to be used, so the hand models used in these studies are discussed firstly. The most common scenario of using a mobile phone is being held by a hand in talking position while the mobile phone is operated in the GSM system (Global System for Mobile Communication). Thus, the findings of the studies in this scenario are summarized and organized in terms of the parameters of antenna performance and geometry. Finally, it is now known that the hand can significantly degrade antenna performance. Some solutions have been proposed to reduce this degradation, which are included in this review.

3.1   The Hand Models for Evaluating Hand Effects

Real human hands are a common choice for measurement studies [57, 58, 59]. Although measurement with real human hands provides a realistic estimation of hand effects, the uncertainty of hand position and grip remains a challenge of this method.

Regarding simulation, simple hand models were used in many papers [60, 61, 62, 63, 64, 65, 54]. The typical geometry of a simple hand model is shown in Figure 3.1(a), which uses bricks to represent palm, thumb and fingers. The obvious disadvantage of a simple model is that it may not precisely reflect the effects of a real hand. For example, the variety of finger positions cannot be represented with a simple hand model. Thus, the estimation of input impedance and near-field absorption is not as accurate as using a realistic hand model. However, a simple model also has some advantages. Compared to the computer-aided design (CAD) file of an anatomical hand, it is much easier to define and model, so it is more reproducible and suitable for a parametric study. One of the studies in this thesis used simple hand models to investigate the hand effect at all possible hand positions on different mobile phone models. Also, the computational resources required for simulation using a simple hand model are less expensive.
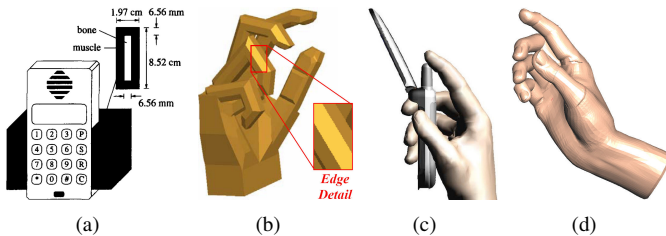
Figure 3.1: Different types of hand phantom used in hand-effect studies: (a) simple hand model [63], (b) semi-realistic hand model [66], (c) realistic hand model [67] and (d) the hand model defined in CTIA [12].

Realistic hand models, as seen in Figure 3.1(c) [67], are now widely used in simulation to obtain a more reasonable estimation of hand effects than from a simple hand model [12, 68, 69, 70, 71, 72, 67]. Both homo-

geneous and inhomogeneous materials are used for this type of phantom. In addition, an anatomical hand model based on MR images has also been used to simulate hand effects [51]. The material properties of an anatomical hand or a homogeneous hand phantom can be obtained in Gabriel's database [31, 32, 41]. Homogeneity is one important issue when using a realistic hand model, which is included in one of the studies in this thesis. A semi-realistic hand model, as seen in Figure 3.1(b), was proposed as a compromise between a realistic and a simple hand phantom [55, 66].

CTIA have defined a realistic, homogeneous hand model as the standard hand phantom for OTA performance measurement to evaluate the influence of a hand (Figure 3.1(d)). Recent studies about mobile antenna design have thus started to use the CTIA hand model [73, 74, 75]. The parameters required to define a standard hand phantom include dimensions, position, grip and material. The dimensions of the hand phantoms are average values of the 50th percentile sizes for men and women, taken from [76, 77, 78, 79]. The grip and position of the hand is of greatest importance. Many studies reviewed in this chapter, including the one conducted in this thesis, have demonstrated that different positioning of hand phantoms induces significantly different antenna performance. The studies in [11, 58] emphasized that multiple hand positions are required to represent the hand effect, so standardization of a hand phantom is difficult. Moreover, [59] concluded that it is difficult to develop a hand phantom suitable for all commercial mobile phones, and measurement with a hand phantom also increases uncertainty. [58] mentioned that homogeneous hand phantoms can represent real humans in terms of loss, but phantom positioning is critical. In any case, it is clear that inclusion of a hand in evaluating antenna performance is necessary [50].

A study regarding hand grip statistics shows that the majority of users have their thumb and fingers on the side faces [11]. However, the human factor studies in [40] and [80] concluded that the most common position of the index finger is actually on the back of the mobile phone for pressing the loud speaker[1], and that makes the index finger much closer to the mobile phone antenna in many cases.

---

[1]This conclusion is also consistent to that from the hand-grip study conducted in CTIA.

3.2   Hand Effects in Talk Mode

A user's hand can affect the radiation performance in terms of input impedance (mismatch), radiation efficiency and radiation pattern. Nowadays, the most common usage of a wireless device in the vicinity of a human body is talking on a mobile phone operated in the GSM900 (880-960 MHz) and GSM1800 (1710-1880 MHz) bands. Studies in this scenario are reviewed in this section, and organized in two aspects;

- The influences of a user's hand on different parameters of the antenna performance, such as mismatch loss and radiation efficiency.

- How different geometrical parameters affect the antenna performance, such as hand position, mobile phone types and their antenna designs.

However, it will be shown that there is no clear and consistant conclusion made among those studies. This indicates the complexity of this topic and importance of the studies in this thesis.

3.2.1   Parameters of Antenna Performance

As discussed in the previous chapter, when a linear antenna is close to planar DLM, the directivity of the antenna on the DLM side could be much higher than that on the free-space side. Thus, the radiation efficiency of the antenna may be lower than 50% while DLM only occupies half space. It was reported that a 900 MHz dipole antenna has only 15% efficiency when it is 6 mm away from a human body [81].

Using a mobile phone in the real world is a much more complex scenario; the near-field distribution varies with different types of mobile phones and antenna design. The head is neither planar nor spherical. More important, the hand only partially covers the mobile phone with numerous hand and finger positions. For a mobile phone with a monopole antenna, half the power was found to be absorbed by the head and hand [62]. A similar conclusion was confirmed by [63]: the head and hand absorbed 48-68% of power from a monopole antenna and different configurations of planar inverted-F antenna (PIFA). In this case, the hand not only absorbs power but may also increase the power absorption in the head by confining the fields under the hand. This implies that the hand effects with hand-only would be milder than that with head-and-hand. It has been suggested that a user's

hand should be away from a PIFA as the human body could decrease radiation efficiency by about 50% [82, 83].

When a whip (monopole) antenna is used at 900 MHz, a study with random field measurement (RFM) showed that the inclination angle of the terminal and protrude length of the antenna by users are responsible for the performance variation among users [84]. At GSM900, a measurement study with 15 users using helix, clamshell with helix and PIFA showed 3-8% efficiency remained mainly because of absorption loss [58]. According to the measurement results, body loss is about 9 dB, 12 dB and 15 dB for a PIFA, monopole and helical antenna, respectively [58]. Another measurement study at GSM1800 with 44 people revealed 3.4 dB and 9.7 dB absorption loss for patch and helical antenna, respectively [57]. A RFM study was conducted to investigate the influence of the human body on the RF signal strength received [85]. The hand effect on transmitted power may not be the same as that on received power as the distribution of signal strength varies with scattering environment. The measurement results concluded that people with a larger hand and body have a stronger influence.

The hand effect on input impedance of a dual-band PIFA was thoroughly analyzed by Boyle *et al.* in [65]. As seen in Figure 3.2, a simple hand model with an index finger was applied. The variables were vertical movement of the hand (d_H) and horizontal movement of the index finger (S_F). The input impedance of the PIFA is basically decomposed into two parts; the fundamental impedance models the behavior of the antenna without the slot, and the slot is equivalent to a parallel L-C circuit. The resonant(antiresonant) frequency due to the fundamental impedance(the slot) is between GSM900 and GSM1800 bands, which results in two bands matched at GSM900 and GSM1800 bands respectively[2]. The investigation in [65] can be summarized as follows: firstly, a user's hand causes the fundamental impedance more resistive and inductive. Only an index finger can change input impedance as much as when the entire antenna is covered. Secondly, proximity of the hand turns the slot on the PIFA from a parallel L-C circuit into L-C-R, and the antiresonance is moved from between GSM900 and GSM1800 to a lower frequency. The movement may induce large mismatch in GSM900 (so the quality factor at this band may be even larger than that without the hand). The measurement study in [11] with different designs of PIFAs confirmed

---

[2]More details of the analysis can be found in [65] and its related works, which are excellent works thoroughly analyzing the behavior of a dual-band PIFA.

this conclusion. In the GSM900 band, the hand causes lossy inductive load to input impedance, but the hand effects could be diverse in the GSM1800 band with different antenna designs.
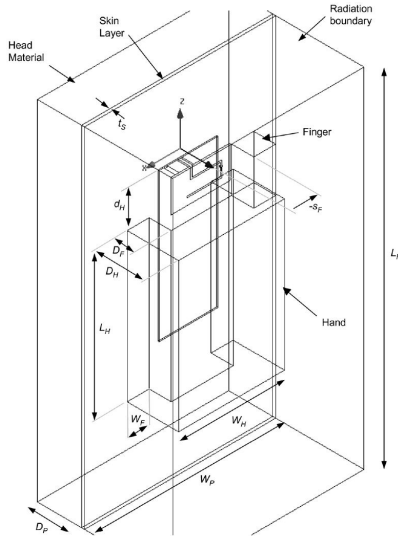
Figure 3.2: The phone and hand model used in [65] for studying the effect of the hand in input impedance.

Regarding mismatch loss, different studies could produce various results because of different antenna designs. Resonance shift of a monopole antenna was observed due to inductive loading from a hand [62]. Note that the inductive loading causes a shift of input impedance toward a lower frequency, but the variation of input impedance is not necessary to be inductive as well. When the antenna is operated close to antiresonance, which is commonly observed in a PIFA design for a commercial mobile phone, the influence of a hand may be inductive or capacitive on input impedance. The simulation results in [63] showed the presence of a hand has little influence on mismatch of a monopole antenna, but it has significant influence on a low-profile antenna, like a PIFA, when it is covered by the hand. This is because the monopole antenna is an external antenna which is not covered by the hand in a common grip, but a part of the hand, such as the index finger,

may easily cover an internal low-profile antenna design. Severe detuning occurs when the index finger touches a helical antenna on a clamshell mobile phone (from 12 dB to 3 dB in return loss, [67]). A similar message was also sent from [55, 65] with a PIFA. Stronger detuning occurs when a PIFA is at the bottom [69]. Mismatch influence of less than 2 dB by a user was reported in a big measurement study at GSM1800 (44 people)[57]. In the chapter about hand effects on OTA performance in this thesis, variation of input impedance of a PIFA due to different touch positions by a index finger is analyzed in more detail.

Compared to mismatch loss and the distortion of the radiation pattern, absorption loss is considered as the most important issue of human body effects [69, 67, 55, 57].

3.2.2 Geometrical Parameters

Small phone size not only makes the antenna but also the chassis (the ground plane or main printed circuit board (PCB) of the mobile phone) and other metal parts of the phone contribute to radiation. For this reason, the position and grip of a user's hand become more important in altering antenna performance of a small mobile phone. The chassis of a mobile phone could be close to or in resonance (especially in GSM900). The chassis then becomes the main radiator and the antenna acts as a resonator for impedance matching [86]. Consequently, it is not surprising to find that loss at 900 MHz is more dependent on hand positions than at 1800 MHz (if the antenna is not covered) [58]. Several measurement studies came to similar conclusions. Hand positions and grip are responsible for the large TRP variation among 13 users and anatomical difference contributes a minor effect. The standard deviation is 3 dB and the difference between minimum and maximum TRP is 8 dB [59, 87]. Compared to the phone-head angle and distance, hand positioning is the main reason for efficiency variation with patch and helix in GSM1800 [88].

As mentioned previously, a small palm-phone distance can cause more loss [69]. Several dB decrease in efficiency due to different palm-phone distances was reported in [54]. It is common to place the index finger on the back of the phone in talk mode, just where the antenna is placed in many candy-bar mobile phones. When the index finger is above the antenna, the influence can be severe (50% of power absorbed by the index finger) and hard to estimate (up to 3 dB variation due to different finger positions) [69].

In fact, the study conducted in this thesis shows the variation could be even higher than 3 dB with a small shift of the index finger position. For a natural grip, the remainder of the fingers and the thumb are placed according to the hand position and palm-phone distance, which are usually on the side faces of a mobile phone. Thus, the positioning of these fingers is considered to be less important. In the RFM study mentioned above [85], the hand's proximity to the feed point has significant influence on the receiving RF signal strength, regardless of body size.

In a long mobile phone, such as a clamshell type, hand positions induce more variation in total efficiency than candy-bar phones [53], but the hand causes more loss on a smaller mobile phone [88, 69]. An internal antenna is usually more sensitive to hand positions than an external antenna as an internal antenna can easily be covered by a user's hand [55]. A PIFA was reported as having better performance regarding interaction to the hand and head than a helical antenna in some studies [11, 88, 83, 58]. Placing a PIFA at the back, away from the user, would cause less body loss [63]. Nevertheless, a helix was also found to perform better than a PIFA when considering the hand only [83].

With respect to operation frequency bands, a mobile phone usually has different human body interaction between GSM900 and GSM1800. It has been shown that mobile phones in GSM900 are about 3 dB worse than GSM1800 in body loss (PIFA, helix, clamshell with helix), but GSM1800 has more loss in the hand (slightly more than half of the total loss in GSM900, twice more than the head in GSM1800) [58]. In GSM1800, as it has a more complex near-field distribution than GSM900, a bigger variation of mismatch efficiency was found due to hand positions and grip [58]. According to this paper, the total efficiency was -13.3 dB and -11.2 dB for GSM900 and GSM1800, respectively, and influence on mismatch in GSM900 was more pronounced than that in GSM1800. Antenna performance at 900 MHz is sensitive to hand positions on the phone, and would be more sensitive at 1800 MHz if the hand covers the antenna [54]. The hand effect in mismatch is different in different papers as it depends on mobile phone and antenna designs. If the antenna is not covered by the hand or the index finger in common hand positions and grips, mismatch in GSM1800 is influenced less than in GSM900.

The conclusions made by the studies reviewed above are varied and are even opposite in some cases, which conveys the complexity of this topic. The key issues of the variation include both the mobile phones and the

hands. The mobile phone industry has experienced very fast development, which results in continuous change of mobile phone design, such as dimension, geometry and antenna design. Moreover, due to extreme proximity of the user's hand, various hand models, positions and grips used in those studies lead to different results. The study in this thesis focuses on the influence of different parameters of the hand model.

3.3 Solutions for Suppressing Hand Effects

An early design showed that at 150 MHz the vicinity of the human body to a business portable radio can alter the impedance matching of its helical antenna [89]. The mismatch loss can be adjusted by changing the capacitors in the matching network. The adjustment is based on body-device distance sensed in real time and simulation results obtained beforehand. However, the situation is challenging in mobile phone antennas because of the higher frequency and smaller devices. A higher operating frequency makes the user's hand electrically larger so that the influence on antenna performance is more considerable. Smaller devices lead to more compact and complex antenna designs, which are usually sensitive to changes in their vicinity.

If a hand holds only the chassis part of a mobile phone without covering the antenna, a balanced antenna design can suppress the hand effects [90]. A balanced antenna, such as a half-wavelength monopole antenna or the folded antenna in [90], does not depend on the chassis in radiation, so the influence from the hand is minimized. Moreover, the current on an antenna can be blocked from the chassis by adding a choke [50]. Studies show that a choke not only decreases the power absorbed by the hand (about 50%) but also reduces the SAR in the head. In addition, some modification to the chassis can also mitigate hand effects. For example, adding a floating metal strip next to the chassis as a reflector in Uda-Yagi antenna can prevent the fields in the direction of the strip side [91]. Moreover, a practical design proposed by Kim *et al.* cancels the current on the chassis by two extending strips, as seen in Figure 3.3 [92, 93]. The two strips are folded, and the field is constrained between each strip and the chassis instead of dissipating in the hand. As mentioned in previous sections, antenna performance can be greatly varied by different hand positions. A sensor was proposed in [94] to detect the hand position. Two electrodes are placed on the chassis (or on antenna), and the hand position can be recognized by reading the

capacitance variation between the electrodes.
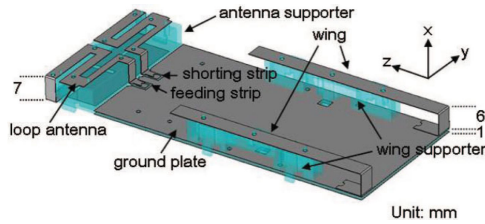
Figure 3.3: The two strips (wings) are added to the chassis to reduce hand effects [92].

There are also some solutions to improve the mismatch loss due to the hand in this situation. As reviewed above, slots on a PIFA are known as the most sensitive part of the antenna with respect to vicinity of a hand in terms of mismatch because of a strong reactive E- and H-field [65], so removing the slot from a PIFA design is considered a solution against the hand effect on mismatch. Using lumped elements to replace the slot has been shown to be useful [65]. A similar idea was also proposed by the same author [95]. Two single-band antennas without slots are designed for the transmission and receiving band, respectively. They are placed next to each other and use an active circuit to switch between two antennas. Moreover, if a PIFA has multiple slots, Boyle *et al.* reported that it would also perform slightly better than a regular single-slot design against hand effects because of the lower E- and H-field on each slot [11]. A small antenna has been suggested to reduce the chance of being covered by the index finger [70]. This study also showed that placing superstrate on a PIFA can improve the mismatch loss caused by the hand.

Before technology of multiple-input and multiple-output (MIMO) receives wide attention, multi-antenna operation has been proposed as an approach to suppress hand effects [96]. Two antennas are placed far from each other, and the one with the higher RF signal received becomes the active antenna[3]. This idea can be well implemented in MIMO communication. The element that has the best performance (not covered by the hand) can be used in communication [97]. Choosing two out of four elements to conduct

---

[3]This is similar with the selection combining method in MIMO

maximum ratio combination (MRC) has a 5 dB better performance than a two-element device with MRC.

Chapter 4

Hand Effect on OTA Performance

4.1 Introduction

The objectives of this chapter are to determine the effect of different hand models and usage patterns on mobile phone antenna performance in both talk mode and data mode[1]. The referenced parameters included radiation and mismatch efficiency as well as TRP. The RF dielectric properties and material composition of the hand, the grip of the hand on the phone, and the placement of the hand and mobile phone against the head have been investigated in detail. These data allow the setting of the necessary specifications and the general requirements for a hand phantom to evaluate mobile phone antenna performance.

At the time that these standards were being drafted, standardized hand phantoms had not been developed, so analysis of hand effects was limited. The hand grips used in most of the studies above are not sufficient to represent a realistic environment because of various reasons such as un-realistic hand grip, simplified hand model, limited hand positions, grips and dimen-

---

[1]The study in the talk mode has been published as *Effects of Hand Phantom on Mobile Phone Antenna Performance* in IEEE Transactions on Antennas and Propagation, 2009. The study in the data mode is published as *The influence of the user hand on mobile phone antenna performance in data mode* in European Conference on Antennas and Propagation, 2009.

sions. Thus, the influence of the user's hand on mobile phone antenna performance might be underestimated. In this thesis, the hand grip is chosen with the index finger pressed to the back of the phone with a realistic hand model to represent more realistic hand grips on mobile phones.

Considering feasibility and repeatability of OTA measurement with a hand phantom practically, the important issues include:

- Fixture design: A hand phantom fixture includes a device to fix hand position with regard to the head phantom and a spacer in the hand phantom to fix the mobile phone position with regard to the hand phantom. A good fixture design ensures an easy measurement procedure and low uncertainty of hand positioning. The material used for the fixture should be transparent enough in the RF range not to alter the measurement result.

- Phantom material: The material properties of a hand phantom should fit that in Gabriel's database [41]. Homogeneity of each hand phantom has significant influence on the repeatability of measurement. In addition, mechanical flexibility is also important. The hand phantom should be flexible enough to tolerate small difference of mobile phone dimensions but not too soft.

The influence of the user hand is not only noticeable in the talk mode, but also it is significant in the data mode (when the user is browsing or typing text with the mobile phone). Thus, the hand effects in OTA performance have also been studied in data mode in this chapter. In addition, in the above literature review, it is mentioned that in GSM1800, a PIFA's behavior is complicated and hard to estimate when an index finger is above it [11, 69]. This issue is also analyzed in the section of data mode.

4.2   Method and Models

The effects of hand parameters on OTA performance were treated as independent of each other as a first approximation. The parameters considered in this study for evaluating the effect of the user's hand were TRP and the Effective Isotropic Radiated Power (EiRP) defined as follows [12]:

$$\text{TRP} = \int_{\theta=0}^{\pi} \int_{\phi=0}^{2\pi} EiRP(\theta, \phi) \sin\theta d\theta d\phi$$

$$\text{EiRP}(\theta, \phi) = P_T \cdot G_T(\theta, \phi)$$

where P_T and G_T are the power delivered to the antenna and the antenna gain, respectively.

In addition, for simplicity, TRP can be defined approximately as

$$\text{TRP (W)} = \text{Conducted Power (W)} \cdot \text{E}_{mis} \cdot \text{E}_{rad},$$

where E_{mis} and E_{rad} are the mismatch efficiency and radiation efficiency of the antenna, respectively.

The elements of the numerical models were the head phantom, different mobile phone models and hand phantoms. The Specific Anthropomorphic Mannequin (SAM) phantom [14] as defined in the standards was used. The study was conducted with four different phones: a candy bar phone with an external helix antenna (P1), a clam shell phone also with an external helix antenna (P3), and candy bar phones with internal PIFA at the top (P2) and at the bottom (P4) (Figure 4.1). All phones are commercial phones (the P2 and P4 are identical CAD files but rotated by $180\,^\circ$). The numerical models of these phones have been developed for other studies [67, 98, 99], the experimental validation of which showed deviations of less than 15% for different loading conditions. In this study, only the relative differences were compared for which an uncertainty of less than 0.1 dB has been predicted.

(a)   (b)   (c)   (d)
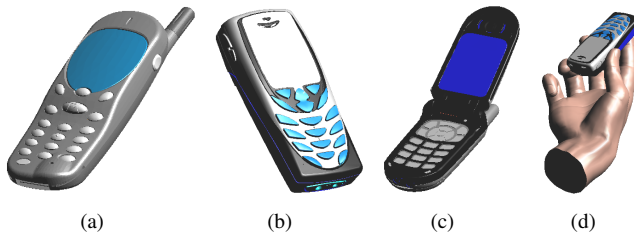
Figure 4.1: The four mobile phone models used to investigate the influence of user hand on mobile phone antenna performance; (a) candy-bar phone with helix antenna (P1), (b) candy-bar phone with PIFA at top (P2), (c) clam shell phone with helix antenna (P3) and (d) candy-bar phone with PIFA at bottom (P4).

In order to test the maximum sensitivity of the various hand parameters, the mobile phones were evaluated in the right $15\,^\circ$ tilted position of

the SAM head phantom [14] (Figure 2.5). To determine the sensitivity of
different parameters of the hand, a real hand model with two different con-
figurations was used in this study, i.e. an inhomogeneous anatomical hand
model (Figure 4.2(b)) with skin, muscle and bone tissues, and a homoge-
neous anatomical hand model (Figure 4.2(c)) with homogeneous dielectric
and conductivity. A major challenge was to manipulate the hand such that a
natural grip for each of the phones could be realized. For this purpose, so-
phisticated hand modeling software (Figure 4.2(d)) has been developed, the
generalized version of which has recently been integrated into SEMCAD X.

(a)   (b)   (c)   (d)
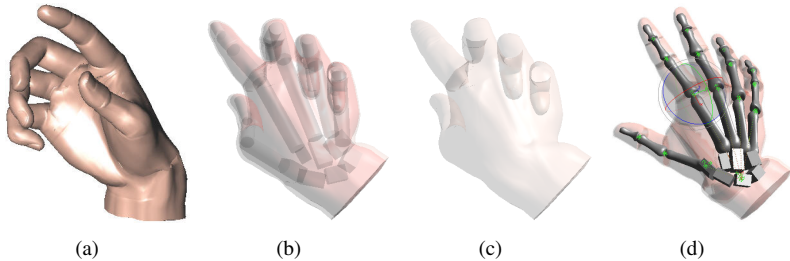
Figure 4.2: The numerical models of the hand phantoms used to investigate
the influence of user hand on mobile phone antenna performance; (a) the
real hand model (b) Inhomogeneous (H1), and (c) homogeneous (H2) hand
models; (d) illustration of hand phantom modeling engine.

The dimensions of the hand model used in this study are presented in Ta-
ble 4.1. The dimensions used in the simulations are the average of male and
female hands reported in [76]. The material properties of the hand models
are shown in Table 4.2. RF dielectric properties of the homogeneous hand
phantom are based on the human tissue measurement data as described in
[41] and the values are the average between the dry and wet hands.

The simulation results of the four mobile phones with homogeneous and
inhomogeneous hand phantoms are shown in Table 4.3. The difference be-
tween homogeneous and inhomogeneous hand phantoms is 0.7 dB for P2,
but much less for the other phones. This means that a homogeneous hand
phantom may accurately represent a human hand in real usage conditions
and can be used in OTA measurements. Therefore, the rest of the study was
carried out using a homogeneous hand phantom. The conducted power in

Hand Dimensions	mm
Wrist Width	63.8
Hand Length, Center of Wrist to Tip of Middle Finger	185.9
Palm Length, Middle Crease to Distal Palm Crease	91.3
Hand Width	92.4

Table 4.1: Dimensions of the simulated hand phantom.

	H1			H2
900 MHz	Skin	Muscle	Bone	Homogeneous Model
Dielectric Constant	41.4	55.0	12.5	36.2
Conductivity (S/m)	0.87	0.94	0.79	0.79
1800 MHz	Skin	Muscle	Bone	Homogeneous Model
Dielectric Constant	38.8	53.4	11.7	32.6
Conductivity (S/m)	1.22	1.39	0.29	1.26

Table 4.2: The material properties of the inhomogeneous (H1) and homogeneous (H2) hand phantoms used in the simulations.

this report was normalized to 1 W, or 30 dBm, for calculating TRP. Both mismatch efficiency and radiation efficiency were taken into consideration for TRP calculations.

4.3 Effects of the Hand Phantom

The parameters of the hand phantom on the influence of mobile phone antenna performance are studied thoroughly in this section. The results are separated into four parts:

- The parameters of the hand phantom with negligible influence on mobile phone antenna performance

  - Hand phantom material dielectric properties
  - Wrist tilt and length

- The parameters of the hand phantom with significant influence on mobile phone antenna performance

	P1		P2	
900 MHz	H1	H2	H1	H2
Radiation Efficiency	0.164	0.162	0.081	0.067
Mismatch Efficiency	0.460	0.466	0.786	0.809
TRP (dBm)	18.78	18.78	18.04	17.34
	P3		P4	
Radiation Efficiency	0.113	0.116	0.130	0.122
Mismatch Efficiency	0.783	0.810	0.807	0.814
TRP (dBm)	19.47	19.73	20.21	19.97
	P1		P2	
1750 MHz	H1	H2	H1	H2
Radiation Efficiency	0.323	0.324	0.108	0.107
Mismatch Efficiency	0.931	0.930	0.675	0.691
TRP (dBm)	24.78	24.79	18.63	18.69
	P3		P4	
Radiation Efficiency	0.109	0.113	0.122	0.125
Mismatch Efficiency	0.880	0.875	0.765	0.775
TRP (dBm)	19.82	19.95	19.70	19.86

Table 4.3: Comparison of radiation performance between inhomogeneous (H1) and homogeneous hand phantoms (H2) with the four mobile phone models (Figure 4.1).

- Size of the hand phantom
- Palm-phone distance
- Vertical positions of the hand phantom
- Index finger positioning of the hand phantom
  - Index finger positioning on the candy bar mobile phone with an internal PIFA at top
  - Index finger positioning on the clam shell mobile phone with an external helix antenna at the hinge part

The effects of the index finger positions of the hand phantom are discussed in an individual section because of their importance.

4.3.1   Parameters with Low Influence on OTA

Hand Material Properties

The effects of tolerances in dielectric parameters of hand phantom materials were assessed by using different permittivity and conductivity values to simulate dry and wet hands. In [41], it has been shown that the differences in permittivity and conductivity of dry and wet palms are of the order of 35% of their average. Five sets of different materials (M0-M4) are shown in Table 4.4 (M0: ϵ_r is 32.6 and σ is 1.26 (S/m)).

	M1	M2	M3	M4
Dielectric Cons.	32.6*1.15	32.6*1.15	32.6*0.85	32.6*0.85
Conductivity	1.26*1.15	1.26*0.85	1.26*1.15	1.26*0.85

Table 4.4: Four different sets of material properties of hand phantoms to test the influence of the mobile phone antenna performance due to the variation of the material properties.
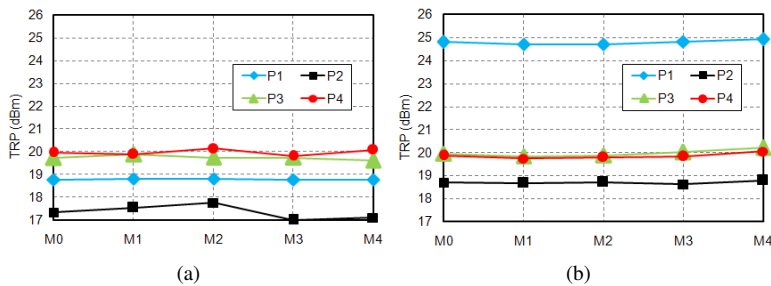
Figure 4.3: Effect of the hand phantom material properties on radiation performance at (a) 900 MHz and (b) 1750 MHz with four different mobile phone models (Figure 4.1).

As seen in Figure 4.3, TRP values are not sensitive (less than 0.5 dB difference) to tolerances in material properties of hand phantoms at both frequency bands. Since the mobile phone PCB (printed circuit board) is the main radiator at 900 MHz [86], the existence of the hand phantom reduces TRP values for all phone models at this frequency. However, since the hand

does not cover the external antenna of P1, higher TRP values are obtained
compared to other phone models at 1750 MHz.

Wrist Length and Position

Five wrist models with different lengths and different tilt angles were em-
ployed to study the effect of the wrist on antenna performance (Figure 4.4).

(a)   (b)   (c)   (d)   (e)
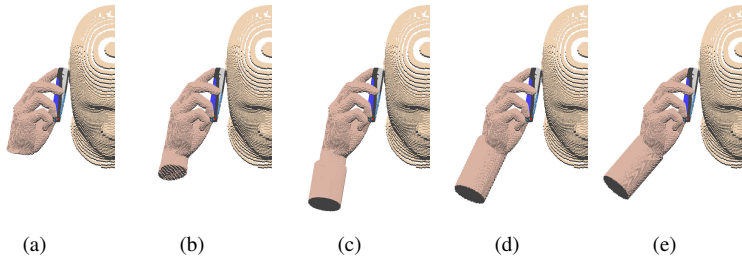
Figure 4.4: The hand phantom wrists with different length and position-
ing for evaluating the influence of different wrist configurations on mobile
phone antenna performance: (a) no wrist, (b) 3cm-long wrist, (c) 10cm-long
wrist, (d) 10cm-long, $15°$-tilted wrist and (e) 10cm-long, $30°$-tilted wrist.

(a)   (b)
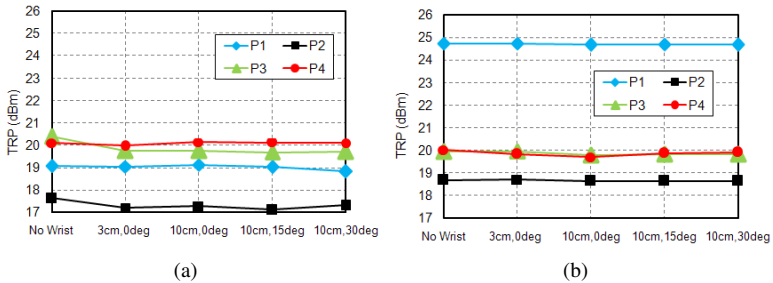
Figure 4.5: Effect of different wrist sizes and positions on radiation perfor-
mance at (a) 900 MHz and (b) 1750 MHz of the four mobile phone models
(Figure 4.1).

   The simulation results in Figure 4.5 show that the presence of the wrist

has no significant influence on TRP. The wrist is relatively far from the antenna, even in the case of P4 whose antenna is at the bottom and therefore closer to the wrist. In addition, most of the radiated energy in the direction of the wrist is already absorbed by the palm.

4.3.2 Hand Size

The size of the hand and the palm-phone distance were investigated using all four phone models. The original hand size of the model used in this study is close to the average of female and male hand sizes, [76]. The smallest female hand and the largest male hand reported in [76] differ by about 20% from the average hand size. Therefore, the five different hand sizes presented in Figure 4.6 were used in the simulations. The results presented in Figure 4.7 demonstrate that the radiation performance of the antenna is more sensitive to hand size when the antenna is located at the bottom of the phone. However, larger hands do not always result in lower TRP values. If two hands have the same grip style, the bigger hand has larger palm-phone distance and antenna performance is also sensitive to the palm-phone distance.

| (a) | (b) | (c) | (d) | (e) |
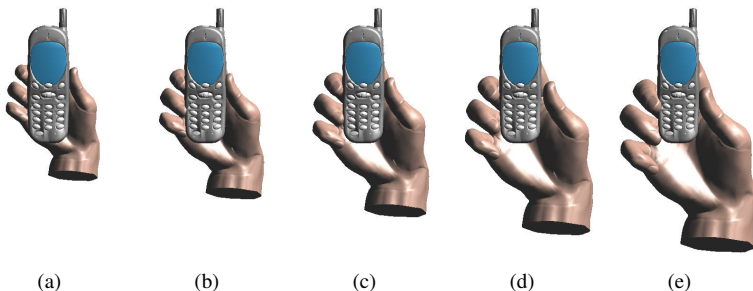
Figure 4.6: Five different hand sizes in the simulations for evaluating the influence of the hand phantom sizes on the mobile phone antenna performance: (a) 80%, (b) 90%, (c) 100%, (d) 110%, and (e) 120% of the average hand size.
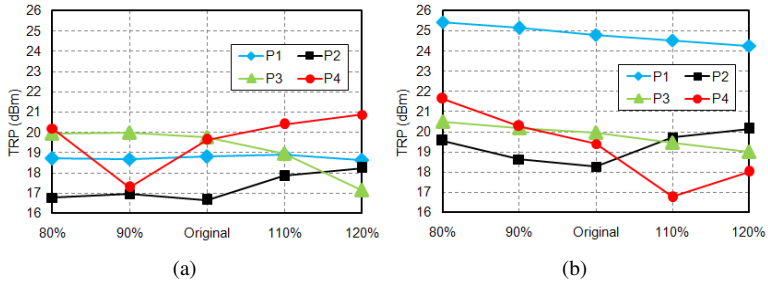
Figure 4.7: Effect of hand phantom size on radiation performance at (a) 900 MHz and (b) 1750 MHz.

4.3.3   Palm-Phone Distance

The palm-phone distance (D) is defined between the bottom of the mobile phone housing to the center of the palm (Figure 4.8). D was chosen as 13 mm, 30 mm and 45 mm in this investigation. Three hand grips with different palm-phone distances were used to illustrate the effect of palm-phone distance (Figure 4.9).
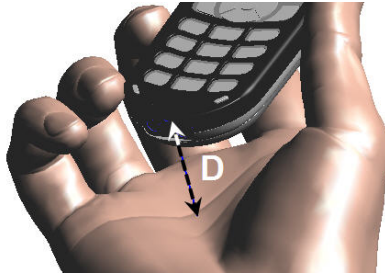
Figure 4.8: The palm-phone distance (D) defined in this paper is from the bottom of the housing to the center of the palm.

In each grip, the index finger was placed on the side of the mobile phones to isolate the effect of index finger positioning. The simulation results in Figure 4.10 show that the performance of P4, whose antenna is at the bottom, is very sensitive to palm-phone distance at 1750 MHz, as expected. P3
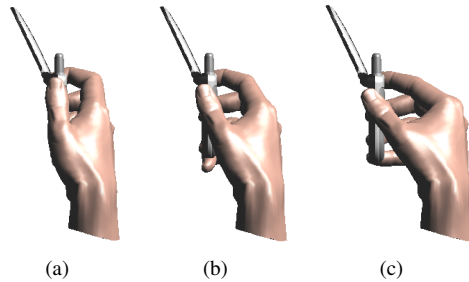
Figure 4.9: Three grips of the hand phantoms with different palm-phone distances, D = (a) 13 mm, (b) 30 mm, and (c) 45 mm, for evaluating the influence of palm-phone distance on mobile phone antenna performance.

has higher TRP compared to previous simulations at 900 MHz, and the TRP of all models (except P1) is higher at 1750 MHz. This implies that the index finger plays a significant role on mobile phone antenna performance.
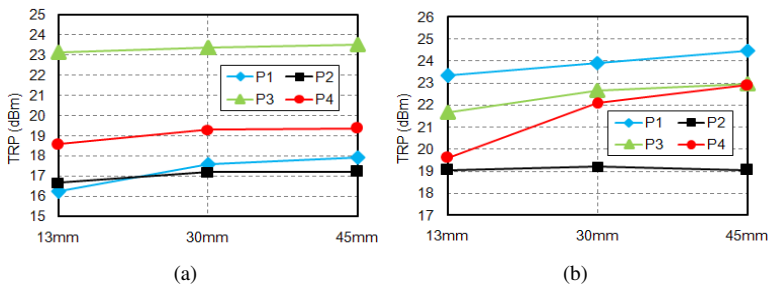
Figure 4.10: Effect of different palm-phone distances on radiation performance at (a) 900 MHz and (b) 1750 MHz.

4.3.4 Vertical Positioning

In this section, P2 and P4 models are simulated with hand phantoms to investigate the effect of vertical positioning on antenna performance. In simulations with P2, because the index finger significantly changes the radiation

performance, two sets of simulations were performed: 1) P2 + hand with index finger at four different vertical locations and 2) P2 + hand without index finger at eight different vertical locations. For simplifying the simulations, the second configuration was chosen to simulate the grip with the index finger placed on the side of the mobile phone instead of on its back. Eight different vertical locations of the hand phantom on the mobile phone were used in this section as shown in Figure 4.11. Row 1 is such that the location of the fingers are at the top of the phone, as shown in Figure 4.12(c). In row 8, the thumb is at the bottom of the phone Figure 4.12(b). The hand without index finger was simulated at all eight vertical locations (from row 1 to row 8), whereas the configuration with index finger was simulated at four locations from row 5 (the tip of index finger at top of the phone, Figure 4.12(a)) to row 8. The distance between each row is 10 mm.

(a)   (b)
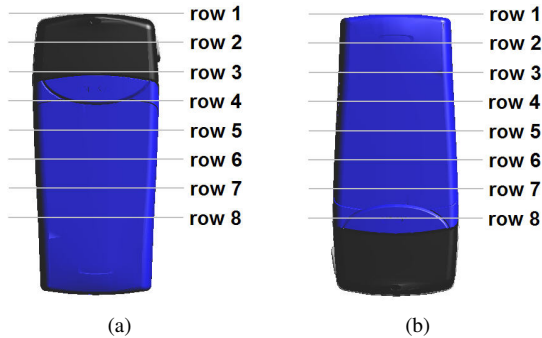
Figure 4.11: (a) P2 and (b) P4 are set in 8 rows to investigate the influence of vertical positions of the hand phantom.

The simulation results, ratio of total efficiency ($E_{total}(dB)$) are presented in Figure 4.13 with the following definitions:

$$E_{total}(dB) = 10 \cdot \log(E_{total, \text{ with hand}}/E_{total, \text{ without hand}}), \qquad (4.1)$$

where E_{total} is E_{mis} times E_{rad}. These simulation results show that the efficiency of the antenna is higher when the hand is placed at a lower position, i.e., further away from the antenna. TRP values change significantly at both frequencies when the index finger is moved from row 6 (above the

(a) (b) (c)
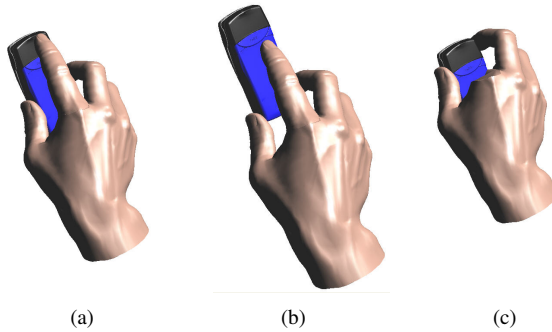
Figure 4.12: Vertical positioning on the P2 model: (a) hand with index finger at row 5 and, (b) at row 8; (c) hand without index finger at row 1.

antenna) to row 7 (below the antenna). Another interesting observation is that in the 900 MHz simulation without the index finger, when the hand is placed at lower positions (row 6 - row 8), the efficiency of the antenna with the hand is higher than that without hand. In the cases that have higher efficiency, the head phantom also absorbs lower power compared to without hand. Thus, the distortion of near-field distribution due to the hand phantom may reduce power absorption by the head to enhance radiation efficiency in certain grips.
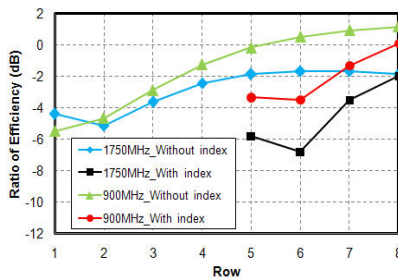
Figure 4.13: Effect of different vertical positions of the hand phantom on P2 model.

Four different vertical positions of the hand, with and without index finger, were used in simulations with P4 (Figure 4.14). When the hand is positioned at row 1, the index finger lays at the top of the mobile phone. The distance between each row is 6mm. The computed results in Figure 4.15 indicate that the index finger causes approximately a 1dB reduction in TRP values for all cases since the finger limits the radiation ability of the PCB. The influence of the index finger on P4 performance is similar to the influence of the palm on P2 performance. In addition, less than 1.5 dB difference in TRP is observed due to different vertical positions of the hand with respect to the phone.

(a)   (b)
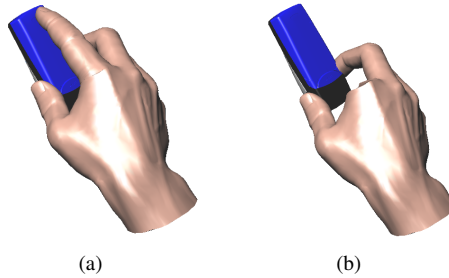
Figure 4.14: Vertical positioning on P4: (a) hand with index finger at row 1, and (b) hand without index finger at row 4 for simulating the grip when the index finger is at the side of the mobile phone instead of at the back.

4.4   Index Finger Positions

The existence of the index finger in the vicinity of the antenna significantly changes its performance. P2 and P3 were chosen to evaluate the variation of antenna radiation performance due to different index finger positioning.

4.4.1   Candy Bar Mobile Phone

In P2 simulations, sixteen different index finger positioning scenarios were simulated (Figure 4.16). The distance between rows and columns are 6 mm

(a)   (b)
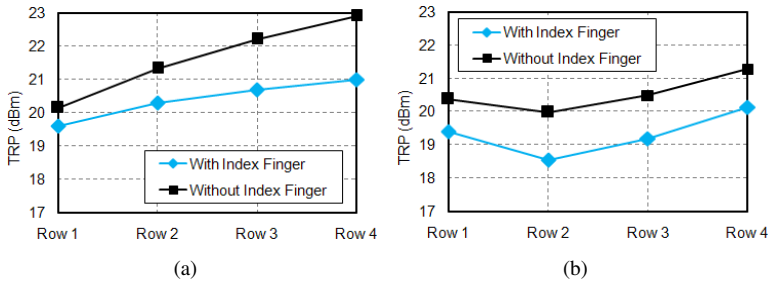
Figure 4.15: Effect of different vertical positions of the hand model on P4 at (a) 900 MHz and (b) 1750 MHz.

and 10 mm, respectively. Figure 4.17 presents the simulated TRP values at 900 MHz and 1750 MHz. Up to 5 dB difference in TRP values due to different positioning of the index finger are seen. The difference is more than 3 dB when the index finger is shifted only 6 mm vertically and 10 mm horizontally. Both mismatch and radiation efficiency significantly changes in the presence of the index finger.

(a)   (b)
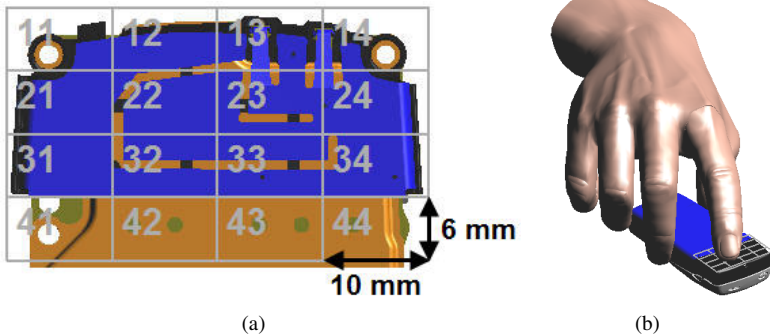
Figure 4.16: Index finger positioning on P2 model for investigating the sensitivity of mobile phone antenna performance due to the shift of index finger touching locations: (a) 16 index finger locations, and (b) index finger at [row 3, column 3].

(a)   (b)
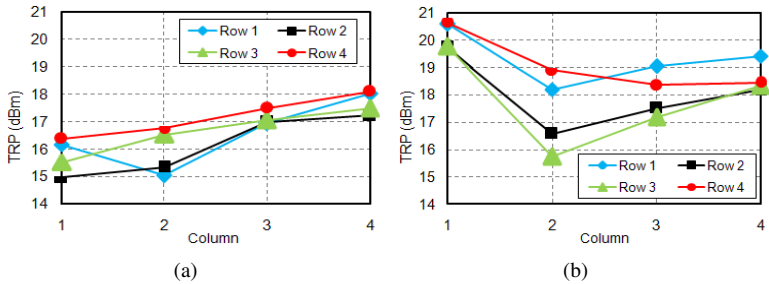
Figure 4.17: Effect of different index finger positions on the P2 model on TRP at (a) 900 MHz and (b) 1750 MHz.

Figure 4.18 is the simulated E-field and H-field distribution at 1750 MHz. The fields are recorded in a plane 1.5 mm above the antenna. Both the electric and magnetic fields above the antenna slot ([row 3, column 2] and [row 3, column 3]) are very strong. Thus, when the index finger is placed on these locations, both mismatch and radiation efficiency seriously degrade due to distortion and absorption of E- and H-field by the lossy hand. Moreover, when the index finger is on row 4, it still degrades the radiation efficiency, but does not significantly affect the mismatch efficiency of the antenna.

(a)   (b)   (c)
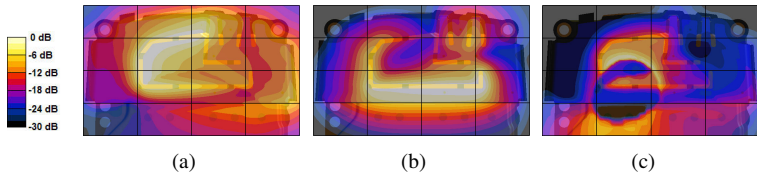
Figure 4.18: The field distribution 1.5 mm above the P2 antenna at 1750 MHz; (a) E-field and (b) H-field in free space, and (c) the E-field distribution when the index finger is placed on [row 3, column 2].

Furthermore, different index finger touching areas also change the antenna performance in addition to its positioning. In order to examine this effect, the index finger at [row 3, column 2] on P2 was simulated with different touching areas as shown in Figure 4.19. The simulation results in Figure 4.20 demonstrate that TRP values degrade up to 3.5 dB due to lower

both mismatch and radiation efficiencies.

(a)   (b)   (c)
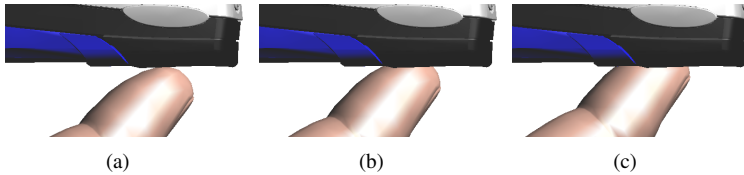
Figure 4.19: Different index finger touching areas ((a) just touched, (b) medium press, and (c) hard press) when the index finger is touching [row 3, column 2] (Figure 4.16) for evaluating the variation of mobile phone antenna performance due to different pressing strength by the index finger.
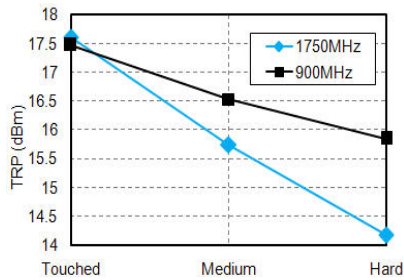
Figure 4.20: Effect of different index finger touching areas on radiation performance of the P2 model when the index finger is touching location 32 as shown in Figure 4.16.

4.4.2   Clam Shell Mobile Phone

In P3 simulations, six different index finger positioning scenarios were used as shown in Figure 4.21. Figure 4.22 highlights the effect of the absorbing index finger in the vicinity of the close near-field of the external antenna of the phone in terms of decreased radiated power.

The change in TRP when the index finger in row 1 is moved from column 1 to column 2 is opposite at 900 MHz and 1750 MHz. A closer investigation of the free-space E-field distribution through the center of the antenna
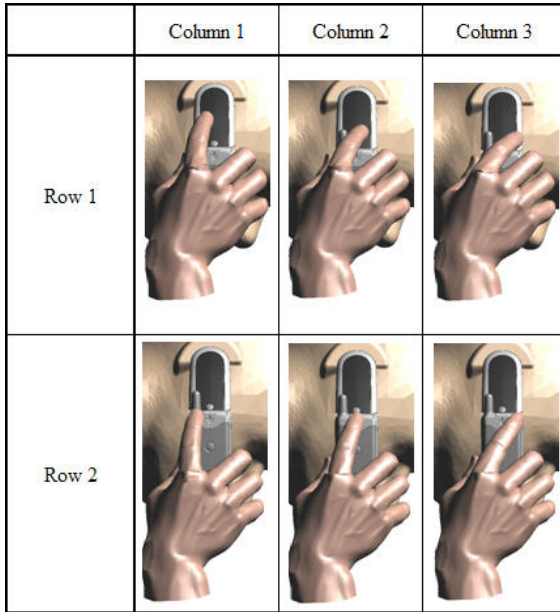
Figure 4.21: Index finger positioning on P3 model.
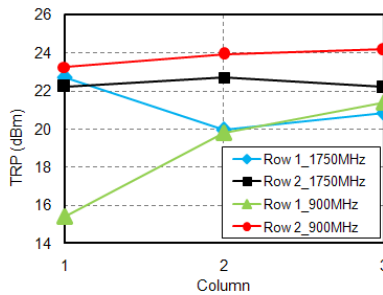
Figure 4.22: Effect of different index finger positioning on radiation performance of the P3 model.

(Figure 4.23) reveals that the field at the tip of the antenna is stronger at 900 MHz than at 1750 MHz. Thus, the antenna experiences severe detuning

at 900 MHz when the finger is placed on this location.
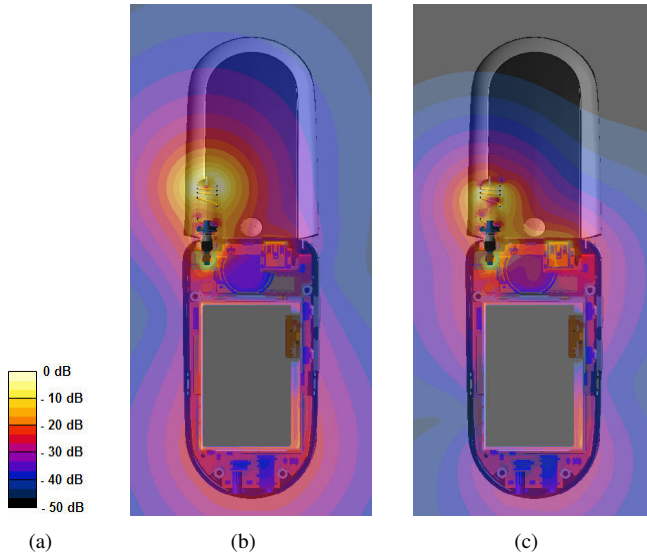
Figure 4.23: E-field distribution at middle of the antenna of the P3 model at (b) 900 MHz and (c) 1750 MHz.

4.5 Data Mode

In the above sections, the effects of user hand in the talk mode (Figure 2.5) have been thoroughly investigated. The effects of the user hand in the data mode (Figure 4.24) are studied in this section. According to the studies above, the grip and the position of the hand phantom are of great importance to the mobile phone antenna performance. Therefore, only the influences of hand grip and position are discussed in this study.

The objectives of this section are to determine the effect of various hand grips and positions on the mobile phone antenna performance in the data mode. Instead of phone + head + hand on talk mode, the configuration of this study is phone + hand. The referenced parameters included radiation

Figure 4.24: The influence of a user's hand on the mobile phone antenna performance is analyzed in data mode, that is, typing message or browsing.

and mismatch efficiency as well as TRP. These data allow the setting of the necessary specifications and the general requirements for a hand phantom to evaluate mobile phone antenna performance. In addition, a method is proposed in this section to analyze the influence due to the user hand.

For this particular phone, P2, the area above the antenna is the most sensitive to the antenna performance. In order to have a comprehensive study of the antenna performance influence due to the hand, different hand grips were set to place the index finger on all possible locations above the antenna. There are four different grips shifted to four different locations (Figure 4.25). As the study above, there are 16 scenarios simulated at 1750 MHz to evaluate the effect of the hand on the efficiencies and the TRP (Figure 4.25(a)).

| (a) | (b) | (c) | (d) |
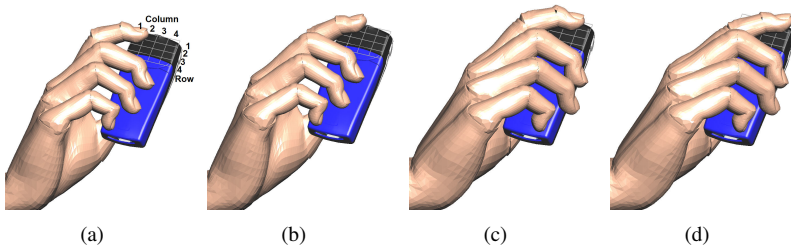
Figure 4.25: Four different grips, like the hand grip in Figure 4.24, are set to cover each column, and the grips are shifted down to each row. The columns and the rows are defined in Figure 4.16(b).

The simulation results are shown in terms of TRP, and radiation efficiency, and the radiation efficiency is presented as ratio between with and without hand in dB (E_{rad}(dB)). The definitions of the two ratios are

$$E_{rad}(dB) = 10 \cdot \log(E_{rad, \text{ with hand}}/E_{rad, \text{ without hand}}). \qquad (4.2)$$

The simulation results are shown on Figure 4.26. Considering the positioning error of the hand phantom in terms of TRP, the uncertainty is up to 6 dB for 6 mm vertical shift ([row 3, column 1] to [row 4, column 1]). The variation of TRP due to 10 mm horizontal shift is also up to 4 dB ([row 3, column 2] to [row 3, column 3]). Besides, according to results in talk mode, the variation of TRP due to different index finger touching area can be up to 3 dB. Therefore, the change of TRP for the 6 mm positioning error of the hand phantom can be about 8 dB in this case.

(a)   (b)
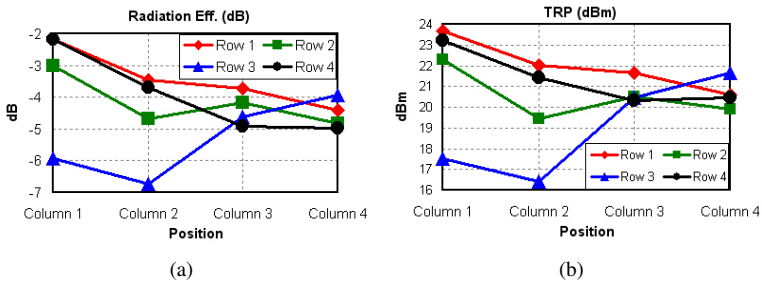
Figure 4.26: The simulated (a) radiation efficiency and (b) TRP at 1750 MHz for different index finger positions (Figure 4.25(a))
.

To analyze the impact of the hand phantom, the variation of mismatch efficiency due to different index finger positions is smaller than that of radiation efficiency (Figure 4.26). Thus, during the development of a mobile phone antenna, the influence will be underestimated significantly by only considering impedance mismatch. However, some analysis of the input impedance as shown in Table 4.5 can be quite helpful to understand the behavior. When the index finger is at the gray and white locations, it induces capacitive and inductive effects, respectively. Usually, a dielectric object causes an inductive effect when it is close to a resonant antenna, but the index finger causes both inductive and capacitive effect when it is at different

positions, as illustrated in Figure 4.27. There are three input impedances for three cases; no hand, index finger at [row 2, column 1] (white location) and [row 2, column 2] (gray location). Since the gray locations are above the resonant arm of the antenna at DCS band, like "resonant locations", it shifts the resonance toward lower frequencies if the index finger is on these locations. This shifts the input impedance at DCS band closer to anti-resonance with lower input reactance. In addition, the index finger at gray locations also decreases the quality factor more than it on white locations and that also decreases the input reactance. Therefore, there is capacitive effect induced by the hand phantom. If the index is on the white locations in Table 4.5, like [row 2, column 1] in Figure 4.27, it shifts the resonance less and decreases the quality factor less. Therefore, the index finger on these locations induces inductive effect, as expected.

	Column 1	Column 2	Column 3	Column 4
Row 1	$68 + j43$	$107 + j48$	$134 + j29$	$163 + j24$
Row 2	$100 + j63$	$232 + j27$	$188 + j20$	$185 + j16$
Row 3	$105 + j76$	$247 + j46$	$183 + j29$	$168 + j29$
Row 4	$66 + j59$	$94 + j72$	$90 + j66$	$104 + j53$
No Hand	$42+j43$			

Table 4.5: The corresponding input impedance (Ohms) when the index finger on the 16 positions defined in Figure 4.16(b).

(a)   (b)
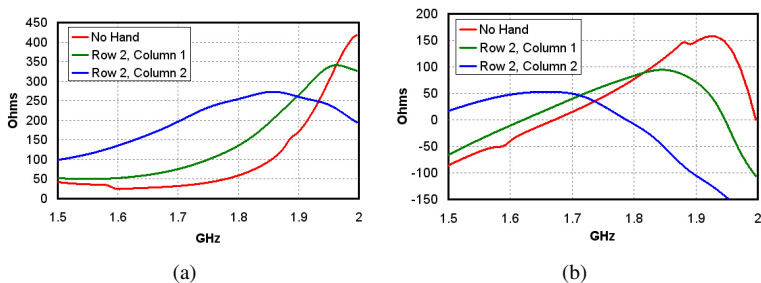
Figure 4.27: (a) Input resistance and (b) reactance (Ohms) for the index finger position at [row 2, column 1], [row 2, column 2] and without hand.

The input resistance can be separated into radiation resistance and loss

resistance by using radiation efficiency. Regarding radiation resistance, the 16 locations can be separated in gray, white and dark gray locations (Table 4.6). The index finger on the resonant locations (gray locations) shifts the input impedance closer to anti-resonance, causing higher input resistance. There are more radiated energy on the dark gray locations, like "radiated locations", and the index finger decreases the radiation resistance significantly. The white locations are neither resonant locations nor radiated locations. The influence of these locations on the radiation resistance is minor compared to the other cases.

	Column 1	Column 2	Column 3	Column 4
Row 1	18.4	21.6	25.4	26.3
Row 2	22.4	35.3	32.1	27.2
Row 3	12.0	23.4	28.2	30.4
Row 4	17.8	18.0	13.0	14.8
No Hand	24.4			

Table 4.6: The corresponding radiation resistance (Ohms) when the index finger at different positions

.

	Column 1	Column 2	Column 3	Column 4
Row 1	49.6	85.4	108.6	136.7
Row 2	77.6	196.7	155.9	157.8
Row 3	93.0	223.6	154.8	137.6
Row 4	48.2	76.0	77.0	89.2
No Hand	17.6			

Table 4.7: The corresponding loss resistance (Ohms) when the index finger at different positions

The variation of loss resistance (Table 4.7) due to the index finger on different locations is caused by both the E- and H-field strength above the antenna. Figure 4.18(a) and Figure 4.18(b) shows the E- and H-field distribution at the plane 1.6mm above the antenna in free space at 1750 MHz respectively. Since the field concentrates more above the resonant arm, the loss resistance is higher than the other cases when the index finger is on the resonant locations. The location [row 3, column 2] has both the highest E- and H-field and the highest loss resistance among the 16 locations.

Chapter 5

Hand Effect on Head SAR

The objective of this study is to investigate the hand effect on SAR performance. Firstly, a simplified scenario (generic hand and phone models with a flat head phantom) was applied to have basic understanding of the effect[1]. Then, in realistic scenario, over a large sample of mobile phones are used in several different hand grips and positions[2]. Numerical simulations are conducted using a wide range of hand grips and positions with four mobile phone models. Conclusions are drawn regarding the types of hand grips and positions that result in increased psSAR in the head. To verify that the psSAR increases seen in the simulations are also found in reality, measurements are made using 46 commercial mobile phones using a human hand in different grips. Finally, the considerations of the hand effect on the head psSAR are discussed. In this study, the change of the head psSAR due to the hand is defined as

$$\Delta psSAR(dB) = 10 \cdot \log_{10}(\frac{\text{psSAR}_{\text{with hand}}(\text{W/kg})}{\text{psSAR}_{\text{no hand}}(\text{W/kg})}), \qquad (5.1)$$

Throughout this chapter, the psSAR value is normalized to the antenna forward power, except where indicated. Each psSAR value in Equation 5.1

---

[1]This part of the study is published as *Analysis of the Hand Effect on Head SAR with Generic and CAD Phone Models Using FDTD* in IEEE International Symposium on Antennas and Propagation, 2011

[2]This part of the study has been published as *Influence of the Hand on the Specific Absorption Rate in the Head* in IEEE Transactions on Antennas and Propagation.

is determined by averaging the SAR over a 1-gram or 10-gram cubical mass centered at each point, then selecting the maximum value over all points. Therefore, Equation 5.1 represents the ratio of the highest psSAR values regardless of location. This is important, as the presence of the hand may cause a shift in the location of the psSAR. To specifically refer to the change in the 1-gram or 10-gram psSAR, the variables $\Delta psSAR_{1g}$ and $\Delta psSAR_{10g}$ are used. The absolute values of psSAR are not presented in this paper as these are dependent on the power level of the device and the operating mode. The focus of the paper is the investigation of the mechanisms that change the *psSAR*.

5.1   Simplified Scenario

5.1.1   Methods and Models

According to the study in [52], the effect of the user's hand on the SAR in the head is more pronounced at higher frequencies. The simulation frequency in this study is therefore selected to be 1800 MHz. A previous study about the hand effect on Over-The-Air (OTA) parameters indicates that the mobile phone antenna performance is sensitive to the hand- and particularly the finger-position [42]. Therefore, in this study, a generic hand phantom is used to exclude the variable of finger position. The hand phantom consists of three bricks which represent the palm and the fingers, as shown in Figure 5.1(a). The hand phantom is not further simplified as having only the palm, since it was found in this study that in almost all the cases the hand phantom model that raises the SAR significantly includes fingers. In addition, a flat head phantom is used as the simplification of the SAM head phantom. The movement of the hand phantom is described on Figure 5.1(b). The hand phantom is moved in Y-direction from the top to the bottom of the phone, and in Z-direction from 10 mm to 60 mm above the antenna. The movement resolution is 10 mm and 5 mm in Y- and Z-direction, respectively.

The phone models are placed 5 mm above the flat head phantom. Figure 5.2(a) shows the candybar and clamshell model with PIFA. The antennas tested with the candybar model are straight and bent monopole, PIFA fed at the center and the corner of the short-edge of the ground plane, dual-band PIFA and monopole antenna. In addition, clamshell phone models are also investigated. Different locations of the PIFA and the flexible PCB are exam-
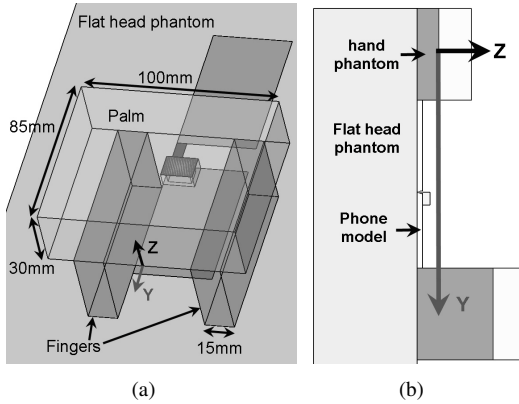
Figure 5.1: (a) The flat head and generic hand phantom are used to investigate the effect of the hand on the SAR. (b) The hand phantom is moved in Y- and Z-direction and the simulation results are recorded when the hand phantom is at every location.

ined with the generic clamshell phone models. Also, the effect of ground-plane dimensions on the SAR is investigated with both phone models. Other parameters studied include the dimensions of the hand phantom and the material variation of the hand phantom. All the simulation results, such as the reflection coefficient, the total absorbed power by head and hand, and the value and the location of the 1g-averaged peak-SAR as well as $\Delta psSAR$ are recorded as 2-D matrices. The material properties of the head and hand phantom are set as that provided in the Over-The-Air (OTA) standard [12]. (head: $\epsilon_r = 40$, $\sigma = 1.4$ (S/m)) (hand: $\epsilon_r = 26.96$, $\sigma = 0.99$ (S/m))

5.1.2 Results

The observations from the simulation results are as follows. Firstly, the SAR is very sensitive to hand position. Figure 5.2(b) shows the $\Delta psSAR$ as a function of hand phantom location, and it varies dramatically with different hand positions. Hence, it is critical in this study to consider all the possible positions for the hand. The maximum value of $\Delta psSAR$ varies significantly with the dimensions of the ground plane. The variation of the maximum

increase due to different lengths of candybar (5 cm - 17 cm) and clamshell
(9.5 cm - 19.5 cm) phone models is 0.7 dB and 1.2 dB, respectively. In addi-
tion, a narrower ground plane causes higher increase of SAR for these cases.
The change in width (6 - 3 cm) of the candybar and clamshell models can
result in an increase of SAR by 0.53 dB and 0.56 dB, respectively. Regard-
ing the clamshell model, the highest increase occurs when the antenna is
next to the flexible PCB, as shown in Figure 5.2(a). After the hand position
with the highest increase is found, a generic index finger touching the back
of the phone is added. The index finger at different positions raises the SAR
further. In this case, the highest value of $\Delta psSAR$ due to the hand phantom
with the index finger is 3.48 dB. The hand grip with the index finger that
causes the highest increase is shown in Figure 5.3.

(a)   (b)
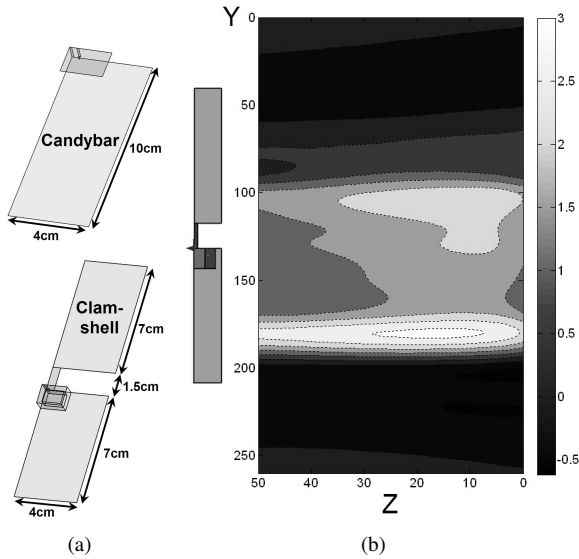
Figure 5.2: (a) Different configurations and antennas are tested on the can-
dybar and the clamshell generic phone models. (b) The $\Delta psSAR$ of the
generic clamshell phone model when the hand phantom is at different posi-
tions in Y- and Z-direction (mm).

Note that the head phantom used in this study is different from the SAM

head in terms of geometry. Besides, for the same type of the antenna, near-field distribution might vary significantly with different designs. Thus, the results obtained in these simplified configurations can serve as a basis for defining more realistic scenario, but investigation with realistic models is also necessary.
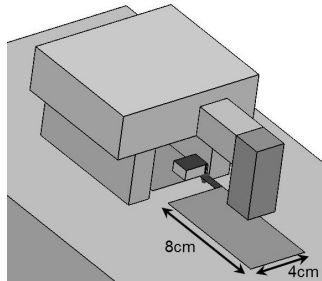
Figure 5.3: The generic-hand grip that results in the highest increase of $\Delta psSAR$ with the generic clamshell phone model.

5.2 Realistic Scenario

5.2.1 Numerical Simulations

Models and Method

The simulation frequencies selected in this study are 900 MHz, 1750 MHz and 1800 MHz. The model resolution is about 0.1 to 0.2 mm, depending on the phone models. Five to seven layers of uni-axial perfect matching layer (UPML) are used as the absorbing boundary surround the modeling space [19], with at least 0.25 wavelengths of free space between the model and the absorbing layers.

Four mobile phone models have been selected for this study, including two generic designs and two CAD models (Figure 5.4). The generic mobile phones both have a clamshell style with three metal parts representing the top half, the bottom half and a conductive element (flexible PCB) joining the two halves at the hinge. These models have a single-band PIFA at 900 MHz (phone 1) or 1800 MHz (phone 2). The two CAD mobile phone models

have either a clamshell style with an external helical antenna (phone 3) or
a bar style with a PIFA (phone 4). The details of the CAD models are
reported and have been validated with measurements in previous studies
[42, 98]. The antennas in phone 3 and phone 4 were re-designed using
genetic algorithm optimization and thus their performance may be different
from those of commercially-available mobile phones [72].

(a) phone 1   (b) phone 2   (c) phone 3   (d) phone 4
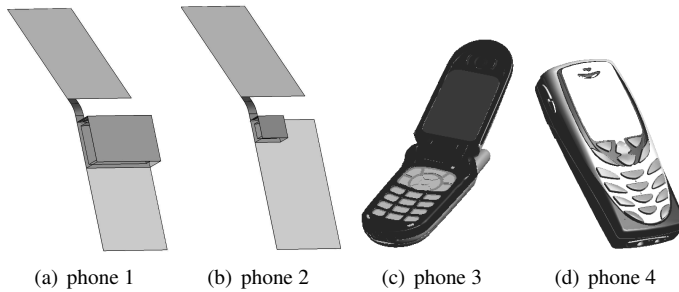
Figure 5.4: The mobile phone models used to investigate the effect of the
user's hand on SAR in the head are the generic clamshell model with a
single-band PIFA at (a) 900MHz and (b) 1800MHz, (c) a CAD model hav-
ing a clamshell style with an external helical antenna operating at 1750 MHz
and (d) a CAD model having a bar style with an internal PIFA operating at
1750 MHz (phone 4).

The mobile phone models are placed in the cheek position against the
SAM head, as defined in [14]. For phone 4, heterogeneous head models
were also used. A previous study of the hand effect on OTA parameters
reports that the mobile phone antenna performance is sensitive to the hand
position [42]. Thus, it is important to define a rigorous process in order to
observe the range of $\Delta psSAR$ that may occur. The process makes use of
a generic block model of the hand as shown in Figure 5.5. This generic
hand consists of three bricks which represent the palm spaced away from
the back face of the mobile phone and the fingers holding the sides. The
generic hand is used because it can be well defined and controlled by scripts
for automated simulations and optimization. To find the hand position that
maximizes $\Delta psSAR$, the generic hand is moved in the Y-direction from the
top to the bottom of the phone, and the palm spacing is moved in the Z-

direction over a 60 mm range, as shown in Figure 5.5. The fingers are touching the cheek, and the finger length L varies according to the hand position. In the coordinate system, $(Y, Z) = (0, 0)$ corresponds to the top of the inside of the palm touching the top of the outer surface of the antenna. The movement resolution is 10 mm in both Y- and Z-directions. The hand position that maximizes $\Delta psSAR$ is then selected. Next, the generic hand model is substituted with a CTIA-defined homogeneous anthropomorphic hand. The anthropomorphic hand is used in two different grips:

- Grip 1: identical to the CTIA-defined grips shown in Figure 2.6 for the specific mobile phone type (bar or clamshell). The position of the hand on the mobile phone model is based on the position of the generic hand that maximizes $\Delta psSAR$.

- Grip 2: the fingers of the hand are posed using the Poser tool in SEM-CAD X [17] so that the hand grip corresponds as close as possible to the grip of the generic hand that maximizes $\Delta psSAR$ while still conforming to the range of realistic hand grips [80].
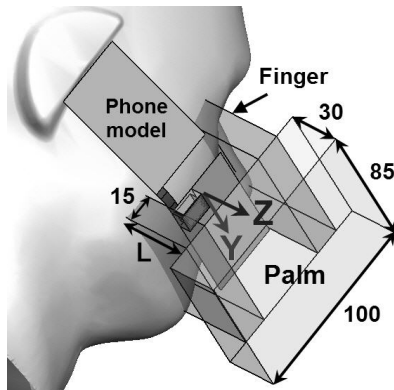
Figure 5.5: The generic hand model shown holding phone 2 to the SAM head. The generic hand consists of three blocks representing the palm, the thumb and the other fingers gripping the sides of the phone. The hand phantom is moved over a wide range of positions along the length of the phone (Y-direction) and palm distances to the back of the phone (Z-direction).

Results

The simulation results quantify how sensitive $\Delta psSAR$ is to the hand position. $\Delta psSAR_{1g}$ is shown as a function of hand position in Figure 5.6 for phone 2 and Figure 5.7 for phone 4. The total variation of $\Delta psSAR_{1g}$ is about 3.5 dB for phone 2 and 2.1 dB for phone 4. For phone 2, 30% of the hand positions result in positive values of $\Delta psSAR$, while for phone 4, it was found for 95% of the hand positions. The 90th percentile value of $\Delta psSAR_{1g}$ is 0.5 dB and 1.8 dB for phone 2 and phone 4, respectively.
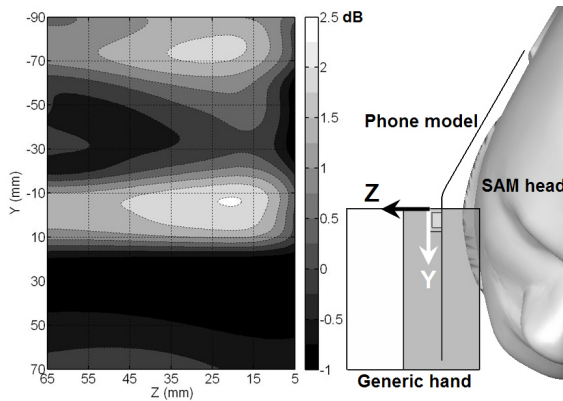
Figure 5.6: The $\Delta psSAR_{1g}$ for phone 2 at 1800MHz is represented as a function of the generic hand position.

Based on the position of the generic hand that maximizes $\Delta psSAR$, the phones were simulated with the anthropomorphic hand phantom. For phones 1, 2 and 3, both grip 1 and grip 2 are applied. Due to the small size of phone 4, it was not possible to position the anthropomorphic hand in grip 1 and use a realistic grip (the index finger would be above the top of the phone). Thus, only grip 2 is used for phone 4. Figure 5.8 and Figure 5.9 show the hand grips applied on phone 1 and phone 4, respectively.

Phone 4 with grip 2 is also simulated with anatomical head models, as shown in Figure 5.10. The setup is identical to that of Figure 5.9 except that the SAM head is replaced by the heads of the Visible Human [100] and the Duke (adult male) and Ella (adult female) models of the Virtual Family [101]. The ears of the models are compressed to represent the force exerted
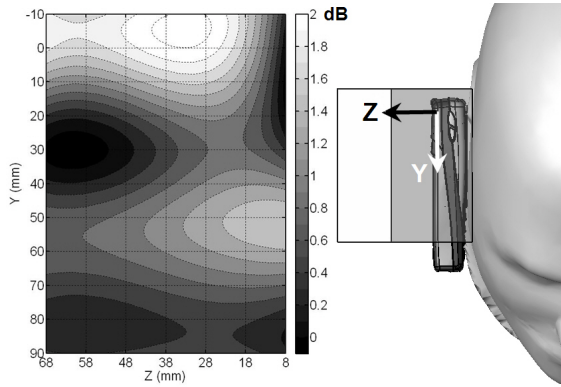
Figure 5.7: The $\Delta psSAR_{1g}$ of phone 4 at 1750MHz is represented as a function of the generic hand position.
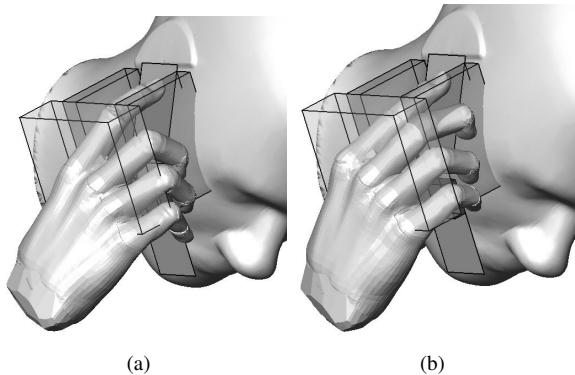
Figure 5.8: The generic hand at the position that maximizes $\Delta psSAR_{1g}$ and the corresponding anthropomorphic hand phantom in (a) grip 1 and (b) grip 2 on phone 1.

by the mobile phone [102].

Table 5.1 shows the simulation results of the four mobile phone models with the hand grips where the highest values of $\Delta psSAR$ were observed. For the results normalized to the same forward power to the antenna, maximum

(a)   (b)
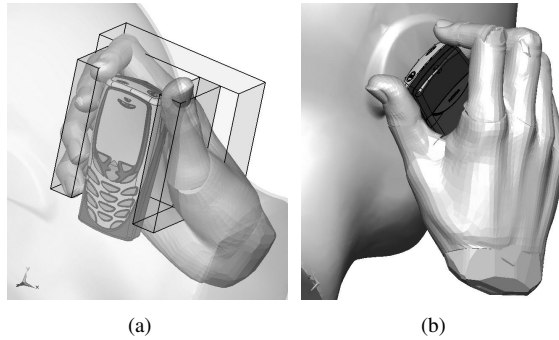
Figure 5.9: The generic hand at the position on phone 4 that maximizes $\Delta psSAR_{1g}$ and the corresponding anthropomorphic hand phantom in grip 2. The views show (a) the front of the mobile phone model, looking through a transparent SAM, and (b) the back of the mobile phone model.

(a)   (b)
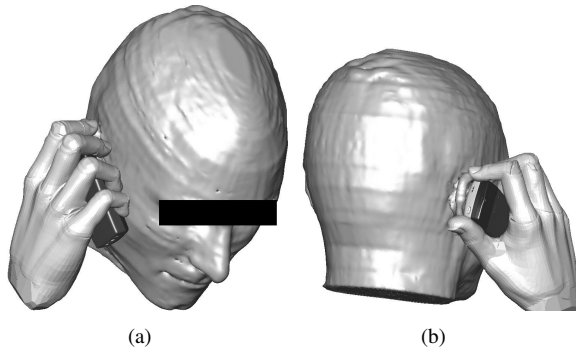
Figure 5.10: The phone 4 with grip 2 as seen in Figure 5.9 is simulated with anatomical head models. In addition to the Duke model seen here, the heads of Ella and Visible Human model are also used in this study.

$\Delta psSAR_{1g}$ values higher than 2 dB are consistently observed for both frequencies and all four phone models investigated. The S_{11} data shows how the antenna match, and therefore the delivered power, are influenced by the presence of the hand. As the hand is in the antenna near field, it can in gen-

eral strongly affect the delivered power, depending on its size and position, and on the antenna and mobile phone design. It is interesting to note that the results presented in Table I are not consistently or strongly biased by the anthropomorphic hands in the grips presented. The change in the delivered power ranges from -0.8 dB (phone 3, grip 2) to +0.7 dB (phone 2, grip 1), and it is less than the change in *psSAR* in all cases. This leads to the conclusion that the increase in *psSAR* presented in Table I is more strongly affected by the disturbance of the fields than the change in the antenna match. For other cases not presented in Table I, the effect of antenna match could be substantial.

The same results are shown normalized to the feed point current in Table 5.1. The increase of psSAR is also over 2 dB for phone 3 and phone 4. $\Delta psSAR$ is not as high for phone 1 and phone 2. Note that the hand grips have been chosen to maximize $\Delta psSAR$ based on power normalization rather than current normalization. For all but one case in Table 5.1, the antenna radiation efficiency, η_{rad}, and the total radiated power, TRP, drop by at least 3 dB when the hand models are included. The hand absorbs a significant amount of power as expected [42].

Table 5.2 shows the results when anatomical head models are used instead of SAM for phone 4. The psSAR in the external ear (pinna) is excluded from the 1-gram and 10-gram averaging for the $\Delta psSAR$ results shown. RF exposure standards from ICNIRP [43] and IEEE [44] have different approaches for how the psSAR limits in the pinna are taken into account. It is outside the scope of this work to deal with the complexities of this pinna issue. $\Delta psSAR$ in SAM also excludes the ear, as the ear is lossless. Table 5.2 shows that $\Delta psSAR$ for the anatomical heads is similar or higher to those for SAM, regardless of whether the psSAR is normalized to current or power. The use of anatomical heads therefore do not change the conclusions of this study.

5.2.2 Measurement

Models and Method

SAR measurements were made with 46 commercial mobile phones in order to determine the effects of the hand on the psSAR in commercial mobile phones. All of the general styles are included: bar (including personal digital assistants), clamshell and slide, as shown in Table 5.3. All of the mobile

	Antenna parameters			$\Delta psSAR$ normalized to power		$\Delta psSAR$ normalized to current	
Phone 1 (900MHz)	S_{11} (dB)	$\eta_{rad}(\%)$	TRP (dBm)	$\Delta psSAR_{1g}$(dB)	$\Delta psSAR_{10g}$(dB)	$\Delta psSAR_{1g}$(dB)	$\Delta psSAR_{10g}$(dB)
No hand	-7.1	56.6	26.6	-	-	-	-
Generic hand, maximum grip	-6.5	12.8	20.0	2.3	2.1	-6.0	-6.2
Anthropomorphic hand, grip 1	-11.4	24.3	23.5	2.4	2.1	0.8	0.5
Anthropomorphic hand, grip 2	-11.5	23.9	23.5	2.6	2.1	0.8	0.3
Phone 2 (1800MHz)	S_{11} (dB)	$\eta_{rad}(\%)$	TRP (dBm)	$\Delta psSAR_{1g}$(dB)	$\Delta psSAR_{10g}$(dB)	$\Delta psSAR_{1g}$(dB)	$\Delta psSAR_{10g}$(dB)
No hand	-10.6	58.2	27.3	-	-	-	-
Generic hand, maximum grip	-4.3	8.0	17.0	2.1	1.7	-1.1	-1.5
Anthropomorphic hand, grip 1	-6.4	14.3	20.4	2.2	1.9	0.8	0.5
Anthropomorphic hand, grip 2	-6.5	14.3	20.5	2.5	2.1	0.6	0.2
Phone 3 (1750MHz)	S_{11} (dB)	$\eta_{rad}(\%)$	TRP (dBm)	$\Delta psSAR_{1g}$(dB)	$\Delta psSAR_{10g}$(dB)	$\Delta psSAR_{1g}$(dB)	$\Delta psSAR_{10g}$(dB)
No hand	-6.8	43.8	25.4	-	-	-	-
Generic hand, maximum grip	-8.1	6.3	17.3	0.7	0.1	4.1	3.5
Anthropomorphic hand, grip 1	-9.2	35.4	24.9	1.7	1.7	3.2	3.2
Anthropomorphic hand, grip 2	-12.4	17.9	22.3	2.1	1.8	4.7	4.4
Phone 4 (1750MHz)	S_{11} (dB)	$\eta_{rad}(\%)$	TRP (dBm)	$\Delta psSAR_{1g}$(dB)	$\Delta psSAR_{10g}$(dB)	$\Delta psSAR_{1g}$(dB)	$\Delta psSAR_{10g}$(dB)
No hand	-7.4	32.1	24.2	-	-	-	-
Generic hand, maximum grip	-7.5	3.4	14.4	2.0	2.2	2.7	2.9
Anthropomorphic hand, grip 2	-8.8	8.0	18.4	2.5	2.4	2.3	2.2
Phone 4 (1750MHz), Duke head	S_{11} (dB)	$\eta_{rad}(\%)$	TRP (dBm)	$\Delta psSAR_{1g}$(dB)	$\Delta psSAR_{10g}$(dB)	$\Delta psSAR_{1g}$(dB)	$\Delta psSAR_{10g}$(dB)
No hand	-10.5	36.8	25.3	-	-	-	-
Generic hand, maximum grip	-9.9	2.8	14.0	2.1	1.5	4.3	3.7
Anthropomorphic hand, grip 2	-12.0	6.5	17.9	2.6	2.5	3.5	3.3

Table 5.1: The simulation results of the four mobile phone models with the
hand phantoms at the position that causes the highest increase of the 1-gram
and 10-gram peak spatial-averaged SAR. η_{rad} is the radiation efficiency of
the phone model.

Head model	Power normalized		Current normalized	
	$\Delta psSAR_{1g}$ (dB)	$\Delta psSAR_{10g}$ (dB)	$\Delta psSAR_{1g}$ (dB)	$\Delta psSAR_{10g}$ (dB)
SAM	2.5	2.4	2.3	2.2
Duke	2.6	2.5	3.5	3.3
Ella	3.1	3.4	4.1	4.4
VH	2.9	2.8	4.0	3.9

Table 5.2: $\Delta psSAR$ in anatomical head models with phone 4 and the corre-
sponding anthropomorphic hand phantom in grip 2.

phones were operated in GSM mode aside from two in WCDMA mode. A
base station simulator was used to establish the call at the center channel
of the band and maintain a fixed output power of the mobile phone. The

measurements with each mobile phone were repeated and psSAR variations less than 5% were observed.

Frequency	bar	clamshell	slide	total
900 MHz	4	8	8	21
1800 MHz	24	9	13	46

Table 5.3: The number of each type of commercial mobile phone measured in this study.

Measurements were made using an iSAR system (SPEAG, Zurich, Switzerland) [56]. The top surface of the system follows the ear-to-mouth line of the SAM, as specified in [14, 103]. This line is extruded in an orthogonal direction (see Figure 5.14). The thickness of the outer shell is 2 mm, except at the ear spacer where it is 6 mm, as specified in [14, 103]. The 256 electric field probes are arranged in a planar array which is conformal and 4 mm below the shell. Cubic spline interpolation is applied between the measured points, and the psSAR is estimated using the algorithms derived from [104, 105]. The probes are embedded in a lossy dielectric material having dielectric parameters over a wide frequency range, at least 600-6000 MHz, within 10% of the target values for human tissue that are standardized in [14, 103]. The short measurement time ($< 1\,$s) compared to conventional systems ($> 300\,$s) makes it practical to perform the large number of measurements in this study. The position of the mobile phone is secured by a dielectric phone holder. A comparison study between iSAR and a standard SAR measurement system, DASY52 (SPEAG, Zurich, Switzerland) shows that the difference in psSAR is within $\pm$ 0.5 dB for most transmitters [56]. The repeatability of iSAR measurements is within 0.2 dB.

A human right hand, as seen in Figure 5.11 is used, with dimensions shown in Table 5.4. The hand dimensions are close to the CTIA-defined hand phantom [12]. The original hand grip applied in this study is based on the grip studies [12, 80] (Figure 5.11(a) and Figure 5.11(b)). The hand is moved vertically (Figure 5.11(c)) and horizontally (Figure 5.11(e)) with different palm-phone distances (Figure 5.11(d)). This does not cover the full range of hand positions possible, but it is intended to represent a subset of realistic hand positions. The maximum psSAR among all the hand grips and positions is recorded for each mobile phone.

Hand Dimensions (mm)	Tester	CTIA
Wrist Width	57	61.4
Wrist Circumference	162	162.9
Hand Length	189	186.5
Hand Circumference	192	200.2
Palm Length	110	105.7
Hand Width	79	85

Table 5.4: Dimensions of the tester's hand and the CTIA-defined hand phantom. Hand length is the distance from the center of wrist to the tip of the middle finger. Palm length is the distance from the middle crease to distal palm crease.

Results

The maximum $\Delta psSAR_{1g}$ values obtained for the mobile phone models is shown in Figure 5.12. Previous studies suggest that the increase of psSAR due to hand is more pronounced at higher frequencies [52]. Indeed, the data show that a narrower range of maximum $\Delta psSAR_{1g}$ values is observed at 900 MHz than at 1800 MHz, and that the percentage of mobile phones exhibiting a significant increase in psSAR is less at 900 MHz than at 1800 MHz. For example, the number of mobile phones exhibiting $\Delta psSAR_{1g}$ values above 0.5 dB is 5 out of 21 at 900 MHz and 21 out of 46 at 1800 MHz.

5.2.3   Discussion

Influence of Hand Position

The proximity of the user's hand significantly perturbs the near-field distribution around the mobile phone. To illustrate this point, Figure 5.13 shows the SAR distribution in SAM from phone 2 with and without the anthropomorphic hand phantom in grip 1. In the absence of the hand, the SAR is more evenly spread out, while the presence of the hand results in a more concentrated absorption pattern for this case. The observed changes in the pattern have several non-independent causes 1) reflections by the hand resulting in a confinement of the RF energy between head and hand, 2) detuning of the antenna, 3) modification of the RF coupling between the electrical components in the phone and therefore on the current distribution inside the

(a) (b) (c) (d) (e)
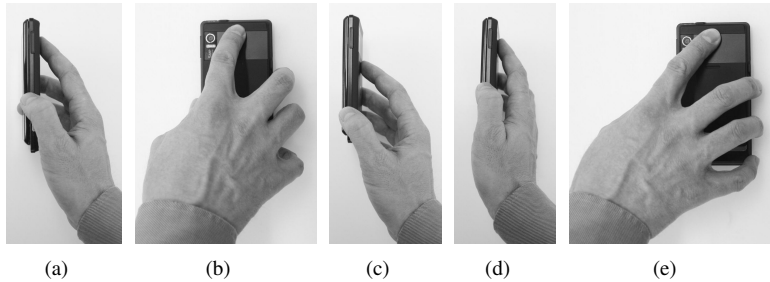
Figure 5.11: The hand grip and movement applied to obtain the maximum $\Delta psSAR$ value. The original grip (a), (b) is shifted (c) to different positions, posed (d) with different palm-phone distances and moved to the left (e) and right sides.

(a) (b)
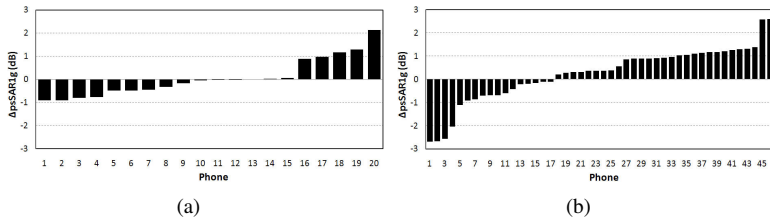
Figure 5.12: $\Delta psSAR_{1g}$ for (a) 21 mobile phones at 900 MHz and (b) 46 Mobile phones at 1800 MHz.

phone. In the simulated cases, if the palm of the hand is very close to the antenna (less than 15 mm), the strongly increased absorption inside the hand reduces the psSAR in the head (as seen in Figure 5.6 and Figure 5.7). At palm-phone distances of 15 mm to 35 mm, the psSAR in the head increases for the cases at 1750 and 1800 MHz. The psSAR then drops at larger palm-phone distances. The psSAR in the head is also sensitive to the hand location, with highest psSAR values when the top of the palm is directly over the antenna.

The higher range of $\Delta psSAR$ values and more frequent occurrence of high values may be due to the shorter wavelength of 1800 MHz. At shorter wavelengths, the mobile phone and the hand are electrically larger and there
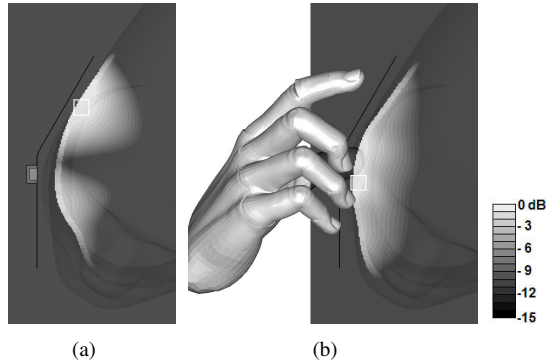
Figure 5.13: The distribution of 1g-averaged SAR of phone 2 in the SAM (a) without the hand and (b) with the anthropomorphic hand in grip 1. (The white squares are the hotspots.

are more opportunities to influence both the near field distribution and the currents on the mobile phone. This result is consistent with the general finding of Francavilla and Schiavoni [52]. Additional studies at other frequencies would be needed to see if this trend continues.

Suitability of the Hand Model

To examine if a homogeneous hand can approximate the effect of a real hand, a comparison is made between the CTIA-defined hand and the tester's hand for one mobile phone at a frequency near 1800 MHz (Figure 5.14). SAR measurements are made on the iSAR for both left and right hands. Efforts were made by the tester to pose the hand as closely as possible to the grip used by the CTIA-defined hand. The measurement results as seen in Table 5.5 show that the difference between the hand phantom and the human hand is small (within 0.25 dB). This suggests that a human hand can be approximated by the homogeneous hand model for this purpose. An interlaboratory comparison study between seven laboratories found that the reproducibility of psSAR measurements with a CTIA-defined hand phantom at 900 and 1800 MHz was within acceptable levels, resulting in only a modest increase in the measurement uncertainty compared to psSAR mea-

surements without a hand model [106].

(a)   (b)
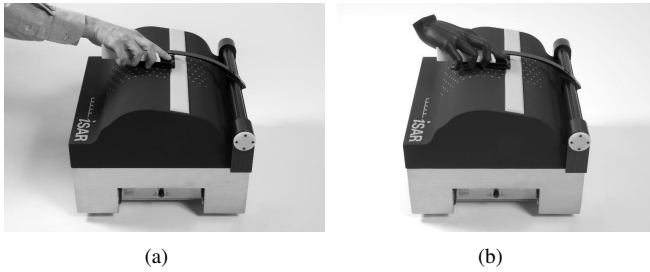
Figure 5.14: psSAR measurement of a mobile phone using (a) the tester's hand and (b) the hand phantom.

$\Delta psSAR_{1g}$ (dB)	Tester	CTIA	Difference
Right hand	0.89	0.81	-0.08
Left hand	-0.31	-0.57	-0.25

Table 5.5: $\Delta psSAR_{1g}$ for the measurement setup shown in Figure 5.14 with the tester's hand and the CTIA-defined hand model.

Antenna Design Considerations

It was shown in Figure 5.6 and Figure 5.7 that psSAR in the head can be very sensitive to the hand position. Given that the psSAR is caused by currents on the radiating structure [38], the psSAR is also sensitive to the design of the antenna and mobile phone. However, the complexity of mobile phone design makes it difficult to devise simple antenna design rules that are guaranteed to mitigate the hand effect. Proposals to keep the current from flowing on the mobile phone chassis have been proposed such as creating a current choke [50]. Modifications to the mobile phone chassis can be made to keep the current from flowing on areas influenced by the hand [92]. To suppress regions of high electric field concentration on the antenna, such as slots on PIFA antennas, the slots can be replaced by lumped elements [65].

A practical approach for a specific mobile phone design is to identify and change the primary design features that cause the psSAR increase. This

approach is demonstrated for phone 2, where high values of psSAR in the head have been identified with enhanced currents on the flexible PCB. The current on the flexible PCB can be reduced by changing the locations of the antenna or the flexible PCB, as shown in Figure 5.15. Each configuration was simulated with the generic hand in the same range of hand positions as described previously. The results were used to produce the distribution of $\Delta psSAR$ with position as shown in Figure 5.6, and the highest value of $\Delta psSAR$ was recorded. These maximum values, given in Table 5.6 show how sensitive the hand effect can be to a small number of mobile phone parameters.

(a)   (b)   (c)
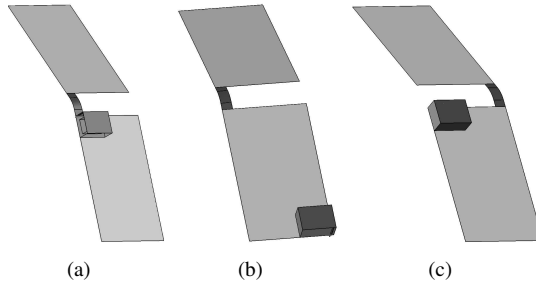
Figure 5.15: (a) The original model of phone 2 and modifications to change the location of (b) the antenna and (c) the flexible PCB.

	Original	Move antenna	Move flexible PCB
$\Delta psSAR_{1g}$ (dB)	2.1	0.45	-0.2

Table 5.6: Maximum $\Delta psSAR_{1g}$ in SAM over all positions of the generic hand. Results are shown for the designs of Figure 5.15.

Chapter 6

Mechanisms of RF EM Field Absorption in Human Hands and Fingers

This chapter analyzes in detail the causes of higher psSAR in the hand and proposes correction factors to be applied to the flat phantom measurements. The hand has a complex anatomy, and the myriad possible hand positions on a wireless device can have a dramatic effect on the antenna performance [80, 42] and psSAR [54, 55]. The SAR in biological tissues in the near field of an RF source is determined from the induction of magnetic fields generated from source currents [38]. The psSAR in the hand may be affected by standing waves in tissue layers [107, 39] and partial-body resonance effects. Resonance effects for the whole body [108] and partial-body regions (e.g., torso, legs) [109] have been quantified, but possible resonances in fingers and hands have not been studied in detail.

An objective of this chapter is to investigate the mechanisms of RF absorption in the human hand[1]. A further objective is to estimate the maximum psSAR10g value in a hand relative to that in the flat phantom defined in IEC 62209-2. After introducing the applied method and models, the first part of this chapter is an initial investigation of psSAR10g in an anatom-

---

[1]This study has been published in IEEE Transactions on Microwave Theory and Technology as *Mechanisms of RF Electromagnetic Field Absorption in Human Hands and Fingers*[110].

ical hand model exposed to dipole antenna sources at several frequencies. The results show that the psSAR10g could be substantially higher in the fingers than in a flat phantom, so further investigation is warranted. Cylindrical and brick models of the fingers and palm are used to investigate the physical mechanisms of increased psSAR in more detail. The exposure of fingers in the far-field and the near-field are also studied using plane waves and dipole antennas, respectively. Finally, we present the maximum value of the psSAR10g computed in the human hand, normalized to that in the standardized flat phantom.

6.1 Method and Models

Two and three-dimensional numerical modeling has been performed with SEMCAD X. The frequencies of interest are 900, 1800, 2450 and 3700 MHz. At least 8 layers of UPML are placed at 0.15 wavelength away from the simulated objects. The grid resolution is always less than 1 mm and it is finer at higher frequencies. One-dimensional modeling has also been performed analytically using transmission line theory [111].

The investigation examines the RF absorption of anatomical hand models, simplified cylindrical and brick models, and a standardized flat phantom defined in IEC 62209-2 [103]. The detailed anatomical hand model and dielectric cylindrical model representing the fingers are shown in Figure 6.1. The flat phantom is represented as a lossy medium, with permittivity and conductivity corresponding to head tissue simulating liquid (HTSL) [103], and a lossless 2 mm thick shell (relative permittivity of 3.0) between the lossy medium and the source. For the 1D and 2D analysis, the shell is not modeled. The influence of the lossless shell on the psSAR is negligible for frequencies below 2 GHz. At frequencies between 2 GHz and 3.8 GHz, the absence of the shell underestimates the psSAR by 8% or less [112]. The influence of the shell is therefore small compared to the other enhancements observed in this study. The size of the flat phantom is at least 20% larger than the dipole antenna sources used, as per the requirements of IEC 62209-2 [103]. The flat phantom is set as an infinite half-space. Unless stated otherwise, the cylindrical models used in this study have a defined length and diameter and hemispherical caps on either end, with a radius equal to the radius of the cylinder. The anatomical hand is acquired from the Duke model of the Virtual Family [102]. There are 7 tissues in this hand model: blood,

bone, fat, muscle, marrow, skin and subcutaneous adipose tissue (SAT).

While it is obvious that a hand and a flat phantom have very different geometries, there is a need to evaluate whether the flat phantom can provide a conservative value for psSAR10g in the hand, so as to guide the development of future revisions of IEC 62209-2.

(a)   (b)
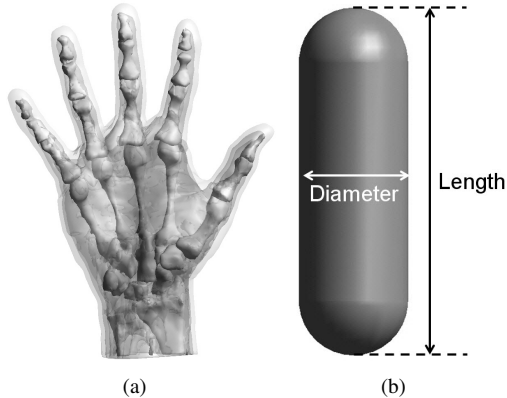
Figure 6.1: The hand models simulated in this study include (a) the right hand of the Duke model from the Virtual Family and (b) a homogeneous cylinder to represent an isolated finger.

The homogeneous cylindrical model is used for a parametric study of the finger within the statistical variations of human finger length and width. The 5th and 95th percentile lengths and widths of the five fingers have been published by Greiner [76] and are shown in Figure 6.2. Based on these values, we have chosen to evaluate cylinders having six diameters between 16 mm and 26 mm and six lengths between 55 mm and 95 mm, as shown by the dots in Figure 6.2.

The material properties (relative permittivity, conductivity and density) of the homogeneous cylinders are calculated as a volume-weighted average of the five tissues in the finger (bone, fat, muscle, skin and SAT). The averaging was performed for the five right-hand fingers of three of the adult models of the Virtual Population (Duke, Ella and Fats (an obese model)) [113]. The properties of individual tissues correspond to the consolidated tissue data base [114]. The resulting material parameters are shown in Ta-
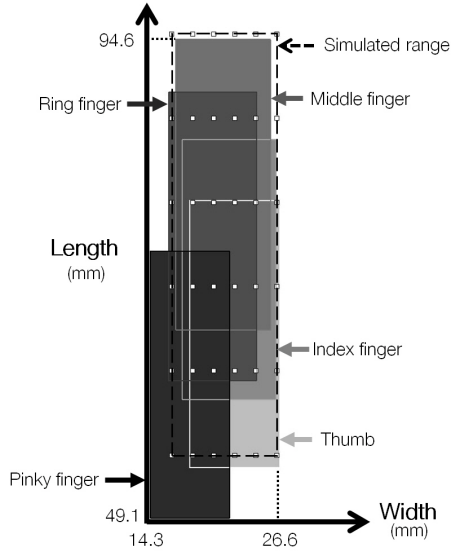
Figure 6.2: Shaded boxes showing the range of 5th to 95th percentile of the five fingers, from [76]. The parameters of the cylindrical model, having six diameters from 16 mm to 26 mm and six lengths from 55 mm to 95 mm, are shown as dots.

ble 6.1 for each frequency investigated.

All models under test (MUT) are illuminated by a plane wave or a half-wavelength dipole antenna for far-field and near-field exposure, respectively. The dipole antennas have 2 mm diameter and they are driven with constant current source. The length of each dipole antenna is tuned to optimize the impedance match in freespace. Although the near-field of contemporary mobile phones is more complex than that of a dipole antenna, the dipole antenna sufficiently represents the mechanism of absorption for the purposes of this study. The results are analyzed in terms of the ratio between the psSAR10g of the MUT and that of a flat phantom, i.e.

$$\Delta psSAR = \frac{\text{psSAR10g}_{\text{hand}}(\text{W/kg})}{\text{psSAR10g}_{\text{flat phantom}}(\text{W/kg})}, \tag{6.1}$$

where psSAR10g$_{\text{hand}}$ and psSAR10g$_{\text{flat phantom}}$ are the psSAR10g in the

Frequency (MHz)	900	1800	2450	3700
Relative permittivity	30	28	27	26
Conductivity (S/m)	0.5	0.8	1.0	1.5

Table 6.1: The material properties of the homogeneous cylindrical finger models, determined from a volume-weighted average of the tissues in the five right-hand fingers of three anatomical models. (Density: $1200 \, \text{kg/m}^3$)

MUT and in a flat phantom under the same exposure condition. A $\Delta psSAR$ greater than one indicates that the flat phantom underestimates the psSAR in the hand.

To validate the cylindrical model, the index finger and thumb from the Duke model are compared with the homogeneous cylinders of similar dimensions. The exposure source is a plane wave with direction of propagation normal to the axis of the cylinders and the E-field parallel to it. The simulation models are shown in Figure 6.3. The fingers are not attached to the hand to compare their absorption pattern to that of the cylindrical model. From Figure 6.4, the average difference in psSAR10g between the cylindrical and anatomical models is 21%, which is small compared with the enhancements shown later in this study. It can therefore be concluded that the cylindrical model is a suitable representation of anatomical fingers in terms of $\Delta psSAR$ over the frequency range of interest.

6.2 Exposure of a Hand from a Dipole Antenna

An anatomical hand model exposed to a resonant half-wave dipole antenna is simulated to determine whether the approach of using a flat phantom provides conservative results. The geometry is shown in Figure 6.5. The distance from the antenna to the middle finger ranges from 2 mm to 200 mm. The $\Delta psSAR$ results are shown in Figure 6.6. The values are above unity for nearly all frequencies and distances shown, indicating that the flat phantom is not a conservative representation for these cases.

Christ *et al.* found that enhancements in psSAR10g by a factor of two are possible due to standing waves within tissue layers (e.g., skin, fat and muscle) having different dielectric properties [107]. However, such enhancements are not expected at very close distances for the hand models in-

(a)   (b)
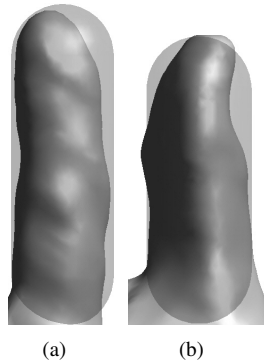
Figure 6.3: Isolated finger models of (a) index finger (length: 70 mm, diameter: 22 mm) and (b) thumb (length: 60 mm, diameter: 22 mm) and corresponding homogeneous cylindrical models having material properties in Table 6.1.

(a)   (b)
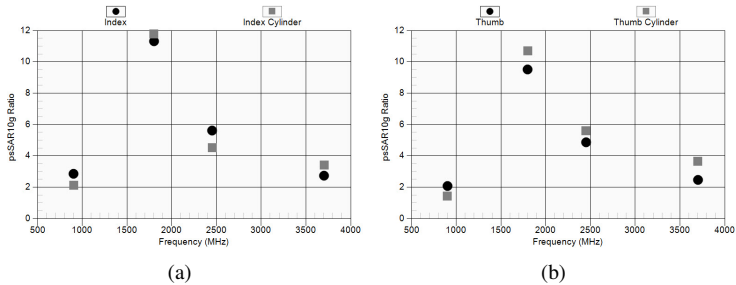
Figure 6.4: Comparison between $\Delta psSAR$ of homogeneous cylinder models and anatomical models of (a) index finger and (b) thumb at the four frequencies investigated.

vestigated here. Investigations of layered finger models by the authors also did not produce significantly higher SAR enhancements than those found with homogeneous models. Additionally, the possible enhancements observed in Figure 6.6 are more than a factor of four. The influence of the finger geometry clearly plays a dominant role in the SAR enhancements. For example, Kühn *et al.* demonstrated that whole-body resonance can in-

duce high whole-body SAR [115] and the resonant frequency depends on the height of the human model. This is investigated in the following section.

(a)   (b)
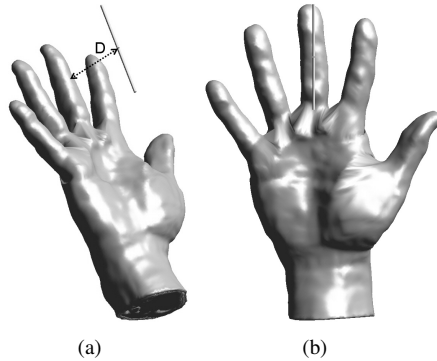
Figure 6.5: Hand and dipole models used in this study to examine the psSAR10g in the hand compared with a defined flat phantom.
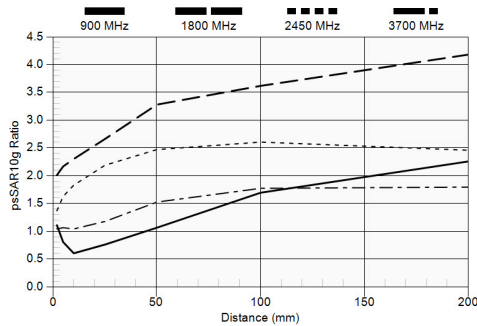
Figure 6.6: The $\Delta psSAR$ of the hand in Figure 6.5 at different distances and frequencies.

6.3   Power Absorption in Cylindrical Tissue Models

The mechanisms of power dissipation in a cylindrical model under plane wave exposure are investigated first. For further simplification, the cylinders used in this section have no round end caps, because these add little to the understanding of the bulk absorption mechanisms. This study is focused mainly on the fields in cylindrical dielectric models. It will be shown that psSAR in the simulated fingers could be much higher than that in the palm of the hand. There is practically no literature on this topic. Authors have dealt with the EM field propagation along the axis of dielectric cylinders [116] or with the backscattering from dielectric cylinders [117], but no analysis is available for EM field inside dielectric cylinders excited by plane waves with direction of propagation normal to the cylindrical axis. The magnitude of E-field of the plane wave is 1 V/m.

6.3.1   Fields in the Cross-Section of an Infinitely Long Cylinder

One- and two-dimensional scenarios are studied as shown in Figure 6.7. The excitation is a plane wave at 900 MHz with incidence normal to the cylinder axis (X direction). The slab is referred to as a flat phantom if it is infinitely thick. Both the slab and cylinder have the material properties of Table 6.1. Note that HTSL is not used here for the slab in order to study the effect of the geometry alone. The cylinder is illuminated by plane waves with both E- and H-polarization. The power dissipated in a slab (1D) and a cylinder (2D) were calculated analytically and numerically, respectively.

The definition of dissipated power density (DPD) as given in Equation 6.2 is applied to evaluate the absorbing efficiency of a cylinder of diameter D as compared to a slab with width D; both have the same length L:

$$\mathrm{DPD} = \mathrm{P_d}/(D \cdot L) \; (W/m^2), \tag{6.2}$$

where $\mathrm{P_d}$ is total power dissipated in this region. Since both structures
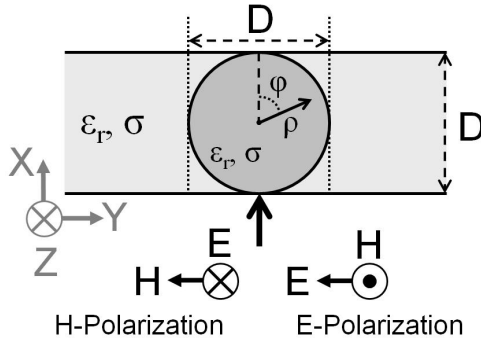
Figure 6.7: A slab and a cylinder with thickness and diameter D are illuminated by a plane wave at 900 MHz with normal incidence.

are infinitely long in the Z direction, DPD can be rewritten as

$$\lim_{L \to \infty} \text{DPD} = \frac{1}{D} \iint_S P(x, y) dx dy \ \ (W/m^2), \tag{6.3}$$

where $P(x, y)$ represents the power dissipation (W/m^3) in the cross section of the slab or the cylinder at (x, y). Figure 6.8 shows a comparison of DPD between flat phantom, slab and cylinder models having identical dielectric parameters. D is normalized to the unit of the wavelength in the material of the cylinder, or λ_d. The DPD caused by a plane wave with E-polarization can be significantly higher in cylinders than that in slabs. Thus, a cylinder of diameter D is electrically wider than a slab with width D regarding absorbed power, or has higher absorbing efficiency. This implies that fingers are potentially under greater exposure than the palm from a normally incident plane wave.

When a cylinder is illuminated by a plane wave, the phase of the field inside the surface of the cylinder is quite uniform if the cylinder has a small diameter in terms of the wavelength in the dielectric material. Thus, in a first approximation, the E_z field generated by the external sources inside a cylinder of small radius has a radial distribution given by the function J_0, Bessel function of the first kind of order zero. The absorption (or equivalent area) of the cylinder increases with its radial dimension and reaches its peak when $D/\lambda_d \simeq 0.3$ (i.e., $\pi D/\lambda_d \simeq 1$, Figure 6.9(a)). This condition
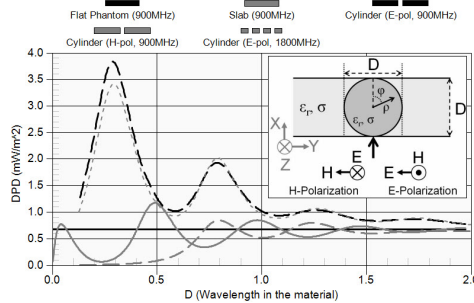
Figure 6.8: Dissipated power density (DPD in mW/m^2) in the following structures illuminated by a plane wave ($|E| = 1$ V/m): a flat phantom, a slab with thickness D and a cylinder with diameter D. For the cylinder, both E and H polarizations are shown at 900 MHz, and E polarization is shown at 1800 MHz.

supports standing waves circling the interior cylindrical surface. Two more peaks are observed for $D/\lambda_d \simeq 0.8$ ($\pi D/\lambda_d \simeq 2.4$, Figure 6.9(b)) and for $D/\lambda_d \simeq 1.2$ ($\pi D/\lambda_d \simeq 3.8$, Figure 6.9(c)). The value of 2.4 is recognized as the first zero of the J_0 Bessel function and 3.8 as the first zero of the J_1 Bessel function. The two Bessel functions J_0 and J_1 dominate the transverse absorption of infinitely long dielectric cylinders with the radii of our interest. The radial solution of the wave equation in cylindrical coordinates is given by $F(\rho) = A_0 J_0(k_\rho \rho) + A_1 J_1(k_\rho \rho) \cos \phi$, where $k_\rho = 2\pi/\lambda_d$, the coordinates of ρ and ϕ are shown in Figure 6.7. This clearly is seen in Figure 6.9(b) where the strong excitation of $J_1(k_\rho \rho)$ causes first the shift of a single focus and then the presence of two focal areas within the cylindrical cross section. As the excitation of J_1 is less pronounced with respect to that of J_0 and of other incipient Bessel functions of higher order, a single major focal area emerges. It is worth noticing that with this last diameter ($D/\lambda_d \simeq 1.2$) the dielectric cylinder starts to cast a shadow at its back side.

The same simulation was also conducted at 1800 MHz (see Figure 6.8). The results are very similar with that at 900 MHz, which confirms the analysis above. The focusing effects are insignificant for the H-polarization compared to those of the E-polarization as the cylinder is not thick enough to support high displacement current in ϕ direction. If D is very large, sev-

(a)   (b)   (c)
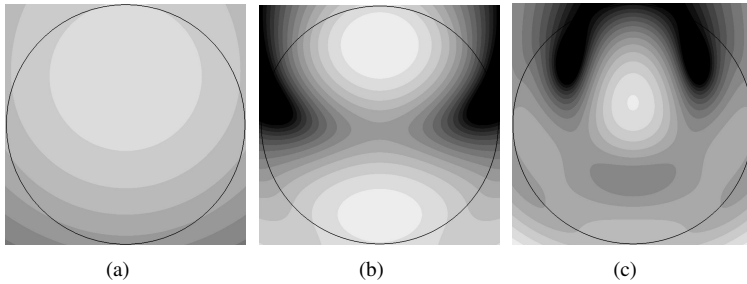
Figure 6.9: The RMS values of the E-field in the cylinders with the diameter is (a) 18 mm (0.3 λ_d), (b) 48 mm (0.8 λ_d) and (c) 76 mm (1.27 λ_d). (The maximum values are 0.92 V/m, 0.5 V/m and 0.4 V/m, respectively. Each color step = 1 dB)

eral wavelengths, the power dissipated in the cylindrical model and the slab converge to that of the flat phantom.

6.3.2 Fields in Dielectric Cylinders of Finite Length

The effect of the length of the cylindrical models is also studied in light of the theory of partial-body resonance. It is well-known that whole-body resonance can cause substantially high whole-body SAR [115]. Moreover, partial-body resonance may also play an important role in psSAR [109].

Figure 6.10 shows the z component of E-field (E_z) along the z-axis of a 330 mm long ($L = \lambda_0$, wavelength in freespace) cylinder illuminated by an E-polarized plane wave source at 900 MHz. Cylinder diameters of 5 mm and 20 mm are shown. E_z is much higher than the other field components inside the cylinders. The spikes at both ends are due to the boundary conditions on the electric field. The continuity of the normal component of the vector $\vec{D}$ (electric displacement) causes a substantial electric field discontinuity equal to the dielectric constant of the cylinder ($\epsilon_r = 30$). In the case of 5 mm diameter, the incident field is not disturbed considerably by an electrically thin dielectric cylinder ($\pi D/\lambda_d << 1$), so E_z is quite uniform along the cylinder. This phenomenon is independent of the length L of a thin cylinder. The field changes significantly within a thick cylinder (D = 20 mm or $\pi D/\lambda_d \simeq 1$). The E-field distribution along the axis of the 20 mm

thick cylinder follows a sinusoidal function.
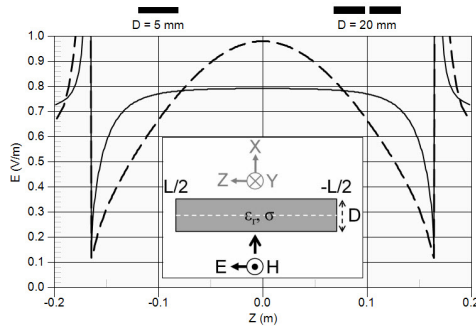
Figure 6.10: The E-field (RMS value) along the axis of a dielectric cylinder with length 330 mm (λ_0, wavelength in freespace) diameter 5 mm ($\pi D/\lambda_d \ll 1$, solid) and 20 mm ($\pi D/\lambda_d \simeq 1$, dash) illuminated by an E-polarized plane wave at 900 MHz.

If a cylinder is infinitely long, no standing waves are expected in its axial direction. When the cylinder has finite length and large enough diameter, the accumulated charge at the ends of cylinder drives the displacement current as standing waves in axial or Z direction. The total E_z, incident plus scattered, must be identical just outside both bases of the cylinder. This boundary condition can be satisfied only if the E_z field is supported by spatial harmonics of the type $\cos[(2n + 1)\pi z/\lambda_0]$, $|z| < L/2$, where λ_0 is the free space wavelength and $n = 1, 2, \cdots$. This phenomenon is similar to what happens in a transmission line open at both ends. The fields supported by dielectric cylinders with $\pi D/\lambda_d \simeq 1$ or greater are quite complex. The field E_z excites a magnetic field in the circumferential direction (ϕ), or H_ϕ, which, in concomitance with the incident H_y component, gives rise to the radial components, E_ρ and H_ρ. Only H_z is absent from this structure.

If the cylinder is shorter than λ_0, only the first spatial harmonic exists, as seen in Figure 6.10. More spatial harmonics can be observed in longer cylinders. Figure 6.11 shows the E-field in the cylinders when the length is 1.5, 2 and 3 λ_0. The third and fifth harmonic can be clearly observed when the length is 2 and 3 λ_0, respectively. In the case of 1.5 λ_0, the third harmonic is weak and combined with the first harmonic resulting in flat field distribution at the center. Note that although the fields presented are

inside the cylinder, the periodicity of the spatial harmonics follows λ_0. This result agrees with previous studies that conclude that partial-body resonance depends on the wavelength in freespace [109].
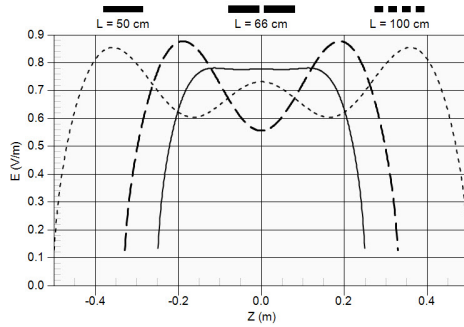
Figure 6.11: The E-field (RMS value) along the axis of the cylinders when the length is 1.5 λ_0 (solid), 2 λ_0 (dash) and 3 λ_0 (dot). The diameter is 20 mm and the plane wave frequency is 900 MHz.

In order to evaluate the influence of the spatial harmonics on psSAR10g, cylinders of different lengths with a fixed diameter (20 mm, corresponding approximately to the average finger width as shown in Figure 6.2) were simulated at four frequencies: 900, 1800, 2450 and 3700 MHz. The simulation results are shown in Figure 6.12. The partial-body resonance appears periodically. The first peaks at 900 and 1800 MHz are caused by the first spatial harmonic. They do not occur at the same electrical length as the electrical sizes of the diameters are different. At 900 MHz, there is a local minimum at the length 1.5 λ_0. The first spatial harmonic is dominant when the cylinder is shorter than this length so the psSAR is located at center of the cylinder (see Figure 6.10). However, increasing the length of the cylinder enhances the third harmonic so the psSAR location shifts towards the end of the cylinder (see Figure 6.11). The results at 900 and 1800 MHz show that only the first partial-body resonance is important as it causes the highest psSAR considering different lengths.

The psSAR patterns vs. cylinder length at 2450 MHz and 3700 MHz are significantly different from those at the lower frequencies due to their electrically large diameter. As mentioned previously, $J_1 \cos(\phi)$ has a significant role in the field distribution on the cross-section as the diameter is
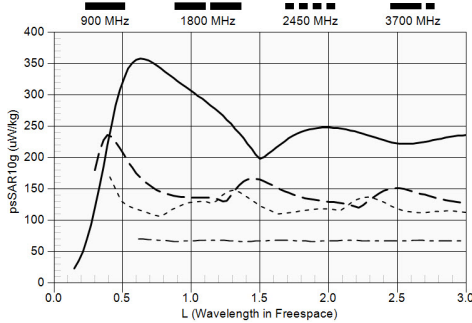
Figure 6.12: The psSAR10g (μW/kg) in cylinders with D = 20 mm and different lengths L illuminated by a plane wave with E-polarization ($|E|$ = 1 V/m) at four frequencies (shown in MHz).

Figure 6.13: E-field in the cylinder (L = 245 mm, D = 20 mm) at 2.45 GHz, incident wave traveling in X+ direction with E-polarization. ($E_{max, RMS}$ = 0.7 V/m, each color step = 1 dB)

close to one λ_d (20 mm is about 0.85 λ_d at 2450 MHz). The combination of $J_1 \cos(\phi)$ and the third longitudinal spatial harmonics leads to the field distribution seen in Figure 6.13. The spatial harmonic causes more absorption peaks, which makes the averaged power dissipation more uniform in the Z direction. Thus, if the cylindrical diameter is larger than λ_d, the psSAR value has less dependence on the cylinder length. This can be observed in Figure 6.12 for the frequency 3.7 GHz. Given the difference in the geometry of the boundary conditions of the field incident on a slab and those on a finite cylinder, it is not surprising that the results presented above show a substantial divergence in absorbed peak power levels vs. frequency in the two dielectric structures.

6.4 Far-Field Exposure

This section consists of two parts. In the first part, the cylindrical models in Figure 6.1(b) are simulated with the dimensions of the fingers shown in Figure 6.2. In the second part, the fingers are attached to a parallelepiped solid of simulated tissue representing the palm of a hand and the arm. $\Delta psSAR$ as defined in Equation 6.1 is used to evaluate the psSAR10g in the MUT. The source is an E-polarized plane wave propagating in the direction normal to the axes of the fingers.

6.4.1 Absorption of Fingers

The dimensions and material parameters of the cylinders are set as that in Figure 6.2 and Table 6.1, respectively. Simulation results are shown in Figure 6.14. According to the study above, the behaviors of power dissipation depends on the length and diameter normalized to λ_0 and λ_d, respectively. The normalized values are shown in Table 6.2. The results in Figure 6.8 and Figure 6.12 can be used to interpret the results in Figure 6.14 considering the ranges shown in this table.

Frequency (MHz)	900	1800	2450	3700
Length (λ_0)	0.17-0.29	0.33-0.57	0.45-0.78	0.68-1.17
Diameter (λ_d)	0.26-0.43	0.51-0.83	0.68-1.10	1.01-1.64

Table 6.2: The range of length and diameter in Figure 6.14 in terms of λ_0 and λ_d, respectively.

The enhancement of the psSAR10g in the cylinder models compared to the flat phantom is most pronounced at 1800 and 2450 MHz due to the first partial-body resonance; the resonance occurs for $L \simeq 0.5\lambda_0$ in Figure 6.12. Enhancement factors more than 10 can be observed for plane wave exposure under certain conditions. In addition, a strong dependence on the cylinder diameter is observed at 1800 MHz. At 900 MHz, as the cylinders are electrically short, the $\Delta psSAR$ is predominantly sensitive to the cylinder length. At 3700 MHz, the cylinders have diameter and length electrically larger than λ_d and λ_0, respectively, so influence of length is not as significant. However, high $\Delta psSAR$ is still observed at this frequency.
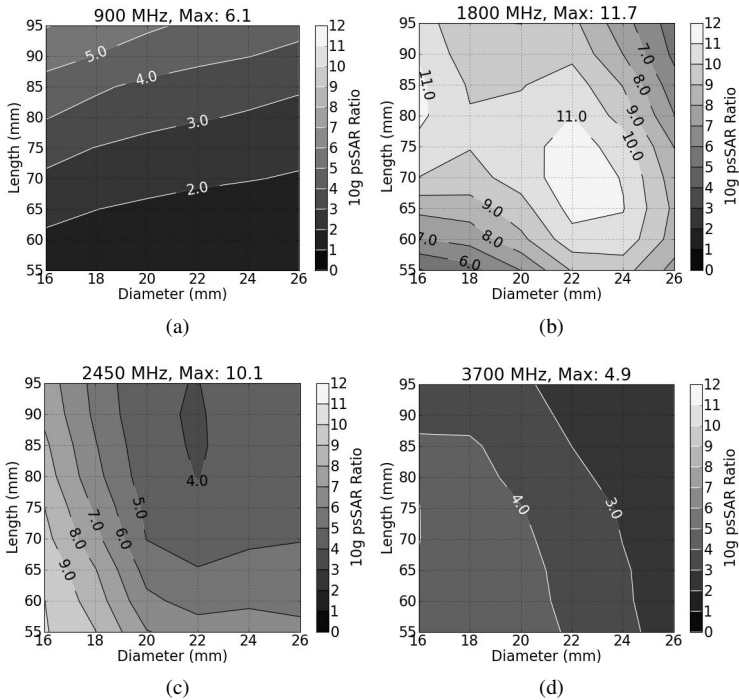
Figure 6.14: $\Delta psSAR$ of the cylinders illuminated by a plane wave at (a) 900 MHz, (b) 1800 MHz, (c) 2450 MHz, and (d) 3700 MHz.

6.4.2   Fingers, Palms, and Arms

An isolated cylinder was used to understand the physical mechanisms of psSAR enhancement, but it is not a realistic model for the human finger that is attached to the hand. To better represent the palm and arm, parallelepiped solids (blocks) are attached. Three models are used, as seen in Figure 6.15. They represent finger and palm (model 1), finger and palm perpendicular to the arm (model 2) and finger and palm parallel to the arm (model 3). The sizes of the palm and arm (derived from the dimensions of the Duke model) are fixed as shown in Figure 6.15, while the dimensions of the cylinder change in the ranges defined in Figure 6.2. All models are homogeneous

in dielectric properties, as defined in Table 6.1. Although the material properties do not match those of a palm, the models have a shape resembling that of the metacarpal geometry. The plane waves illuminating the three models travel in the X direction with E-field parallel to the fingers (see Figure 6.15). For each model at each frequency, the cylinder geometry causing the highest $\Delta psSAR$ is recorded and the results are shown in Figure 6.16.

(a) Model 1   (b) Model 2   (c) Model 3   (d) Model 4   (e) Model 5
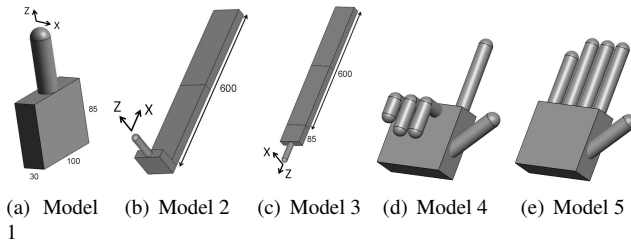
Figure 6.15: The models represent hand and arm (mm); (a) hand-only (model 1), (b) hand perpendicular to arm (model 2) and (c) hand parallel to arm (model 3). (d) Model 4 and (e) model 5 have five fingers in different grips and the index fingers have the dimensions resulting in the highest psSAR in model 1.

The psSAR10g is still substantially underestimated by flat phantom measurements in the three models at all the frequencies. In the cylinder-only model, partial-body resonance is pronounced at 1800 MHz and 2450 MHz. However, in model 1, adding the palm causes a downward shift in the frequency at which the absorption effects are most pronounced, with a maximum enhancement more than 20 at 900 MHz. Besides, the models are electrically thinner at lower frequencies so that $\Delta psSAR$ at 900 MHz in model 1 is greater than in the cylinder-only model at 1800 MHz. At 900 MHz, $\Delta psSAR$ is higher in model 2 than in model 3 as the plane wave has higher coupling in model 2 than that in model 3. This happens because the sharp bend in model 2 prevents the arm from being tightly coupled with the palm, so the finger and palm can have a damped partial-body resonance. In model 3, the resonance of the palm is damped by the presence of the arm. The structure in model 3 is expected to have its partial-body resonance at about 220 MHz. This structure is of little interest in the band 900 MHz to 3700 MHz and is given no further consideration. When the frequency is higher than

1800 MHz, the difference among the three models is negligible.

The hand models with single finger (model 1 to 3) were used for the reasons of simplicity and more important, worst-case evaluation. This is demonstrated with the simulation of the models having the other fingers and thumb (model 4 and model 5 in Figure 6.15). The finger dimensions resulting in the highest psSAR found in model 1 are applied to these two models at the four frequencies. Model 4 can be thought to represent a simplified model of a hand gripping a device. Model 5 is for evaluating the influence of the other fingers. As seen in Figure 6.16, the psSAR induced in model 4 is similar with that in model 1 (within 14 %), and model 4 always has higher psSAR than model 5 (by 14 - 154 %) due to absorption by adjacent fingers. Thus, model 1 is a reasonable choice for conservative estimation and for identifying the physical mechanisms because of its simple geometry.
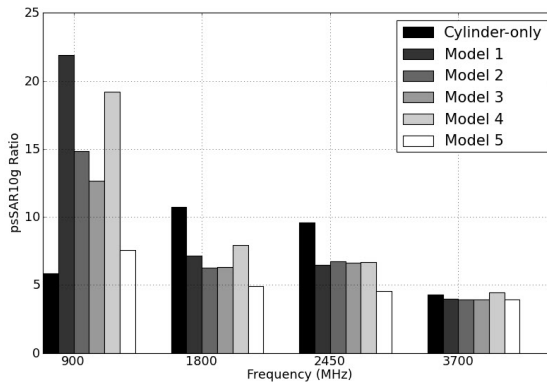
Figure 6.16: The highest value of $\Delta psSAR$ for plane wave exposure of the cylinder-only model and model 1-3 shown in Figure 6.15 when cylinder dimensions vary in the range shown in Figure 6.2. The finger dimensions on model 4 and 5 are fixed. The index fingers on these two models have the dimensions causing the highest psSAR in model 1.

6.5 Near-Field Absorption

Plane waves were used to investigate the mechanism of SAR in a hand and arm exposure in the far-field, but the most common scenario of exposure is in the vicinity of a radiating device such as a mobile phone. Dipole antennas are used to represent the radiator for near-field exposure (Figure 6.17). The simulated psSAR in each case is normalized to a reference current as magnetic induction is the major mechanism of the power absorption in the near-field.
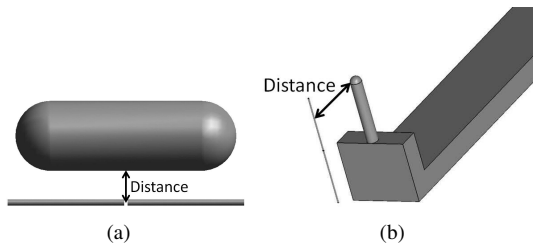
Figure 6.17: The setup for near-field exposure; a dipole antenna illuminates (a) a cylinder only and (b) model 2 defined in Figure 6.15.

The cylinder models causing the results of the cylinder-only case at each frequency in Figure 6.16 were exposed to a dipole antenna with different distances (Figure 6.17(a)). One cylinder model was used at each frequency. Simulation results of $\Delta psSAR$ in the cylinder models are shown in Figure 6.18. When the dipole is electrically far, the $\Delta psSAR$ is, as expected, close to that for far-field exposure. When the dipole is close to the cylinder, the SAR is much closer to that in a flat phantom. As mentioned before, magnetic induction is the dominant mechanism for SAR in near-field and geometry of the tissue is less significant under this mechanism. Thus, the difference of psSAR10g between cylinder and flat phantom is much less in the near-field, but the underestimation by flat phantom measurement is still considerable in most cases.

As stated earlier, model 2 is of greater interest for partial resonances than model 3. Thus, for obtaining a realistic worst-case envelope of psSAR10g, model 2 is also exposed to the same dipole antennas. The cylindrical finger models were simulated with dimensions described in Figure 6.2 and the
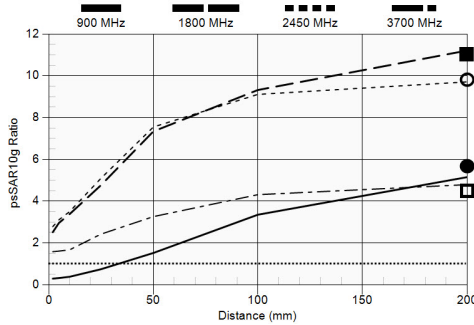
Figure 6.18: $\Delta psSAR$ of the cylinders when illuminated by the dipole antenna from different distances. The markers on the right side are the results of the cylinder-only case in Figure 6.16. (solid circle: 900 MHz, solid square: 1800 MHz, hollow circle: 2450 MHz, hollow square: 3700 MHz)

geometry having the highest $\Delta psSAR$ is shown in Figure 6.19 at each frequency and each distance. The presence of palm and arm reduces the effect of partial-body resonances of the fingers and therefore lower $\Delta psSAR$ values are observed than in Figure 6.18. The slight variations of the plots in Figure 6.19 are due to the changes of beam shape in the near-field of the dipole and its repositioning with respect to the target tissue as different fingers maximize $\Delta psSAR$ for different distances from the RF source.

Comparing the results of Figure 6.19 and Figure 6.6, it is observed that the values of Figure 6.19 are higher. This is expected, as Figure 6.6 represents only a single hand geometry. Although measurements with a flat phantom may not provide a conservative psSAR result, the flat phantom is convenient to use in the laboratory. Measurements in a hand model are impractical, due to the need to insert electric field probes in the dielectric medium with sufficient volume of material around it to prevent errors due to air-tissue boundary effects. Instead, the results of Figure 6.19 can be used as correction factors from measurements in a flat phantom to conservative values in the hand. Results can easily be generated for other frequencies and distances using the models described. A closed-form expression could also be developed to describe the correction factor.
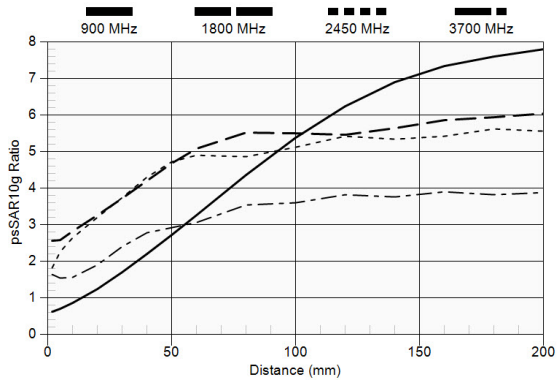
Figure 6.19: $\Delta psSAR$ of model 2 (see Figure 6.15) when illuminated by the dipole antenna at different distances.

Chapter 7

Conclusions from Studies of Hand Effects

The effects of hand parameters on mobile phone antenna performance in terms of OTA parameters and SAR are studied in this thesis. The parameters are assumed to be independent as a first approximation.

In the OTA part, both the talk mode (when the user is talking on the mobile phone) and data mode (browsing or typing messages) are investigated. The inhomogeneous hand can be well replaced with a homogenous hand of appropriate dielectric parameters. Variations of up to 15% can be tolerated since the effect is lower than 0.5 dB. The effect of the wrist is very small. Significant effects were found for hand grip, including hand size, palm-phone distance and the vertical positions of the hand phantom. The most important factor is the index finger positioning and its touching area on the back of the mobile phone. Since the index finger may be close to the antenna, a slight shift or mis-positioning of the index finger can lead to strong variation in OTA. The OTA performance of mobile phones can be strongly impaired by the hand and therefore tests without the hand will not provide meaningful assessments of the performance under real-life conditions. However, the hand geometry as well as the exact position of the phone inside the hand must be very precisely defined in order to obtain highly reproducible results in future OTA measurements.

In addition, the effect of hand grip and position on mobile phone an-

tenna performance in data mode in terms of OTA parameters is also studied
using one of the commercial mobile phone models in the talk mode study.
Various hand grips and positions cause significant change in OTA perfor-
mance. The uncertainty of positioning error of the hand phantom is about
8 dB of TRP within 6 mm shift, and the variation of radiation efficiency due
to different hand positions is higher than that of the mismatch efficiency. In
addition, the analysis of the simulation results suggests a method to estimate
the influence of the hand phantom on this mobile phone. This investigation
is an important database for the standards establishment of including a hand
phantom in mobile phone antenna OTA measurement. Based on this study,
suggestions for the CTIA standard are as following;

- A homogeneous hand phantom with the material properties suggested
  by Gabriel should be able to represent the effect of a real human hand.
  The material properties should allow 15% uncertainty in manufacture.

- The dimensions of the hand phantom should be at average of statistics.

- The wrist is not necessary.

- The grip is one of the most important factors, and different types of
  mobile phones, like candybar or clamshell, are held in different ways
  in real-world usage. Thus, the hand phantoms should be in different
  grips for different types of mobile phones.

- Precise and robust fixture is necessary for suppressing the uncertainty
  of measurement results.

The hand effect on head SAR was studied in both simplified and realistic
scenarios. In the simplified scenario, the generic mobile phone models and
phantoms are used in this study. It is found that firstly, the head SAR can be
increased significantly by the user hand. Besides, the head SAR is very sen-
sitive to the hand position, and only some positions cause significant SAR-
increase. In the realistic scenario, both simulation and measurement results
show that the hand in some cases can significantly increase the psSAR in the
head. The highest increase was found to be approximately 2.5 dB. This in-
crease is consistent between simulations and measurements, it is consistent
over different models of the hand and head, and it is consistent over differ-
ent frequencies (900 and 1800 MHz). Simulations conducted over a wide
range of hand positions were used to find the conditions over which the

maximum increase occurred. The measurement results show that this effect is more pronounced and occurs more often at 1800 MHz than at 900 MHz. Simulations at 1800 MHz over a wide range of hand positions found that higher psSAR in the head occurs when the palm is over the antenna with a minimum palm-antenna spacing. At closer distances, the psSAR in the head decreases. The psSAR in the head is sensitive to the hand position, with variations of more than 3 dB observed. The CTIA-defined hand model gives similar results as a real hand, and psSAR increases in the SAM head have been replicated in anatomical heads.

A main objective of this work was to investigate the psSAR increases in SAM, as this is the head phantom used by international measurement standards. The results support the conclusion that significant and reproducible psSAR increases in SAM are possible when the hand is introduced. Therefore, the influence of the hand is an important factor to consider for future revisions of these standards. Possible considerations, such as the addition of hand models in SAR measurement procedures or the application of scaling factors to account for hand effects, require further work. This study reports the highest increases in psSAR in the head, but it does not investigate the likelihood of such an increase among the user population. It also does not address compliance with regulatory limits, as it is outside the scope of this investigation.

The mechanisms of SAR enhancement in the hand are thoroughly investigated in this part of thesis over the 900 to 3700 MHz frequency range. It is clearly shown that psSAR10g in the hand can be significantly underestimated by measurements in a flat phantom unless correction factors are applied. The results demonstrate that fingers have their own resonance modalities for the absorption of RF energy. The absorption of the fingers is much larger than predicted by simple, flat phantom models used so far to estimate the exposure of these organs. Using homogeneous models, the effects of finger geometry have been investigated statistically, and formulas have been used to describe the SAR enhancement due to cylindrical geometry and partial-body resonance. The analysis in this paper shows the physical mechanism of the enhanced absorption that would remain otherwise hypothetical or unexplained in the existing literature.

The models were exposed to plane waves and dipole antennas for far-field and near-field exposures, respectively. Published statistics on finger length and width were used, together with weighted-average dielectric parameters from anatomical models, to conduct parametric numerical analyses

of the issue. When hand and arm models were included, the changes in the frequency and magnitude of the psSAR10g enhancement were described. The simulation results of hand models exposed to fields from dipole antennas at different distances provide the envelope of psSAR10g in the hand compared to a flat phantom. This information could serve as database for correction factors from widely-accepted flat phantom measurements to conservative exposure values in the hand of a wireless device user.

Part II

Hyperthermia Treatment Based on Non-invasive EM Power

Chapter 8

Introduction of the Hyperthermia Study

8.1 Background

Hyperthermia treatment (HT) is a type of thermal therapy for cancer treatment that involves heating the target tissue (tumor) to $39\,°\mathrm{C} - 45\,°\mathrm{C}$ for about 30 min - 1 hour, mostly as an adjuvant modality with the standard treatments such as radiation therapy and chemotherapy. The thermal effects on tissues at different temperatures are shown in Figure 8.1 [118]. The technology applied for low ($39\,°\mathrm{C} - 41\,°\mathrm{C}$) and moderate ($41\,°\mathrm{C} - 45\,°\mathrm{C}$) temperature HT is discussed in this report. Thermal power can lead to cancer cell damage, usually with minimal injury to normal tissues. More important, for some types of cancer, heating the tumor can enhance the efficacy of radiation therapy and chemotherapy. The possibility of this enhancement has generated wide interest in developing equipment for conducting HT.

8.1.1 Engineering of Hyperthermia Treatment

The equipment that delivers thermal energy to the tissues is called an *applicator*. The thermal source is usually ultrasonic or electromagnetic power absorption. There are four different types of HT: whole-body, (loco-)regional, superficial and interstitial/intracavity [118, 119]. Whole-body hyperthermia

Thermal Therapy Treatment Options

Cryotherapy
T < −50°C for >10 min
ΔT = −90°C

Mechanisms
Freeze/Thaw transition
Disrupts cell membrane
Complete cellular destruction

Potential HT Techniques
Thermal Conduction

Equipment Availability
100% Commercial

Moderate Cooling
T = 0–10°C for 10 min
ΔT = −37–27°C

Mechanisms
Decrease blood perfusion, pO_2
Decrease permeability, extravasation
Decrease cellular metabolism
Slow nerve conduction

Potential HT Techniques
Thermal Conduction

Equipment Availability
100% Commercial – Ice Packs

Low Temp Hyperthermia
T = 39–41°C for 1–72 hrs
ΔT = 2–4°C

Mechanisms
Increases perfusion, permeability, pH, pO_2
Increases metabolic activity, drug uptake
Radiosensitization, Chemosensitization

Potential HT Techniques
Whole Body
Thermal Conduction, Perfusion
External
RF, MW, US
Interstitial–Intracavitary
RF, MW, US
Thermal Conduction
Ferroseeds, Thermorods
DC Resistance Wires
Hot Water Tubes
Fiberoptic Diffuser Crystals

Equipment Availability
40% Commercial
60% University – Under Development

Moderate Temp Hyperthermia
T = 41–45°C for 30–60 min
ΔT = 4–8°C

Mechanisms
Increases perfusion, permeability, pH, pO_2
Increases metabolic activity, drug uptake
Radiosensitization, Chemosensitization
Some cell kill at higher temperatures/doses

Potential HT Techniques
External
RF, MW, US
Interstitial–Intracavitary
RF, MW, US
Thermal Conduction
Ferroseeds, Thermorods
DC Resistance Wires
Hot Water Tubes
Fiberoptic Diffuser Crystals

Equipment Availability
40% Commercial
60% University – Under Development

Thermal Ablation
T > 47–50°C for >10 min
ΔT = >10°C

Mechanisms
Protein Denaturization
Necrosis
Coagulation
Not subtle effects

Potential HT Techniques
External
RF, MW, US
Mechanically Scanned Focused US
Electrically Focused US Arrays
Interstitial–Intracavitary
RF, MW, US
Thermal Conduction

Equipment Availability
75% Commercial
10% PMA
50% IDE Trials
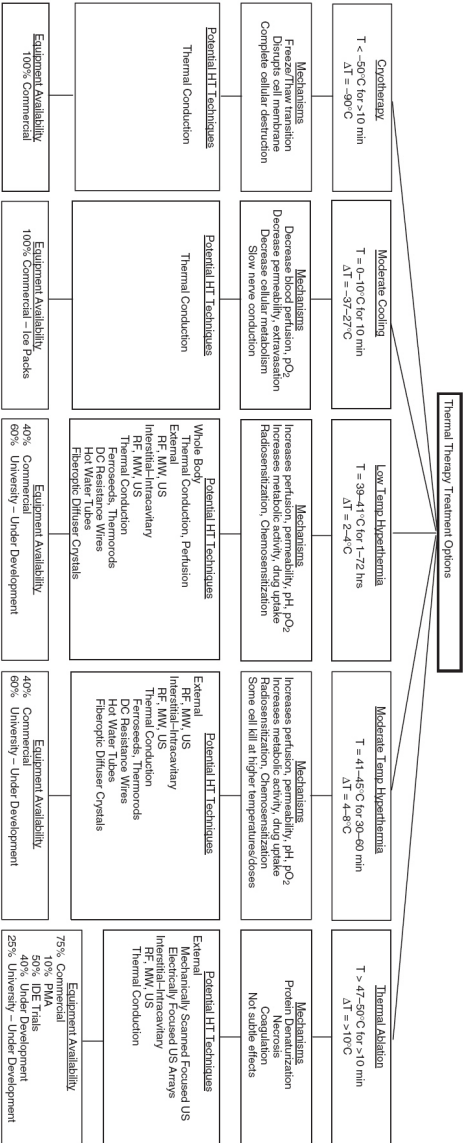40% Under Development
25% University – Under Development

Figure 8.1: The effect and usage of thermal energy on tissues at different temperatures [118]. Low and moderate temperature hyperthermia are discussed in this report.

is not a common approach due to reasons of medical efficacy and safety. The temperature in whole-body hyperthermia can only reach up to $41.8\,°C$ without jeopardizing the patient's life [120]. Compared to the non-invasive HT techniques, the methods for interstitial/intracavity HT are more varied and well-established, and a large temperature range is available with this modality [121]. Under exposure to extremely low frequency (ELF) magnetic fields, invasive HT can also be conducted with implants[1]. These methods include magnetic seeds implanted in the target as the thermal source [122], and, more important, magnetic nanoparticles or magnetic fluid. A tumor filled with magnetic fluid becomes more lossy and heatable by an ELF H-field, which is a novel and seemingly promising method [123, 124]. Compared to invasive HT, regional and superficial hyperthermia are more suitable for heating tumors of larger size. This review focuses only on the technologies for regional and superficial HT with non-invasive EM applicators (but not including intracavity methods).

The behavior of the EM field at the RF and MF range in a human body is very complicated. It is very difficult to have only one design of hyperthermia applicator to heat different sizes of tumors in different regions [125]. Thus, it is necessary to have specifically designed applicators for cancers in different regions of body such as the brain, breast, superficial region (depth < 4cm), pelvic region, extremities and the head and neck region. The EM power can be delivered with single or multi-element operation. Multi-element operation with precise control of the amplitude and/or phase of each input is called *Phased Array*.

The success of HT strongly depends on the interdisciplinary collaboration between medicine and engineering [126]. Moreover, multiple engineering disciplines are involved. The work on the engineering side is mainly in four domains:

- Applicator design: this includes RF circuit and radiation scenario design. For the RF circuit, fabrication, power amplification, feeding structure and feedback measurement are involved. For the radiation scenario, not only the single element and phased array designs are considered, but also applicator dimensions, shape of water bolus, patient position, etc.

---

[1]Note that the ELF in this thesis is defined as the frequency for the problem which can be analyzed with quasi-static approach.

- Thermometry: thermal distribution in tissues is very difficult to predict because of the complicated and nonlinear thermal behavior in tissues and vasculature. However, the temperature distribution in the tumor is critical to the efficacy of hyperthermia. The accuracy and comprehension of thermal measurement is therefore one of the most important factors for HT performance.

- Numerical tools: these include electromagnetic and thermal simulation tools, data acquisition and processing, feedback control, user interface and optimization algorithms of excitation coefficients for phased array. The simulation tools are usually combined with the optimization called *Treatment Planning Tools* [127, 128].

- Clinical implementation: integration is always important to multi-discipline application, which includes clinical feasibility, repeatability and quality assurance. One of the key issues of public acceptance to a medical modality is repeatability. The performance has to be repeatable in different places, with different technicians and on different patients. Therefore, quality assurance becomes a necessary procedure for guaranteeing the repeatability [129].

This review focuses on applicator design and optimization algorithms of excitation coefficients, namely, the amplitude and phase of each excitation source.

The evaluation of the performance of a hyperthermia applicator is based on several considerations. The first is the level and distribution of the SAR or temperature of the target. This issue is directly responsible for the medical efficacy of HT. Secondly, the targeting of the thermal pattern, or the concentration of the energy, in the human body is also of importance. If the normal tissues surrounding the target are also heated excessively, the patient may experience pain or even tissue damage. Consequently, the delivered power, as well as the thermal energy in the tumor, has to be limited. Finally, because the clinical process of HT usually takes about one hour, patient comfort, such as breathing restrictions, pressure from the water bolus, burning feeling on the skin and pressure or pain due to hotspots, during the treatment is also considered a significant topic.

8.2 Why Hyperthermia?

Hyperthermia is not a novel way of curing disease or lesions as it can be dated back to 3000 BC [130, 131, 119]. In the last century, hyperthermia was found to be helpful in cancer treatment [119]. The efficacy of HT was at first only concerned with the direct killing of cancer cells. Recent studies, however, have shown that the adjuvant effects of HT with standard treatments are more important and practical [132]. In addition, it is very important to have significant indicators of SAR or temperature, which strongly correlate to clinical response [133]. Thermal dosimetry of HT is therefore also discussed in this section.

8.2.1 Biological Background of Hyperthermia Treatment

There are two main mechanisms of the medical efficacy of HT, the direct and the adjuvant effect. In terms of the direct effect, cancer cells can be killed or damaged directly by high temperature. It is well known that cell survival rate drops dramatically when the temperature is higher than $43\,^\circ$C [130, 134, 135], so a thermal source, like EM fields, concentrated on a tumor can kill the cancer cells directly by excessive heat. Besides, a tumor is more sensitive to high temperature than normal tissues for the following reasons. Firstly, the vasculature in a solid tumor is generally chaotic and full of premature vessels. When the temperature increases, the vascular collapse in the tumor is much more severe than that in normal tissues [119]. The haphazard vasculature also limits the delivery of nutrition and oxygen when the tumor grows. Consequently, that causes hypoxia, low pH and poor nutrition condition, which make the cancer cells more sensitive to high temperature [125, 131, 119]. Finally, cells are more susceptible to heat when they are under the S-phase in the replication process, and cancer cells usually have a longer S-phase than normal cells [120]. Therefore, cancer cells are generally weaker than normal cells under exposure to heat [126, 119]. More detailed biological rationale of HT on cell-level has been reported in [120, 125, 131].

In addition to the direct effect of heat on cancer cells, there is a more important and well-known advantage of using hyperthermia: it can be an adjuvant modality with radiotherapy (RT) or chemotherapy (CT) as it is able to enhance the efficacy of both these standard treatments without additional significant toxicity. As mentioned above, cancer cells usually have

the characteristics of low pH, poor nutrition and a longer S-phase during the cell division cycle, which are also the conditions of high radiation resistance [120, 135]. Thus, hyperthermia has complementary efficacy combined with RT. HT can also increase the radiosensitivity of the cancer cells as the blood flow and oxygenation in the tumor is increased when a temperature of $39 - 41\,°C$ is reached (the low temperature hyperthermia in Figure 8.1). Therefore, the increased blood flow and oxygenation in the tumor can enhance the radiosensitivity and drug delivery for RT and CT respectively [120, 136, 131]. This characteristic of enhancing RT and CT by HT is considered much more important than the direct effect of HT. RT and CT are well-established modalities, but the side effects of both may seriously affect the patient's quality of life. Therefore, HT plus RT or CT can provide not only a better clinical response, but also fewer side effects because a lower dose of RT or CT is required. The enhancement happens even when the tumor temperature is lower than $41\,°C$. For this reason, reaching $43\,°C$ is not now considered a necessary goal in bimodality (CT+ HT or RT+ HT) or trimodality (CT+ RT+ HT) treatment, which is good news from the engineering aspect [126, 125, 137, 138].

8.2.2　Thermal Dosimetry

Although the biological rationale for hyperthermia treatment is quite strong, the correlation between thermal dose and clinical response is still unclear, and this is one of key issues for public acceptance of hyperthermia treatment [139, 140]. The effects of thermal dose include not only those on different kinds of tumors but also the thermal thresholds for various healthy tissues. The most common methods of quantifying thermal dose are the cumulative number of equivalent minutes at $43\,°C$ (CEM43 $°C$), minimum temperature in the tumor (T_{min}) and the 90th percentile of the tumor temperature distribution (T_{90}). The CEM43 $°C$ is defined as

$$\text{CEM43}\,°C = \int_{t_{start}}^{t_{stop}} R^{43-T}\, dt \tag{8.1}$$

$$= t R^{43-T} \qquad \text{when T is constant,} \tag{8.2}$$

where t is the time during the treatment in minutes and T is the temperature. R is the number of minutes needed to compensate for a $1\,°C$ tem-

perature change either above or below the breakpoint, which is generally chosen as $43\,°C$ [139]. In many cases, R is 0.5 or 0.25 when T is higher and lower than $43\,°C$, respectively. However, as different values of R and the breakpoint are suggested in different reports, both values are not yet uniquely determined [139]. Besides, T_{90} and T_{min} can also be combined with the concept of CEM43$\,°C$ as CEM43$\,°CT_{90}$ and CEM43$\,°CT_{min}$, respectively. Significant correlation between CEM43$\,°CT_{90}$ and clinical response has been reported in [140].

Practically speaking, it is difficult to obtain the entire temperature distribution in the treated region. In addition, an indicator with one value is required clinically instead of a curve or distribution. Some modified definitions of temperature indicators are therefore applied in clinical application. With regard to HT+ RT for locally advanced cervical cancer (LACC), two indicators have been found to have a significant correlation with tumor control and survival [138]. They are TRISE and modified CEM43$\,°CT_{90}$. The definition of TRISE is

$$\text{TRISE} = \frac{\sum_{n=1}^{n=max}(\text{ALT50} - 37\,°C) \times dt}{450}, \tag{8.3}$$

where n and dt are the number and the duration of the treatments, respectively; T50 is the temperature exceeded by 50% of sites monitored in the bladder, vaginal and rectal lumen, and ALT50 (All Lumen T50) is defined as the value averaged over all treatments. In addition, the definition of modified CEM43$\,°CT_{90}$ is

$$\text{CEM43}\,°CT_{90} = \sum_{n=1}^{n=N} \int_{0}^{t_{total}} \Delta t R^{(43-T90)}, \tag{8.4}$$

where t_{total} is the time for the treatment, which is 90 minutes in [138]; N and Δt are the number and the time interval of the treatments, respectively (N is 5 in [138]); T90 is the value averaged of the All Lumen T90 during Δt; R is 0.5 or 0.25 when T is higher and lower than $43\,°C$, respectively.

With respect to the evaluation of HT performance, SAR$_{ratio}$ appears to be the indicator preferred for target-SAR analysis, hotspot analysis (in healthy tissues) and the optimization of excitation coefficients among the 24 indicators evaluated in [133]. It is defined as

$$\text{SAR}_{ratio} = \frac{\text{SAR(V1)}}{\text{SAR}_{target}}, \tag{8.5}$$

where SAR(V1) is the SAR averaged in the one percent of the patient volume with the highest SAR, or the hotspot; SAR_{target} is the SAR averaged in the target volume.

8.2.3   Clinical Results

There have been many clinical trials of HT, with both positive and negative results [135, 141, 125, 131, 119]. Table 8.1 shows the positive effect of combining HT with RT, CT or RT+ CT in cancer treatment [131]. In addition, a report of a 12-year follow-up of patients who took RT with and without HT shows that RT+ HT has significantly better results than RT alone in terms of both tumor control and overall survival rate (Figure 8.2) [142]. Moreover, a recent study also shows that RT+ HT can offer similar efficacy to the standard treatment of RT+ CT for local advance cervical cancer (LACC), i.e. patients under RT+ HT have the same response rate but without the side effects due to CT. [138].

Tumor	Treatment	Patients	End point	Effect with HT	Effect without HT
Head and neck	RT	41	CR rate	83%	41%
			5-year LC	69%	24%
			5-year survival	53%	0%
Melanoma	RT	70	CR rate	62%	35%
			2-year LC	46%	28%
Breast	RT	306	CR rate	59%	41%
Glioblastoma multiforme	Surgery, RT	68	Median survival	85 weeks	76 weeks
			2-year survival	31%	15%
Bladder, cervix and rectum	RT	298	CR rate	55%	39%
			3-year survival	30%	24%
Rectum	RT, surgery	115	5-year survival	36%	7%
Bladder	CT	52	PR rate	66%	22%
Cervix	RT	64	CR	55%	31%
Various	RT	92	Response	82%	63%
Lung	CT	44	Response	68%	36%
Cervix	RT	40	CR	85%	50%
Rectum	RT	14	Response	100%	20%
Oesophagus	RT, CT, surgery	53	Palliation	70%	8%
Oesophagus	RT	125	3-year survival	42%	24%
Rectum	RT, surgery	122	PR rate	23%	5%

Table 8.1: Clinical trials showing positive results of cancer treatment using HT combined with standard treatments [131]. (CR: complete response, LC: local control, PR: partial response)
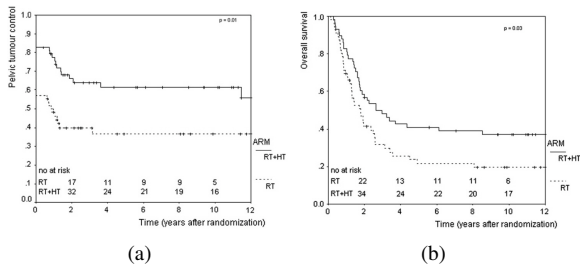
Figure 8.2: The (a) local tumor control and (b) overall survival rate in the 12-year long-term study of clinical trials using hyperthermia treatment [142].

However, some clinical trials have shown that including HT does not significantly improve the response rate [131, 143]. Table 8.2 shows the results of the clinical trials not gaining significant benefit from HT [131]. In this table, the first and second trials were important references for the efficacy of hyperthermia treatment in the United States. As the results of these two trials showed no significant improvement by adding HT, hyperthermia treatment is still not widely accepted in the United States [125, 131, 132]. However, the failure of the two clinical trails, including a recent one [143], could be due to insufficient thermal coverage of the tumor and poor treatment scheduling [131, 125, 119]. Heating tumors with external EM power is a great engineering challenge. It is very difficult to manipulate the distributions of EM energy, especially in the deep regions of highly lossy and inhomogeneous environments like tissues. Predicting the thermal distribution due to SAR is also challenging [134, 126]. For this reason, it can easily happen that the treated tumor is not heated uniformly with sufficient power. Furthermore, the adjuvant effect of HT was not considered as the major goal, so the treatment schedule was not set to maximize the adjuvant effect [132]. Therefore, these clinical trials also underline the importance and urgency of developing better applicators and an optimal treatment plan.

Besides adding HT as an adjuvant to RT or CT, trimodality treatment, i.e. HT+ RT+ CT, also seems encouraging for cancer treatment [137]. However, not many clinical trials have investigated trimodality. This is because RT and HT may heighten the toxicity from CT, and much more investigation is still needed to find the optimal treatment plan. The parameters of this

Tumor	Treatment	Patients	End point	Effect with HT	Effect without HT
Various	RT	145	CR rate	32%	30%
Various	RT	173	2-year survival	36%	29%
Head and neck	RT	65	CR rate	74%	58%
Various	RT	15	Better response	47%	7%
Breast	RT, surgery	507	5-year survival	73%	67%
Cervix	RT	50	18 months LC	70%	50%
Stomach	RT, Surgery	193	5-year survival	51%	45%
Oesophagus	CT	40	PR rate	41%	19%

Table 8.2: Clinical trials showing non-significant results of cancer treatment using HT combined with standard treatments [131]. (CR: complete response, LC: local control, PR: partial response)

optimization include the dose and the sequence of the three modalities [137]. Theoretically, the three modalities can enhance the efficacy of each other, and trimodality could be a promising future cancer treatment [142].

8.3   Contents

In this part, the rest of the study of the hyperthermia applicator using noninvasive EM power is organized as follows;

- Review of the technology of HT using noninvasive EM power to have overview about the designs and methods in this field have been developed and tested.

- Propose a novel applicator design for this region. Currently, there is only one practical design for the tumors at head and neck region, so having another design with better performance is significant issue.

- Discussion and summary

Chapter 9

Review of Hyperthermia Treatment Technology Based on Noninvasive EM Power

The objective of this chapter is to review the technologies of the external applicators using EM power that are used in hyperthermia treatment. The review is divided into five parts:

- Low frequency methods: as most living tissues are very lossy to EM power, penetration depth is always a difficulty of applicator design. Thus, applicators operated at low frequency (from 4MHz up to 100MHz) were quite popular in 1980s. The heating mechanisms for low frequency applicators can be categorized as capacitive coupling (E-field dominant) and inductive coupling (H-field dominant).

- Multi-element operation: applicators using an antenna array have many advantages over single-element operation. Firstly, a multi-element applicator conforms to the body's shape better than a single element for superficial hyperthermia. In addition, as the input amplitude and phase of each element of a phased array can be adjusted, the appli-

cator can generate better energy concentration and penetration depth due to coherence. Furthermore, the adjustment can also be used to steer the thermal distribution. However, in terms of applicator design, phased array is much more challenging than single-element. The topics discussed in this section include superficial hyperthermia using antenna array, the phased-array designs for heating the tumors in different regions (head-and-neck, breast and pelvic) and algorithms for optimizing the excitation coefficient.

- Other methods: some novel methods have recently been developed for enhancing the thermal performance or reducing the engineering complexity. The novel methods reviewed in this report include heating breast tumors using ultrawide-band microwave, field concentration with metamaterial lenses, and using reflectors as a continuous array to generate focus.

- Summary and discussion: this section includes a summary of the HT techniques mentioned in this report, the technical challenges and expertise required for developing a complete solution for HT, and a summary of the many purposes for which the water bolus is used in external applicator designs.

9.1   Low Frequency Methods

In hyperthermia treatment, low frequency is defined as lower than about 100MHz. Because of the electrical size and properties of tissues, penetration depth in tissues is the greatest advantage of HT at low frequency. The applicator operated at low frequency may also provide better thermal coverage in some cases. The two ISM bands, 13.56MHz and 27.12MHz, are commonly used for the low frequency applicators.

When the operated frequency is lower than 13.56MHz (ISM band), quasi-static approximation is a simple but fairly accurate method of predicting the field distribution [144, 145]. For frequencies higher than 27.12MHz, calculation or simulation with full-wave models becomes necessary as the coherence of EM fields in tissues can already be observed [146]. Thus, the prediction of the electromagnetic field in the treated region is much more difficult at higher frequencies without proper numerical tools.

A few decades ago, low frequency techniques were popular because it is easier to predict the field (quasi-static), and the cost of the applicator design is also lower. More important, the EM power at low frequency provides much better penetration depth than at high frequency [147, 126]. Although electromagnetic focusing is a weak characteristic at low frequency, some tumors still can be heated by the thermal preference due to the difference in the physiological properties between the tumor and healthy tissues. The vasculature in most solid tumors is immature, so the perfusion cooling ability in the tumors is worse than that in normal tissues. Therefore, the thermal pattern could still be "selective" when the applicator works in an unfocused manner [148].

However, if the treated tumor is close to large vessels, the cold spot in the tumor due to the vessels becomes a challenging issue [134]. In addition, relying on the thermal preference implies that the thermal distribution depends heavily on the inhomogeneity of tissues with less or no control. This weakness may induce unavoidable cold spots in the tumor and hot spots in healthy tissues. At high frequency, the coherence can concentrate the EM power on the tumor better, but the penetration depth is shallower. In general, the engineering complexity of applicator design is higher at higher frequency. Therefore, the trade-off between focusing, penetration and engineering complexity is critical in the frequency selection for a HT applicator design [149, 150, 151].

In this review, the techniques of hyperthermia applicators with non-invasive EM fields at low frequency are categorized in three parts. The first two parts are the applicators using capacitive and inductive coupling with single element, respectively. Although the fields in this range of frequencies may be not strictly quasi-static, there is still only an electrical or magnetic field dominant. Thus, the principles and performance characteristics of these two methods are quite different. The section ends with a discussion on focusing EM fields at low frequency because, as mentioned above, the field concentration is a challenge for applicator design at low frequency.

9.1.1 Capacitive Coupling

Capacitive coupling using external EM power was the earliest method of conducting HT as it is straightforward and has good penetration depth. The conduction current induced by an E-field is the source of the thermal energy. The basic design uses two metal plates as a pair of electrodes placed at

opposite sides of the treated region and excited with anti-phase. The E-field between the electrodes induces conduction current in tissues as the heating source. The three-electrode applicator is another typical design (Figure 9.1) [152]. The conduction current in the tissues can be manipulated by adjusting the magnitude and phase of the voltage on each electrode. Water boluses filled with de-ionized water are placed between the electrodes and the tissues for cooling the superficial part of the tissues and for better coupling of the E-field.

However, one of the significant disadvantages of this type of applicator is excessive heating of the subcutaneous fat layer. The dominant E-field component of the applicators is perpendicular to the surface of the patient. If the difference in permittivity between tissues is significant, such as between muscle and fat, the boundary condition induces much higher E-field in the tissues with lower permittivity. A simple example provided in [147] shows that at 27.12MHz the power absorbed by fat can be eight times higher than that by muscle. Thus, the thickness of a patient's fat layer is limited to 0.5cm [134] or 1.5cm [144, 141] for HT with electrode applicators .
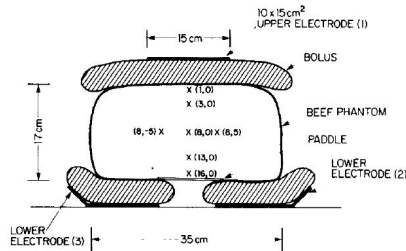

Figure 9.1: A three-electrode capacitive applicator proposed in [152]. The magnitude and phase of the excitation on each electrode can be adjusted to manipulate the fields. The boluses are filled with de-ionized water to reduce the temperature on the surface of the tissues.

Recently, different configurations of the electrodes have been reviewed with numerical simulations using a finite-element method under quasi-static conditions [144]. As seen in Figure 9.2, five electrode applicators for heating pelvic tumors were studied. The first one is the original design, and it shows a dramatically excessive E-field deposited in the fat layer. The second design significantly improves the excessive superficial heating and generates

more uniform thermal distribution in the tumor. The third and forth scenarios are the applicator in Figure 9.1 operated in different modes of excitation. Although the design provides the flexibility to control the fields, the problem of excessive heating of the fat layer still exists. Finally, the fifth design generates the most uniform field in the treated region and the highest flexibility of field manipulation.

Overheating of the fat layer is always the critical problem for electrode applicators, so they are only suitable for patients with a large tumor and a thin fat layer [144, 141]. To overcome this problem, two designs were proposed to provide E-field polarization parallel to the interface [153, 154].

Firstly, as seen in Figure 9.3, a pair of ring electrodes is excited by a RF source at 13.56MHz or 27.12MHz to heat the homogeneous cylindrical phantom [153]. Because the electrodes are placed in the direction parallel to the phantom axis, the E-field polarization is also parallel to the phantom surface. Consequently, the superficial heating problem can be significantly improved. In addition, the SAR pattern in Figure 9.4 shows the applicator is able to provide a uniform thermal pattern in cylindrical phantoms with different thicknesses (7.7, 13.5 and 24cm). A more uniform SAR pattern is observed within thinner phantoms. Note that a water bolus is not added in the experiment.

The second design proposed to provide a parallel E-field is shown in Figure 9.5; a coaxial TEM applicator [154]. Although this design is listed in capacitive coupling in this review, the heating mechanism is radiative coupling. Those applicators which will be shown in the Multi-Element Section conduct HT also with radiative coupling, but the coaxial TEM applicator is a single-element design. The patient is placed inside the inner conductor of a huge coaxial cable. For skin cooling, the inner conductor is filled with water instead of using a conventional water bolus, and this method can reduce the pressure on the patient due to the water and also avoid the small air gaps between the patient and water bolus. There is an aperture between the inner and outer conductor of the applicator (Figure 9.5(b)), and the E-field with parallel polarization "leaks" out from this aperture to heat the patient (Figure 9.5(a)). The SAR pattern can be slightly modified by adjusting the size of the aperture.
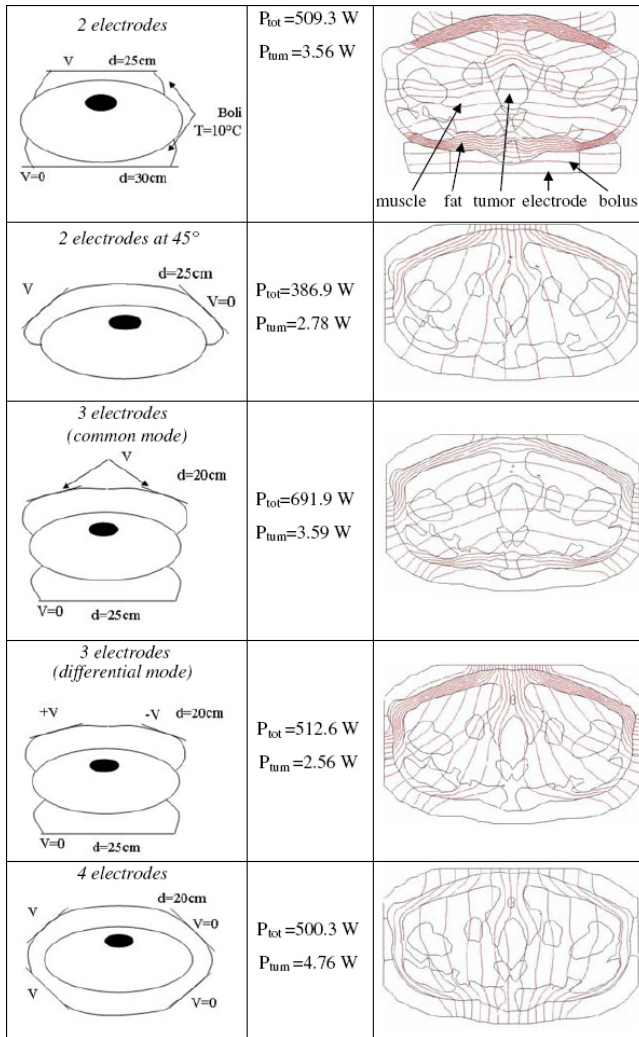
Figure 9.2: Five different configurations and the E-field distributions of capacitive coupling hyperthermia with electrodes [144].
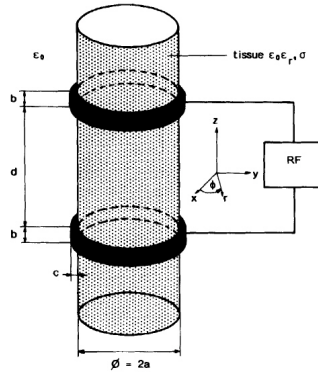
Figure 9.3: The applicator consists of a pair of capacitive ring plates to provide E-field with parallel polarization to the phantom surface [153].
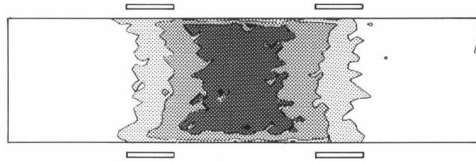

Figure 9.4: The SAR distribution of the applicator in Figure 9.3 with 15cm-separated capacitive ring plates in the 13.5cm thick cylinder phantom with a 0.2cm gap between the ring and the phantom [153].

9.1.2 Inductive Coupling

In capacitive coupling, the E-field is the source of thermal energy. The magnetic field, or H-field, can also be used at low frequency as the source for HT, and this is called inductive coupling. As the magnetic field is dominant in inductive coupling, the eddy current induced in tissues is the heating source in the patient instead of the conduction current. The difference in permittivity between tissues such as fat and muscle is not significant to the static (or quasi-static) H-field, so the problem of excessive heating of the fat layer does not exist in inductive coupling.

There are three basic ways of conducting HT with inductive coupling: concentric, pancake and coaxially paired coils, as shown in Figure 9.6 [155].
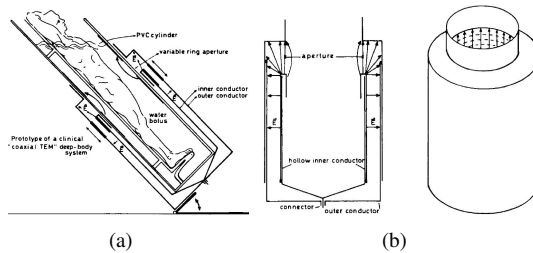
(a)   (b)

Figure 9.5: The coaxial TEM applicator proposed in [154]. (a) The patient is placed inside the inner conductor filled with water and (b) heated by the power emitted from the aperture between the inner and outer conductor.

These methods are usually operated at lower than 30MHz. Compared to the pancake approach, coaxially paired coils provide better penetration depth (Figure 9.7(a)) [155]. In addition, for the same configuration, the applicator with the largest coil size has less superficial heating and therefore better penetration depth (Figure 9.7(b)). For the method with the concentric coil, a lower operation frequency ($<$ 13.56MHz) generates a more uniform H-field in a 15cm radius cylinder phantom [156] (Figure 9.8). However, the induced E-field, or eddy current, is the actual thermal source, and it has the same distribution as the vector potential [157]. Due to the skin-effect, the current induced is still higher in the superficial region even with a uniform H-field [158]. Therefore, capacitive coupling may overheat the fat layer due to the difference in permittivity, but inductive coupling could also cause excessive heat in the superficial region because of the skin-effect. For that reason, surface cooling using a water bolus is also necessary for the inductive applicators.

In addition to these basic methods, several important designs with inductive coupling are introduced in the following. The first one is named *Magnetrode*, as shown in Figure 9.9 [145]. It is a realistic design of the concentric-coil concept. Practically, the coil system needs to be operated in resonance for impedance matching and higher efficiency. Thus, a capacitor is required to compensate the inductance from the coil, but normal lumped capacitors are not able to handle the system power up to 500W-1000W. The magnetrode has a single-turn current sheet as the concentric coil. The current sheet overlaps at the feeding position without contact to provide the
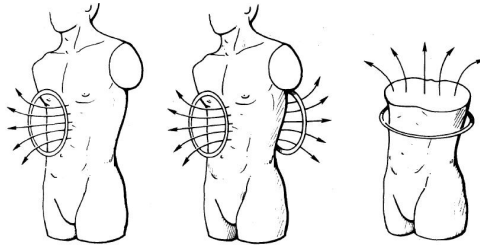
Figure 9.6: Three basic methods of inductive coupling with loop(s): pancake (left), coaxially paired coils (middle) and concentric (right) [155].
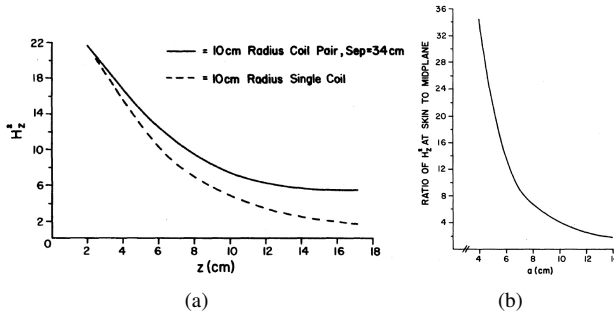
Figure 9.7: (a) The pancake coil (dashed line) versus the coaxially paired coils (solid line) in terms of H-field square along with depth. (b) Comparison of different paired coils sizes in terms of the ratio of H-field square between skin and the center of the body [155].

capacitance for resonance. In addition, a transformer is added for matching the input resistance, and the two adjustable capacitors are tuned for different loads (patients). Clinical results shows that the magnetrode is able to heat a tumor in the liver effectively [148].

Some studies and applicator designs have used helical coils [159, 160]. The coils are operated at half or full-wavelength resonance. However, several limitations with this type of designs are mentioned in [161], for example, sharp resonance and load-dependency. Besides, the EM power pattern depends greatly on the load and is not easily controlled. Finally, these ap-

Figure 9.8: The magnetic fields of a concentric coil in a 15cm radius cylinder phantom at different frequencies [156]. The electrically smaller loops generate a more uniform magnetic field.
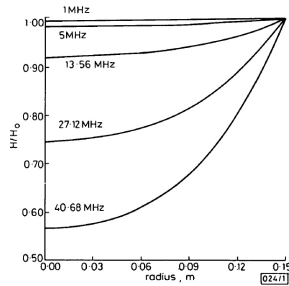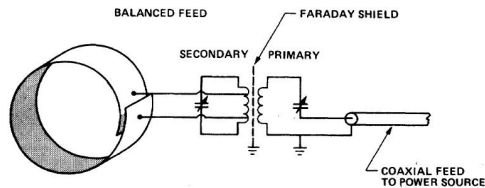

Figure 9.9: The magnetrode proposed in [145]. It consists of a rolled conducting sheet as the concentric loop and matching circuit. The overlapped part of the sheet provides capacitance to make the applicator work in resonance.

plicators are usually longer than 30cm, and so are only available for extremities. In [162], the pitch angle of the helical coil applicator is optimized. The study suggests that the direction of the current should be parallel to the phantom axis, which implies that a helix may not be an ideal structure for inductive HT.

Consequently, applicator designs with a parallel current direction were proposed [163, 146]. The first design was reported in [163], and the enhanced design is called the twin-dipole applicator (Figure 9.10) [146]. The two conducting strips are placed parallel to the phantom axis and excited as two in-phase current sources at 27MHz, which inherently produce coherence inside the phantom to improve the penetration. The parallel plates at both sides of the current sources are the capacitors for tuning the applica-

tor operated in resonance. The current sources are also excited by the two smaller feed loops to increase the input resistance. Figure 9.11 shows the SAR distribution normalized along with the depth of the cylindrical phantom with simulating materials of fat and muscle. The coherence produced by the two in-phase current strips causes two SAR-peaks in the phantom. However, as the SAR peaks occur inside the phantom instead of in the superficial part or fat layer, the problem of excessive surface heating is significantly improved with this design using coherence.
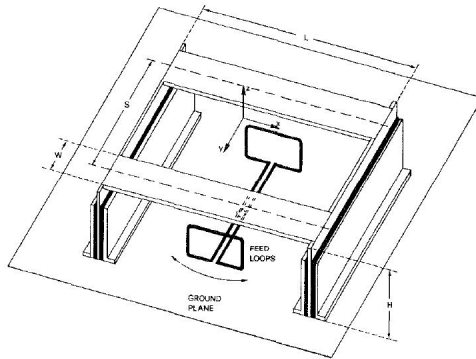
Figure 9.10: The twin-dipole applicator proposed in [146]. The two current strips are the current sources to heat the phantom whose axis is in the X-direction.

Another applicator design, called the inductive aperture-type applicator, or IATA, was proposed with the same current direction [164]. The heating source is a one-turn, square metal strip as a current sheet (Figure 9.12). The current sheet induces a strong eddy current in the tissues and clinical tests show that the applicator is able to heat a large tumor at significant depth [164]. This work is listed as a radiative applicator in [164] but the heating mechanism is inductive coupling. Other clinical results using this applicator suggest that the IATA is suitable for large or superficial lesions [165].

Another design using a current sheet as the heating source was proposed in [166]. The concept is similar to the IATA, but it is much lighter and smaller (Figure 9.13). The applicator can be applied to a large range of frequencies as it has tuning geometry, i.e. adjustable capacitance to compensate for the inductive reactance from the current sheet. This applicator
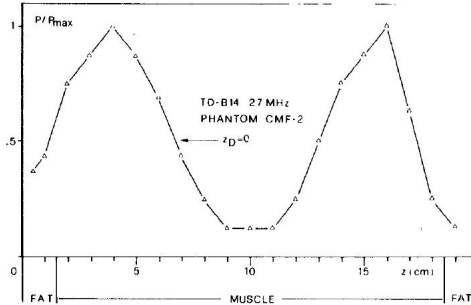
Figure 9.11: The SAR distribution normalized in the cylindrical phantom with the twin-dipole applicator [146]. The coherence makes the peak-SAR occur inside the phantom instead of at the surface.
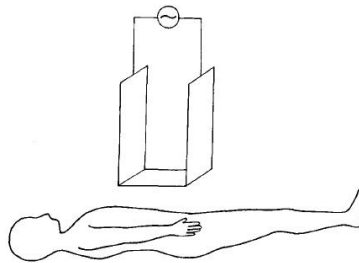
Figure 9.12: The Inductive Aperture-Type Applicator, or IATA, proposed in [164]. The metal sheet is excited with RF source as the thermal source.

can also be used as elements in an array for conducting superficial hyperthermia.

9.1.3   Focusing Techniques

Field concentration and manipulation are very important issues of hyperthermia performance, but these, however, are also the major disadvantages of the low frequency approach [167]. Because of the long wavelength, the EM fields are difficult to concentrate in tissues and the field distribution strongly depends on the inhomogeneity of the tissues. Nevertheless, there
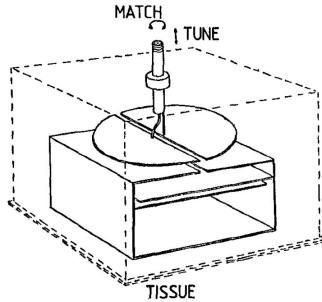
Figure 9.13: An applicator design using a current sheet as the thermal source that is light and small [166]. The overlapping part of the current sheet and the feeding disk provide tunable capacitance to the applicator resonant with different loading.

are still some methods manipulating EM power in tissues at low frequency. Most of them are comprehensively summarized in [168]. Focusing techniques can be a new design or the combination of single-applicator designs. For example, Figure 9.14 shows the application of two IATAs (Figure 9.12) to create a peak of eddy current in the phantom [168].
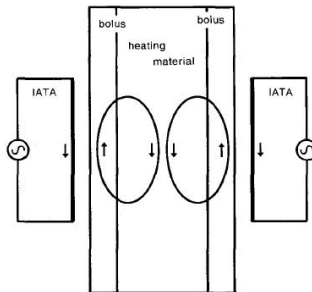
Figure 9.14: Combination of two IATAs (Figure 9.12) to achieve peak E-field at the center of the phantom [168].

Because of simplicity, portability and cost, two applicator designs for breast tumors using adjustable magnetic flux were suggested [169, 170]. To

control the magnetic flux in the tissue, the two designs use ferrite cores with shielding plates operated at 4MHz. Figure 9.15 depicts the configuration and the magnetic flux generated. By adjusting the positions of the ferrite cores and the shielding plates, the magnetic flux can be controlled to heat breast lesions.
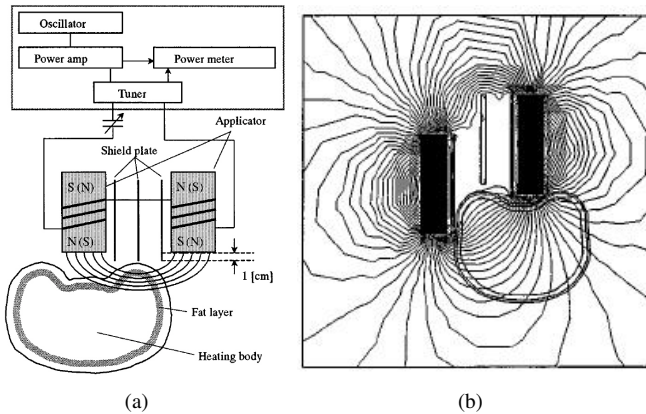
Figure 9.15: (a) The configuration and (b) the simulation result of the inductive hyperthermia system using a pair of ferrite cores. The magnetic flux is adjustable by changing the positions of the ferrite cores and the shielding plates [170].

Another example of field concentration by combining different applicators is shown in Figure 9.16 [171]. The design combines the ring capacitor plates applicator (Figure 9.3, [153]) and the twin-dipole applicator (Figure 9.10, [146]). As the illustration in Figure 9.16 shows, the induced currents from the two applicators have a constructive and destructive combination at different locations in the phantom. Thus, the E-field (or SAR) in the phantom is not only concentrated inside the phantom, but also has a single-bell distribution instead of double-bell.
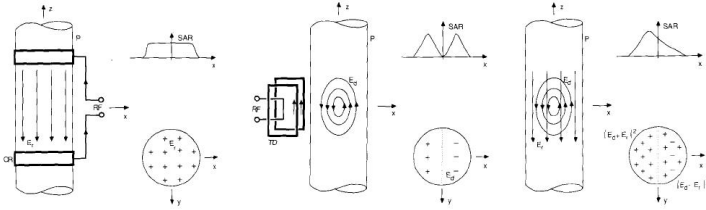
Figure 9.16: Illustration of the focusing method by combining the ring applicator (Figure 9.3) and the twin-dipole applicator (Figure 9.10) [171]. The constructive and destructive combinations of the E-fields from the two applicators generate a SAR distribution with a single peak in the phantom.

9.2 Multi-Element Operation

In the section above, hyperthermia techniques with external EM power at low frequency (up to 100MHz) were reviewed. Although an EM field has better penetration depth in tissues at lower frequency, lack of coherence results in the field distribution being mainly determined by the material properties and geometry of the tissues. That results in unexpected hot spots in healthy tissues and/or insufficient SAR in part of the treated tumor. Therefore, interest has recently been growing in multi-element designs [16]. The frequency used in array application ranges from 70MHz (for the pelvic region) to 2.45GHz (for the superficial region). The advantages of using an antenna array include better coverage for superficial hyperthermia, higher power focused in deep regions and the ability to steer the EM field distribution by different settings of the excitation coefficients.

However, applicator design using an antenna array is a great engineering challenge. It includes antenna and array design, patient positioning, optimization of excitation coefficients and clinical considerations. The review of phased array starts with the applicators treating superficial tumors. Without the problem of penetration depth, hyperthermia for the superficial region is easier and has better results than deep-region HT. Applicator designs using phased array for treating deep-seated tumors in different regions are then discussed, and the regions heated include the pelvic region, head and neck, breast and extremities. In phased array, the EM fields in tissues are not only determined by hardware design, such as antenna arrangement,

but also by the magnitude and phase of each element input, or the excitation coefficient. Hence, techniques to find the optimal arrangement of excitation coefficients are also reviewed.

9.2.1   Array Designs for Superficial Hyperthermia

The thermal pattern for superficial hyperthermia (SH) needs to be broad, shallow (<3-4cm) and adjustable [16]. Small and light radiating elements are also required for practical reasons [172]. Array applicators have advantages over single-element applicators [173]. An antenna array can have broad and uniform coverage with reasonable weight. In the case of a single element, each applicator would need to be uniquely manufactured to conform to a patient's body, whereas a multi-element array could repeatedly be re-configured to conform to any patient's body shape. Moreover, steering power deposition is also possible by an array to avoid undesired hot spots [174]. Three kinds of SH applicators are introduced in this section: waveguides, microstrip antennas and current sheets. To evaluate the performance of SH, the Effective Field Size (EFS) is defined as the area enclosed by the 50% ISO-SAR contour at a depth of 1 cm to quantify the heating area.

Waveguide Designs

An applicator using waveguide is one of the earliest examples of using thermal energy for therapeutic purposes [175]. The dominant E-field component of a rectangular waveguide is tangential to the surface, so the fat layer is not overheated. Waveguide is also able to carry very high power because of its strong mechanical structure [16]. As the E-field in the dominant mode, such as TE_{10} in a rectangular waveguide, is not uniform on the aperture, the SAR distribution below the aperture is not uniform either. Several designs improved this by loading dielectric in the waveguide or horn antenna [16]. In addition, many waveguide applicators are filled with water to decrease the size and reflection on the interface [176, 177]. To enhance the EFS, an active slot antenna array was proposed by adjusting the amplitude and phase of each element [178]. In addition, a modified horn antenna applicator called the Lucite Cone Applicator (LCA) at 433MHz was proposed [179, 180]. Compared to conventional horn antenna applicators, the two walls parallel to the E-field of the LCA are made of Lucite instead of metal, and a PVS

cone is inserted in the applicator (Figure 9.17). This design has a larger EFS than conventional horn antennas.
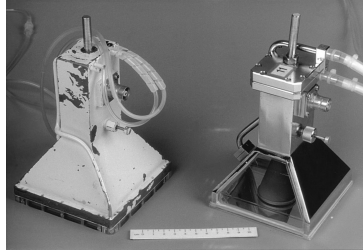
Figure 9.17: The conventional horn antenna applicator (left) and the proposed Lucite Cone Applicator (right) to enhance the EFS [179].

In [181], the authors proposed a modified water-loaded box-horn applicator. A box-horn applicator (Figure 9.18(a)) can provide a more uniform E-field at the aperture because both TE_{10} and TE_{30} are propagating modes. Moreover, the box-horn can be further modified to offer a bigger aperture for SH without decreasing the field uniformity. A comprehensive analysis of the modified box-horn shows significantly better performance in array application than conventional horn antennas [182] and negligible mutual coupling between the box-horns [183].

Water bolus is also used in SH applicator design. The study of the water bolus effect with water-loaded waveguide for SH shows that a thicker water bolus is not significant to penetration depth but can change the shape of the effective field from elliptical to circular [184].

Microstrip Antenna Designs

SH applicators using microstrip antennas have some advantages over waveguide applicators, such as smaller size, reduced weight and lower cost. Applicator designs with microstrip antennas operating at 433MHz or 915MHz for SH were therefore developed [172]. However, some disadvantages exist in conventional rectangular or circular microstrip antennas for SH application. Firstly, the near-field is not symmetric for microstrip antennas and that causes non-uniform field distribution [185]. Secondly, because the resonance of the microstrip antennas occurs in the substrate, a significant

Figure 9.18: (a) The box-horn applicator has a more uniform E-field at the aperture than conventional horn antennas because both TE_{10} and TE_{30} propagate. (b) The modified box-horn applicator provides a larger aperture for superficial hyperthermia [181].

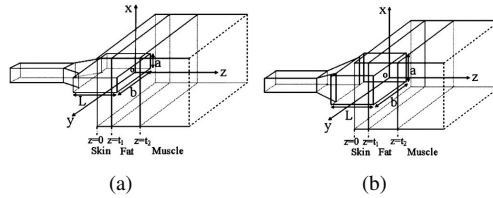difference in permittivity between the substrate and the water bolus results in mismatch and poor efficiency [174]. Adding a superstrate layer above the antenna can improve the mismatch problem [172]. Finally, a certain distance is required between the antenna and the tissues (>3cm) because the near-field has a strong E-field component normal to the patient's skin [172]. This problem can be solved by applying a thicker water bolus.

With respect to the different shapes of microstrip antennas, the annular-slot microstrip antenna has the smaller size, better transmission efficiency to the water bolus and a circularly symmetric SAR distribution compared to the rectangular microstrip antenna [174]. If more than one frequency is considered in the same applicator, a microstrip spiral antenna provides broad bandwidth as the radiation mechanism is based on traveling wave [174]. It has been applied to an array design [186]. As the near-field of a spiral antenna is not evenly distributed, a rotating spiral antenna was investigated [187]. The rotation extends and smoothes the heating pattern, and the system is operated at 400MHz instead of 915MHz for deeper penetration (3cm). The array using spiral antennas for SH is also commercialized [188] and has a third-party performance evaluation [189]. Figure 9.19 shows the array, named SA-812, used in this evaluation. Antenna 1 is larger than the others for filling the null-field area between Antenna 1 and the surrounding elements. The evaluation shows that the applicator is able to cover a region up to 12cm in diameter and 2cm in depth. In addition, different shapes of heating pattern are also possible with this applicator.

Another SH applicator design, called the Contact Flexible Microstrip
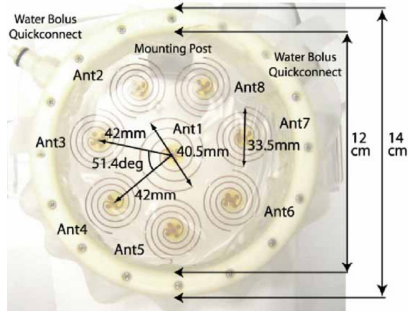
Figure 9.19: The commercialized applicator for SH (named SA-812 [188]) using a spiral antenna array. Its performance is evaluated in [189].

Applicator (CFMA), is shown in [190] and the operation principle is analyzed in [191]. The geometry of the CFMA is shown in Figure 9.20 and the tissue treated is placed below the silicon bolus. There are capacitive and inductive CFMA for 70MHz and 434MHz, named CFMA-70 and CFMA-434, respectively [192]. The two ends of the electrodes, left side of e_1 and right side of e_2, are short and open circuit for inductive and capacitive CFMA, respectively. The excitation is placed between the shield electrode and the active irradiating electrodes. For inductive CFMA, only e_1 or e_2 is excited. For capacitive CFMA, both e_1 and e_2 are excited, and an external inductor connects the two excitations to compensate for the capacitance brought by the two electrodes. The performance of the CFMA-70 was recently evaluated and compared to CFMA-434 and 70MHz waveguides [192]. Compared to CFMA-434, the CFMA-70 produces a larger EFS and deeper penetration, and is insensitive to bolus thickness. The CFMA-70 has a larger EFS than the 70MHz waveguide, but a larger normal E-field component. This induces hotspots at tissue interfaces.

Recently, interest has been growing in multi-functional applicator designs for SH. A relatively early design uses two antennas to conduct SH and non-invasive thermometry respectively [193]. As shown in Figure 9.21, a spiral antenna was chosen as the thermal sensor receiving the blackbody radiation from tissues because of its high directivity. The square annular slot dual-concentric-conductor (DCC) aperture is responsible for SH because DCC has larger EFS and a more uniform field.
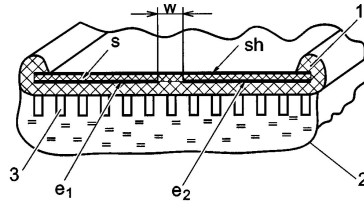
Figure 9.20: The contact flexible microstrip applicator (CFMA) designed for superficial hyperthermia [191]. e_1 and e_2: active irradiating electrodes; sh: shield electrode; s: substrate; w: inter-electrode gap; 1: silicon frame; 2: thin silicon bolus; 3: silicon lugs.
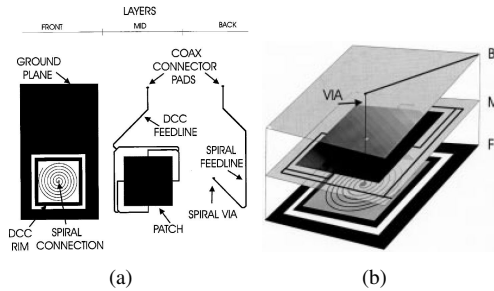
Figure 9.21: The dual-mode applicator design for SH and non-invasive thermometry [193]. (a) The spiral antenna and the square dual-concentric-conductor (DCC) annular-slot antenna are designed for radiometric sensing of blackbody radiation and conducting SH, respectively. (b) The water bolus and tissues treated are placed below the front layer (F).

A multilayer conformal applicator was developed for SH treatment of recurrent breast cancer in the chest wall [194, 195]. The DCC antenna shown in Figure 9.21 was also used in this applicator design [195]. The applicator, as shown in Figure 9.22, is able to administer a thermal and a radiation dose simultaneously. The layer of thermal catheters is for thermometry. The microwave (MW) PCB array with the MW connectors is an array of microstrip antennas as the radiators for SH treatment and spaced by a water bolus for skin-cooling. Above the antenna array, the brachytherapy source catheters offer radiotherapy at the same time to maximize the efficacy of hyperthermia

treatment as an adjuvant modality. The air gaps between a patient's skin and the water bolus is always an issue that significantly affects the heating performance as the water bolus does not conform the body's shape well. In this design, the shape of the applicator is designed as a vest (Figure 9.23). During treatment, the air bladder is inflated to significantly improve the contact, or reduce the air gaps, between the applicator and tissues.
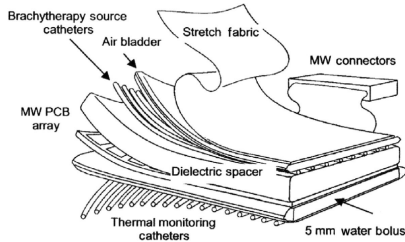
Figure 9.22: The multilayer conformal applicator proposed in [194] includes thermal catheters, a water bolus, a microstrip antenna array, brachytherapy source catheters and an air bladder.

Figure 9.23: The multilayer conformal applicator in Figure 9.22 is like a vest for the treated patient. The inflated air bladder can significantly reduce the air gaps between the water bolus and a patient's skin [195].

Current Sheet Designs

In the review of low frequency techniques, an inductive applicator with a current sheet was introduced with the advantage of smaller size and reduced

weight (Figure 9.13 [166]). The current sheet applicator was also applied in an array design for SH [196, 173]. This study suggests that coherent operation is not necessary and incoherent operation may have better thermal performance for SH. For instance, if the fat layer is thicker than 2mm, incoherent operation produces a broader EFS, as shown in Figure 9.24.

(a)   (b)
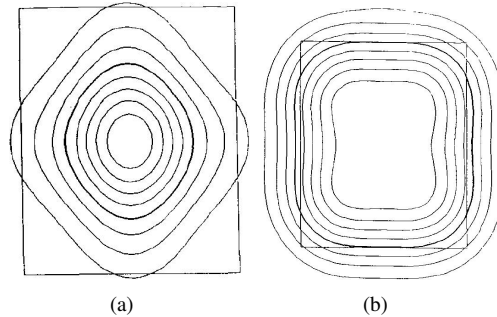
Figure 9.24: The field distribution of (a) the coherent and (b) incoherent operation of the array consisting of current sheet applicators. The rectangular box shows the size of the array and the contours are $|E|^2$ with 10% interval [173].

9.2.2 Phased Array Designs for Deep-Seated Tumors

For deep-seated tumors, the most important issues for HT are penetration depth, field manipulation and effective heating volume. Considering these three issues, phased array is a reasonable choice because of the following advantages. Firstly, the coherence of the EM field in tissues produced by multiple radiators means that the field strength does not decay exponentially along with depth. Secondly, as there are multiple radiators, the area illuminated on the superficial region is much larger than that with a single element. Thus, much higher total power can be delivered without excessive heat on the skin, which indicates higher thermal exposure of the target and deeper penetration in tissues. Finally, combinations of excitation coefficients of the phased array provide much more flexibility for field manipulation in tissues. The manipulation can be applied to avoid discomfort caused by hot spots in healthy tissues and to concentrate more power on the cold region of the

target.

In early designs, such as [197, 16, 198, 199], only the first and the second advantages applied because the optimization of excitation coefficients is a challenging issue. The considerations for a phased array design for deep-seated tumors include:

- Array design: antenna design, the number and arrangement of the antennas and frequency selection.

- Radiation environment: patient position, water bolus, patient geometry [200] and tumor size/location.

- RF circuit: impedance match, power delivery and feedback measurement.

- Practical issues: fabrication, water bolus (shape and circulation), cost and the influence of the additional objects such as fixture and thermometry.

Because of geometrical differences and the inhomogeneity of the human body, specific design of applicators is necessary for tumors in different regions. In this section, a review of applicator design is divided by treated regions, i.e. the pelvic region, head and neck, extremities and breast. In addition, some studies about choosing the number and arrangement of antennas for a phased array applicator are also reviewed.

Pelvic Region

Tumors in the pelvic region, such as cervical and rectal cancer, are typical targets for deep-heating applicators. The most common designs for this region are the Sigma-family applicators, i.e. *Sigma-60*, *Sigma-Eye* and *Sigma-60-Ellipse* from BSD Medical Corporation [188, 201]. Figure 9.25 shows the Sigma-60 and the Sigma-Eye applicator. '60' and 'Eye' indicate the diameter and the shape of the applicators, respectively. Figure 9.26 shows a patient undergoing hyperthermia treatment with a Sigma-60. In addition to these three applicators, there is another Sigma-family applicator with a similar design but different size (30cm diameter), named mini-annular phased array (MAPA) in [202] (and also a 40cm-diameter design). MAPA only has four pairs of dipole antennas and is designed for treating extremities [202].
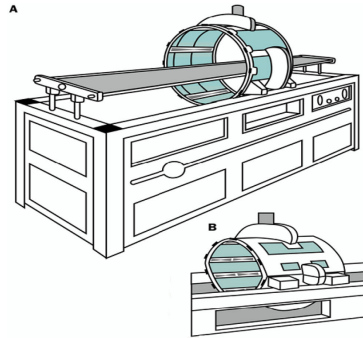
Figure 9.25: Hyperthermia applicators for deep-seated tumors in the pelvic region from BSD Corporation; (a) Sigma-60 and (b) Sigma-Eye [201]
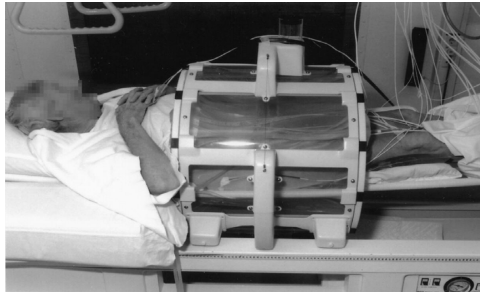
Figure 9.26: A patient undergoing hyperthermia treatment with the Sigma-60 applicator [201].

It was also used in an investigation of conducting HT with non-invasive thermometry using magnetic resonance imaging (MRI) [203].

The Sigma-60-Ellipse has a similar antenna design and arrangement as the Sigma-60, but is able to treat larger patients (Figure 9.27). The heating performance of the Sigma-60-Ellipse has been compared to the Sigma-60 (75-90MHz) and the Sigma-Eye (100MHz) and shows that the three applicators have similar thermal performance [201]. Table 9.1 shows the comparison between the three Sigma-family applicators. Electrically short dipole antennas are used as the radiators in these applicators. As two radiators

are connected to one amplifier output in this design, the number of driving ports is half that of the radiators. Figure 9.28 shows the feeding structure as an example. In the Sigma-60 and the Sigma-60-Ellipse, each ring in the transversal plane has four pairs of radiators. The Sigma-Eye has two more rings in the Z-axis (patient axis) and more radiating elements. The idea of having more rings is to provide the ability to steer the SAR not only in the X-Y plane but also in the Z-axis. However, since the Sigma-Eye has many more radiating elements, the engineering complexity is also significantly higher. The comparison between the Sigma-60 and the Sigma-Eye reported in [204] suggests that both applicators are feasible in clinical application. In addition, the Sigma-60 and the Sigma-Eye are more suitable for the pelvic region and upper abdomen (including the liver), respectively.

Figure 9.27: An improved design of the Sigma-60, the Sigma-60-Ellipse [201]. It has similar performance but a bigger treatment area for larger patients.

The feeding structure of two antennas connected to one input raises the complexity of impedance matching, numerical modeling, estimation of uncertainty budget and unbalanced current (or *sheath current* as referred to in [205]) [206, 205]. As seen in Figure 9.28, a short-circuit stab is added to compensate for the capacitance from the pair of short dipole antennas. Both numerical and measurement validation approaches were proposed in [206] to control the input signal precisely. FDTD in one dimension is applied as the numerical tool, and three measurement approaches are combined to estimate the behavior of the feeding network. Moreover, in this feeding

	Sigma-60	Sigma-Eye	Sigma-60-Ellipse
Frequency (MHz)	60-120	100	80-100
Antenna length (cm)	45	14	45
Array diameter (cm)	58	38×53	37×53
Length (cm)	~ 36	~ 50	~ 50
Drive ports	4	12	4
Radiators	8	24	8

Table 9.1: Comparison between the Sigma-60, the Sigma-Eye and the Sigma-60-Ellipse in terms of physical configuration [201]. The length is the bolus-patient contact length.

structure, it is necessary to add ferrite rings to the feeding coaxial cable to suppress unbalanced current; but ferrite rings are not MR-compatible. Three feeding structures were therefore suggested in [205] to obtain sufficient impedance matching without unbalanced current or ferrite rings. A long-term (15 years) clinical study reports that the Sigma-60 is reproducible in generating $40 - 40.5\,^{\circ}$C in cervical tumors on 444 patients [200].
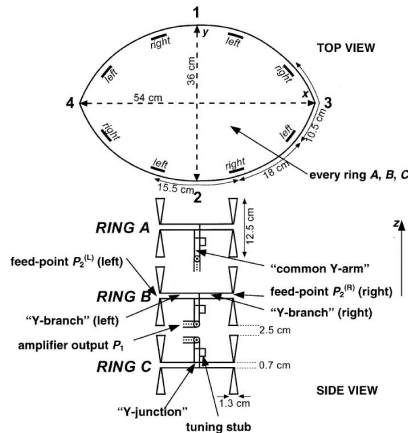
Figure 9.28: The arrangement and feeding structure of radiating elements in the Sigma-Eye applicator [206].

Beside the Sigma family of applicators, another applicator design compatible with MRT was developed in [207]. The applicator consists of 12 WAter-COated Antenna (WACOA) modules fed independently (Figure 9.29). Each module consists of a modified dipole antenna, water, feeding and tuning structure. The tuning structure can be adjusted for different patients to ensure impedance matching in each case. Thus, no external feeding circuit is needed in this applicator (Figure 9.30). The WACOA applicator is operated at 100MHz and there are two rings that each consist of six independent dipole antennas (Figure 9.31). The dipole antennas are operated in full-wavelength resonance or anti-resonance (or *voltage resonance* as referred to in [208, 207]). Because wave impedance in water is much lower than in air, the resonant or anti-resonant resistance of a dipole antenna is also much lower. Thus, the resonant resistance is too low to match 50 Ohms, but the anti-resonance provides good matching to 50 Ohms and also a broader bandwidth. In addition, a full-wavelength dipole has a sharper beam in the longitudinal direction than a half-wavelength dipole.
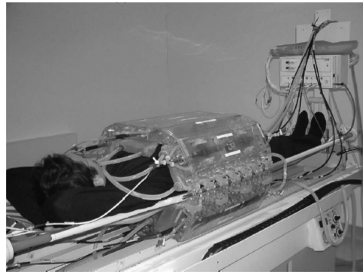
Figure 9.29: The configuration of a patient being treated with the WACOA applicator [207].

Compared to the Sigma family, WACOA does not need an external circuit for impedance matching and unbalanced current suppression, and each antenna is fed independently. The modeling complexity is therefore much lower. That leads to faster and more accurate numerical simulations and lower uncertainty in practical usage [208]. Unfortunately, there is no report of clinical trials with this applicator.

In addition to dipole antennas, waveguide radiators are also used to conduct HT in the pelvic and esophageal regions. The original design in clinical
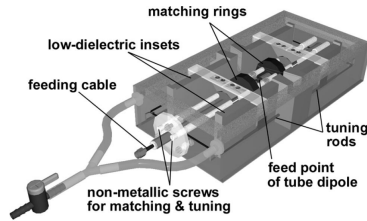
Figure 9.30: The geometry of a single WOCOA module [208]. The tuning structure means that the WACOA module does not need an external matching circuit.
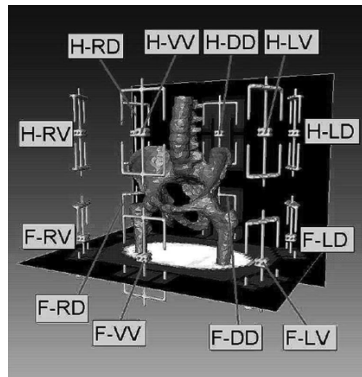
Figure 9.31: The antenna arrangement of the WACOA applicator for HT in the pelvic region [207]. 12 full-wavelength dipole antennas are placed on the two rings.

use at the Academic Medical Center (AMC) in Amsterdam is called AMC-4. This has four 70MHz waveguide radiators surrounding the treated region. Furthermore, a novel applicator named AMC-8 has been evaluated with homogeneous phantoms [209]. This applicator has one more antenna ring than the AMC-4, i.e. eight waveguide radiators (Figure 9.32). Compared to the AMC-4, the AMC-8 has more accurate targeting and is able to reach higher tumor temperatures.

In addition to the above designs, other theoretical studies have been con-
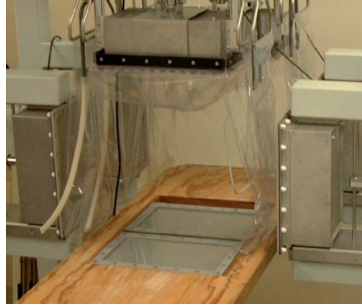
Figure 9.32: The HT applicator using eight 70MHz waveguides at the Academic Medical Center (AMC) in Amsterdam, called AMC-8 [209]. The AMC-8 consists of two four-element rings.

ducted using planar or curved waveguide arrays for deep-region hyperthermia [210, 211]. These studies, however, have not yet produced validation results with measurements or more realistic scenario simulations.

Head and Neck

In an early design, coherence in a homogeneous neck phantom was demonstrated experimentally with an applicator consisting of four water-filled horn antennas [198]. However, no applicator was proposed for clinical trials of deep-seated tumors in the head and neck region until the HYPERcollar applicator [212, 213].

The whole HYPERcollar applicator system includes the antenna array (HYPERcollar), water bolus system and positioning system (Figure 9.33) [213]. The water bolus system circulates the water to maintain the water temperature. The positioning system locates and fixes the patient's position.

The HYPERcollar is operated at 433.92MHz (ISM band), and the power delivered by each antenna is up to 150W. The antenna array consists of two rings of radius 40cm with six radiating elements on each ring. The elements between the rings are staggered, and a cylindrical conducting plate is used as the ground plane. Figure 9.34(a) shows a homogeneous phantom tested with the HYPERcollar. A water bolus filled with de-ionized water is placed between the radiating elements and the patient. The staggered arrangement reduces the mutual coupling between the elements and uniforms the incident
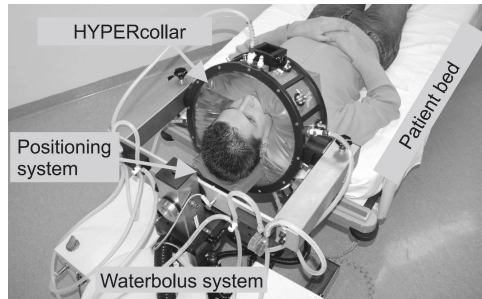
Figure 9.33: The HYPERcollar system for tumors in the head and neck region. It consists of the HYPERcollar antenna array, positioning system and water bolus system. A healthy volunteer was placed in the HYPERcollar applicator for a feasibility test [213].

wave around the patient. The arrangement thus provides more flexibility for steering the fields. The rationale of the HYPERcollar configuration is reported in [214, 215, 216, 212]. The radiating elements are patch antennas with coaxial input (Figure 9.34(b)). The patch antenna is inexpensive, light, easy to construct, smaller and has no need of a matching circuit. The element design was simulated by FDTD [17] and validated by measurements to show the feasibility for different conditions, such as water temperature and patient load [217]. The phase I clinical trials show promising results for this design [212].

Breast Region

The two designs already reported above for deep-region hyperthermia, i.e. the Sigma family and the HYPERcollar, have been modified for HT for tumors in deep regions of the breast [218, 219]. The applicator shown in Figure 9.35 is the modification of the Sigma-60. Four pairs of dipole antennas operate at 140MHz. Good validation agreement is obtained when the applicator is filled with de-ionized water without a human phantom. One study [219] has compared the efficacy between EM and ultrasonic power in breast hyperthermia using numerical simulation [17]. The two EM applicators tested in the study are the original and the modified HYPERcollar. As seen in Figure 9.36, both breasts have to be placed in the original HYPER-

(a)   (b)
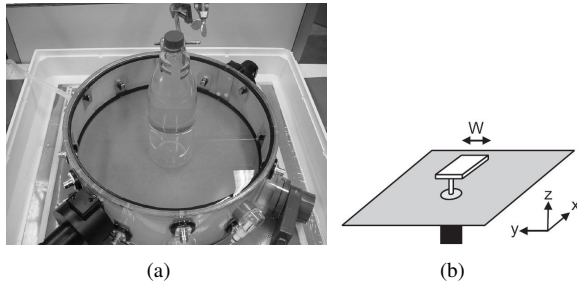
Figure 9.34: (a)The two antenna rings with six elements on each ring in stagger. (b) Patch antennas are chosen as the radiating element because they are light, small, self-matching and low cost [217].
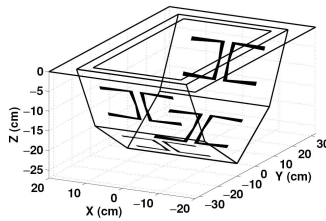
Figure 9.35: The applicator for the breast modified from the Sigma-family applicators [218].

collar whilst the modified applicator is able to treat each breast individually. Compared to the original HYPERcollar, the modified applicator has better efficiency, but does not improve focusing.

A spherical slot array has also been suggested as a hyperthermia applicator for the breast [220]. The applicator design is a concentric hemisphere with slots as radiators (Figure 9.37); a and b are the inner and outer radius of the cavity, respectively. The radiators are four slots on the inner side of the cavity, and the radiated power is inherently focused on the center of the hemisphere. As it is light and easy to handle, the applicator is suitable for heating spherical tissues such as breasts [220].

(a)   (b)
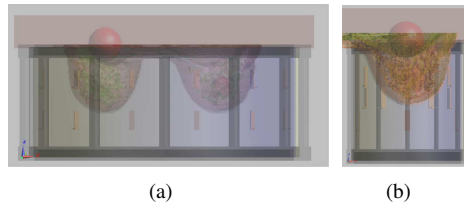
Figure 9.36: Configurations of (a) the original HYPERcollar and (b) the modified HYPERcollar with the tested breast tissue [219].

(a)   (b)   (c)
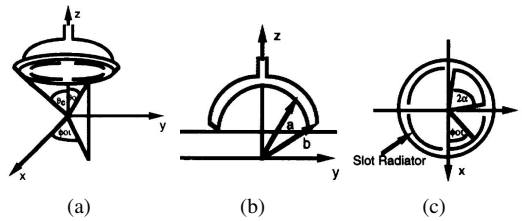
Figure 9.37: A spherical slot array proposed in [220]. The inner side of the concentric hemisphere has four slots. The treated region, such as a breast, is covered by the applicator and heated by the power radiated from these slots.

Antenna Arrangement and Patient Positioning

The number and arrangement of antennas are important in phased array applicators. For cylindrical phased arrays such as the Sigma family, more antenna rings and more antennas per ring generally provide better focusing in more tissue regions and give more tolerance in positioning [149, 150, 151]. However, the number of antennas in an applicator is limited by some practical problems such as applicator size, mutual coupling between antennas, the number of power amplifiers, the complexity of steering the field and the simulation time for treatment planning. Optimization of antenna number and arrangement is therefore a critical issue in phased array design for deep hyperthermia [150, 214, 212].

The study in [221] numerically demonstrates that if all antennas can be positioned perpendicular to the focal point, which may not be at the center of the applicator, the focusing performance can be improved. This phe-

nomenon underlines the importance of patient positioning. Recently, two studies have reported the influence of patient positioning in SAR performance with the Sigma-Eye and the Sigma-60 [222, 223]. The three positioning directions investigated were lateral (left-right hand), anterior-posterior (back-front side) and patient axis (head-feet). The studies show that patient positioning in the lateral direction is less sensitive and can also be accurate in practical applications. The anterior-posterior direction is more sensitive and more difficult to position precisely. In addition, the optimal position in the patient axis may not be at the center of the applicator. A positioning error of less than 1cm in all three directions is recommended when the Sigma-60 is used [223]. These studies highlight not only the importance of precise patient-positioning but also the requirement of real-time thermal measurement to calibrate the positioning error with the Sigma-family applicators. Moreover, although the EM or thermal distribution can be manipulated by adjusting the excitation coefficients, the performance of an applicator also strongly depends on the physical geometry, which includes not only the phased array but also the patient position. Therefore, it is also possible to optimize the patient position to enhance the performance. The parameters of this optimization include the array geometry, patient position and tumor location [224].

9.2.3 Optimization of Excitation Coefficients

For superficial hyperthermia, concentration of EM power with a multi-element applicator is not a significant issue because a broad but shallow thermal distribution is required. However, for HT for deep-seated tumors the concentration of EM power on the desired region is critical. The field distribution not only depends on physical geometry but also on the excitation coefficients. For this reason, optimizing the excitation coefficients (magnitude and phase of each input) is an important topic in phased array heating of deep-seated tumors. Optimization is a great challenge due to the following reasons. Firstly, the geometry of human tissues is extremely complicated, and so the behavior of EM fields is also complicated and not easy to manipulate. In addition, the clinical preparation time before HT needs to be short on both comfort and cost grounds. The setting of excitation coefficients may be changed during the treatment based on a patient's feedback or measured results, and thus the process of the optimization needs to be fast enough in clinical application. Finally, the distributions of SAR and temperature are

sometimes significantly different. Thermal distribution in the human body can not yet be simulated accurately due to complicated vasculature and the nonlinear thermal behavior in tissues [225, 226]. Thermal measurement is still necessary in clinical application because of the inaccuracy of thermal simulation.

To steer the fields precisely requires:

- Fast and accurate EM/thermal simulation

- An efficient algorithm to optimize the excitation coefficients

- Comprehensive and accurate thermal measurement during the treatment.

In spite of these difficulties, field manipulation is critical in hyperthermia performance as it means the patient is able to withstand the treatment for a sufficient time without comfort issues and the tumor can be heated with fewer or no cold spots.

The review of optimization of excitation coefficients is divided in two subsections by time. The optimization methods proposed in the last century only tried to optimize the EM power within simplified human models. The methods developed recently have better performance and take more consideration of practical issues. The tools applied in these methods include numerical algorithms, hardware and patient feedback. All of these methods try to find the optimal excitation coefficients based on more realistic conditions.

Early Methods

The Method of Moments (MoM) and Green's function were considered as numerical tools for optimization. In [227], the method firstly simplifies the slice of the target tissue in a patient's anatomical model into 235 subvolumes and calculates the deposited EM power in each subvolume with Green's matrix. Then, the desired power is set in the focused region, and the ratio between the summation of the power in the subvolumes of the unfocused region and that in the focused region is minimized. The minimization is conducted with the steepest descent method using the Fletcher-Powell approach. The parameters of minimization include both the amplitude and phase of each excitation. The scenario studied in [227] is a hexagonal planar array in stratified inhomogeneous media (water and tissues). The focal

point is set several centimeters away from the array instead of at an infinite distance as in conventional array design.

Moreover, in [228], a layered cylindrical phantom is used to simulate the human, and $|E|^2$ in the phantom is calculated using Green's function for layered media [229]. The fields due to four waveguide elements are optimized with the following requirements using the penalty function method. Firstly, minimize the square error between the calculated field and desired field in the target. Then, constrain the field outside the target to be lower than a certain level. Also, MoM is applied to solve a layered elliptical phantom for a circularly arranged array with a PEC reflector behind [230]. The excitation coefficients are optimized by conjugate field matching with consideration of mutual coupling.

With respect to hardware, a convenient and simple but invasive method was demonstrated in [231]. In the receiving mode, a set of signals (magnitude and phase) are received by the applicator elements from the probe inserted in the tumor (Figure 9.38(a)). With the reciprocal property of this network, the conjugate of the signals received are transmitted by the elements to create a focal point at the location of the probe (Figure 9.38(b)).

(a)   (b)
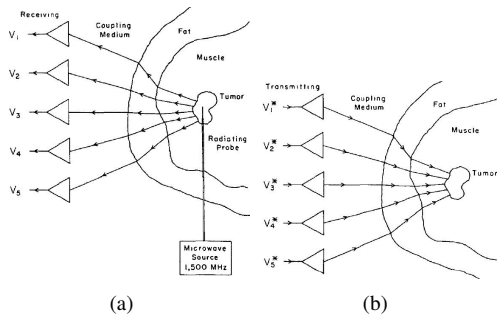
Figure 9.38: The method proposed in [231] includes (a) the receiving mode to obtain the focusing excitation coefficients and (b) transmitting mode to conduct hyperthermia according the excitation coefficients obtained in the receiving mode.

A method to optimize the excitation coefficients with external E-field sensors was suggested in [232]. As shown in Figure 9.39, in addition to the four radiating elements for administering the thermal dose, a sensor is

placed in the target and three sensors are placed on the surface away from the target as the centers of null-field areas. The feedback signals from the three null-field sensors and the one target sensor are calculated with the modified steepest decent method to focus the EM power on the target sensor whilst making the three null-field sensors receive the lowest EM field. Thus, because the areas around the null-field sensors also have low field strength, the deposited power can be focused in the target without excessive heat in healthy tissues. Animal tests and clinical trials were conducted using this approach with two waveguide radiators [233, 234]. As described above, the adaptive phased array had one E-field probe inserted in the target tumor and several probes attached to the skin of the patient. The radiators (two waveguide antennas in this case) were adaptively controlled by these probes to generate focus and null-field areas in the tumor and in healthy tissues, respectively.
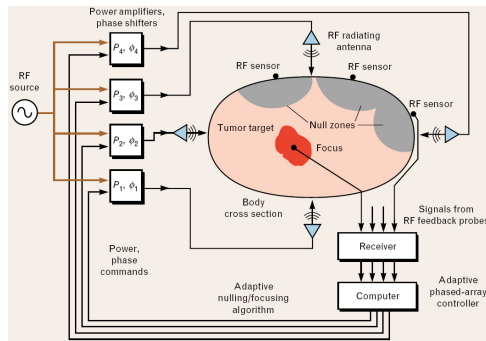
Figure 9.39: Excitation coefficient optimization with four E-field sensors [232]. The target sensor is inserted in the tumor; the three null-field sensors placed on the surface are the centers of the null-field areas.

Several problems were found in the early methods of optimizing excitation coefficients. First of all, the human models were over simplified. This simplification leads to inaccurate field distribution predictions, which may cause hotspots or underestimation of the target temperature. Secondly, thermal result was not considered, and therefore the optimized excitation coefficients may not be optimal. Thirdly, the time required for the optimization was too long for clinical application. Finally, there were usually

only several measurement points for the methods using hardware. A few measurement points are not enough to find the optimized excitation coefficients. Therefore, optimization methods with better performance were still required.

Recent Methods

To overcome the problem of optimization time, [235] shows a fast method of maximizing the ratio of the absorbed power on the target and the rest region. The ratio is turned into a generalized Eigenvalue problem [236],

$$\mathbf{A}p = \lambda \cdot \mathbf{B}p. \tag{9.1}$$

- p: the Eigenvector which represents the excitation coefficients.

- **A** and **B**: the matrices characterize the deposited power distributions in the target and the rest region respectively.

- λ: the Eigenvalue, or the ratio of deposited power between the target and the rest region.

The largest Eigenvalue is desired and the corresponding Eigenvector, or the excitation coefficients, is the optimized result. The iterative process of optimization can therefore be reduced into a generalized Eigenvalue equation to save optimization time. Moreover, genetic algorithms (GA) are also applied in the optimization with finite element method (FEM) [237] and FDTD [238]. The factor of evaluating the fitness of the goal is called the object function, and six different object functions were tested with the method of FEM+GA [239]. It appears that the most suitable object function was different for the scenarios simulated.

Although optimizing the excitation coefficients based on temperature could provide better performance, calculation of the thermal result from EM fields in the optimization process requires an unacceptably long time in clinical application. Thus, several methods have been proposed to try to conduct temperature-based optimization within a clinically reasonable time. In [240], the process of obtaining optimized excitation coefficients based on the temperature distribution is:

- Build the numerical model of the patient with computed tomography or MRI.

- Simulate the EM fields and thermal distribution with a low resolution patient model to obtain the optimized excitation coefficient vector $\vec{v}$. The corresponding SAR and temperature distributions are represented as SAR^{LR} and T^{LR} respectively.

- Obtain the SAR distribution on the high resolution model (SAR^{HR}) from SAR^{LR} by using the quasi-static zooming technique and calculate T^{HR} accordingly. Note that both the SAR^{HR} and T^{HR} distributions are based on the $\vec{v}$ derived in the previous step.

- When the excitation coefficients are being optimized with the high resolution model, the new corresponding temperature distribution on the high resolution model ($\text{T}_2^{\text{HR}}(x, y, z)$) can be approximated as

$$\text{T}_2^{\text{HR}}(x, y, z) \approx \frac{\text{T}_2^{\text{LR}} - \text{T}_{00}}{\text{T}_1^{\text{LR}} - \text{T}_{00}}(\text{T}_1^{\text{HR}} - \text{U}_{00}) + \text{U}_{00}, \qquad (9.2)$$

where T_1^{LR} and T_2^{LR} are the thermal distributions of the current and next iteration, respectively. T_{00} and U_{00} are the boundary conditions for the low and high resolution scenarios, respectively.

Thus, the thermal result is in high resolution to maintain accuracy, but the optimization is mainly conducted with the low resolution model for a short optimization time. This method was applied on 16 oesophageal cancer patients with the AMC-4 applicator at 70MHz [241]. The AMC-4 applicator is similar to the AMC-8 (Figure 9.32) but has only one ring of waveguide radiators. Three settings of excitation coefficients were tested;

- Calculated: the setting is optimized by the method mentioned above.

- Clinical: the setting is optimized based on clinical experience.

- Mixed: the calculated excitation amplitude is applied with the clinical excitation phase.

The measurement results show that the mixed setting induces higher tumor temperature than the other two settings. Moreover, the calculated setting can heat the tumors more effectively, that is, less total power delivered with similar tumor temperature.

Another method of reducing the computation time of temperature-based optimization is to reduce the computational dimensions by Model Order

Reduction (MOR) techniques [242, 226]. Firstly, consider the SAR value at a point in a tissue due to M elements:

$$\text{SAR} = \frac{\sigma}{2} \sum_i \sum_j u_j^* \mathbf{E}_j^\dagger \mathbf{E}_i u_i, \tag{9.3}$$

where u_i and u_j are the i_{th} and j_{th} excitation coefficient in M elements, respectively. $\mathbf{E}_i$ and $\mathbf{E}_j$ are the E-fields due to i_{th} and j_{th} element, respectively. The E-field, or SAR, in tissues due to each source can be simulated with regular numerical methods like FDTD [17]. The simulated SAR is the source in the Bio-Heat Transfer Equation (BHTE) and, during the temperature-based optimization, MOR is applied to reduce the computational dimensions of BHTE. BHTE is incorporated with nonlinear behavior, that is, temperature-dependent perfusion rate, and MOR is available only for a linear system. Therefore, the matrix has to be separated into linear and nonlinear parts:

$$\frac{d\mathbf{x}}{dt} = \bar{\mathbf{K}}_L \mathbf{x} + \mathbf{K}_N(\mathbf{x}) + \mathbf{b} \tag{9.4}$$

where $\mathbf{x}$ is the temperature and $\mathbf{b}$ represents the effects of both applied power and perfusion. $\bar{\mathbf{K}}_L$ and $\mathbf{K}_N(\cdot)$ are the linear and nonlinear matrices, respectively. To reduce the scale of Equation 9.4, the MOR technique, named the Karhunen-Loève transform or KL transform, is used (Figure 9.40) [226]. After the reduction, the calculation of BHTE from the EM field takes a much shorter time, and the temperature-based optimization can be fast enough for clinical practice.
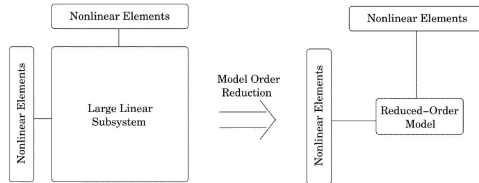

Figure 9.40: Model Order Reduction applied to reduce the scale of the linear part of the calculation of thermal distribution from EM fields (BHTE) in temperature-based optimization [226].

A different optimization approach reported in [225] is based on solving BHTE by measuring temperature distribution using Magnetic Resonance Thermometry (MRT). Firstly, the BHTE is transferred into finite-difference time-domain form, so the temperature at time step k+1 at point x can be predicted from the temperature at time step k at and around x. The unknown parameters of this equation are the influences on current temperature at and around x, and the thermal sources (or sinks) due to EM power and physiology. The excitation coefficients can be optimized by the generalized Eigenvalue method (Equation 9.1) if these unknown parameters are identified. To find the unknown parameters, the finite-difference BHTE can be converted into matrix form:

$$\mathbf{y}[k] = \bar{\mathbf{S}}[k]\theta, \tag{9.5}$$

where $\mathbf{y}[k]$ is the vector representing the temperature distribution predicted at time step k; $\bar{\mathbf{S}}$ is the regressor matrix which contains past measurements and the excitation coefficients; θ represents all the unknown parameters in BHTE, which is determined by using recursive least squares method:

$$\hat{\theta}[k+1] = \hat{\theta}[k] + \bar{\mathbf{R}}[k]\big(\mathbf{y}^{meas}[k+1] - \bar{\mathbf{S}}[k]\hat{\theta}[k]\big), \tag{9.6}$$

where $\mathbf{y}^{meas}[k+1]$ and $\bar{\mathbf{R}}$ are the temperature distribution measured and the update matrix, respectively. Therefore, unknown parameters are refined by the temperature measured during this process. It usually needs N^2 measurements to identify the parametric model θ for an array with N elements. Once these unknown parameters are found, the connection between the temperature and the excitation coefficients is established. Again, the optimal excitation coefficients can be found by the generalized Eigenvalue method to maximize the ratio of temperatures in the target and healthy tissues.

Nevertheless, the interval time between the N^2 measurements could be up to about 10 minutes due to thermal dissipation [243]. In addition, these linearly independent thermal patterns are not usually focused in the treated region. Thus, the clinical preparation time with unfocusing power can be very long if the applicator has many elements. Two solutions have been demonstrated for solving these two problems, i.e. long interval time and unfocusing power delivery [243]. As the temperature decay of thermal dissipation is known to be exponential in form, it is possible to compensate for the cumulative effect in the measurement interval. The preparation time

can thus be significantly reduced due to a shorter interval time. The second solution is for the problem of the long unfocusing input sequence. Firstly, the thermal distribution can be connected to excitation coefficients ($\vec{u}$) with a system matrix,

$$\text{T}(t, x_i, y_j, z_k) = \vec{u}^H \cdot \left[S_{i,j,k} \right] \cdot \vec{u}, \tag{9.7}$$

where H indicates the complex conjugate transpose, $\vec{u}$ represents the set of excitation coefficients, and $\left[S_{i,j,k} \right]$ is the system matrix that needs to be filled. The system matrix represents the relationship between the excitation coefficients and the temperature at the location (x_j, y_j, z_k). In [225], M^2 linearly independent measurement results are required to fill the system matrix for a M-element applicator, but this method sets each input in a focused manner and the procedure is:

- The initial estimate of $\vec{u}$ is derived from the optimized results of numerical simulations, so it is in a focused manner. The simulation model can be simplified for shorter simulation time. Then, the first thermal image is measured accordingly.

- The first approximated system matrix can be obtained using least-squares error approximation.

- The temperature ratio between the tumor and the rest region can be turned into the generalized Eigenvalue problem as in [235]. The matrix of this Eigenvalue equation is the summation of the system matrices at every point in the tumor. The Eigenvector corresponding to the largest Eigenvalue is the input for the next iteration.

- The above procedure is repeated until all the required thermal images are gathered.

The required thermal images for the exact system matrix could be more than M^2 as it is possible that not all the inputs are linearly independent of each other. However, no unfocused input is applied during the collection of the measurement results.

A further improvement is proposed by the concept of *virtual sources* [244]. A virtual source is a set of excitation coefficients. N linearly independent virtual sources can be set to represent M physical elements with $N < M$ such that $N^2 \ll M^2$. Therefore, as only N^2 thermal images are

needed instead of M^2, the time required for filling the system matrix can be much shorter. The excitation coefficients are optimized before the treatment by numerical simulations with a simpler model, and the system matrix in this optimization is the arithmetically averaged system matrices in the tumor. The virtual sources are the first few Eigenvectors of this optimization from numerical simulations. The numerical and experimental validation of this method shows application feasibility on soft-tissue sarcoma in the extremities [245, 246].

Apart from the methods mentioned above, there is a simple but efficient approach to optimize excitation coefficients that is based on patient feedback. If feedback of the patient being treated can be considered in the optimization, the optimization process is much simpler and still includes physiological information [247, 248]. Figure 9.41 shows the process of obtaining the optimal excitation coefficients with the complaint-adaptive method. First, the patient's numerical model is built and the EM field of this model is simulated with the applicator being used. Then, an initial optimization of the excitation coefficients is conducted numerically to obtain the first estimation of the excitation coefficients in the clinical application. If no complaint is received from the patient after some time undergoing HT with the optimized excitation coefficients, the input power is increased to enhance thermal performance in the tumor. If the patient complains of discomfort or pain in a certain region, the region is weighted in the optimization settings. The excitation coefficients are re-optimized to reduce the power in this region. This process is iterative until the maximum power acceptable for this patient has been reached. The optimization algorithm can be the generalized Eigenvalue method [235] so that all optimizations before and during the treatment can be completed in a very short time [120]. Although the optimization is based on SAR, this method is able to effectively reach the maximum power that can be delivered to each patient individually.

9.3   Other Hyperthermia Modalities with External EM Fields

In the previous sections, low-frequency and multi-element applicators have been reviewed. In addition to these designs, there are also many novel approaches developed for conducting hyperthermia treatment in deep regions.
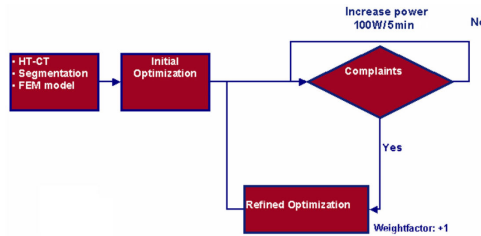
Figure 9.41: The process of complaint-adaptive power density optimization proposed in [247].

These approaches include the application of lenses (including metamaterial), reflectors and ultrawide-band microwave to concentrate EM power on deep-seated tumors.

9.3.1 Lens

An early design combining a waveguide radiator and a lens to create field concentration is shown in Figure 9.42 [249]. The lens consists of a curved opening, metal plates and is filled with dielectric. The dielectric is used to match the material difference between the waveguide and tissues (or water). The metal plates divide the opening into some sub-elements, and the curved opening makes the "array" generate coherence in the tissues.
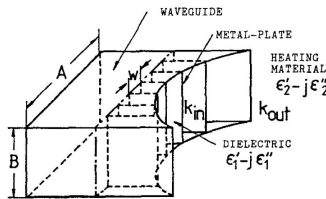
Figure 9.42: The applicator with lens shown in [249]. The lens has metal plates and is filled with dielectric and a curved opening. It can concentrate the field emitted from the waveguide on the center of the curve.

Since the curved opening is not easy to apply on patients, another design with a flat opening was proposed in [250] and is shown in Figure 9.43.

To create the phase difference of waves separated by the metal plates, the curved side of the metal plates is placed inwards in the waveguide. Due to manufacturing difficulties, this design is also further modified by a waveguide radiator that is partially filled with dielectric [251].
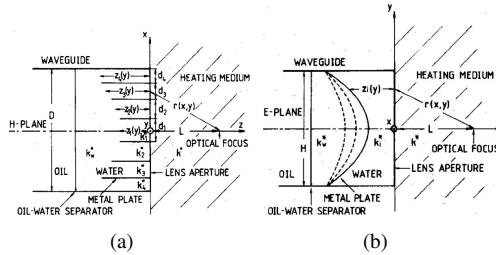
Figure 9.43: The improved design of the lens over that in [249]. The applicator is shown on two perpendicular planes on (a) and (b), respectively. The curvature is inward, and the flat opening makes it more clinically applicable.

Interest recently has been growing in the study and applications of metamaterials, also in hyperthermia [252]. Figure 9.44 shows how the irradiative fields are concentrated by using a metamaterial lens. As negative transmission index is possible in left-handed metamaterials (LHM), LHM can focus the EM field radiated by a point source in tissue, like the breast, when the material properties and relative distances between the three layers are properly designed.
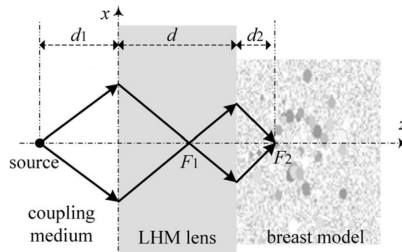
Figure 9.44: The negative transmission index of the left-handed metamaterial can be applied to focus EM fields in breast tissue [252].

A study of field concentration in breast tissue with a LHM lens was conducted by 2D FDTD in [252] (Figure 9.45). Four radiating sources were aligned with the target and four LHM lenses were placed between each radiating source and the tissue. Promising results were obtained in this study, although there are still many unsolved issues such as matematerial manufacture, 3D study and measurement validation.
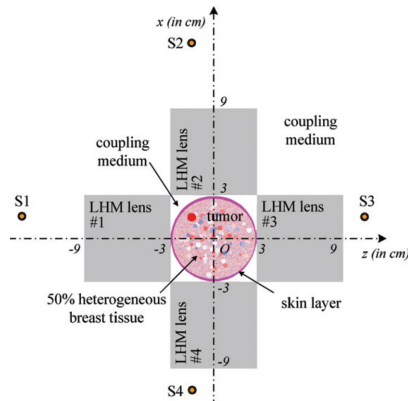
Figure 9.45: The 2D numerical study of breast HT using LHM lens [252]. Four radiating sources (S1-S4) are aligned with the tumor and four LHM lenses are placed between each source and the breast.

9.3.2   Reflectors

Focusing the EM field in a treated region with reflectors was suggested in an early design [199]. Properly designed reflectors may provide better concentration and emission suppression. In [253], field concentration is generated in a ellipsoidal cavity that has two foci (Figure 9.46). This applicator is designed for heating brain tumors and this idea is developed from radiometry for brain temperature and conductivity [254]. The antenna and the human head are placed on the two focal points in this beamformer. The opening on the right side is for patient access. The operation frequency is 1-4GHz depending on the penetration depth and heating volume.

As seen in Figure 9.47, the wave radiated from the antenna is focused in the head. This applicator has been validated with phantoms and healthy
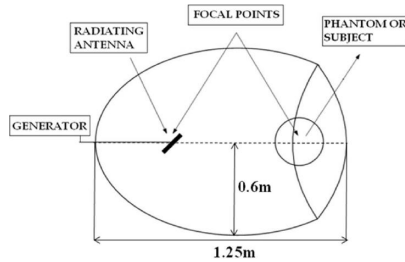
Figure 9.46: An ellipsoidal cavity with an antenna inside was proposed as a hyperthermia applicator for brain tumors [253]. The antenna and patient's head are placed at the two focal points of this cavity. The opening on the right is for patient access

volunteers. Furthermore, in addition to carefully choosing operation frequencies and the size of the ellipsoid, two methods have also been shown to enhance the concentration: filling the cavity with low-loss/high-permittivity material and covering the head with one or several dielectric layers [254]. Both can reduce the reflection on the tissue-air interface and consequently enhance the power deposition in the target. The cavity filled with dielectric is more portable because the physical size is smaller for the same frequency.
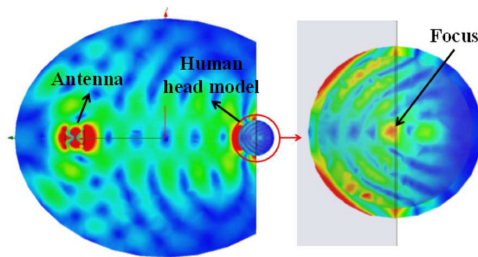
Figure 9.47: The EM field radiated by the antenna from a focal point is re-focused at the other focal point where treated target is located [253].

Another applicator design with reflectors was proposed for treating breast tumors in [255]. As shown in Figure 9.48, the breast being treated is soaked in a water-filled therapy tank which contains a pair of radiating elements

with two reflectors, or mirrors as referred to in [255]. The radiated EM fields are reflected and concentrated in the treated region by the two mirrors. A 2D numerical study was conducted to find the optimal curvature of the mirrors [255]. For given regions for the mirrors as well as the locations of radiators and target, a ray-tracing technique was applied to find the curvature of the mirror that makes all the traces emitted from the radiator reach the target. The optimized curve is shown in Figure 9.49. Both a generic phantom and a real breast model were tested in this 2D study.

A - Deformable Mirror   B - Source   C-Therapy Tank
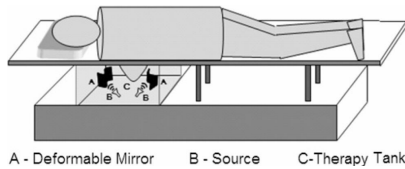
Figure 9.48: The configuration of the applicator for breast tumors proposed in [255]. The treated breast is placed in the therapy tank. The EM field is radiated from a pair of antennas and concentrated on the tumor by a pair of mirrors.
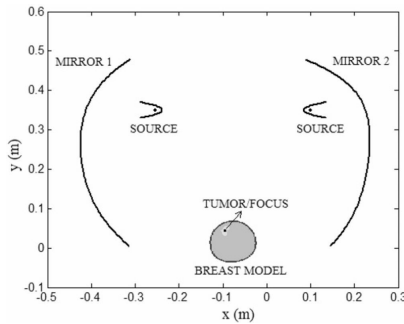
Figure 9.49: The shape of the mirrors in [255] is optimized in a 2D study with a ray-tracing technique.

A multimode cavity was developed in [256] to administer thermotherapy. The patient being treated is partially placed in a cavity that allows many high order modes. These modes can be manipulated by choosing the loca-

tions of excitation, and the tuning probes and the fields can be concentrated by coherence between these modes.

9.3.3   Ultrawide-Band Microwave

Recently, there has been growing interest in both imagining and hyperthermia treatment of breast tumors using Ultrawide-Band (UWB) microwave (1-10GHz) [257, 258]. Early-stage breast cancer detection is critical for breast cancer treatment in terms of clinical response. In addition to regular imaging techniques such as X-ray, MRI and ultrasound, alternative methods are also being developed to enhance comfort, ionized radiation exposure and cost. UWB Microwave imaging is one of the approaches that appears to have a promising future [257].

The basic concept of breast cancer detection using UWB radar is to first place radiators around the breast under detection (Figure 9.50). Secondly, each antenna transmits a UWB signal into the breast in sequence and the other antennas receive the backscattered signal. Post-processing of these backscattered signals, such as microwave imaging via space-time (MIST) beamforming [259], depicts the profile of energy scattered in the breast. As the permittivity of the tumor and normal tissues are significantly different in the breast (more than 2 times different in the RF and microwave frequency range), the scattered energy from the tumor is significantly different from healthy breast tissue. A tumor size smaller than 0.5cm can be detected using UWB radar [257].

As UWB radar is able to precisely describe the energy profile, reciprocity of electromagnetic waves can also be applied to generate energy concentration in the target [258]. The process of transmission signal is shown in Figure 9.51. Finite Impulse Response (FIR) filters are used for compensating for the dispersive effect of the UWB signal and the time-delay vector is used for creating coherence of the UWB signal on the treated tumor. The setting of the FIR filters and the time-delay vectors is based on the received signals in the cancer detection [258]. In addition, UWB has been numerically proven to give better performance in HT than narrow band signal [260]. In addition to MIST beamforming, a time reversal (TR) technique using UWB was also demonstrated for hyperthermia treatment and it shows similar performance to MIST [261]. This method was firstly developed and applied to the therapy using ultrasound, and it is also based on reciprocity of sonic waves. Moreover, a numerical study shows that a data-adaptive

beamforming method, called the Robust Capon Beamformer (RCB), can be combined with TR to generate tighter focus than MIST beamforming [262].

(a) (b)
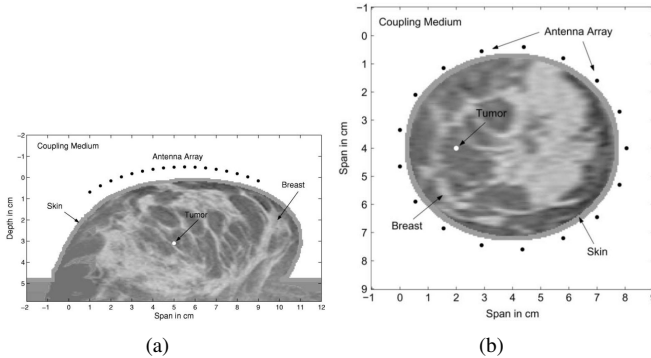
Figure 9.50: The two configurations of cancer detection and hyperthermia treatment using UWB microwave [258]; (a) supine (face-up) position, suitable for small breast volumes and tumors adjacent to the chest wall and (b) prone (face-down) position, easier to access full volume of breast.
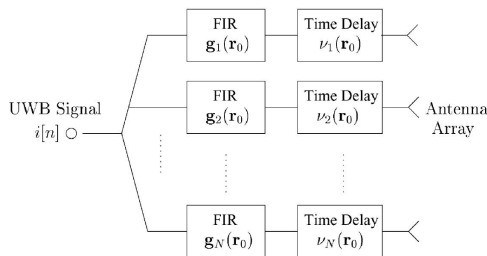
Figure 9.51: Process of emission signals on each antenna for hyperthermia treatment using UWB. The FIR filters and time delays are for compensation of dispersion and coherence generation on the tumor, respectively [258].

9.4 Discussion and Summary of the Hyperthermia Review

The techniques of hyperthermia treatment using external electromagnetic power, such as low frequency approaches, antenna array and other strategies, have been reviewed in this report. In this section, some general topics of non-invasive HT with EM power are discussed. First is a summary of all the methods reviewed in this report. Then, since the water bolus is used in almost all external applicator designs, the reasons for using a water bolus are summarized. Finally, since hyperthermia treatment is a highly interdisciplinary application, the technological challenges and expertise required in this modality are discussed.

9.4.1 Summary of the Applicators Based on Non-Invasive EM Power

Low frequency applicators (from lower than 4MHz to about 100MHz) use capacitive (E-field dominant) or inductive (H-field dominant) mechanisms to heat patients, mostly with a single element. These methods may provide sufficient penetration depth for deep-seated tumors, but the SAR or thermal distribution strongly depends on the geometry of the tissues. For inductive coupling, the eddy current distribution depends greatly on the conductivity of the tissues. Thus, unexpected or undesired hot spots may emerge due to the complicated distribution of conductivity [168]. Moreover, the eddy current induced with inductive coupling is mainly in the superficial region due to the skin effect. Capacitive coupling may overheat the fat layer because of the significant difference in permittivity between fat and other soft tissues. In addition, although some focusing techniques have been proposed, the focusing performance of low frequency applicators is still limited. This may induce hotspots and cold spots in healthy tissues and the tumor, respectively, and both would significantly decrease the treatment efficacy. Therefore, the low frequency applicators reviewed seem not to be suitable for the general application of HT. However, as they are simpler to engineer, these methods may still be suitable for heating large tumors or for biological research [141]. Moreover, there is growing interest in a HT approach using magnetic nanoparticles [123, 263]. The material properties of the treated tumor is changed by injecting the fluid with magnetic nanoparticles, or magnetic

fluid. The patient is exposed to a low-frequency magnetic field which induces heat on the tissues dosed with magnetic fluid [264].

Due to the disadvantages of low frequency applicators, more recent studies have focused on developing applicators using antenna array at higher frequencies (from 70MHz to 150MHz for the pelvic region, 434MHz for the head and neck region, and 400MHz to 2450MHz for superficial regions). Superficial hyperthermia with an antenna array is easier from an engineering point of view because of penetration depth and no need for a complicated algorithm to optimize the excitation coefficients. Thus, some applicators for superficial hyperthermia have been commercialized [188]. One of the novel designs is able to conduct brachytherapy and HT at the same time by using a multi-layer applicator. For deep regions, although phased array provides the possibility of manipulating deposited energy, it creates many more engineering challenges. The first of these is accurately predicting the thermal distribution and comprehensive thermal measurement. The lack of these causes the entire treatment to have no solid base from both the engineering and medical perspectives. Secondly, where RF and microwave are concerned, the human body is extremely inhomogeneous and has very complicated geometry. Optimal parameters such as frequency, antenna number and antenna arrangement are different in different regions of the human body, and they may not be easily found or realized. Finally, for every given scenario, there should always be an optimal set of excitation coefficients to contribute the highest efficacy of hyperthermia treatment. The optimization techniques include numerical methods (such as generalized Eigenvalue equation and mode-order reduction) and measurement using magnetic resonance thermometry. Because of theoretical and practical reasons, these optimization algorithms may also be difficult to develop and implement.

The engineering difficulties and performance limitations of phased array encourage research on alternative methods of conducting hyperthermia treatment for deep-seated tumors, such as metamaterial, reflectors and UWB microwave. Most of this research is still in the stage of numerical studies or has only been validated with simple phantoms, and no further measurement validation or clinical trials have so far been reported. However, these methods have good theoretical support. In addition, the target region for most of the techniques introduced in this section is the breast. The material properties of tumor and breast tissues are very different to EM power at RF or MF, so the focusing performance should be better than the treatment in other regions. Therefore, these methods appear to be promising and should

be worth further investigation in the future.

9.4.2   Water Bolus

A water bolus is common in most applicator designs. It is placed between the heating sources (coils, antennas, etc.) and the patient. The water bolus has multiple functions [134]:

- Reduce the reflection: the material properties of tissues are very different from that of air. The water bolus makes transmission of the EM field into the tissue with less reflection from the surface.

- Surface cooling: excessive superficial heating is a common problem in hyperthermia treatment. A water bolus with water circulated at a constant temperature can cool down the skin. Thus, the delivered power can be higher without burning the skin.

- Positioning: patient positioning is one of the important causes of uncertainty. The water bolus can be used as a fixture to anchor the patient to the applicator and thus reduce the uncertainty of patient positioning.

- Suppressing the emission: because of the great difference in permittivity between water and air, the water bolus can keep the leakage of the EM field at a safe level.

- Decreasing the antenna size: for the phased array approach, the number of antennas is important to the performance. Because of the high permittivity of water, the water bolus helps in increasing the antenna number by decreasing the antenna size significantly.

- Isolated from tissues: as the antennas need to be close to the tissues for superficial hyperthermia, the presence of a thin water bolus ensures that the resonance and impedance matching of the antennas is not influenced by the geometry and material properties of the tissues.

- Broader bandwidth: the wave impedance in water is much lower than that in air, so the input impedance around anti-resonance might also be much lower than that in free-space. For this reason, resonant types

of antenna, such as dipole and slot antennas, can be operated in anti-resonance and the impedance bandwidth is broader than that in reso-nance [208, 207].

Therefore, and especially for superficial hyperthermia, water bolus de-sign is also significant for thermal performance. This includes the shape [265, 184] and the water temperature [266] of the water bolus.

9.4.3 Technical Challenges and Expertise Required

Although many clinical trials have reported positive results by using HT as an adjuvant modality, it is still not globally accepted. As well as political issues, there are still many technical challenges facing hyperthermia treat-ment. First is the SAR performance of the applicators. As mentioned above, it is very difficult to concentrate EM power on deep-seated tumors without creating excessive heat in normal tissues. In addition, prediction and mea-surement of the thermal distribution in the tumor and normal tissues is an-other complicated issue. One of the most important factors determining the thermal distribution is blood flow. As vasculature is massive and intricate, especially for capillaries, estimation of thermal performance in tissues by numerical simulation is not easy and is not accurate enough. Furthermore, the thermal characteristics of tissues and blood flow keep changing with dif-ferent temperatures, and so temperature measurement during treatment is necessary [134]. For HT, the temperature in the tumor is the decisive factor in the clinical response [135], and thermometry is therefore essential in de-termining the performance of HT. Moreover, repeatability is also one of the important issues in clinical application. Hyperthermia treatment with each applicator design has to be repeatable at different times and at different sites to allow multi-center studies. Clinically, therefore, quality assurance of ap-plicators becomes significant [129, 267]. Finally, the treatment scheduling is of course also significant. It should be scheduled to maximize synergis-tic effects between the modalities and minimize the toxicity brought by RT and CT [131, 137]. For example, both normal tissues and tumor cells have thermotolerance but at different levels. That affects the thermal dose and the interval between the treatments [135].

Hyperthermia treatment is an interdisciplinary application. In engineer-ing, expertise in many different fields is required:

- Medical/biological support from hospitals: this includes biological knowledge, target selection, performance evaluation, clinical feasibility and trials, etc.

- Thermal engineering: although electromagnetic power is delivered, thermal energy is the source of medical efficacy. Thus, thermal engineering is also critical in this application. The mission of thermal engineers includes development and realization of thermometry, interpretation of thermal distribution in tissues, etc.

- Antenna and RF-circuit engineering: this covers applicator design and patient position. The fabrication of applicators and measurement validation require the expertise of RF engineering.

- Numerical engineering and computer science: for the development of numerical EM/thermal simulation tools, algorithms for optimizing excitation coefficients, data process and acquisition during measurement or clinical application, and user interface of treatment planning tools.

- Integration: the integration of these professions is obviously of importance. It needs to accomplish compatibility and cooperation between these domains, analysis of results and quality assurance.

Chapter 10

A Novel Applicator for Hyperthermia Treatment in the Head and Neck Region

10.1 Introduction

The current standard treatments for cancer in the head and neck region (H&N), excluding the eyes, brain and skin (Figure 10.1), are radiation therapy and chemotherapy [212]. However, the treatments are not very effective and additionally a side effect of these therapies is damage to healthy tissue. As there are many important tissues in the H&N region, these side effects may seriously affect the patient's quality of life. Problems can include difficulty in eating, swallowing and speaking [212].

On the other hand, so far only minor unwanted toxicity has been found following hyperthermia treatment (HT) and this is a unique feature in cancer treatments [212]. The most common side effects are burns on the skin or unwanted heating of other regions giving pressure sensations. More important, it is reported that radiation therapy or chemotherapy combined with HT for tumors in H&N region can enhance local tumor control and/or survival rates, as seen in Table 8.1. The results of the clinical trials in Section 8.2.3 show that HT is a very effective treatment for H&N cancer when well controlled.
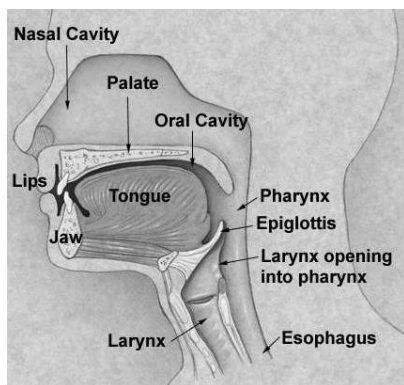
Figure 10.1: The sagittal view of the head and neck (H&N) region [212]

As discussed in Section 9.4.3, effective and efficient HT is an interdisciplinary engineering problem with significant challenges. Using a phased array is a common approach for HT on deep-seated tumors, such H&N cancer (see more details in Section 9.2.2). However, the applicator design proposed in this study is quite different from conventional antenna array for telecommunication purpose [217]. Conventional antenna arrays are designed to transmit EM power forming different far-field beam shapes. Phased array applicators for HT are not designed to generate particular far-field radiation patterns but to provide a desired field distribution in a given volume (tumor) in the near field. Of particular importance is that the target is in a highly inhomogeneous and lossy environment with complex geometry (the H&N region) instead of free space, making predictions complex.

The first hyperthermia applicator designed specifically for the H&N region with clinical trials is reported in [217, 213], named HYPERcollar (which is also introduced in Section 9.2.2). Two six-element circular arrays with radiating elements consisting of planar inverted-L antennas (PILAs) operated at 433.92 MHz, which is a frequency of an ISM Band. Most fundamental studies about applicator design for the H&N region have been done in [214, 215, 216] which include analysis of single element, arrangement of elements in the array, evaluation of heating performance and human phantom design, etc. This first design had several issues with substantial room for improvement. Firstly, PILAs are not the best choice. As the an-

tenna elements are 3D structures operated in water, durability and mechanical strength are critical issues with minor impacts able to cause significant changes. Additionally, they are smaller than the antennas used in this study, but as the radiating environment is not lossless (deionized water), the benefit of reduced size may result in undesirable efficiency reduction. From the point of view of the applicator array itself, there should be more elements in front of the H&N region to provide greater heating and/or better focusing in the target region.

Therefore, this study proposes a novel hyperthermia applicator for the H&N region to overcome the disadvantages for HYPERcollar[1]. This chapter is divided into five parts:

- Introduce the numerical methods used for EM simulations and field optimization, human phantom models and the parameters for evaluating the performance.

- Analysis of the applicator design, which includes the design considerations and analysis of single element as well as 2D analysis in the vertical and horizontal planes of the proposed applicator to aid understanding of the EM behavior of the array.

- Describe the final configuration of the applicator and the refinements of the design.

- Investigate clinical-related issues, such as treatment planning, simulation time control and sensitivity to the errors of patient positioning and excitation coefficients.

- The performance the applicator design is numerically validated with a real patient. The applicator is also manufactured and has measurement results which well agree with the simulation results.

10.2 Methods and Models

10.2.1 Numerical Methods

The EM performance of the proposed applicator is studied based on numerical simulation. During the development stage, the manufacture of a real

---

[1]This study is published as *A Novel Hyperthermia Applicator for Head and Neck Region* in IEEE International Symposium on Antennas and Propagation, 2009

applicator is relatively more time and cost-consuming than simulation. Additionally, simulation provides much more information about the EM field distribution than measurement, and it is very helpful to have a greater insight into the EM behavior of a new applicator. Therefore, the design and optimization of the applicator were carried out in the numerical domain. The commercial FDTD-based EM simulation software, SEMCAD X, was used for the EM simulation.

For a given configuration of a patient and an applicator, there is always an optimized distribution of excitation coefficients (input amplitude and phase of each element), which is difficult to obtain without an optimization tool (see Section 9.2.3 for review of the optimization algorithms). This is therefore another important reason for using SEMCAD X for hyperthermia applicator design: it provides a field optimizer to optimize the excitation coefficients of each antenna to achieve maximum SAR in the target region and minimum SAR in other tissues [238]. The optimization approaches are the generalized Eigenvalue method [235] (see Equation 9.1) and genetic algorithm [237, 239]. This provides important information about the optimum performance with a given scenario. All the hyperthermia performance data shown in this study are the results after using the field optimizer.

10.2.2   Human Models

Two human models were utilized, a simplified phantom and a full human model. The first of the two phantoms consists of a SAM head [12] with a skull, inhomogeneous neck and homogeneous shoulders is for parametric study and analysis of the applicator design (Figure 10.2). This phantom was developed as a reasonable compromise between realism with bone and some inhomogeneous tissues and ability to provide fast simulation times. This was vital if the full range of optimization and tests were to be performed. Target regions were defined in the neck and not in the head in this study so the inhomogeneity of the head is less important than the neck. As the material properties of bone are considerably different from other soft tissues, the skull is therefore still included. The dimensions of the inhomogeneous neck model follow average values and it includes muscle, bone, cartilage, spinal cord and trachea [215] (Figure 10.3). In addition, the material properties of human tissues at 433MHz are taken from the values in the Gabriel database [268] as shown in Table 10.1.

In order to validate the performance of the applicator design, a real pa-
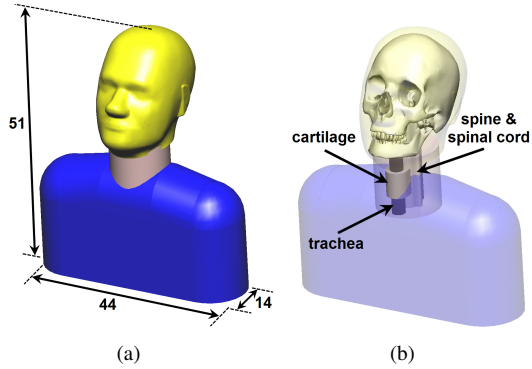
Figure 10.2: The human phantom used in this study for evaluating the performance of the applicator (unit: cm). The material of the head and the shoulders are set as muscle.
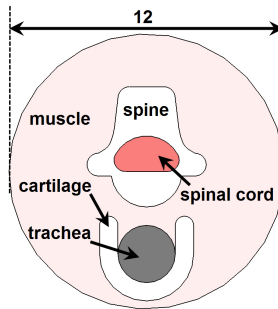
Figure 10.3: The inhomogeneous neck model in the human phantom (unit: cm) [215].

tient with a tumor in H&N region is also applied in this study. As seen in Figure 10.4, the CAD file of the patient is built with MR images with 3 mm resolution. In fact, building CAD file of each patient individually is an important step in treatment planning as discussed later in this chapter.

433MHz	Muscle	Bone	Cartilage	Spinal Cord
Permittivity	57	13	45	42
Cond. (S/m)	0.8	0.09	0.6	0.45
Density (kg/m^3)	1050	1595	1100	1050

Table 10.1: The material properties of human tissues at 433MHz (Trachea is set as air).
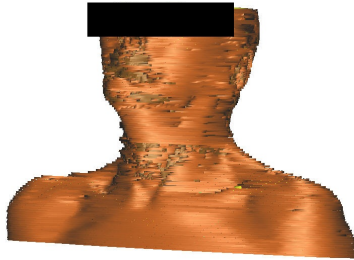
Figure 10.4: A CAD file of a real patient with a tumor is used to validate the applicator design.

10.2.3   Metrics for Performance Assessment

Six target regions in the neck of the simplified phantom were identified as possible locations of a tumor (Figure 10.5). Three locations are set in the neck (Figure 10.5(a)), and each location has a top and a bottom region (Figure 10.5(b)). As skin usually absorbs a higher SAR than muscle, excluding the skin (4 mm depth) from the target regions can produce a more realistic estimation of the power that is absorbed in the target. Only the regions on one side are defined because it was envisaged that applicator designs would have symmetry, therefore, performance expected to be identical on each side.

As emphasized in both Chapter 8 and Chapter 9, uniformly heating a tumor is one of the most critical (and technically challenging) issues for effective HT, as well as achieving the temperature required for effective HT (see Section 8.2.2 for more details regarding the thermal dosimetry). Following this idea, two parameters are used in this study to evaluate the SAR performance of the applicator in each target region, that is, 50%-SAR and
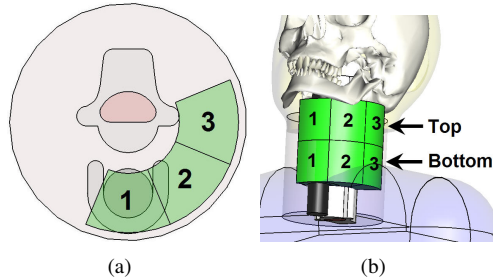
Figure 10.5: (a) Three locations in the neck and (b) each location has a top and a bottom region. The six target regions are set as possible locations of a tumor in the neck.

Targeting Ratio (TR). They are defined with cumulative histogram of SAR over a target region, as seen on Figure 10.6. Over 50% and 75% of the target-region volume are heated with SAR higher than 50%-SAR and 75%-SAR, respectively. Thus, this parameter is used to evaluate the exposure level of the target region. TR is defined as the ratio of 75%-SAR and 50%-SAR, which evaluates the homogeneity of heating performance. If TR is close to 1, the target is illuminated more uniformly. The blue curve in Figure 10.6 clearly shows better TR than the red curve, which indicates the heating pattern is more homogeneous. If it is expected that whole tumor is heated with at least 200 W/kg SAR and the SAR distribution decays linearly in the tumor, 50%-SAR and TR should be 400 W/kg and 67%, respectively.

Note that the above parameters are for studying the EM behavior of this applicator and are different to the performance indicators for clinical response as reviewed in the previous chapter. The ratio of hotspot-SAR between tumor and healthy tissues, as discussed in Section 8.2.2, is also a meaningful indicator for the level of the input power available for safety consideration [133]. However, this indicator does not show the transmission efficiency from the antennas to the target (50%-SAR) nor the field homogeneity in the target (TR). Thus, the hotspot-SAR ratio will be used only in the validation of a real anatomical model.
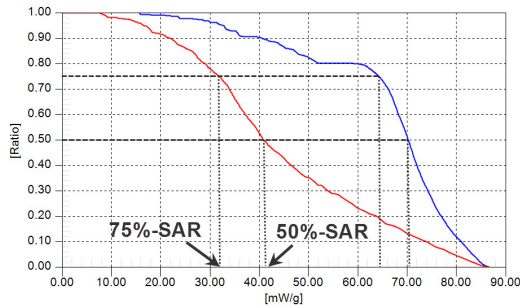
Figure 10.6: 50%-SAR and Targeting Ratio (TR) are defined with cumulative histogram. The blue curve is an example of heating with good homogeneity and therefore good TR.

10.3 The Applicator Design

10.3.1 Design Considerations

Elements

As seen in Section 9.2.2, the radiation elements used in phased-array applicator for deep-seated tumor could be electrically small dipole antennas (Sigma-family), modified full-wavelength dipole antennas (WACOA), open-end waveguides (AMC-8) and PILAs (HYPERcolloar). Electrically small dipole antennas require matching circuit which increases complexity and uncertainty. Besides, they inherently have narrow bandwidth and therefore are sensitive to the change of the environment, such as different material properties of water due to different temperatures. Full-wavelength dipole and open-end waveguide are too big to have more than 6 elements in a ring or to have more than two rings, which limits the ability of steering the fields. The disadvantages of PIFA have been reviewed in Section 10.1.

To avoid those problems, the elements should preferably use thin and planar structures, so they can be manufactured precisely with phtolithographic processes and are mechanically strong enough to against the pressure from water bolus. Additionally, the design can be such that the elements are outside the water bolus and this can prevent erosion of the elements due to be soaked into water and therefore improve their durability.

The elements should be self-resonant with broad bandwidth and be matched without using matching circuits. In addition, low mutual coupling is also beneficial as this will allow greater flexibility in the choice of element disposition also more elements could be placed in an applicator. More elements might be beneficial to provide better steering performance in order to have more power coupled into the patient without exceeding the power handling capabilities or each element. The polarization of radiating E-field should be parallel to the neck [110]. The beamwidth of each element needs to be broad enough to cover whole neck so that the focus of the power disposition can be anywhere in the neck.

Phased Array

To make an applicator capable of focusing energy into a specific region, a number of individual sources are required where the amplitude and phase of the sources are individually controllable. This is known as a phased array. In general, we can say that to focus energy at a given point in a dielectric body, the elements must be placed around that body. For this reason, a ring architecture is adopted. The diameter of the ring needs to be large enough to allow easy placement of the patient and to provide the ability to shift the patient into an optimum position. Nevertheless, if the ring is too large, the target region may not have sufficient exposure with a given amplifier output power. This is a disadvantage considering the cost.

A single ring of elements/sources would only provide the ability of steer the focus in two dimensions, therefore elements/sources must also be added in the third dimension. However, the height is limited by the size of H&N region. Considering the number of elements, it is clear that ideally there should be as many as possible while the mutual coupling is acceptable. However, there is an important trade-off with overall complexity which means that more is not necessarily better. With aid of Field Optimizer, one can easily determine the contributive elements (the elements having significant contribution to the target). If the applicator and/or the patient position are not designed properly, it may happen that only a few contributive elements focus the power on the target. This leads to insufficient SAR and/or little possibility of manipulating the field distribution. Therefore, one of the goals in this study is to maximize the number of contributive elements in each treatment. The work to achieve this goal includes optimization of element arrangement and the patient's position.

Water Bolus

The reasons for using a water bolus were discussed in Section 9.4.2 and cover both the patient's comfort and treatment performance. Although there are advantages of using water bolus, it may degrade the focusing ability of the antenna array. If the interface between water and air is close to the elements, the reflection from the interface may smear the beam as well as the focusing ability in the patient axis. Thus, the water bolus needs to be longer than the array in the patient axis.

10.3.2　Single Element Analysis

The antennas used in this array are cavity-backed slot antennas fed with microstrip lines and coaxial cables (Figure 10.7). The slot is often treated as equivalent magnetic dipole without the metal ground plane. When the slot is formed on a ground plane or a PCB, all the dimensions can be controlled very accurately due to the use of accurate photolithographic techniques in defining the structure. Hence all the individual elements in an array can be almost identical. The symmetric geometry makes the far- and near-field pattern symmetric. Thus, the EM power is radiated toward the target regions more effectively and the behavior of the EM wave is simpler.
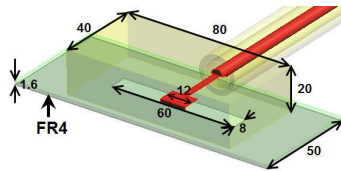
Figure 10.7: The dimensions of a single element, the cavity-backed slot antenna, of the applicator (mm). It consists of a metal cavity and a ground plane with a slot and FR4 dielectric fed by a microstrip line and a coaxial cable

A slot antenna, when operated in air and radiating from the front and back, will have an essentially omnidirectional radiation pattern. In this application, however, the front interfaces with a water bolus of high permittivity while the rear interfaces with air. This has two consequences: firstly, the length of the slot for operation at 433.92 MHz is substantially reduced due to

the high permittivity, and secondly, most of the radiated field is "attracted" into the high permittivity region even with the absence of the cavity. The phenomenon can be explained with image theory and has been analyzed in the application of radar imaging in earth and is observed even when the antenna is resonant in air [22, 23]. The cavity ensures that there is no radiation from the back of the array. The dimensions of the cavity are not critical and have very small influence on the performance.

Furthermore, the antennas of the applicator can be operated with high input power (up to 100 W for each element in this study). Slot antennas provide excellent mechanical strength in real-world usage against pressure and erosion due to water because of their simple and printed structure. In addition, the mutual coupling between the elements is lower compared to regular dipole antennas [25], so the antenna performance is less sensitive to the patient loading. In addition, because of the lower mutual coupling, the behavior of a complete array can be approximated to the combination of each individual element. Thus, the proposed applicator can be analyzed by two separate 2D studies.

In free space, impedance matching at half-wavelength resonance of a slender slot antenna is very difficult because of the high anti-resonant resistance [25]. However, the wave impedance in water is much lower and so is the anti-resonant resistance. As most of the power is radiated into the water, the input impedance of the slot antenna around anti-resonance (Figure 10.8(a)) can be matched to 50 Ohms with broad bandwidth (Figure 10.8(b)), a similar concept to the antenna design in [208]. Although the applicator is operated at a single frequency (433 MHz), broad bandwidth is still necessary to deal with the change in the environment such as the temperature-dependent material properties of the water [212]. As the S_{11} curve is not symmetric with respect to the minimum reflection frequency, neither the S_{11}-minimum frequency nor the frequency at which the impedance is entirely real are at 433 MHz in order to better tolerate environmental change. Thus, unlike the Sigma-family applicators [206, 205], this applicator design does not need any external matching circuit. The disadvantages of requiring external matching circuits were discussed in Section 9.2.2.

(a)   (b)
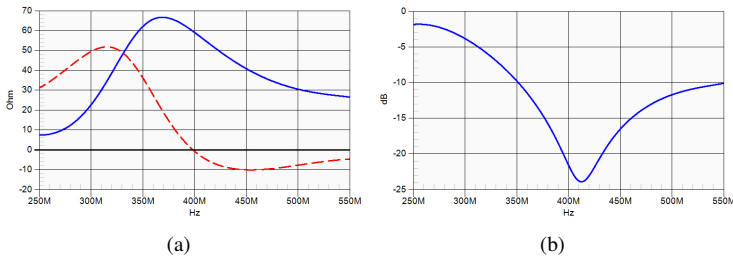
Figure 10.8: The performance of a single element in terms of (a) input impedance (solid: real, dash: imaginary) and (b) S_{11} (dB). The antenna is matched to 50 Ω in the water with broad bandwidth.

10.3.3   2D Analysis of the Applicator

The analysis of an applicator can be separated into two orthogonal 2D studies in the horizontal and vertical planes, as seen in Figure 10.9. Providing the applicator conforms to some basic structural rules. This ability can reduce the problem size dramatically and allow more situations to be studied. The studies provide a physical insight into the EM behavior of the applicator and serve to find the optimum arrangement of the elements and patient positions for different target regions. Therefore, the investigation in this section will be used to refine the overall applicator performance as shown later in Section 10.4.

In the horizontal 2D analysis, a single eight-element circular array is employed with the neck model placed at the center (Figure 10.9(a)). As mentioned in Section 10.3.1, the number of elements are determined by the issues including cost consideration (number of amplifiers), complexity and heating performance. In fact, this design has more elements than all the applicators for deep-seated tumors reviewed previously. In the vertical 2D analysis, three elements are placed vertically in line with the human phantom (Figure 10.9(b)). The number of elements in vertical direction is limited by the length of a human neck and mutual coupling between elements but this is also the first applicator design with three rings.

The separation of the two studies is meaningful only if the mutual coupling between elements is low enough so that the two studies are independent from each other. The S-parameter of the elements in Figure 10.9(a)
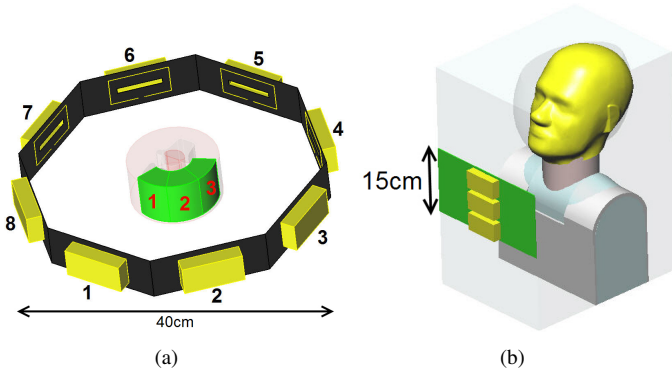
Figure 10.9: The scenarios for analyzing the applicator in the (a) horizontal and (b) vertical 2D planes.

and Figure 10.9(b) is shown in Figure 10.10(a) and Figure 10.10(b), respectively. The elements have good S_{11} (lower than -15 dB) with low mutual coupling (also better than -15 dB), so the two 2D studies are available for simplifying the scenario without compromising the EM behavior.
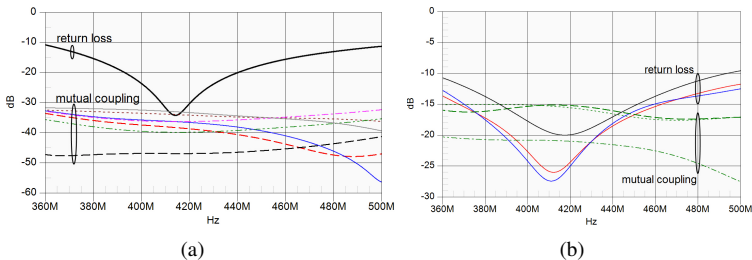
Figure 10.10: The simulated S_{11} and mutual coupling of elements in the 2D horizontal and vertical planes (Figure 10.9). The results of good impedance matching and weak mutual coupling indicate that the analysis of the applicator can be the combination of the 2D studies on two individual planes.

Horizontal Plane Analysis

In this analysis, to make it a true 2D case, the Absorbing Boundary Conditions (ABCs) are attached on both vertical sides. Only one ring array and three target regions are investigated, as seen in Figure 10.9(a). In order for more elements to have a significant contribution, it is important to know the contribution from each element to a target region. Thus, the neck phantom is placed at the center and the SAR performance on target region 1 due to each element recorded. In addition, the SAR results on the superficial region are recorded separately. The 50%-SAR on the superficial region and target region 1 due to each element are shown in Figure 10.11. Although deionized water is filled between the applicator and the patient to reduce the reflection, the skin region still has a much higher exposure than the deep region of the neck because of the high conductivity of the tissues. Thus, it is necessary to exclude the superficial region from the exposure evaluation of the target regions. In addition, only the three elements in front of the target region make a significant contribution, i.e. elements 1, 2 and 8. Moreover, element 1 has a higher contribution than elements 2 and 8. If the tumor is at target region 1 and element 2 (or element 8) delivers the same power as element 1, the applicator may create other hot spots in undesired regions. The results validate the rationale of having the third ring in this applicator as it provides more elements at "line-of-sight" positions to the target regions. Furthermore, it also suggests that more elements would have a significant contribution if the patient position allows for more elements with line-of-sight.
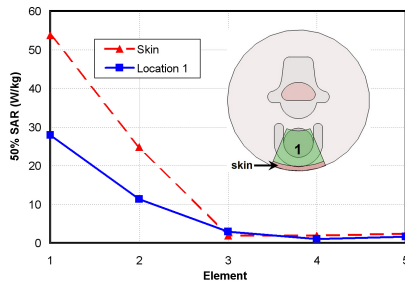
Figure 10.11: The 50%-SAR in target region 1 from each element on the 2D horizontal plane. The skin thickness is 4 mm. The maximum power of each antenna is 100 W.

According to [221], the SAR performance of a ring-array applicator can be improved if all the elements are directed toward the target. This implies that for a given applicator and target location, there should be an optimum patient position in the applicator for the performance of HT. For this reason, the neck is shifted in five directions for 5 cm in this study, as depicted in Figure 10.12. The 50%-SAR and TR are recorded and shown in Figure 10.13(a) and Figure 10.13(b), respectively. As previously mentioned, the SAR performance reported is after using the field optimizer. Due to of the inhomogeneity of the neck, the simulation results are not straightforward.

Target region 3 has the highest 50%-SAR and TR with the shift 2 position. Although target region 1 and 2 do not have the highest 50%-SAR with the shift 1 position, they have the highest TR. Besides, target region 1 and 2 have a similar exposure quantity in the shift 1 position and this is good for large tumor treatment. Figure 10.14(a) and Figure 10.14(b) are the 1g-averaged peak spatial SAR ($psSAR_{1g}$) distribution while the power is focused on target region 1 with the phantom at the center and shift 1 position, respectively. When the phantom is at the shift 1 position, the target region experiences higher exposure. In addition, the shape of the SAR pattern is also different for the two phantom positions. Target region 1 is more uniformly illuminated with the shift 1 position. A similar phenomenon is observed when the power is focused on target region 3 with the shift 2 position. Therefore, shift 1 and shift 2 positions are applied in the proposed applicator for heating target region 1/2 and target region 3, respectively[2].

---

[2]There were unexpected physical phenomena in the Sigma-60 applicator revealed with FDTD simulation and reported in [269]. Sigma-60 is a commercial HT applicator heating the tumors in pelvis region with a circular antenna array whose diameter is 60 cm and operated between 60-120 MHz (please see Section 9.2.2 for more details about Sigma-60.). The phenomena of high stored energy and the EM mode flipping are due to resonance on its transverse plane at around 110 MHz. The applicator proposed here is electrically much larger than Sigma-60 (more than 2 times larger in the diameter), so, unlike Sigma-60, it behaves more like a scattering and propagating problem than a resonator. Therefore, those two phenomena are not observed in this work. Nevertheless, the third phenomenon, the whispering-gallery transmission, occurs in this design as well. In Figure 10.14, it is clearly seen that a hotspot is generated at the opposite side of the activated antennas because of coherence.
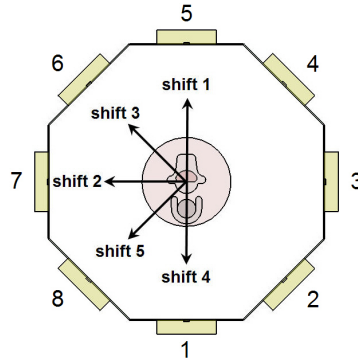
Figure 10.12: The neck is shifted in five directions for 5 cm in order to investigate the effect of the patient position in the horizontal plane in terms of SAR performance.
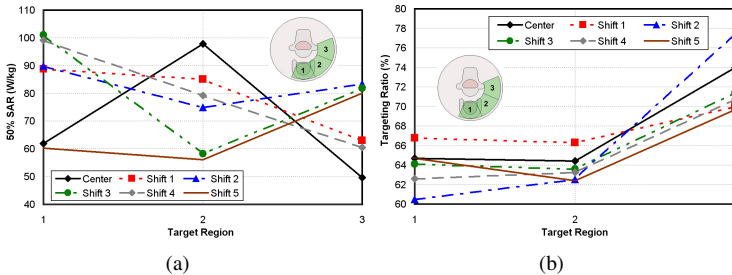
Figure 10.13: The simulation results of the setup defined in Figure 10.12 in terms of (a) 50%-SAR and (b) TR at the three target regions.

Vertical Plane Analysis

The effect of patient position with respect to the elements in column 1 and column 2 (defined in Figure 10.19) is studied with the scenario shown in Figure 10.9(b) and Figure 10.15. ABCs are attached around the models. The variable of the patient position is H, as defined in Figure 10.16. The center of the top element is at the same height as the patient's chin if H=0, while H<0 means that the center is lower than the chin.
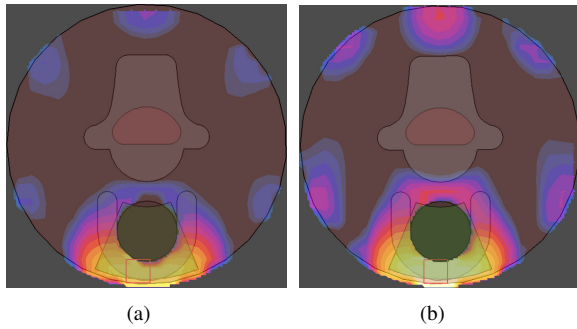
Figure 10.14: The distribution of psSAR$_{1g}$ when the phantom placed at the (a) center and (b) shift 1 position and the power is focused on target region 1. The red cube is the location of the hotspot. Each color step indicates 1 dB difference.
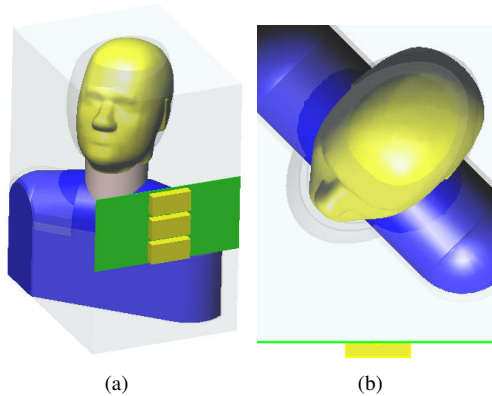
Figure 10.15: The configuration for studying patient positioning with respect to the elements in column 2.

The 50%-SAR on the target regions from the elements in columns 1 and 2 are shown in Figure 10.17(a) and Figure 10.17(b), respectively. TR in this case basically follows the trend of 50%-SAR, so only 50%-SAR is shown here. The SAR exposure is higher when the patient is placed higher. Fur-

(a)   (b)
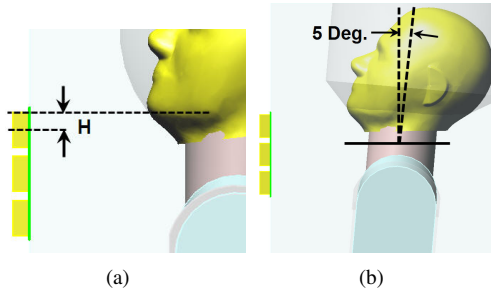
Figure 10.16: (a) The definition of the column position, H. H < 0 means the center of the top element is lower than the patient's chin. (b) The patient is in the tilted position where H is -2 cm.

thermore, the tilted patient position, as shown in Figure 10.16(b), causes significant enhancement for location 2. Figure 10.18 shows a slice of the SAR distribution when the power is focused on the location 2-top (defined in Figure 10.5) and the treated region is partially covered by the mandible. In addition, the location 2-top (and location-3 top) is deeper than the other target regions. The tilted and higher patient position can help to avoid shadowing by the mandible.

(a)   (b)
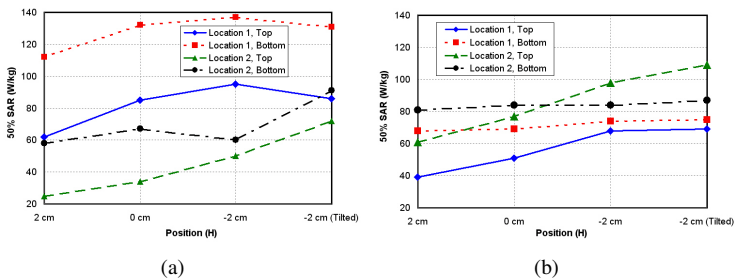
Figure 10.17: The 50%-SAR of the target regions at location 1 and 2 when the elements in (a) column 1 and (b) column 2 with different positions. (H is defined in Figure 10.16)
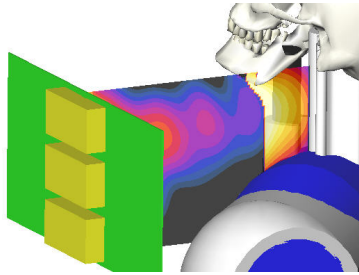
Figure 10.18: The SAR distribution when the power is focused on target region 2-top, which is a deeper target region. The mandible has significant influence on the SAR exposure of this target region.

10.4 Applicator Refinement

10.4.1 Final Configuration

The applicator proposed in this study is shown in Figure 10.19 which consists of three 40 cm diameter circular antenna arrays, each 5 cm high, with a total of 20 elements. The dimensions are 40 cm×40 cm×15 cm. The assumed maximum power for each element is 100 W and it is operated in the 433 MHz ISM-band. In addition, 16 amplifiers are used in the manufacture of the applicator system instead of 20 for cost consideration. Although the applicator has 20 elements, not all of them deliver significant high power during treatment. As will be seen in the following section, only the elements with line-of-sight to the target make a significant contribution to the power focused on the target.

As aforementioned, maximizing the number of the contributive elements (the elements which have significant contribution to the target) is important for the performance. This is the reason behind the addition of the third ring in this design (Figure 10.19) so that more elements cover the targets at lower positions, such as [target region 1, bottom] defined in Figure 10.5. As the third ring is placed lower than the shoulders, only four elements are in this ring. More elements may produce better HT performance [149], but each ring can have no more than eight elements due to the number of the amplifiers.

A water bolus filled with deionized water is placed between the appli-

cator and the patient, like many other designs. The relative permittivity and conductivity of $25\,^{\circ}$C deionized water are 78 and 0.04 S/m at 433 MHz, respectively.
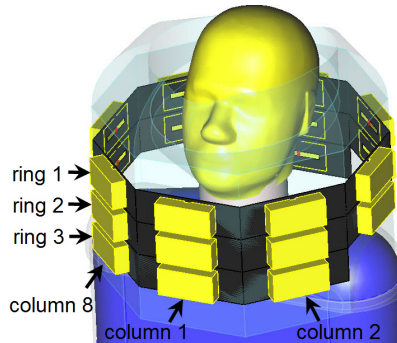
Figure 10.19: The applicator proposed for hyperthermia treatment in the head and neck region. It is a 40 cm diameter antenna ring array with 20 cavity-backed slot antennas operated at 433 MHz. A water bolus is filled between the applicator and the patient.

10.4.2   Air Masks

In this applicator deployment, air masks can be placed on the patient's head, chest and shoulders, as seen in Figure 10.20. These air masks play the role as spacers to keep those parts of the body from direct contact to the water bolus. They are made for improving the performance of HT and for the patient's comfort, namely to:

- Isolate the patient from high SAR in unnecessary regions. For example, the back of the patient's head is very close to the element at (ring 1, column 5) (see Figure 10.19). This element is important for canceling the unwanted hot spot at back of the neck due to the coherence generated by the front elements. However, the proximity of the head limits the radiation power available from this element. The air mask can prevent the head being heated by this element so it can emit enough power to cancel the hot spot. Therefore, the front elements can deliver more power without heating undesired regions.

- Aid precise positioning of the patient when these masks are made of hard material.

- Reduce the pressure on the patient's body due to the weight of the water.

- Help the patient not to feel cold due to the water on these masked regions.

- Enable the patient to breathe easily.

(a)　　　　　(b)　　　　　(c)
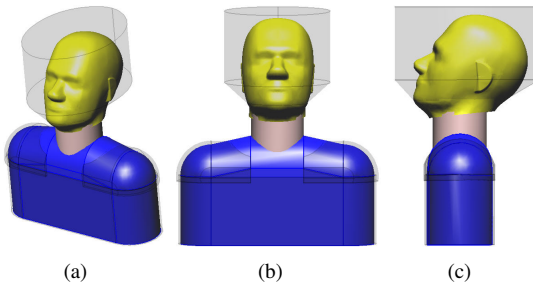
Figure 10.20: The masks applied on the patient's head and shoulders for HT performance and comfort issues.

10.4.3　Optimum Patient Positions for the Proposed Applicator

According to the study in Section 10.3.3, the patient should be placed in different positions within the proposed applicator depending on the tumor's location for optimum performance. The proposed applicator is thus simulated with the human phantom in three different positions for the three locations defined in Figure 10.5.

Optimization of Patient Position

Considering the energy focusing performance, the positioning of the patient should be as important as the applicator design, but there is little analysis

about this issue. In this study, patient position is also optimized based on the tumor location. The optimized positions of a patient within the applicator for a tumor at locations 1, 2 and 3 are shown in Figure 10.21. For the six target regions defined in this study, the vertical patient position should be as high as possible (limited by the shoulders) to effectively expose the target regions to more elements. Moreover, investigation of the vertical 2D plane suggests that the patient should be tilted for higher exposure, especially at location 2.

When the tumor is at location 1, the patient is shifted in the posterior direction for 5 cm so that location 1 is at the center of the applicator. In addition, as seen in Figure 10.21(a), the patient is also tilted by 6 degrees[3]. Although the tilt does not affect the performance at location 1 significantly, it is helpful for location 2. Thus, the position is also suitable for treating a large tumor. The angle of tilt is limited by the size of the patient's head and the size of the applicator. In the horizontal 2D study, location 1 and 2 have similar SAR performance with the shift 1 position (defined in Figure 10.12). The patient position for location 2 is therefore the same as that for location 1. Nevertheless, as the target region of location 2-top is deeper and partially covered by the mandible, the patient's head is tilted by 8 degrees to avoid the coverage, as shown in Figure 10.21(b)[4]. The problem of mandible shadowing also occurs for the target region of location 3-top, so the head is again tilted for this target region. The patient is in the shift 2 position for location 3 and the element at ring 3, column 8 is moved to the diagonal location so that it heats location 3 more effectively (Figure 10.21(c)).

The Performance with the Patient Position Optimization

The three patient positions shown in Figure 10.21 are compared to the original position at the center of the applicator with the patient axis perpendicular to the horizontal applicator plane. In addition to 50%-SAR and TR, the parameters compared also include the number of the contributive elements. A contributive element is defined as the element whose delivered power is higher than 10% after the field optimization for the given target region. This

---

[3]Practically speaking, it would be easier to locate the patient at this position by shifting and tilting the applicator instead of moving the patient.

[4]Tilting patient's head requires corresponding the images and the CAD file. Typically, the images of the patient are made for RT so regular position is used. Therefore, treatment with this position may be clinically challenging.
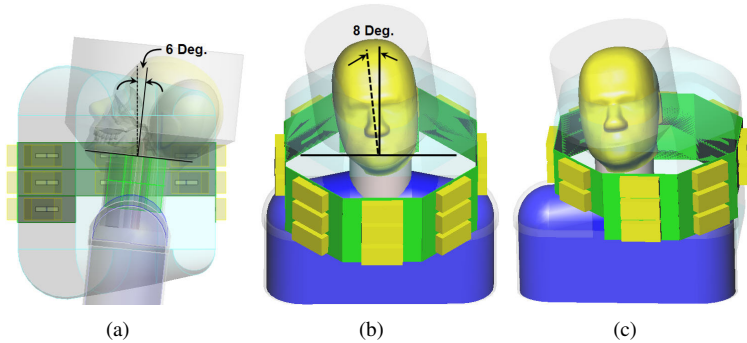
Figure 10.21: The optimized patient positions for tumor at (a) location 1, (b) location 2 and (c) location 3.

is an important parameter in clinical application. Having more contributive elements not only increases the SAR performance, but also provides higher flexibility in manipulating the field by adjusting the excitation coefficients. The thermal properties of tissues are non-linear and the thermal behavior of vasculature (especially for capillaries) still can not be accurately modeled. Thus, as mentioned in the previous chapter, numerical simulation, especially for thermal simulation, is not yet fully reliable for clinical application, so field manipulation based on measurements or patient feedback during the treatment is still required. More contributive elements means more parameters are available to manipulate the field in order to avoid hotspots in healthy tissues and to concentrate higher power in the target.

The optimization of a patient's position enhances the 50%-SAR in most target regions (Figure 10.22), especially for locations 1 and 3. Location 3 received a much higher SAR in the optimized patient position while being under-dosed in the original position. More important, the optimization greatly increases the number of contributive elements for all the target regions (Figure 10.23). Figure 10.24 shows the contribution of each element for each target region. Only elements with line-of-sight contribute significantly to a given target region as the tissues are very lossy. The positioning optimization activates all the possible elements that are able to contribute significantly. However, this optimization does not significantly improve the TR for most target regions, as seen in Figure 10.25. This parameter strongly

depends on the operation frequency because it is a result of coherence. Thus, patient position has no significant influence on the TR, which also suggests that having more elements may not improve it.
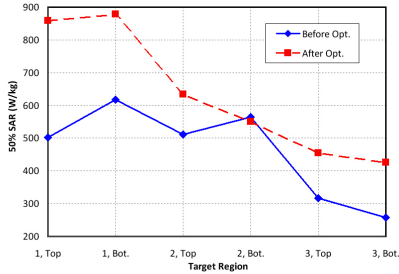
Figure 10.22: The comparison of 50%-SAR before and after the optimization of patient position (W/kg). It shows the optimization increases the exposure significantly in almost all the target regions.
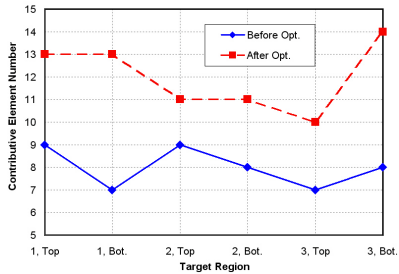
Figure 10.23: The comparison of contributive element number before and after the optimization of patient position. More contributive elements provide higher flexibility in field manipulation.
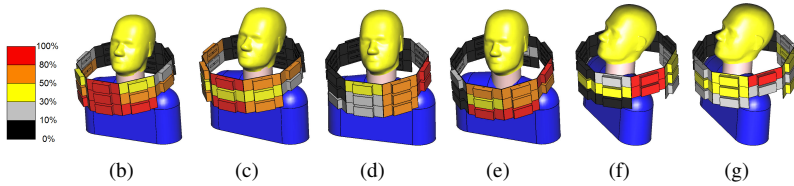
Figure 10.24: Contribution from each element when the target region is (a) location 1-top, (b) location 1-bottom, (c) location 2-top, (d) location 2-bottom, (e) location 3-top and (f) location 3-bottom. The element colors indicate the contribution level of each element after field optimization.
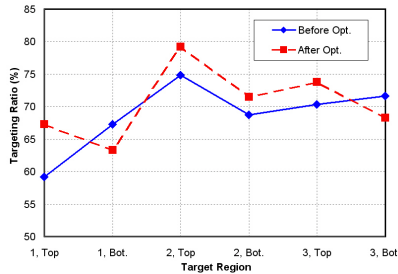
Figure 10.25: The comparison of TR (%) before and after the optimization of patient position.

10.5 Clinical Considerations

Several important issues from a clinical aspect are considered in this section. First is the treatment planning which includes the process of a HT to a patient with the proposed applicator and how a model of the applicator and an image-based model of the patient are used to determine the best settings for a treatment. Besides, simulation time is important in clinical application for arranging the treatment schedule, also too long simulation times are unacceptable for economic reasons. Finally, it is necessary to evaluate the uncertainty budget in reality. This study considers sensitivity of the patient positioning error and the uncertainty of excitation coefficients.

10.5.1   Treatment Planning

As discussed in Section 9.2.2, it is important to find out the optimum excitation coefficients of the array for concentrating EM power in the tumor, and numerical simulation plays an important role for this purpose. The treatment planning for this applicator will basically follow that suggested in [212]. Namely, for each treatment, the procedure would be:

1. Build numerical model of the patient. Simulating with every patient individually is important to obtain accurate estimation, so building CAD model of the patient is necessary as the first step. The images of the patient from a MRI or CT scanner are segmented with a commercial software, like iSEG [270]. Then each image becomes a slice of CAD model with thickness based on resolution of the scanner. The full CAD model of the patient is stack-up of the slices.

2. Simulate the scenario. The patient model will be placed in this applicator and each excitation source will be simulated individually. Then the generalized Eigenvalue method mentioned in Section 10.2.1 and Section 9.2.3 is used to optimized the combination of the E-field generated by each source and therefore the excitation coefficients.

3. Treat the patient. The patient position has to follow that in the numerical simulation. The optimization result at Step 2 is the initial setting of the excitation coefficients. During the treatment, re-optimization of the SAR distribution is needed because of the following reasons:

   • The thermal and SAR pattern are not necessarily the same (see Section 9.2.3 for more details). The optimization is SAR-based, and the thermal information usually relies on measurement clinically. Thus, the SAR distribution will be re-optimized based on thermal measurement result.

   • The simulation model may not be the same as reality. The potential differences include water bolus shape, patient's position and motion, uncertainty of magnitude and phase of each source, etc.

   • High temperature in the skin or other tissues is a typical uncomfortable feeling for the patient during the treatment. When it happens, tuning the SAR distribution is required so that the patient can finish the treatment.

Simulation results and the optimization algorithm in Step 2 are employed for the optimization. This approach is similar with the one mentioned in Section 9.2.3 adjusting SAR distribution based on the patient's feedback. This real-time optimization will be conducted during the whole treatment.

10.5.2 Simulation Time Control

EM simulations of the treatment plan are required to be completed in one night as efficient utilization of the HT facility in each hospital is important in terms of cost. However, this is a great challenge for applicators with many elements. The proposed applicator has 20 elements and so 21 simulations are required for the field optimization [238]. The total simulation time of these 21 simulations is too long for clinical requirements. In order to reduce the number of simulations without affecting hyperthermia performance, only the contributive elements for the given target region are activated and the rest of the elements are off. Thus, only 11 to 14 simulations (depending on the target regions, Figure 10.23) are required for each treatment. The 50%-SAR and TR of each target region in Figure 10.26 show no significant degradation in SAR performance when only the contributive elements are activated. Table 10.2 shows the simulation time required for each target region and all of them can be completed in about 5 hours. The simulation uses CUDA technology with S1070 configuration consisting of four C1060 graphic cards from NVIDIA [271]. The detailed simulation settings are provided in Table 10.3[5].

10.5.3 Sensitivity of Patient Positioning

Seven scenarios of mis-positioning the patient are simulated to evaluate the effect of the positioning error (Figure 10.27). The human phantom is shifted in five directions for 5 mm, and the head as well as the patient axis are tilted by 3 degrees. The target region is location 1-bottom and the parameters evaluated are:

---

[5]The current latest graphic card from NVIDIA is M2090 (with Fermi GPU) and is much faster than the C1060 model. Thus, it is expected that the simulations here can be finished in 3.5 hours instead of 5 hours.

(a)   (b)
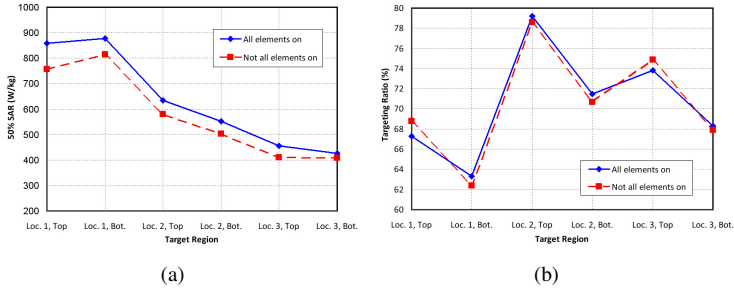
Figure 10.26: The (a) 50%-SAR and (b) TR on the target regions when all
the elements or only the contributive elements are activated.

Top locations	Location 1	Location 2	Location 3
Element Number	13	11	10
Sim. time (hours)	4.1	3.8	3.8
Bottom locations	Location 1	Location 2	Location 3
Element Number	13	11	14
Sim. time (hours)	4.1	3.5	5.1

Table 10.2: The simulation time required for the treatment in each target
region by using hardware acceleration (Element Number: the number of
elements activated.)

- Shift (mm): the shifted distance of the $psSAR_{10g}$ locations between
  that in the original and the mis-positioned scenarios.

- SAR (W/kg): the $psSAR_{10g}$ for the given scenario.

- SAR (%): the error of the $psSAR_{10g}$ between original and the mis-
  positioned scenarios.

- Spinal cord (W/kg): the $psSAR_{1g}$ on the spinal cord[6].

---

[6]$psSAR_{10g}$ is better correlated to temperature rise. However, spinal cord is thin and long,
which makes the extraction of $psSAR_{10g}$ difficult. More important, spinal cord is a critical
tissue for safety, a more conservative measure is necessary. Therefore, $psSAR_{1g}$ is used here.

Parameters	Value
Computational Domain	$46 \times 44 \times 55$ cm^3
Min. Mesh Resolution	$1 \times 1 \times 1$ mm^3
Grid Number	8.4M cells
Simulation time per element	16 - 28 minutes

Table 10.3: The settings of the simulations of the proposed applicator with the human phantom.

(a)   (b)   (c)   (d)
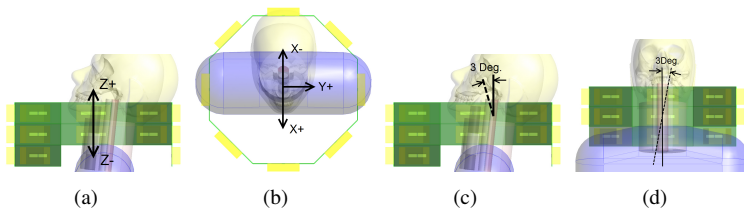
Figure 10.27: The seven scenarios for testing the sensitivity of mis-positioning the patient; the shifts in (a) patient axis (Z), (b) anterior-posterior (X) and lateral (Y) directions are 5mm, and the tilts of (c) the head and (d) the whole body are 3 degrees.

The simulation results show that a 5 mm or 3 degree positioning error is acceptable (Table 10.4). The head tilt and lateral shift (Y+) are relatively insignificant in the uncertainty budget. The mis-positioning in the anterior-posterior (X) and patient axis (Z) directions is more important. The results are consistent with those reported in [223]. In addition, besides the shifting errors, the angle of the patient body (or the applicator) also needs to be precise.

Practically, a certain level of uncertainty exists for the input amplitude and phase of each element. So, the influence of the uncertainty in hyperthermia performance is also evaluated. The scenario is the applicator with the phantom at the position for target region 1 (Figure 10.21(a)) and the power is focused on [target region 1, bottom]. The amplitude and phase of each element is randomly generated within defined uncertainty levels from 0.05 to 0.15 with 0.025 interval. The maximum input voltage is 10 V and the phase variation range is 180 degrees. For example, if the uncertainty

	Shift	SAR (W/kg)	SAR(%)	Spinal cord
Original	-	1158	-	16.5
Tilted head	0.0	1154	-0.3	14.7
Tilted body	8.3	1162	0.3	18.0
Z+	8.3	1107	-4.4	17.4
Z-	4.0	1212	4.7	16.1
X-	12.6	1076	-7.1	17.8
X+	5.3	1131	-2.3	17.3
Y+	3.6	1161	0.3	17.0

Table 10.4: The simulation results for the seven scenarios defined in Figure 10.27 for the positioning sensitivity analysis.

level is 0.1, the variations in amplitude and phase are ±0.5 V and ±9 degrees, respectively. For each level of uncertainty, the random values are set on three configurations, that is, amplitude-only, phase-only and amplitude-and-phase. If the original excitation coefficient is [8V, 30Deg.] with 0.1 uncertainty, the input amplitude and phase are random values in [8±0.5 V, 30 Deg.] for amplitude-only, [8 V, 30±9 Deg.] for phase-only and [8±0.5 V, 30±9 Deg.] for amplitude-and-phase, respectively. Each configuration has 20 simulations for each level of uncertainty. The evaluated parameter is the percentage error of $psSAR_{10g}$.

Simulation results are represented as standard deviation of the error, as seen in Figure 10.28. The error is relatively linear to the uncertainty level for the three configurations. The phase error has a slightly more significant influence than the amplitude error. The $psSAR_{1g}$ cumulative histogram of [target region 1, bottom] of the worst cases for the three configurations at 0.15 uncertainty is shown in Figure 10.29. It shows that the SAR distribution is changed significantly when both amplitude and phase vary and unwanted hot spots emerge in this case. Therefore, based on the simulation results, if a 10% error is considered, the uncertainty of amplitude and phase should be lower than 0.125 (±7-8% in terms of power) and 0.1 (±18 Deg.), respectively.
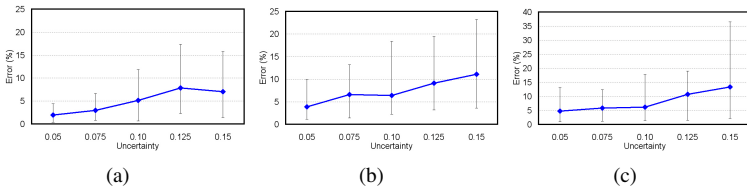
Figure 10.28: The standard deviation of $psSAR_{10g}$ error with different levels of uncertainty in terms of (a) amplitude, (b) phase and (c) amplitude and phase.
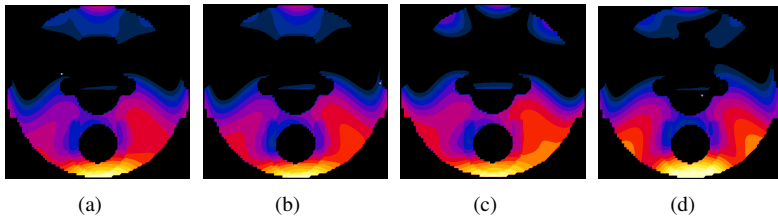
Figure 10.29: The SAR distribution in the neck when (a) having original settings and the worst-cases in (b) Figure 10.28(a), (c) Figure 10.28(b) and Figure 10.28(c), respectively. Each color step indicates one dB difference.

10.6 Validation

10.6.1 Performance With A Real Patient Model

In addition to the simplified human phantom, the proposed applicator was simulated with the model of a real cancer patient derived from [212] (Figure 10.30(a)). As the tumor is at [target region 1, bottom] (defined in Figure 10.5), the patient is placed as shown in Figure 10.30(b).

The simulation results are represented in three different ways. First is the gray iso-surface representing a $psSAR_{1g}$ value of 200 W/kg (Figure 10.31(a)). The surface almost covers the entire tumor, demonstrating that the applicator accurately targets the power on the tumor. Figure 10.31(b) shows a sagittal view of the $psSAR_{1g}$ distribution in the patient. It is clear that the applicator heats the tumor effectively without inducing a

(a)   (b)
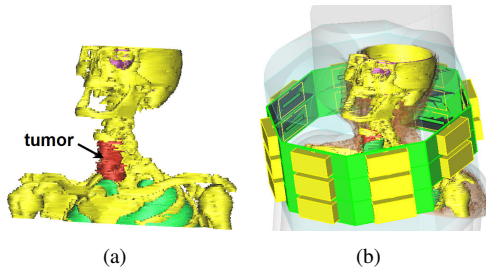
Figure 10.30: (a) The real patient model and (b) the configuration of the applicator with the patient.

high SAR in the spinal cord. Finally, the statistical results of the SAR performance of this treatment are shown in Table 10.5. The SAR ratio is the defined as the ratio of the psSAR_{1g} in the tumor and in the healthy tissues. The results confirm that the EM power is well concentrated on the tumor. The power delivered by each element is listed in Table 10.6 and shows that the activated elements are utilized efficiently. The three activated elements in the third ring deliver very higher power (more than 74%) and this endorses the importance of the third ring in this applicator design.

(a)   (b)
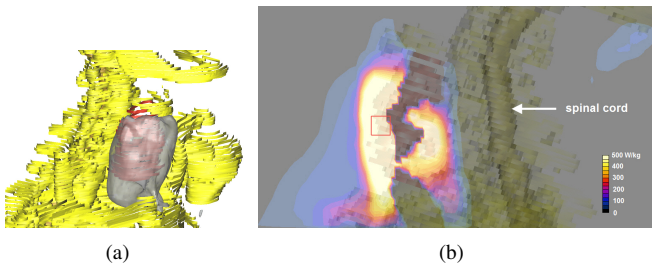
Figure 10.31: (a) The gray iso-surface represents a psSAR_{1g} value of 200 W/kg. It shows that almost the entire tumor is illuminated with sufficient EM power. (b) The psSAR_{1g} distribution in the patient (W/kg) shows that the power is concentrated in the tumor without heating other tissues.

Parameters	Values
50%-SAR of the tumor	424 W/kg
90%-SAR of the tumor	144 W/kg
Targeting Ratio (TR)	61.8%
200 W/kg $psSAR_{1g}$ coverage on the tumor	83.7%
$psSAR_{1g}$ of the spinal cord	17.8 W/kg
SAR ratio	0.984
Total simulation time	7.1 hours

Table 10.5: The simulation results of the applicator with a real patient model in terms of $psSAR_{1g}$

Element	1	2	3	4	5	6	7	8
Input power	100	91.2	16.5	off	off	off	17.7	59.3
Element	9	10	11	12	13	14	15	16
Input power	26.3	55.3	30.3	off	off	off	56.6	85.4
Element	17	18	19	20	-	-	-	-
Input power	63.1	off	50.8	87.1	-	-	-	-
Total power				740W				

Table 10.6: The power delivered by each element (W) in the simulation with the real patient model.

10.6.2 Measurement Results

The applicator proposed in this study was also manufactured for a validation study, as seen in Figure 10.32. There are 24 elements; three rings with 8 elements on each ring. The dimensions the applicator follow those shown in Figure 10.7 and Figure 10.9. Each element is fed with a coaxial cable. The cylindrical phantom and the water bolus is filled with body simulating liquid (BSL) at 450 MHz and deionized water, respectively. The permittivity and conductivity of the BSL is 79.5 and 0.047 at 450 MHz, respectively. The mutual coupling between two elements was measured and simulated to validate the simulation results used above. A two-port vector network analyzer (VNA) was connected to the elements measured while the rest are loaded with 50 Ohm resistors.

In order to evaluate the worst case of mutual coupling, the two elements measured are assumed to have simultaneous conjugate matching [111], as il-
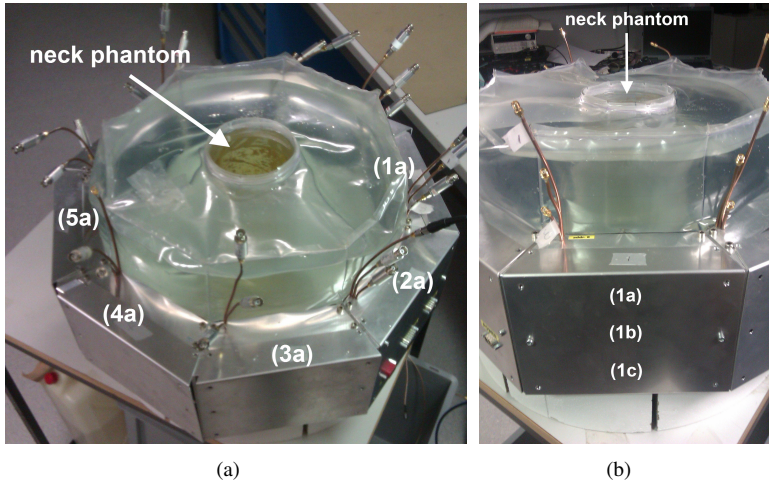
Figure 10.32: The manufactured applicator for measurement validation.

lustrated in Figure 10.33. $\mathbf{S}^{ij}$ is the two-port S-matrix of ith and jth element by measurement or simulation. $\mathbf{S}^i$ and $\mathbf{S}^j$ represent the matching circuits making both ith and jth element have conjugate matching[7]. $\mathbf{S}^{\text{tot}}$ is the total S-matrix of the three networks, and the mutual coupling in $\mathbf{S}^{\text{tot}}$ is named as maximum mutual coupling (MMC). The magnitude of MMC between element *1a* and the other elements are shown in Figure 10.34. Similar with the simulation results above, the highest MMC occurs between element *1a* and *1b* while the rest of results are lower than -20 dB. Thus, the MMC(*1a*, *1b*) are used in the validation between simulation and measurement.

The simulation model is shown in Figure 10.35, which is based on the CAD file of the manufactured applicator. Figure 10.36 shows the magnitude and phase of MMC(*1a*, *1b*) in both simulation and measurement. The results agree well with each other in both magnitude and phase. The small discrepancy should be due to the uncertainty of the water-bolus shape in measurement. The water bolus in a different shape leads it a different scattering environment and therefore different mutual coupling results. In ad-

---

[7]The matching circuit is composed of a quarter-wavelength transformer and a parallel reactance which can be realized with an open or short stub.
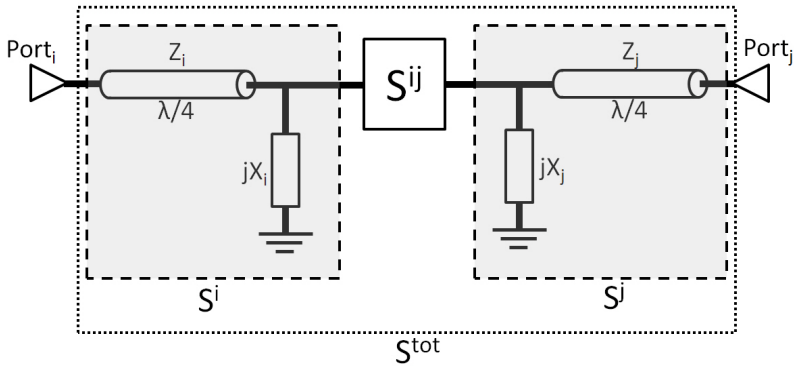
Figure 10.33: The mutual coupling between Port$_i$ and Port$_j$ is measured when both ports have conjugate matching simultaneously.
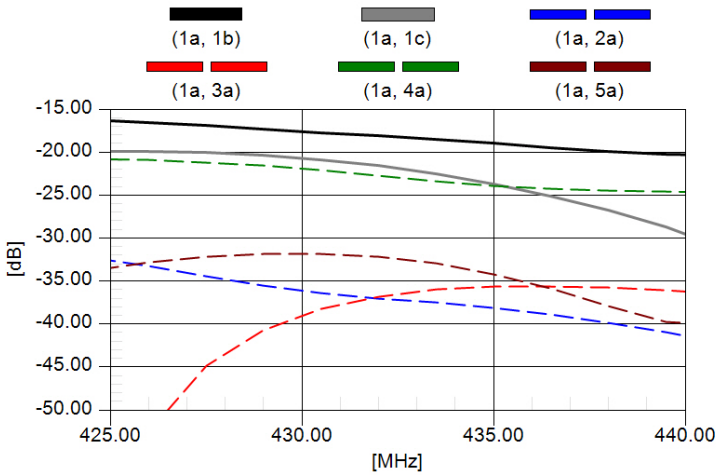
Figure 10.34: The maximum mutual coupling between element *1a* and the other elements (see Figure 10.32 for the definition of the elements).

dition, the uncertainty in synchronization of the reference position of the simulation and measurement results can cause error in the phase of MMC.
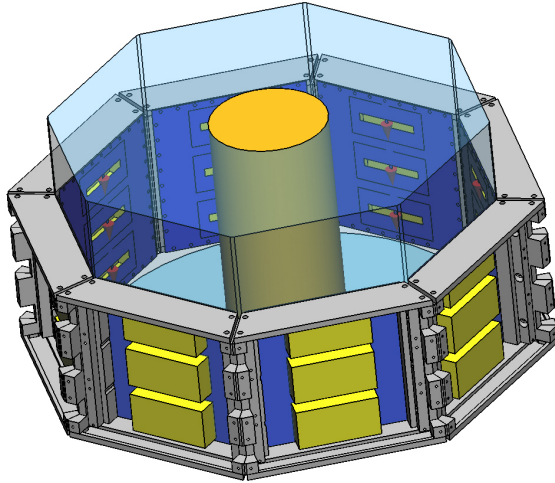
Figure 10.35: The numerical model of the manufactured applicator.

| (a) | (b) |
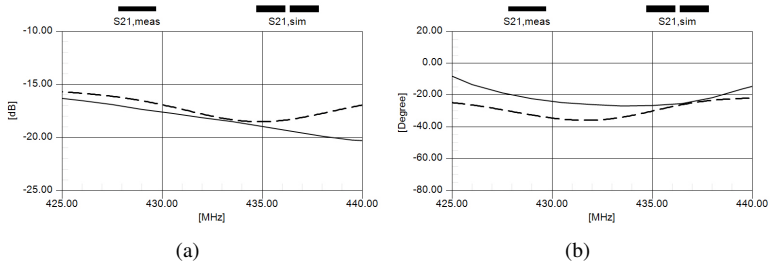
Figure 10.36: The (a) magnitude and (b) phase of maximum mutual coupling between element *1a* and *1b* (MMC(*1a*, *1b*)). The measurement and simulation model are shown in Figure 10.32 and Figure 10.35, respectively.

10.7 Discussion

This design exhibits improvement compared to HYPERcollar. The radiating elements are slot antennas whose planar structure ensures precise manufacture and robust mechanical strength against water bolus. Because of low mu-

tual coupling between slot antennas, the total number of elements has been greatly increased from 12 to 20. Thus, steering the SAR distribution becomes more flexible and hence it is possible to heat a tumor more uniformly with higher power. Additionally, this design does not need to have staggered arrangement to reduce mutual coupling so more elements are placed in front of the patient. Moreover, the design has been further refined. Patient's position is optimized based on the tumor location. Human anatomy is higher inhomogeneous and has complex geometry. Having many elements does not necessarily mean better heating performance as there may be only a few of element provide significant contribution. The goal of the positioning optimization is to have as many elements as possible having significant contribution. This optimization is missing in all of the previous designs.

Chapter 11

Conclusion of the Hyperthermia Study

The studies about hyperthermia treatment (HT) in this thesis focus on the technology using noninvasive electromagnetic power, and they are the review of HT technology and a novel design of phased array for head and neck region. Before the studies, the biological rationale and clinical trials of hyperthermia treatment has been briefly introduced to report the medical background of this application.

The technology of hyperthermia treatment using non-invasive electromagnetic power has been reviewed in this report. The biological rationale of hyperthermia treatment and the clinical trials are also reported. The review of the biological rationale shows that hyperthermia is an effective adjuvant modality to standard treatments (radiotherapy and chemotherapy) for some types of cancer, such as tumors in the head and neck region, breast cancer, melanoma and cervical cancer. In addition, thermal dosimetry has also been highlighted as one of the principal issues of public acceptance and clinical application. Thus, indicators that might link the thermal dose and clinical response have been summarized.

The review of the techniques is divided in three parts: low frequency approaches, phased array and other methods. Most low frequency applicators were designed in the 1980s. Due to the penetration depth and engineering difficulties, these applicators, usually with a single element, are operated

at a frequency lower than about 100MHz. However, unexpected hot and cold spots frequently appear in healthy tissues and the cancer, respectively, with these applicators, and so many more recent studies have focused on applicators using multiple antennas, or the phased array, at higher frequency. The phased array is much better at manipulating EM fields and creating coherence, but its engineering is also much more complicated. For superficial hyperthermia, phased array has conformal coverage of a large area with uniform SAR distribution. The applicators are also designed for different regions, such as the head and neck region, the abdomen and pelvic region, the brain, extremities and the breast. In addition to hardware design, algorithms for optimizing excitation coefficients are also critical in deep-region hyperthermia. Optimization algorithms include the generalized Eigenvector method, model order reduction, and algorithms based on temperature measurement with magnetic resonance thermometry. In addition to the two major concepts (low frequency and phased array), other methods are also proposed. These methods include the application of lenses, reflectors and ultrawide-band (UWB) microwave. Lenses, artificial geometry or metamaterial, are added between the radiators and the patient to concentrate power. Reflectors are applied to surround the radiators and the treated region, and they act as a continuous array to generate field concentration. The technique of UWB microwave in breast-tumor imaging is applied in a phased array to heat tumors in deep regions of the breast instead of using a single frequency or narrow band.

Several general issues have been discussed. First, the applicators reviewed in this report are summarized. Secondly, the reasons for using a water bolus in almost all non-invasive applicator designs are discussed. Finally, because hyperthermia treatment is a highly interdisciplinary application, the challenges encountered and the expertise required in engineering aspects are also summarized.

Besides, a novel applicator for hyperthermia treatment of cancer in the head and neck region has been proposed. The design is a 40cm diameter circular array consisting of 20 cavity-backed slot antennas surrounding the patient. Both the applicator design and the patient's position have been optimized for different target regions. The simulation results show that the applicator can provide sufficient exposure to all possible locations of a tumor in the neck of a patient with good targeting of EM power. Clinical issues have also been considered, i.e. patient positioning error, excitation coefficients uncertainty and simulation time control. Finally, an actual pa-

tient model was used to observe the performance of the proposed applicator in real usage.

The proposed applicator has the following advantages over previous designs:

- The cavity-backed slot antennas provide excellent mechanical strength against pressure and erosion due to the water.

- The elements in the additional third ring make a significant contribution, so more elements are available in each treatment.

- Comfort issues are taken care of by adding air masks on the patient's head and shoulders.

- Optimization of patient position for different target regions significantly increases the performance of the applicator.

However, several issues still need to be considered. First of all, full validation of the manufactured applicator is required. In addition to mutual coupling, it is also important to validate the SAR distribution due to different schemes of power concentration. Besides, it is necessary to evaluate the practical feasibility of the air masks for the patient. Last but not least, tumors in the head, such as those in the tongue and the nasal cavity, have not been considered in this study. These will be more difficult to heat because they are covered by the skull or mandible.

Appendix A

List of Acronyms

ABC	Absorbing Boundary Condition
ALT	All Lumen Temperature
CAD	Computer Aided Design
CEM	Cumulative number of Equivalent Minutes
CTIA	Cellular Telecommunications & Internet Association
CT	Chemotherapy or Computer Tomography
CPU	Central Processing Unit
CPML	Convolutional Perfect Matching Layer
CPW	Co-Planar Waveguide
DCS	Digital Cellular System
DPD	Dissipated Power Density
EFS	Effective Field Size
EM	Electromagnetic
E-field	Electrical field
FDTD	Finite-Difference Time-Domain
GA	Genetic Algorithm
GSM	Global System for Mobile Communications

GPU	Graphic Processing Unit
H&N	Head and Neck
HTSL	Head Tissue Simulating Liquid
HT	Hyperthermia Treatment
H-field	magnetic field
IT'IS	Foundation for Information Technologies in Society
ISM	Industry, Science and Medicine
LACC	Locally Advanced Cervical Cancer
MCells	Million Cells
MF	Microwave Frequency
MIMO	Multiple-Input and Multiple-Output
MRI	Magnetic Resonance Imaging
MRT	Magnetic Resonance Thermometry
MUT	Models Under Test
OTA	Over-The-Air
PCB	Printed Circuit Board
PDA	Personal Digital Assistant
PEC	Perfect Electric Conductor
PIFA	Planar Inverted-F Antenna
PML	Perfectly Matched Layer
psSAR	peak spatial Specific Absorption Rate
psSAR10g	peak spatial Specific Absorption Rate averaged over 10 g
RCS	Radar Cross Section
RF	Radiofrequency
RMS	Root Mean Square
RT	Radiotherapy
S-Parameter	Scattering-Parameter
SAM	Specific Anthropomorphic Mannequin

SAR	Specific Absorption Rate
SAT	Subcutaneous Adipose Tissue
SEMCAD	Simulation Platform for Electromagnetic Compatibility Antenna Design and Dosimetry
SH	Superficial Hyperthermia
SMA	SubMiniature version A
SMS	Short Message Service
SPEAG	Schmid & Partner Engineering AG
TEM	Transverse Electric and Magnetic
TE	Transverse Electric
TM	Transverse Magnetic
TIS	Total Isotropic Sensitivity
TR	Target Ratio
TRP	Total Radiated Power
UPML	Uni-axial Perfect Matching Layer
VNA	Vector Network Analyzer
WACOA	WAter COated Antenna
WLAN	Wireless Local Area Network

Bibliography

[1] R. W. P. King, G. S. Smith, M. Owens, and T. T. Wu. *Antennas in matter*. The MIT Press, 1981.

[2] J.D. Irving and R.J. Knight. Numerical simulation of antenna transmission and reception for crosshole ground-penetrating radar. *Geophysics*, 71(2):K37, 2006.

[3] K.J. Ellefsen and D.L. Wright. Radiation pattern of a borehole radar antenna. *Geophysics*, 70(1):K1, 2005.

[4] I.F. Akyildiz and E.P. Stuntebeck. Wireless underground sensor networks: Research challenges. *Ad Hoc Networks*, 4(6):669–686, 2006.

[5] A. Rosen, M.A. Stuchly, and A. Vander Vorst. Applications of RF/microwaves in medicine. *IEEE Transactions on Microwave Theory and Techniques*, 50(3):963–974, 2002.

[6] P.S. Hall and Y. Hao. *Antennas and propagation for body-centric wireless communications*. Artech House antennas and propagation library. Artech House, 2006.

[7] J. Kim and Y. Rahmat-Samii. Implanted antennas inside a human body: Simulations, designs, and characterizations. *IEEE Transactions on Microwave Theory and Techniques*, 52(8):1934–1943, 2004.

[8] Y. Rahmat-Samii and J. Kim. *Implanted antennas in medical wireless communications*. Synthesis Lectures on Antennas And Propagation. Morgan & Claypool Publishers, 2006.

[9] F. Merli, B. Fuchs, J.R. Mosig, and A.K. Skrivervik. The Effect of Insulating Layers on the Performance of Implanted Antennas. *IEEE Transactions on Antennas and Propagation*, (99):21–31, 2011.

[10] R. Paknys. Uniform asymptotic formulas for the creeping wave field on or off a cylinder. *IEEE Transactions Antennas Propagation*, 41:10991104, Aug. 1993.

[11] T. Huang and K. R. Boyle. User interaction studies on handset antennas. In *The Second European Conference on Antennas and Propagation*, pages 1–6, Nov. 2007.

[12] CTIA test plan for mobile station over the air performance, revision 3.0. *CTIA Wireless Association*, Apr. 2009.

[13] User Equipment (UE) / Mobile Station (MS) Over The Air (OTA) antenna performance. *3rd Generation Partnership Project*, Aug. 2007.

[14] IEEE. IEEE recommended practice for determining the peak spatial-average specific absorption rate (SAR) in the human head from wireless communications devices: Measurement techniques. *IEEE Standard 1528*, pages 1–149, 2003.

[15] Human exposure to radio frequency fields from hand-held and body-mounted wireless communication devices - human models, instrumentation, and procedures - part 2: Procedure to determine the specific absorption rate (SAR) for wireless communication devices used in close proximity to the human body (frequency range of 30 MHz to 6 GHz). *IEC 62209-2*, Feb. 2010.

[16] R. L. Magin and A. F. Peterson. Noninvasive microwave phase arrays for local hyperthermia: a review. *Internation Journal of Hyperthermia*, 5(4):429–450, 1989.

[17] SEMCAD X: EM/T Simulation Platform. www.semcad.com.

[18] K.L. Shlager and J.B. Schneider. A selective survey of the finite-difference time-domain literature. *IEEE Antennas and Propagation Magazine*, 37(4):39–57, 1995.

[19] A. Taflove and S. C. Hagness. *Computational Electrodynamics: The Finite-Difference Time-Domain Method, Third Edition*. Artech House.

[20] W. Yu, X. Yang, Y. Liu, and R. Mittra. *Electromagnetic Simulation Techniques Based on the FDTD Method*. Wiley Series in Microwave and Optical Engineering. Wiley, 2009.

[21] H. King and J. Wong. Effects of a human body on a dipole antenna at 450 and 900 MHz. *IEEE Transactions on Antennas and Propagation*, 25(3):376 – 379, May 1977.

[22] G. Smith. Directive properties of antennas for transmission into a material half-space. *IEEE Transactions on Antennas and Propagation*, 32(3):232–246, Mar. 1984.

[23] S. J. Radzevicius, C.-C. Chen, L. Peters, and J. J Danielsc. Near-field dipole radiation dynamics through FDTD modeling. *Journal of Applied Geophysics*, 52:75–91, 2002.

[24] B. D.Popovic and V. V. Petrovic. Horizontal wire antenna above lossy half-space: Simple accurate image solution. *International Journal of Numerical Modelling: Electronic Networks, Devices and Fields*, 9:191–199, 1996.

[25] R. S. Elliot. *Antenna Theory and Design*. Wiley, 2003.

[26] T. T. Wu, R. W. P. King, and D. V. Giri. The insulated dipole antenna in a relatively dense medium. *Radio Science*, 8(7):699–709, July 1973.

[27] T. Wu, L. Shen, and R. W. P. King. The dipole antenna with eccentric coating in a relatively dense medium. *IEEE Transactions on Antennas and Propagation*, 23(1):57 – 62, Jan. 1975.

[28] R. W. P. King. The many faces of the insulated antenna. *Proceedings of the IEEE*, 64(2):228 – 238, Feb. 1976.

[29] T. W. Hertel and G. S. Smith. The insulated linear antenna-revisited. *IEEE Transactions on Antennas and Propagation*, 48(6):914 –920, June 2000.

[30] R. J. Lytle and E. F. Laine. Design of a miniature directional antenna for geophysical probing from boreholes. *IEEE Transactions on Geoscience Electronics*, 16(4):304 –307, Oct. 1978.

[31] S. Gabriel, R. W. Lau, and C. Gabriel. The dielectric properties of biological tissues: II. Measurements in the frequency range 10 Hz to 20 GHz. *Physics in Medicine and Biology*, 41:2251 2269, 1996.

[32] S. Gabriel, R. W. Lau, and C. Gabriel. The dielectric properties of biological tissues: III. Parametric models for the dielectric spectrum of tissues. *Physics in Medicine and Biology*, 41(11):2271 2293, Nov. 1996.

[33] S. Koulouridis and K. S. Nikita. Study of the coupling between human head and cellular phone helical antennas. *IEEE Transactions on Electromagnetic Compatibility*, 46(1):62 – 70, Feb. 2004.

[34] N. Kuster and Q. Balzano. *Mobile communications safety, Chapter 2*. Chapman and Hall, 1997.

[35] A. Alexiou, P. Kostarakis, and V. N. Christoflakis. Interaction between GSM handset helical antenna and users head: Theoretical analysis and experimental results. *The Environmentalist*, 25:215–221, 2005.

[36] T. Zervosi, A. A. Alexandridis, V V. Petrovic, K. P. Dangakis, B. M. Kolundzija, A R. Djordjevic, and C F. Soras. Mobile phone antenna performance and power absorption in terms of handset size and distance from users head. *Wireless Personal Communications*, 33:109–120, 2005.

[37] M. Sager, M. Forcucci, and T. Kristensen. A novel technique to increase the realized efficiency of a mobile phone antenna placed beside a head-phantom. In *IEEE Antennas and Propagation Society International Symposium*, volume 2, pages 1013 – 1016 vol.2, 2003.

[38] N. Kuster and Q. Balzano. Energy absorption mechanism by biological bodies in the near field of dipole antennas above 300 MHz. *IEEE Transactions on Vehicular Technology*, 41(1):17 –23, Feb. 1992.

[39] A. Christ, T. Samaras, A. Klingenbck, and N. Kuster. Characterization of the electromagnetic near-field absorption in layered biological tissue in the frequency range from 30 MHz to 6000 MHz. *Physics in Medicine and Biology*, 51:4951–4966, 2006.

[40] M. D. Foegelle, K. Li, A. Pavacic, and P. Moller. The development of a standard hand phantom for wireless performance testing: Part 2. *Wireless Design and Development*, 2010.

[41] C. Gabriel. Tissue equivalent material for hand phantoms. *Physics in Medicine and Biology*, 52:4205–4210, July 2007.

[42] C.-H. Li, E. Ofli, N. Chavannes, and N. Kuster. Effects of hand phantom on mobile phone antenna performance. *IEEE Transactions on Antennas and Propagation*, 57(9):2763–2770, Sep. 2009.

[43] ICNIRP. Guidelines for limiting exposure to time-varying electric, magnetic and electromagnetic fields (up to 300 GHz). *Health Physics*, 74:494 – 522, 1998.

[44] IEEE std. c95.1b - 2005 IEEE standard for safety levels with respect to human exposure to radio frequency electromagnetic fields, 3 kHz to 300 GHz. *International Committee on Electromagnetic Safety, The Institute of Electrical and Electronics Engineers*, 2005.

[45] FCC. Evaluating compliance with FCC guidelines for human exposure to radiofrequency electromagnetic fields, additional information for evaluating compliance of mobile and portable devices with FCC limits for human exposure to radiofrequency emissions. *Federal Communications Commission Office of Engineering and Technology Supplement C to OET Bulletin 65*, Jun. 2001.

[46] Q. Balzano, O. Garay, and T. Manning. Electromagnetic energy exposure of the users of portable cellular telephones. *IEEE Transactions on Vehicular Technology*, 44(3):390–403, 1995.

[47] K. A. Meier. *Scientific bases for dosimetric compliance tests on mobile telecommunications equipment*. PhD thesis, Swiss Federal Institute of Technology Zurich, ETHZ, 1996.

[48] N. Kuster, R. Kastle, and T. Schmid. Dosimetric evaluation of hand-held mobile communications equipment with known precision. *IEICE transactions on communications*, pages 645–652, 1997.

[49] F. Meyer, K. Palmer, and U. Jakobus. Investigation into the accuracy, efficiency and applicability of the method of moments as numerical dosimetry tool for the head and hand of a mobile phone user. *Applied Computational Electromagnetics Society Journal*, 16:114–125, 2001.

[50] M. Okoniewski and M. A. Stuchly. A study of the handset antenna and human body interaction. *IEEE Transactions on Microwave Theory and Techniques*, 44(10):1855 –1864, Oct. 1996.

[51] M. Francavilla, A. Schiavoni, P. Bertotto, and G. Richiardi. Effect of the hand on cellular phone radiation. *IEE Proceedings - Microwaves, Antennas and Propagation*, 148(4):247 –253, August 2001.

[52] M. Francavilla and A. Schiavoni. Effect of the hand in SAR compliance tests of body worn devices. In *The Applied Computational Electromagnetics Society Conference*, 2007.

[53] S. I. Al-Mously and A. Z. Abdalla. Hand implications on the coupling between human head and different cellular phones. pages 355 –358, Oct. 2009.

[54] O. Kivekas, J. Ollikainen, T. Lehtiniemi, and P. Vainikainen. Bandwidth, SAR, and efficiency of internal mobile phone antennas. *IEEE Transactions on Electromagnetic Compatibility*, 46(1):71–86, Feb. 2004.

[55] S. I. Al-Mously and M. M. Abousetta. Anticipated impact of handhold position on the electromagnetic interaction of different antenna types/positions and a human in cellular communications. *International Journal of Antennas and Propagation*, 2008, 2009.

[56] *iSAR2 System Handbook*. Schmid & Partner Engineering AG, Zurich. www.speag.com, Nov. 2009.

[57] G. F. Pedersen, K. Olesen, and S. L. Larsen. Bodyloss for handheld phones. In *1999 IEEE 49th Vehicular Technology Conference*, volume 2, pages 1580 –1584 vol.2, July 1999.

[58] K. R. Boyle. The performance of GSM 900 antennas in the presence of people and phantoms. *Twelfth International Conference on Antennas and Propagation*, 1(491):35–38, 2003.

[59] J. Krogerus, J. Toivanen, C. Icheln, and P. Vainikainen. Effect of the human body on total radiated power and the 3-D radiation pattern of mobile handsets. *IEEE Transactions on Instrumentation and Measurement*, 56(6):2375–2385, Dec. 2007.

[60] K.-L. Wong, C.-H. Wu, W.-Y. Li, C.-M. Su, S.-H. Yeh, and C.-L. Tang. Simplified hand model for the study of hand-held device antenna. *IEEE Antennas and Propagation Society International Symposium*, pages 2101–2104, July 2006.

[61] M. Lundmark, R. S. Calvo, P.-S. Kildal, and C. Orlenius. A solid hand phantom for mobile phones and results of measurements in reverberation chamber. In *IEEE Antennas and Propagation Society International Symposium*, volume 1, pages 719 – 722, 2004.

[62] J. Toftgard, S. N. Hornsleth, and J. B. Andersen. Effects on portable antennas of the presence of a person. *IEEE Transactions on Antennas and Propagation*, 41(6):739 –746, Jun. 1993.

[63] M. A. Jensen and Y. Rahmat-Samii. EM interaction of handset antennas and a human in personal communications. *Proceedings of the IEEE*, 83(1):7 –17, jan 1995.

[64] S.Watanabe, M. Taki, T. Nojima, and O. Fujiwara. Characteristics of the SAR distribution in a head exposed to electromagnetic fields radiated by a hand-held portable radio. *IEEE Transactions on Microwave Theory and Techniques*, 44(10):1874–1883, Oct. 1996.

[65] K. R. Boyle, Y. Yun, and L. P. Ligthart. Analysis of mobile phone antenna impedance variations with user proximity. *IEEE Transactions on Antennas and Propagation*, 55:364–372, Feb. 2007.

[66] U. Navsariwala. Accurate and efficient models of the human hand for the prediction of antenna efficiency in mobile devices. *IEEE Antennas and Propagation International Symposium*, pages 1044–1047, June 2007.

[67] P. Futter, N. Chavannes, R. Tay, M. Meili, A. Klingenboeck, K. Pokovic, and N. Kuster. Reliable prediction of mobile phone performance under real usage conditions using the FDTD method. *Proceeding International Symposium on Antenna and Propagation*, pages 355–358, 2005.

[68] C.-M. Su, C.-H. Wu, K.-L. Wong, S.-H. Yeh, and C.-L. Tang. User's hand effects on EMC internal GSM/DCS mobile phone antenna. *IEEE Antennas and Propagation Society International Symposium*, pages 2097–2100, July 2006.

[69] M. Pelosi, O. Franek, G. F. Pedersen, and M. Knudsen. User's impact on PIFA antennas in mobile phones. In *IEEE 69th Vehicular Technology Conference*, pages 1–5, Apr. 2009.

[70] M. Pelosi, O. Franek, M. B. Knudsen, and G. F. Pedersen. Influence of dielectric loading on PIFA antennas in close proximity to user's body. *Electronics Letters*, 45(5):246–247, 2009.

[71] M. Pelosi, O. Franek, M. B. Knudsen, and G. F. Pedersen. Hand phantoms for browsing stance in mobile phones. In *IEEE Antennas and Propagation Society International Symposium*, pages 1–4, June 2009.

[72] E. Ofli, C.-H Li, N. Chavannes, and N. Kuster. Analysis and optimization of mobile phone antenna radiation performance in the presence of head and hand phantoms. *Turkish Journal of Electrical Engineering and Computer Sciences*, 16:67–77, 2008.

[73] K.-L. Wong and C.-H. Chang. On-board small-size printed monopole antenna integrated with USB connector for penta-band WWAN mobile phone. *Microwave and Optical Technology Letters*, 52:2523–2527, Nov. 2010.

[74] K.-L. Wong and C.-T. Lee. Wideband surface-mount chip antenna for eight-band LTE/WWAN slim mobile phone application. *Microwave and Optical Technology Letters*, 52:2554–2560, 2010.

[75] S.-C. Chen and K.-L. Wong. Small-size 11-band LTE/WWAN/WLAN internal mobile phone antenna. *Microwave and Optical Technology Letters*, 52:2603–2608, 2010.

[76] T. M. Greiner. Hand anthropometry of U.S. Army personnel. *United States Army Natick Research, Development and Engineering Center*, Dec. 1991.

[77] Alvin R. Tilley and Henry Dreyfuss Associates. *The Measure of Man & Woman: Human Factors in Design, Revised Edition*. Wiley, 2002.

[78] B. Buchholz, T. J. Armstrong, and S. A. Goldstein. Anthropometric data for describing the kinematics of the human hand. *Ergonomics*, 35(3):261–273, Mar. 1992.

[79] W. D. Bugbee and M. J. Bottm. Surface anatomy of the hand : the relationships between palmar skin creases and osseous anatomy. *Clinical orthopaedics and related research*, (296):122–126, 1993.

[80] M. Pelosi, O. Franek, M. B. Knudsen, M. Christensen, and G. F. Pedersen. A grip study for talk and data modes in mobile phones. *IEEE Transactions on Antennas and Propagation*, 57(4):856–865, Apr. 2009.

[81] H.-R. Chuang. Human operator coupling effects on radiation characteristics of a portable communication dipole antenna. *IEEE Transactions on Antennas and Propagation*, 42(4):556 –560, April 1994.

[82] K. Sato, K. Nishikawa, N. Suzuki, and A. Ogawa. Analysis of antennas mounted on portable equipment near the human body. *Electronics and Communications in Japan (Part I: Communications)*, 80:5463, 1997.

[83] M. A. Ebrahimi-Ganjeh. Interaction of dual band helical and PIFA handset antennas with human head and hand. *Progress In Electromagnetics Research*, 77:225–242, 2007.

[84] N. Igi, H. Hanaoka, and H. Arai. Antenna gain measurement of hand held terminal at 900 MHz. In *IEEE Antennas and Propagation Society International Symposium*, volume 1, pages 274 –277 vol.1, June 1994.

[85] N. T. Atanasov and G. L. Atanasova. An investigation of the effects from the users hand and head over received level and adaptive power control of a GSM mobile phone in typical operating environment. *The Environmentalist*, 27(4):585–591, Dec. 2007.

[86] P. Vainikainen, J.Ollikainen, O. Kivekas, and K. Kelander. Resonator-based analysis of the combination of mobile handset antenna and chassis. *IEEE Transactions on Antennas and Propagation*, 50:1433–1444, Oct. 2002.

[87] J. Krogerus, C. Icheln, and P. Vainikainen. Effect of human body on 3-D radiation pattern and efficiency of mobile handsets. In *Proceedings of the IEEE Instrumentation and Measurement Technology Conference*, volume 1, pages 271 –276, May 2005.

[88] G.F. Pedersen, M. Tartiere, and M.B. Knudsen. Radiation efficiency of handheld phones. *IEEE 51st Vehicular Technology Conference Proceedings*, 2:1381 – 1385, 2000.

[89] K. Ogawa, T. Takahashi, Y. Koyanagi, and K. Ito. Automatic impedance matching of an active helical antenna near a human operator. In *33rd European Microwave Conference*, volume 3, pages 1271 – 1274 Vol.3, 2003.

[90] H. Morishita, H. Furuuchi, and K. Fujimoto. Performance of balance-fed antenna system for handsets in the vicinity of a human head or hand. *IEE Proceedings - Microwaves, Antennas and Propagation*, 149(2):85 –91, April 2002.

[91] D. Manteuffel. A concept to minimize the user interaction of mobile phones. In *IEE Antenna Measurements and SAR*, pages 1 – 4, May 2004.

[92] S.-J. Kim, K.-H. Kong, M.-J. Park, Y.-S. Chung, and B. Lee. Design concept of a mobile handset antenna to mitigate user's hand effect. *Microwave and Optical Technology Letters*, 50:2696–2698, Jul. 2008.

[93] J.-M. Jung, S.-J. Kim, K.-H. Kong, J.-S. Lee, and B.-J. Lee. Designing ground plane to reduce hand effects on mobile handsets. *IEEE Antennas and Propagation International Symposium*, pages 1040–1043, June 2007.

[94] S. Myllymaki, A. Huttunen, V. Palukuru, and H. Jantunen. Capacitive recognition on the user's hand grip position in mobile handsets. *Progress In Electromagnetic Research*, 22:203–220, 2010.

[95] K. R. Boyle, Z. Liu, T. Huang, Y. Sun, A. Simin, E. Spits, O. Kuijken, and T. Roedle. A multi-band, dual-antenna and antenna interface module system for mobile phones. In *International Workshop on Antenna Technology: Small and Smart Antennas Metamaterials and Applications*, pages 53 –56, 2007.

[96] T. Nishikido, Y. Saito, M. Hasegawa, H. Haruki, Y. Koyanagi, and K. Egawa. Multi-antenna system for a handy phone to reduce influence by user's hand. *6th International Symposium on Antennas, Propagation and EM Theory*, pages 348–351, Oct. 2003.

[97] F. Harrysson, J. Medbo, A. Molisch, A. Johansson, and F. Tufvesson. Efficient experimental evaluation of a MIMO handset with user influence. *IEEE Transactions on Wireless Communications*, 9(2):853 –863, Feb. 2010.

[98] N. Chavannes, R. Tay, N. Nikoloski, and N. Kuster. Suitability of FDTD based TCAD tools for RF design of mobilephones. *IEEE Antennas and Propagation Magazine*, 45:52–66, Dec. 2003.

[99] P. Futter, N. Chavannes, N. Nikoloski, and N. Kuster. TCAD of mobile phones: heading for a generic modeling approach. *International Congress of the European Bioelectromagnetics Association*, Nov. 2003.

[100] M.J. Ackerman. The visible human project. *Proceedings of the IEEE*, 86(3):504–511, 1998.

[101] A. Christ, M.C. Gosselin, S. Kühn, and N. Kuster. Impact of pinna compression on the RF absorption in the heads of adult and juvenile cell phone users. *Bioelectromagnetics*, 31(5):406–412, 2010.

[102] A. Christ, W. Kainz, E. G. Hahn, K. Honegger, M. Zefferer, E. Neufeld, W. Rascher, R. Janka, W. Bautz, J. Chen, B. Kiefer, Peter Schmitt, H.-P. Hollenbach, J.-X. Shen, M. Oberle, D. Szczerba, A. Kam, J. W. Guag, and N. Kuster. The Virtual Familydevelopment of surface-based anatomical models of two adults and two children for dosimetric simulations. *Physics in Medicine and Biology*, 55(2), Dec. 2009.

[103] IEC. *IEC 62209-1, Human Exposure to Radio Frequency Fields from Handheld and Body-Mounted Wireless Communication Devices Human models, Instrumentation, and Procedures Part 1: Procedure to Determine the Specific Absorption Rate (SAR) for Hand-Held Devices Used in Close Proximity to the Ear (frequency range of 300 MHz to 3 GHz).* International Electrotechnical Committee, 3, rue de Varemb, P.O. Box 131, CH - 1211 GENEVA 20, Switzerland, 2005.

[104] M. Y. Kanda, M. G. Douglas, E. Mendivil, M. Ballen, A. V. Gessner, and C.-K. Chou. Faster determination of mass-averaged SAR from 2-D area scans. *IEEE Transactions on Microwave Theory and Techniques*, 52(8):2013–2020, Aug. 2004.

[105] M. G. Douglas and C.-K. Chou. Accurate and fast estimation of volumetric SAR from planar scans from 30 MHz to 6 GHz. In *Bioelectromagnetics Society Annual Meeting*, Jun. 2007.

[106] M. G. Douglas, B. Derat, C.-H. Li, X.-W. Liao, E. Ofli, N. Chavannes, and N. Kuster. Reliability of specific absorption rate measurements in the head using standardized hand phantoms. In *European Conference on Antennas and Propagation*, 2010.

[107] A. Christ, A. Klingenbock, T. Samaras, C. Goiceanu, and N. Kuster. The dependence of electromagnetic far-field absorption on body tissue composition in the frequency range from 300 mhz to 6 ghz. *Microwave Theory and Techniques, IEEE Transactions on*, 54(5):2188 – 2195, May 2006.

[108] C. K. Chou, H. Bassen, J. Osepchuk, Q. Balzano, R. Petersen, M. Meltz, R. Cleveland, J. C. Lin, and L. Heynick. Radio frequency electromagnetic exposure: Tutorial review on experimental dosimetry. *Bioelectromagnetics*, 17:195–206, 1996.

[109] R. P. Findlay and P. J. Dimbylow. FDTD calculations of specific energy absorption rate in a seated voxel model of the human body from 10 MHz to 3 GHz. *Physics in Medicine and Biology*, 51:23–39, 2006.

[110] C.-H. Li, M. Douglas, E. Ofli, N. Chavannes, Q. Balzano, and N. Kuster. Mechanisms of RF electromagnetic field absorption in

human hands and fingers. *IEEE Transactions on Microwave Theory and Techniques*, 60(7):2267 –2276, july 2012.

[111] D. M. Pozar. *Microwave Engineering*. Wiley, 2nd edition, 1997.

[112] T. Onishi and S. Uebayashi. Influence of phantom shell on SAR measurement in 3-6 GHz frequency range. *IEICE Transactions on Communications*, 88(8):3257, 2005.

[113] IT'IS Foundation. Virtual population project. *online: www.itis.ethz.ch/vip*.

[114] IT'IS Foundation. Dielectric properties of body tissues. *http://www.itis.ethz.ch/services/tissue-properties/database/*.

[115] S. Kühn, W. Jennings, A. Christ, and N. Kuster. Assessment of induced radio-frequency electromagnetic fields in various anatomical human body models. *Physics in Medicine and Biology*, 54:875, 2009.

[116] Robert E. Collin. *Field Theory of Guided Waves, 2nd Edition*. IEEE Press, 1991.

[117] A.C. Lind and J.M. Greenberg. Electromagnetic scattering by obliquely oriented cylinders. *Journal of Applied Physics*, 37(8):3195–3203, 1966.

[118] P. R. Stauffer. Evolving technology for thermal therapy of cancer. *International Journal of Hyperthermia*, 21(8):731–744, Dec. 2005.

[119] H. R. Moyer and K. A. Delman. The role of hyperthermia in optimizing tumor response to regional therapy. *International Journal of Hyperthermia*, 24(3):251–261, May 2008.

[120] Esra Neufeld. *High Resolution Hyperthermia Treatment Planning*. PhD thesis, ETH Zurich, 2008.

[121] K. Ito and K. Saito. *Antennas for Portable Devices; Chapter 5: Antenna Issues in Microwave Thermal Therapies*. Wiley, 2007.

[122] P. R. Stauffer, P. K. Sneed, H. Hashemi, and T. L. Phillips. Practical induction heating coil designs for clinical hyperthermia with ferromagnetic implants. *IEEE Transactions on Biomedical Engineering*, 41(1):17–28, Jan. 1994.

[123] P. Wust, U. Gneveckow, M. Johannsen, D. Boehmer, T. Henkel, F. Kahmann, J. Sehouli, R. Felix, J. Ricke, and A. Jordan. Magnetic nanoparticles for interstitial thermotherapy - feasibility, tolerance and achieved temperatures. *International Journal of Hyperthermia*, 22(8):673–685, Dec. 2006.

[124] A. Jordan, P. Wust, H. Faehling, W. John, A. Hinz, and R. Felix. Inductive heating of ferrimagnetic particles and magnetic fluids: Physical evaluation of their potential for hyperthermia. *International Journal of Hyperthermia*, 25:499–511, 2009.

[125] P. Wust, B. Hildebrandt, G. Sreenivasa, B. Rau, J. Gellermann, H. Riess, R. Felix, and P.M. Schlag. Hyperthermia in combined treatment of cancer. *Lancet Oncology*, 3:487–497, 2002.

[126] R. B. Roemer. Engineering aspects of hyperthermia therapy. *Annual Review of Biomedical Engineering*, 1(1):347–376, 1999.

[127] J. J. W. Lagendijk. Hyperthermia treatment planning. *Physics in Medicine and Biology*, 45:R61–R76, Jan. 2000.

[128] J. B. van de Kamer, A. A. de Leeuw, S. N. Hornsleth, H. Kroeze, A. N. T. J. Kotte, and J. J. W. Lagendijk. Development of a regional hyperthermia treatment planning system. *International Journal of Hyperthermia*, 17:207–220, 2001.

[129] J. J. W. Lagendijk, G. C. van Rhoon, S. N. Hornsleth, P. Wust, A. C. C. de Leeuw, C. J. Schneider, J. D. P. van Dijk, J. van der Zee, R. van Heek-Romanowski, S. A. Rahman, and C. Gromoll. ESHO quality assurance guidelines for regional hyperthermia. *International Journal of Hyperthermia*, 14:125–133, 1998.

[130] G. M. Hahn. Hyperthermia for the engineer: a short biological primer. *IEEE Transactions on Biomedical Engineering*, 31(1):3–8, Jan. 1984.

[131] J. van der Zee. Heating the patient: A promising approach? *Annals of Oncology*, 13:11731184, 2002.

[132] M. W. Dewhirst, Z. Vujaskovic, E. Jones, and D. Thrall. Re-setting the biologic rationale for thermal therapy. *International Journal of Hyperthermia*, 21(8):779–790, Dec. 2005.

[133] R. A. M. Canters, P. Wust, J. F. Bakker, and G. C. Van Rhoon. A literature survey on indicators for characterisation and optimisation of SAR distributions in deep hyperthermia, a plea for standardisation. *International Journal of Hyperthermia*, 25(7):593–608, 2009.

[134] J. Conway and A. P. Anderson. Electromagnetic techniques in hyperthermia. *Clinical Physics and Physiological Measurement*, 7(4):287–318, 1986.

[135] M. Abe and M. Hiraoka. Localized hyperthermia and radiation in cancer therapy. *International Journal of Radiation Biology and Related Studies in Physics, Chemistry, and Medicine*, 47(4):347–59, Apr. 1985.

[136] C.-W. Song, H.-J. Park, C.-K. Lee, and R. Griffin. Implications of increased tumor blood flow and oxygenation caused by mild temperature hyperthermia in tumor treatment. *International Journal of Hyperthermia*, 21(8):761–767, 2005.

[137] J. W. Bergs, N. A. Franken, J. Haveman, E. D. Geijsen, J. Crezee, and C. van Bree. Hyperthermia, cisplatin and radiation trimodality treatment: a promising cancer treatment? a review from preclinical studies to clinical application. *International Journal of Hyperthermia*, 23(4), 2007.

[138] M. Franckenaa, D. Fatehia, M. de Bruijnea, R. A.M. Cantersa, Y. van Nordenc, J. W. Mensa, G. C. van Rhoona, and J. van der Zeea. Hyperthermia dose-effect relationship in 420 patients with cervical cancer treated with combined radiotherapy and hyperthermia. *European Journal of Cancer*, 45:1969–1978, Jul. 2009.

[139] M. W. Dewhirst, B. L. Viglianti, M. Lora-Michiels, M. Hanson, and P. J. Hoopes. Basic principles of thermal dosimetry and thermal thresholds for tissue damage from hyperthermia. *International Journal of Hyperthermia*, 19(3):267–294, 2003.

[140] E. Jones, T. Donald, M. W. Dewhirst, and Z. Vujaskovic. Prospective thermal dosimetry: The key to hyperthermia's future. *International Journal of Hyperthermia*, 22(3):247–253, 2006.

[141] M. Hiraoka, M. Mitsumori, N. Hiroi, S. Ohno, Y. Tanaka, Y. Kotsuka, and K. Sugimachi. Development of RF and microwave heating equipment and clinical applications to cancer treatment in Japan. *IEEE Transactions on Microwave Theory and Techniques*, 48(11):1789–1799, Nov 2000.

[142] M. Franckena, L. J.A. Stalpers, P. C.M. Koper, R. G.J. Wiggenraad, W. J. Hoogenraad, J. D.P. van Dijk, C. C. Warlam-Rodenhuis, J. J. Jobsen, G. C. van Rhoon, and J. van der Zee. Long-term improvement in treatment outcome after radiotherapy and hyperthermia in locoregionally advanced cervix cancer: An update of the Dutch deep hyperthermia trial. *International Journal of Radiation Oncology, Biology, Physics*, 70(4):1176–1182, Mar. 2008.

[143] A. Vasanthan, M. Mitsumori, J.-M. Park, Z.-F. Zeng, Y.-B. Zhong, P. Oliynychenko, H. Tatsuzaki, Y. Tanaka, and M. Hiraoka. Regional hyperthermia combined with radiotherapy for uterine cervical cancers: a multi-institutional prospective randomized trial of the international atomic energy agency. *Internatinal Journal of Radiation Oncology, Biology, Physics*, 61(1):145–153, 2005.

[144] V. D Ambrosio and F. Dughiero. Numerical model for RF capacitive regional deep hyperthermia in pelvic tumors. *Medical and Biological Engineering and Computing*, 45(5):459–466, May 2007.

[145] R. S. Elliott, W. H. Harrison, and F. K. Storm. Hyperthermia: Electromagnetic heating of deep-seated tumors. *IEEE Transactions on Biomedical Engineering*, BME-29(1):61–64, Jan. 1982.

[146] C. Franconi, C. A. Tiberio, L. Raganella, and L. Begnozzi. Low-frequency RF twin-dipole applicator for intermediate depth hyperthermia. *IEEE Transactions on Microwave Theory and Techniques*, 34(5):612–619, May 1986.

[147] A.-Y. Cheung and A. Neyzari. Deep local hyperthermia for cancer therapy: External electromagnetic and ultrasound techniques. *Cancer Research*, 44(10):4736s–4744, 1984.

[148] F. K. Storm, R. S. Elliott, W. H. Harrison, and D. L.Morton. Clinical RF hyperthermia by magnetic-loop induction: A new approach to

human cancer therapy. *IEEE Transactions on Microwave Theory and Techniques*, 30(8):1149–1158, Aug. 1982.

[149] M. Seebass, R. Beck, J. Gellermann, J. Nadobny, and P. Wust. Electromagnetic phased arrays for regional hyperthermia: optimal frequency and antenna arrangement. *International Journal of Hyperthermia*, 17(4):321–336, 2001.

[150] K. D. Paulsen, S. Geimer, J.-W. Tang, and W. E. Boyse. Optimization of pelvic heating rate distributions with electromagnetic phased arrays. *International Journal of Hyperthermia*, 15(3):157–186, 1999.

[151] H. Kroeze, J. B. van de Kamer, A. A. C. de Leeuw, and J. J. W. Lagendijk. Regional hyperthermia applicator design using FDTD modeling. *Physics in Medicine and Biology*, 46:1919–1935, 2001.

[152] G. H. Nussbaum, J. Sidi, N. Rouhanizadeh, P. Morel, C. Jasmin, G. Convert, J. P. Mabire, and G. Azam. Manipulation of central axis heating patterns with a prototype, three-electrode capacitive device for deep-tumor hyperthermia. *IEEE Transactions on Microwave Theory and Techniques*, 34(5):620–625, May 1986.

[153] G. C. van Rhoon, A. G. Visser, P. M. van den Berg, and H. S. Reinhold. Evaluation of ring capacitor plates for regional deep heating. *International Journal of Hyperthermia*, 4(2):133–142, Mar. 1988.

[154] A. A. C. de Leeuw and J. J. W. Lagendijk. Design of a clinical deep-body hyperthermia system based on the 'coaxial TEM' applicator. *International Journal of Hyperthermia*, 3(5):413–421, 1987.

[155] J. R. Oleson. A review of magnetic induction methods for hyperthermia treatment of cancer. *IEEE Transactions on Biomedical Engineering*, BME-31(1):91–97, Jan. 1984.

[156] J. H. Young, M.-T. Wang, and I. A. Brezovich. Frequency/depth-penetration considerations in hyperthermia by magnetically induced currents. *Electronics Letters*, 16(10):358–359, 9 1980.

[157] C. Polk and J.-H. Song. Electric fields induced by low frequency magnetic fields in inhomogeneous biological structures that are surrounded by an electric insulator. *Bioelectromagnetics*, 11(3):235–249, 1990.

[158] C. Polk. Electric fields and surface charges induced by ELF magnetic fields. *Bioelectromagnetics*, 11(2):189–201, 1990.

[159] P. S. Ruggera and G. Kantor. Development of a family of RF helical coil applicators which produce transversely uniform axially distributed heating in cylindrical fat-muscle phantoms. *IEEE Transactions on Biomedical Engineering*, BME-31(1):98–106, Jan. 1984.

[160] M. J. Hagmann and R. L. Levin. Coupling efficiency of helical coil hyperthermia applications. *IEEE Transactions on Biomedical Engineering*, BME-32(7):539–540, Jul. 1985.

[161] J. L. Guerquin-Kern, M. J. Hgmann, and R. L. Levin. Experimental characterization of helical coils as hyperthermia applicators. *IEEE Transactions on Biomedical Engineering*, 35(1):46–51, Jan. 1988.

[162] M. J. Hagmann. Optimization of helical coil applicators for hyperthermia. *IEEE Transactions on Microwave Theory and Techniques*, 36(1):148–150, Jan. 1988.

[163] J. B. Anderson, A. Baun, K. Harmark, L. Heinzl, P. Raskmark, and J. Overgaard. A hyperthermia system using a new type of inductive applicator. *IEEE Transactions on Biomedical Engineering*, BME-31(1):21–27, Jan. 1984.

[164] H. Kato, M. Furukawa, N. Uchida, T. Kasai, Y. Fujita, F. Koda, H. Kuroda, and T. Ishida. Development of inductive heating equipment using an inductive aperture-type applicator. *International Journal of Hyperthermia*, 6:155–168, 1990.

[165] S. Kuroda, N. Uchida, K. Sugimura, and H. Kato. Thermal distribution of radio-frequency inductive hyperthermia using an inductive aperture-type applicator: evaluation of the effect of tumour size and depth. *Medical and Biological Engineering and Computing*, 37(3), May 1999.

[166] R. H. Johnson, A. W. Preece, J. W. Hand, and J. R. James. A new type of lightweight low-frequency electromagnetic hyperthermia applicator. *IEEE Transactions on Microwave Theory and Techniques*, 35(12):1317–1321, Dec. 1987.

[167] T. C. Cetas and R. B. Roemer. Status and future developments in the physical aspects of hyperthermia. *Cancer Research*, 44:4894–4901, Oct. 1984.

[168] H. Kato and T. Ishida. Present and future status of noninvasive selective deep heating using RF in hyperthermia. *Medical and Biological Engineering and Computing*, 31(1):S2–S11, 1992.

[169] Y. Kotsuka, E. Hankui, and Y. Shigematsu. Development of ferrite core applicator system for deep-induction hyperthermia. *IEEE Transactions on Microwave Theory and Techniques*, 44(10):1803–1810, Oct. 1996.

[170] Y. Kotsuka, M. Watanabe, M. Hosoi, I. Isono, and M. Izumi. Development of inductive regional heating system for breast hyperthermia. *IEEE Transactions on Microwave Theory and Techniques*, 48(11):1807–1814, Nov. 2000.

[171] C. Francomi, L. Raganella, C.A. Tiberio, and L. Begnozzi. Low-frequency RF hyperthermia: IV-a 27 MHz hybrid applicator for localized deep tumor heating. *IEEE Transactions on Biomedical Engineering*, 38(3):287–293, Mar. 1991.

[172] H. R. Underwood, A. F. Peterson, and R. L. Magin. Electric-field distribution near rectangular microstrip radiators for hyperthermia heating: theory versus experiment in water. *IEEE Transactions on Biomedical Engineering*, 39(2):146–153, Feb. 1992.

[173] M. V. Prior, M. L. D. Lumori, J. W. Hand, G. Lamaitre, C. J. Schneider, and J. D. P. van Dijk. The use of a current sheet applicator array for superficial hyperthermia: incoherent versus coherent operation. *IEEE Transactions on Biomedical Engineering*, 42(7):694–698, July 1995.

[174] F. Montecchia. Microstrip-antenna design for hyperthermia treatment of superficial tumors. *IEEE Transactions on Biomedical Engineering*, 39(6):580–588, June 1992.

[175] J.-C. Lin, G. Kantor, and A. Ghods. A class of new microwave therapeutic applicators. *Radio Science*, 17:119S–123S, 1981.

[176] G. A. Lovisolo, M. Adami, G. Arcangeli, and A. Borrani. A multi-frequency water-filled waveguide application thermal dosimetry *in vivo*. *IEEE Transactions on Microwave Theory and Techniques*, 32(8):893– 896, Aug. 1984.

[177] N. K. Uzunoglu, E. A. Angelikas, and P. A. Cosmidis. A 432MHz local hyperthermia system using an indirectly cooled, water-loaded waveguide applicator. *IEEE Transactions on Microwave Theory and Techniques*, 35(2):106– 111, Feb. 1987.

[178] M. Krairiksh, C. Thongsopa, D. Srimoon, and A. Mearnchu. Analysis and design of injection-locking steerable active array applicator. *IE-ICE Transactions on Communications*, E85-B(10):2327–2337, 1999.

[179] T. Samaras, P. J. M. Rietveld, and G. C. van Rhoon. Effectiveness of FDTD in predicting SAR distributions from the Lucite cone applicator. *IEEE Transactions on Microwave Theory and Techniques*, 48(11):2059–2063, Nov. 2000.

[180] P. J. M. Rietveld, W. L. J. van Putten, J. van der Zee, and G. C. van Rhoon. Comparison of the clinical effectiveness of the 433 MHz lucite cone applicator with that of a conventional waveguide applicator in applications of superficial hyperthermia. *International Journal of Radiation Oncology, Biology, Physics*, 43:681–687, Feb. 1999.

[181] R. C. Gupta and S. P. Singh. Analysis of the SAR distributions in three-layered bio-media in direct contact with a water-loaded modified box-horn applicator. *IEEE Transactions on Microwave Theory and Techniques*, 53(9):2665–2671, Sep. 2005.

[182] R. C. Gupta and S. P. Singh. SAR characterization of focused planar array of water-loaded modified box-horns for hyperthermia. *International Journal of Infrared and Millimeter Waves*, 27(2):273–291, Feb. 2006.

[183] R. C. Gupta and S. P. Singh. Mutual coupling between box-horn elements of a phased array terminated in three-layered bio-media. *IEEE Transactions on Antennas and Propagation*, 55(8):2219–2227, Aug. 2007.

[184] M. A. Ebrahimi-Ganjeh and A. R. Attari. Study of water bolus effect on SAR penetration depth and effective field size for local hyperthermia. *Progress In Electromagnetics Research*, 4:273–283, 2008.

[185] I. J. Bahl, S. S. Stuchly, J. W. Lagendijk, and M. A. Stuchly. Microstrip loop radiators for local hyperthermia. *MTT-S International Microwave Symposium Digest*, 81(1):465–467, Jun. 1981.

[186] E. R. Lee, T. R. Wilsey, P. Tarczy-Hornoch, D. S. Kapp, P. Fessenden, A. Lohrbach, and S. D. Prionas. Body conformable 915 MHz microstrip array applicators for large surface area hyperthermia. *IEEE Transactions on Biomedical Engineering*, 39(5):470–483, May 1992.

[187] O. A. Arabe, P. F. Maccarini, E. L. Jones, G. Hanna, T. V. Samulski, M. W. Dewhirst, D. E. Thrall, and P. R. Stauffer. A 400 MHz hyperthermia system using rotating spiral antennas for uniform treatment of large superficial and sub-surface tumors. In *IEEE/MTT-S International Microwave Symposium*, pages 1333–1336, Jun. 2007.

[188] BSD Medical Corporation, http://www.bsdmc.com/.

[189] J. E. Johnson, D. G. Neuman, P. F. Maccarini, T. Juang, P. R. Stauffer, and P. Turner. Evaluation of a dual-arm Archimedean spiral array for microwave hyperthermia. *International Journal of Hyperthermia*, 22:475–490, 2006.

[190] G. Lamaitre, J. D. van Dijk, E. A. Gelvich, J. Wiersma, and C. J. Schneider. SAR characteristics of three types of contact flexible microstrip applicators for superficial hyperthermia. *International Journal of Hyperthermia*, 12:255–269, 1996.

[191] E. A. Gelvich and V. N. Mazokhin. Contact flexible microstrip applicators (CFMA) in a range from microwaves up to short waves. *IEEE Transactions on Biomedical Engineering*, 49:1015–1023, 2002.

[192] N. van Wieringen, J. Wiersma, P. zum voerde sive Voerding, S. Oldenborg, E. A. Gelvich, V. N. Mazokhin, J. D. P. van Dijk, and J. Crezee. Characteristics and performance evaluation of the capacitive contact flexible microstrip applicator operating at 70MHz for external hyperthermia. *International Journal of Hyperthermia*, 25:542–553, 2009.

[193] S. Jacobsen, P. R. Stauffer, and D. G. Neuman. Dual-mode antenna design for microwave heating and noninvasive thermometry of superficial tissue disease. *IEEE Transactions on Biomedical Engineering*, 47(11):1500–1509, Nov. 2000.

[194] T. Juang, P. R. Stauffer, D. G. Neuman, and J. L. Schlorff. Multilayer conformal applicator for microwave heating and brachytherapy treatment of superficial tissue disease. *International Journal of Hyperthermia*, 22:527–544, 2006.

[195] P. Stauffer, J. Schlorff, R. Taschereau, T. Juang, D. Neuman, P. Maccarini, J. Pouliot, and J. Hsu. Combination applicator for simultaneous heat and radiation. In *Annual International Conference of the IEEE Engineering in Medicine and Biology Society*, volume 1, pages 2514–2517, Sep. 2004.

[196] M. K. Gopal, J. W. Hand, M. L. D. Lumori, S. Alkhair, K. D. Paulsen, and T. C. Cetas. Current sheet applicator arrays for superficial hyperthermia of chestwall lesions. *International Journal of Hyperthermia*, 8:227–240, 1992.

[197] P. F. Turner. Regional hyperthermia with an annular phased array. *IEEE Transactions on Biomedical Engineering*, BME-31(1):106–114, Jan. 1984.

[198] E. J. Gross, T. C. Cetas, P. R. Stauffer, R.-L. Liu, and M. L. D. Lumori. Experimental assessment of phased-array heating of neck tumours. *International Journal of Hyperthermia*, 6(2):453–474, 1990.

[199] R. V. Sabariego, L. Landesa, and F. Obelleiro. Design of a microwave array hyperthermia applicator with a semicircular reflector. *Medical and Biological Engineering and Computing*, 37(5):612–617, Sep. 1999.

[200] D. Fatehi, J. van der Zee, M. de Bruijne, M. Franckena, and G. C. van Rhoon. RF-power and temperature data analysis of 444 patients with primary cervical cancer: Deep hyperthermia using the Sigma-60 applicator is reproducible. *International Journal of Hyperthermia*, 23(8):623–643, 2007.

[201] D. Fatehi. *Technical Quality of Deep Hyperthermia Using the BSD-2000*. PhD thesis, Erasmus University Rotterdam, 2007.

[202] P. F. Turner. Mini-annular phased array for limb hyperthermia. *IEEE Transactions on Microwave Theory and Techniques*, 34(5):508–513, May 1986.

[203] J. Delannoy, D. LeBihan, D. I. Hoult, and R. L. Levin. Hyperthermia system combined with a magnetic resonance imaging unit. *Medical Physics*, 17(5):855–860, Sep./Oct. 1990.

[204] C.-H. Cho, P. Wust, B. Hildebrant, R. D. Issels, J. Sehouli, T. Kerner, M. Deja, V. Budach, and J. Gellermann. Regional hyperthermia of the abdomen in conjunction with chemotherapy for peritoneal carcinomatosis: Evaluation of two annular-phased-array applicators. *International Journal of Hyperthermia*, 24:399–408, Aug. 2008.

[205] P. Wust, H. Fhling, and W. Wlodarczyk. Antenna arrays in the SIGMA-eye applicator: Interactions and transforming networks. *Medical Physics*, 28:1793–1805, 2001.

[206] J. Nadobny, H. Fahling, M. J. Hagmann, P. F. Turner, W. Wlodarczyk, J. M. Gellermann, P. Deuflhard, and P. Wust. Experimental and numerical investigation of feed-point parameters in a 3-D hyperthermia applicator using different FDTD models of feed networks. *IEEE Transactions on Biomedical Engineering*, 49(11):1348–1359, Nov. 2002.

[207] J. Nadobny, W. Wlodarczyk, L. Westhoff, J. Gellermann, R. Felix, and P. Wust. A clinical water-coated antenna applicator for MR-controlled deep-body hyperthermia: a comparison of calculated and measured 3-D temperature data sets. *IEEE Transactions on Biomedical Engineering*, 52:505–519, Mar. 2005.

[208] J. Nadobny, W. Wlodarczyk, L. Westhoff, and J. Gellermann. Development and evaluation of a three-dimensional hyperthermia applicator with water-coated antennas (WACOA). *Medical Physics*, 30:2052–2064, Jul. 2003.

[209] J. Crezee, P. M. A. van Haaren, H. Westendorp, M. de Greef, H. P. Kok, J. Wiersma, J. Wiersma, G. van Stam, J. Sijbrands, P. zum

voerde sive Voerding, J. D. P. van Dijk, M. C. C. M. Hulshof, and A. Bel. Improving locoregional hyperthermia delivery using the 3-D controlled AMC-8 phased array hyperthermia system: a preclinical study. *International Journal of Hyperthermia*, 25:581–592, 2009.

[210] R. C. Gupta and S. P. Singh. Elliptically bent slotted waveguide conformal focused array for hyperthermia treatment of tumors in curved region of human body. *Progress In Electromagnetics Research*, 62:107–125, 2006.

[211] R. C. Gupta and S. P. Singh. Rutile-loaded slotted rectangular waveguide array for medical applications. *Microwave Conference Proceedings*, 2005.

[212] M. M. Paulides. *Development of a Clinical Head and Neck Hyperthermia Applicator*. PhD thesis, Erasmus University, 2007.

[213] M. M. Paulides, J. F. Bakker, E. Neufeld, J. van der Zee, P. P. Jansen, P. C. Levendag, and G. C. van Rhoon. The HYPERcollar: A novel applicator for hyperthermia in the head and neck. *International Journal of Hyperthermia*, 23(7):567–576, 2007.

[214] M. M. Paulides, J. F. Bakker, A. P. M. Zwamborn, and G. C. van Rhoon. A head and neck hyperthermia applicator: theoretical antenna array design. *International Journal of Hyperthermia*, 23:59–67, 2007.

[215] M. M. Paulides, D. H. M. Wielheesen, J. van der Zee, and G. C. van Rhoon. Assessment of the local SAR distortion by major anatomical structures in a cylindrical neck phantom. *International Journal of Hyperthermia*, 21:125–140, 2005.

[216] M. M. Paulides, S. H. J. A. Vossen, A. P. M. Zwamborn, and G. C. van Rhoon. Theoretical investigation into the feasibility to deposit RF energy centrally in the head and neck region. *International Journal of Radiation Oncology, Biology and Physics*, 63:634–642, 2005.

[217] M. M. Paulides, J. F. Bakker, N. Chavannes, and G. C. van Rhoon. A patch antenna design for application in a phased-array head and neck hyperthermia applicator. *IEEE Transactions on Biomedical Engineering*, 54:2057–2063, 2007.

[218] L. Wu, R. J. McGough, O. A. Arabe, and T. V. Samulski. An RF phased array applicator designed for hyperthermia breast cancer treatments. *Physics in Medicine and Biology*, 51:1–20, 2005.

[219] J. F. Bakker. Heating breast tumors with an ultrasound or electromagnetic cylindrical phased-array. Master's thesis, Department Imaging Science & Technology, Delft University of Technology, Neatherland, 2008.

[220] M. Krairiksh, T. Wakabayashi, and W. Kiranon. A spherical slot array applicator for medical applications. *IEEE Transactions on Microwave Theory and Techniques*, 43(1):78–86, Jan. 1995.

[221] K. H. Sayidmarie and E. U. Taha. Development of a semi-circle phased array for local hyperthermia. *IEEE International Symposium on Microwave, Antenna, Propagation and EMC Technologies for Wireless Communications*, 2:1430–1434, Aug. 2005.

[222] J. Gellermann, J. Goeke, R. Figiel, M. Weiharuch, C.-H. Cho, V. Budach, R. Felix, and P. Wust. Simulation of different applicator positions for treatment of a presacral tumour. *International Journal of Hyperthermia*, 23(1):37–47, 2007.

[223] R. A. M. Canters, M. Franckena, M. M. Paulides, and G. C. van Rhoon. Patient positioning in deep hyperthermia: influences of inaccuracies, signal correction possibilities and optimization potential. *Physics in Medicine and Biology*, 54:39233936, 2009.

[224] C.-H. Li, M. Capstick, E. Neufeld, N. Chavannes, and N. Kuster. Optimization of patient position in hyperthermia treatment for head and neck region. In *IEEE Antennas and Propagation Society International Symposium*, pages 1–4, Jun. 2009.

[225] M. Kowalski, B. Behnia, A. G. Webb, and J.-M. Jin. Optimization of electromagnetic phased-arrays for hyperthermia via magnetic resonance temperature estimation. *IEEE Transactions on Biomedical Engineering*, 49(11):1229–1241, Nov. 2002.

[226] M. E. Kowalski and J.-M. Jin. Model-order reduction of nonlinear models of electromagnetic phased-array hyperthermia. *IEEE Transactions on Biomedical Engineering*, 50(11):1243–1254, Nov. 2003.

[227] G. Arcangeli, P. P. Lombardini, G. A. Lovisolo, G. Marsiglia, and M. Piattelli. Focusing of 915MHz electromagnetic power on deep human tissues: A mathematical model study. *IEEE Transactions on Biomedical Engineering*, BME-31(1):47–52, Jan. 1984.

[228] K. S. Nikita, N. G. Maratos, and N. K. Uzunoglu. Optimization of the deposited power distribution inside a layered lossy medium irradiated by a coupled system of concentrically placed waveguide applicators. *IEEE Transactions on Biomedical Engineering*, 45(7):909–920, Jul. 1998.

[229] W.-C. Chew. *Waves and Fields in Inhomogenous Media*. Wiley-IEEE Press, 1999.

[230] R. V. Sabariego, L. Landesa, and F. Obelleiro. Synthesis of an array antenna for hyperthermia applications. *IEEE Transactions on Magnetics*, 36(4):1696–1699, Jul 2000.

[231] J. Loane, H. Ling, B.F. Wang, and S.W. Lee. Experimental investigation of a retro-focusing microwave hyperthermia applicator: Conjugate-field matching scheme. *IEEE Transactions on Microwave Theory and Techniques*, 34(5):490–494, May 1986.

[232] A. J. Fenn, V. Sathiaseelan, G. A. King, and P. R. Stauffer. Improved localization of energy deposition in adaptive phase-array hyperthermia treatment of cancer. *Lincoln Laboratory Journal*, 9(2):187–195, 1996.

[233] A. J. Fenn, G. L. Wolf, and R. M. Fogle. An adaptive microwave phased array for targeted heating of deep tumours in intact breast: animal study results. *International Journal of Hyperthermia*, 15(1):45–61, 1999.

[234] R. A. Gardner, H. I. Vargas, J. B. Block, C. L. Vogel, A. J. Fenn, G. V. Kuehl, and M. Doval. Focused microwave phased array thermotherapy for primary breast cancer. *Annals of Surgical Oncology*, 9:326–332, 2002.

[235] T. Koehler, P. Maass, P. Wust, and M. Seebass. A fast algorithm to find optimal controls of multiantenna applicators in regional hyperthermia. *Physics in Medicine and Biology*, 46:2503–2514, 2001.

[236] J. T. Loane and S.-W. Lee. Gain optimization of a near-field focusing array for hyperthermia applications. *IEEE Transactions on Microwave Theory and Techniques*, 37(10):1629–1635, Oct. 1989.

[237] N. Siauve, L. Nicolas, C. Vollaire, and C. Marchal. Optimization of the sources in local hyperthermia using a combined finite element-genetic algorithm method. *International Journal of Hyperthermia*, 20(8):815–833, 2004.

[238] *SEMCAD X Version 14.2, Manual, Chapter 15*. SPEAG, 2010.

[239] N. Siauve, L. Nicolas, C. Vollaire, A. Nicolas, and J. A. Vasconcelos. Optimization of 3-D SAR distribution in local RF hyperthermia. *IEEE Transactions on Magnetics*, 40(2):1264–1267, March 2004.

[240] H. P. Hok, P. M. A. van Haaren, J. B. van de Kamer, J. Wiersma, J. D. P. van Dijk, and J. Crezee. High-resolution temperature-based optimization for hyperthermia treatment planning. *Physics in Medicine and Biology*, 50:3127–3141, 2005.

[241] H. P. Kok, P. M. A. van Haaren, J. B. van de Kamer, P. J. Zum Vrde Sive Vrding, J. Wiersma, M. C. C. M. Hulshof, E. D. Geijsen, J. J. B. van Lanschot, and J. Crezee. Prospective treatment planning to improve locoregional hyperthermia for oesophageal cancer. *International Journal of Hyperthermia*, 22:375–389, 2006.

[242] J. Lienemann. *Complexity reduction techniques for advanced MEMS Actuators Simulation*. PhD thesis, Institute for Microsystem Technology, Albert Ludwig University, Freiburg, Germany, 2006.

[243] K.-S. Cheng, V. Stakhursky, P. Stauffer, M. Dewhirst, and S. K. Das. Online feedback focusing algorithm for hyperthermia cancer treatment. *International Journal of Hyperthermia*, 23(7):539–554, Nov. 2007.

[244] K.-S. Cheng, V. Stakhursky, O. I Craciunescu, P. Stauffer, M. Dewhirst, and S. K. Das. Fast temperature optimization of multi-soruce hyperthermia applicators with reduced-order modeling of 'virtual sources'. *Physics Medical Biology*, 53(6):1619–1635, Mar. 2008.

[245] K.-S. Cheng, Y. Yuan, Z. Li, P. R. Stauffer, P. Maccarin, W. T. Joines, M. W. Dewhirst, and S. K. Das. The performance of a reduced-order adaptive controller when used in multi-antenna hyperthermia treatments with nonlinear temperature-dependent perfusion. *Physics in Medicine and Biology*, 54:1979–1995, 2009.

[246] V. L. Stakhursky, K.-S. Cheng, J. Macfall, P. Maccarin, O. Craciunescu, M. W. Dewhirst, and P. R. Staufferand S. K. Das. Real-time MRI-guided hyperthermia treatment using a fast adaptive algorithm. *Physics in Medicine and Biology*, 54:2131–2145, 2009.

[247] R. A. M. Canters, M. Franckena, J van der Zee, and G. C. Van Rhoon. Complaint-adaptive power density optimization as a tool for HTP-guided steering in deep hyperthermia treatment of pelvic tumors. *Physics in Medicine and Biology*, 53:6799–6820, 2008.

[248] E. van der Wal, M. Franckena, D. H. M. Wielheesen, J. van der Zee, and G. C. van Rhoon. Steering in locoregional deep hyperthermia: Evaluation of common practice with 3D-planning. *International Journal of Hyperthermia*, 24(8):682–693, 2008.

[249] Y. Nikawa, M. Kikuchi, and S. Mori. Development and testing of a 2450-MHz lens applicator for localized microwave hyperthermia (short paper). *IEEE Transactions on Microwave Theory and Techniques*, 33(11):1212–1216, Nov. 1985.

[250] Y. Nikawa, H. Watanabeand M. Kikuchi, and S. Mori. A direct-contact microwave lens applicator with a microcomputer-controlled heating system for local hyperthermia. *IEEE Transactions on Microwave Theory and Techniques*, 34(5):626–630, May 1986.

[251] Y. Nikawa and F. Okada. Dielectric-loaded lens applicator for microwave hyperthermia. *IEEE Transactions on Microwave Theory and Techniques*, 39(7):1178–1178, Jul. 1991.

[252] G. Wang and Y. Gong. Metamaterial lens applicator for microwave hyperthermia of breast cancer. *International Journal of Hyperthermia*, 25(6):434–445, 2009.

[253] I. S. Karanasiou, K. T. Karathanasis, A. Garetsos, and N. K. Uzunoglu. Development and laboratory testing of a noninvasive intracranial focused hyperthermia system. *IEEE Transactions on Microwave Theory and Techniques*, 56(9):2160–2171, Sep. 2008.

[254] I. S. Karanasiou, N. K. Uzunoglu, and C. C. Papageorgiou. Towards functional noninvasive imaging of excitable tissues inside the human body using focused microwave radiometry. *IEEE Transactions on Microwave Theory and Techniques*, 52(8):1898–1908, Aug. 2004.

[255] K. Arunachalam, S. S. Udpa, and L. Udpa. Computational feasibility of deformable mirror microwave hyperthermia technique for localized breast tumors. *International Journal of Hyperthermia*, 23(7):577–589, 2007.

[256] A. J. Sangster and K. I. Sinclair. Multimode degenerate mode cavity for microwave hyperthermia treatment. *IEE Proceedings - Microwaves, Antennas and Propagation*, 153(1):75–82, Feb. 2006.

[257] X. Li, E. J. Bond, B. D. van Veen, and S. C. Hagness. An overview of ultra-wideband microwave imaging via space-time beamforming for early-stage breast-cancer detection. *IEEE Antennas and Propagation Magazine*, 47(1):19–34, Feb. 2005.

[258] M. Converse, E. J. Bond, S. C. Hagness, and B. D. Van Veen. Ultrawide-band microwave space-time beamforming for hyperthermia treatment of breast cancer: a computational feasibility study. *IEEE Transactions on Microwave Theory and Techniques*, 52(8):1876–1889, Aug. 2004.

[259] E. J. Bond, X. Li, S. C. Hagness, and B. D. Van Veen. Microwave imaging via space-time beamforming for early detection of breast cancer. *IEEE Transactions on Antennas and Propagation*, 51(8):1690–1705, Aug. 2003.

[260] M. Converse, E. J. Bond, B. D. Veen, and S. C. Hagness. A computational study of ultra-wideband versus narrowband microwave hyperthermia for breast cancer treatment. *IEEE Transactions on Microwave Theory and Techniques*, 54(5):2169–2180, May 2006.

[261] P. Kosmas, E. Zastrow, S. C. Hagness, and B. D. van Veen. A computational study of time reversal techniques for ultra-wideband microwave hyperthermia treatment of breast cancer. *IEEE/SP 14th Workshop on Statistical Signal Processing*, pages 312–316, Aug. 2007.

[262] B. Guo, L.-Z. Xu, and J. Li. Time reversal based microwave hyperthermia treatment of breast cancer. *Microwave and Optical Technology Letters*, 47:335 – 338, 2005.

[263] G. F. Goya, V. Grazu, and M. R. Ibarra. Magnetic nanoparticles for cancer therapy. *Current Nanoscience*, 4(1):1–16, Feb. 2008.

[264] Magforce corporation, http://www.magforce.de.

[265] M. de Bruijne, T. Samaras, J. F. Bakker, and G. C. van Rhoon. Effects of waterbolus size, shape and configuration on the SAR distribution pattern of the Lucite cone applicator. *International Journal of Hyperthermia*, 22(1):15–28, Feb. 2006.

[266] M. L. van der Gaag, M. de Bruijne, T. Samaras, J. van der Zee, and G. C. van Rhoon. Development of a guideline for the water bolus temperature in superficial hyperthermia. *International Journal of Hyperthermia*, 22(8):637–656, Dec. 2006.

[267] M. de Bruijne, T. Samaras, N. Chavannes, and G. C. van Rhoon. Quantitative validation of the 3D SAR profile of hyperthermia applicators using the gamma method. *Physics in Medicine and Biology*, 52:3075–3088, May 2007.

[268] C. Gabriel and S. Gabriel. Compilation of the dielectric properties of body tissues at RF and microwave frequencies. *www.emfdosimetry.org*, Jun. 1996.

[269] C.E. Reuter, A. Taflove, V. Sathiaseelan, M. Piket-May, and B.B. Mittal. Unexpected physical phenomena indicated by FDTD modeling of the Sigma-60 deep hyperthermia applicator. *IEEE Transactions on Microwave Theory and Techniques*, 46(4):313–319, 1998.

[270] iSEG: Medical image segmentation tool. http://www.zurichmedtech.com/products/cls/components/iseg/.

[271] NVIDIA, http://www.nvidia.com.

Curriculum Vitae

Personal Information

- **Date of birth**   20. May 1979
- **Place of birth**   Taipei, Taiwan
- **Citizenship**   Taiwanese
- **Parents**   Jun-Feng Li and Shiu-Lan Liang

Education

- **Department of Electrical Engineering, National Ilan Institute of Agriculture and Technology (now National Ilan University), Taiwan**
  1994 - 2000

- **Department of Electrical Engineering, National Taiwan University of Science and Technology, Taiwan**
  2000 - 2002

- **Department of Electronic Engineering, National Taiwan University of Science and Technology, Taiwan**
  Master Studies
  2002 - 2004

- **Foundation for Research on Information Technologies in Society, Zurich, Switzerland**
  PhD Studies
  2007 - 2013

Theses

- **Master Thesis** *The Experimental Study of Microstrip-Fed Printed Monopole Antenna*
  Department of Electronic Engineering, NTUST, Taiwan
  Supervisor: Prof. Chin-Wen Hsue, NTUST, Taiwan
  2002 - 2004

Employment

- **Military service, Taiwan**
  2004 - 2005

- **Application Engineer of the Numerical EM Simulation Tool, SEM-CAD X**
  Auden Technology Corp., Taiwan
  Supervisor: Annie Yang
  2005 - 2007

- **Application Engineer of the Numerical EM Simulation Tool, SEM-CAD X**
  SPEAG, Switzerland
  Supervisor: Erdem Ofli
  2010 - Now